

RF-COMPENSATED LANGMUIR PROBE DIAGNOSTICS OF
PULSED PLASMA ION IMPLANTATION SYSTEM

A Thesis Submitted to the
College of Graduate and Postdoctoral Studies
in Partial Fulfillment of the Requirements
for the degree of Master of Science
in the Department of Physics & Engineering Physics
University of Saskatchewan
Saskatoon

By
Ayub Khodae

©Ayub Khodae, December 2019. All rights reserved.

PERMISSION TO USE

In presenting this thesis in partial fulfilment of the requirements for a Postgraduate degree from the University of Saskatchewan, I agree that the Libraries of this University may make it freely available for inspection. I further agree that permission for copying of this thesis in any manner, in whole or in part, for scholarly purposes may be granted by the professor or professors who supervised my thesis work or, in their absence, by the Head of the Department or the Dean of the College in which my thesis work was done. It is understood that any copying or publication or use of this thesis or parts thereof for financial gain shall not be allowed without my written permission. It is also understood that due recognition shall be given to me and to the University of Saskatchewan in any scholarly use which may be made of any material in my thesis.

Requests for permission to copy or to make other use of material in this thesis in whole or part should be addressed to:

Head of the Department of Physics & Engineering Physics
163 Physics Building
116 Science Place
University of Saskatchewan
Saskatoon, Saskatchewan
Canada
S7N 5E2

Or

Dean
College of Graduate and Postdoctoral Studies
University of Saskatchewan
116 Thorvaldson Building, 110 Science Place
Saskatoon, Saskatchewan S7N 5C9
Canada

ABSTRACT

The core of this project focuses on the development of a method for prediction of ion implantation dose in processing plasmas. The vital variable is fluence, i.e. ion implantation dose, which is currently predicted by Lieberman model during high-voltage Plasma Ion Implantation (PII). Chapter 1 starts with an introduction of plasma ion implantation. In chapter 2, a review of Lieberman model's assumptions as well as a discussion on the limitations of model and the observed discrepancies with measurements are provided.

Having a better, more accurate model to get the fluence, is necessary for improving the implantation procedure. Inductively Coupled Plasma (ICP) chambers are used widely for plasma ion implantation. One of the ICP chambers in University of Saskatchewan, ICP-600, is provided with a radio-frequency antenna to provide the power to heat the electrons and therefore ionise the gas. The apparatus is discussed in detail in chapter 3.

To have an understanding of the evolution of the plasma during plasma ion implantation (PII), a full characterisation of plasma is required before and during PII. Acquiring plasma parameters accurately has the utmost importance while characterising plasma with a Langmuir probe. Eliminating radio-frequency waves from the acquired current-voltage curves in a RF-driven plasma has the most effect toward improving electron temperature measurements in such plasmas. In chapter 4, the importance of RF-compensation in design and implementation of Langmuir probes is discussed in detail. Also, a discussion on different current-voltage analysis theories is provided.

The results of this work is presented in chapter 5. Demonstrating the importance, RF-compensated results in the steady state argon plasma will be presented in the first part of the chapter. Finally, the time-resolved characterisation of plasma during PII for a metal target, namely stainless steel and a semiconductor target, i.e. silicon, will be presented and discussed in the later part of the same chapter. These experimental data are an important step in order to develop a more accurate model for plasma ion implantation through detecting and taking into account the effective instabilities during the process.

ACKNOWLEDGEMENTS

I would like to express my utmost appreciation to both of my supervisors, Dr. Michael P. Bradley and Dr. Lénaïc Couëdel for their caring team of supervision and discussion circle, who supported me throughout my M.Sc. study with their expertise and knowledge. I appreciate Dr. Bradley's enthusiastic guidance and insight during my M.Sc. studies, from the start to its end. I thank Dr. Couëdel, who has given me direction so that I could grow, but also left the space so I could find myself as a researcher. I am extremely grateful that I worked with their team and had their generous support during my M.Sc.

I would like to thank Dave McColl for his generous help and tutoring with fabrication and data acquisition technicalities throughout the lab work. I would also like to thank the machine shop team, Ted Toporowski, James McGregor. I also should acknowledge Dr. Amir Farahani's help through discussions.

I would also acknowledge my committee members, Dr. Chijin Xiao, Dr. Robert J. Green and Dr. Andrei I. Smolyakov. They provided me many detailed comments on my thesis and also encouraged me to think about my research in a more conceptual manner. I appreciate all members of UofS Plasma Physics Group for the many helpful and insightful discussions and interactions that I have had with them: Igor, Alex, Joel, William, Sasha, and Jeffery.

I wish to thank the other members of the Department of Physics Engineering Physics for creating such a compelling learning environment. I especially would like to thank the main office staff, Debbie, Marj, and other members who have been supportive and friendly, giving the department an energetic atmosphere.

It is a pleasure to thank my great friends who have always been a major source of support, encouragement and fruitful discussions during all single moments of my life: Zana, Bardia, Jamshid, Arwin, Arash, Azad and many others for discussions and supports. I thank all my family members. My sisters, Saeideh, Roqayeh, Ghomri; and my brothers, Sadi, Najmaddin and Abdulhamid. I have never been able to pursue my curiosities without their unconditional supports. At the end, my warmest gratitude goes to my father and mother, and of course Niyusha, who experienced all the moments in this chapter of my life closely with me, from the start to its end.

To Niyusha.

CONTENTS

Permission to Use	i
Abstract	ii
Acknowledgements	iii
Contents	v
List of Tables	vii
List of Figures	viii
List of Abbreviations	xviii
1 Introduction	1
1.1 Plasma Ion Implantation	1
2 Modelling Plasma Ion Implantation	4
2.1 Lieberman's Sheath Model	5
2.1.1 Transient Matrix Sheath	7
2.1.2 Steady State High Voltage Sheath: The Child-Langmuir Sheath	8
2.2 Validity of Lieberman's Assumptions	9
3 Plasma Ion Implantation (PII) Apparatus	13
3.1 ICP II-600 Chamber	13
3.2 Other Components	15
3.2.1 Gas and Pressure Controllers	15
3.2.2 Power Generator and Controller	16
3.2.3 The Marx High-Voltage Pulser	17
3.2.4 High-Voltage Monitoring	17
3.2.5 Langmuir Probe	17
3.3 Langmuir Probe Data Acquisition System	18
3.3.1 The Data Acquisition Setup For Time-Resolved Measurements	19
4 Plasma Diagnostics: Langmuir Probe	20
4.1 Langmuir Probe	20
4.1.1 Maxwellian Electrons	22
4.1.2 Non-Maxwellian Electrons	22
4.2 Potential Oscillation in RF Plasmas	24
4.2.1 Radio Frequency (RF) Compensation	25
4.3 Design of RF-compensated Langmuir Probe	26
4.3.1 Choke Coils Characterisation	26
4.4 Langmuir Probe Analysis Theories	28
4.4.1 Cylindrical Langmuir Probe With Collisionless Sheath - Orbital Motion Limit (OML) Theory	28
4.4.2 Allen-Boyd-Reynolds (ABR) Theory	30
4.4.3 Bernstein-Rabinowitz-Laframboise (BRL) Theory	31
5 Experimental Results: Steady State and Pulsed Argon Plasmas	32
5.1 Steady State Plasma Characterisation	32

5.1.1	Measurements of Plasma Density at Constant Pressure	32
5.1.2	Measurements of Electron Temperature at Constant Pressure	33
5.1.3	Measurements of Plasma Density at Constant RF-power	36
5.1.4	Measurements of Electron Temperature at Constant RF-power	38
5.1.5	Radial profiles of Plasma Density and Electron Temperature	39
5.2	Pulsed Plasma Studies Using Stainless Steel Target Plate in Argon Plasma	41
5.2.1	Time-Resolved Measurements of Floating Potential in Pulsed Argon Plasma - Stainless Steel Target	43
5.2.2	Measurements of Floating Potential at Constant RF-powers	44
5.3	Pulsed Plasma Studies Using Silicon Target Plate	57
5.3.1	Time-Resolved Measurements of Floating Potential in Pulsed Argon Plasma - Silicon Target	57
5.4	Floating Potential Analysis of Stainless Steel and Silicon Targets	61
5.4.1	Short Time Scale Analysis	61
5.4.2	Long Time Scale Analysis	66
5.5	Time-Resolved I-V Curve Analysis For Pulsed Stainless Steel and Silicon Targets	70
5.5.1	Measurement of Probe Current $I_p(t)$ During Pulsed Target Bias	70
5.5.2	Construction of Time-Resolved IV Curves From Probe Current Measurements In Pulsed Target Regime	71
5.5.3	Analysis of Time-Resolved IV Curves in Pulsed Target Regime	72
5.5.4	Langmuir Analysis of Time-Resolved IV Curves in Pulsed Target Regime	75
5.5.5	Study of Variable Pulse Magnitude: -1 kV vs. -4 kV	76
5.5.6	Study of Variable RF-Power: 120 W vs. 300 W	85
5.5.7	Study of Variable Argon Gas Pressure: 1.5 mTorr vs. 25 mTorr	91
5.5.8	Case Study of Silicon and Stainless Steel Targets - $P_{Ar}= 1.5$ mTorr, $P_{RF}= 120$ W	91
5.6	Plasma Density-Enhancement Effect on Dosimetry	100
5.7	Physical Interpretation of the Results	103
6	Conclusion	112
6.1	Future Work	114
6.1.1	Experimental Frontier	114
6.1.2	Modelling	115
	References	117
	Appendix A RF-compensated Probe: Potential Measurements	121
A.1	Steady State Argon Plasma Potential	121
A.1.1	Plasma Potential at Constant Pressure	121
A.1.2	Plasma Potential at Constant RF-Power	124
	Appendix B Uncompensated Langmuir Probe's Measurements	127
B.0.1	Plasma Density	127
B.1	Overestimation of Electron Temperature by Uncompensated Probe	128
B.1.1	Plasma and floating Potentials	128
B.1.2	Electron Temperature	128
	Appendix C RF-compensated Langmuir Probe Mechanical Design	131

LIST OF TABLES

3.1	Important parameters for ICP-2 chamber	13
5.1	Steady state plasma parameters in upper probe location, i.e. $z_p = 21.7$ cm above the stainless steel target	104
5.2	Steady state plasma parameters in lower probe location, i.e. $z_p = 8.7$ cm above the stainless steel target	104
5.3	A summary of the general tendency of the plasma parameters in ICP, for both upper and lower probe locations. The results are shown for region 1 (before the pulse starts at $t = -5.0 \mu s$) and region 2 (coincides with the rise of the pulse between $t = -5.0 \mu s$ to $t = -4.0 \mu s$).	105
5.4	A summary of the general tendency of the plasma parameters in ICP, for both upper and lower probe locations. The results are shown for region 3 (during the pulse plateau between $t = -4.0 \mu s$ to $t = -1.0 \mu s$) and region 4 (coincides with the fall time of the pulse between $t = -1.0 \mu s$ to $t = -0.0 \mu s$).	106
5.5	A summary of the general tendency of the plasma parameters in ICP, for both upper and lower probe locations. The results are shown for region 5 (after the pulse ends at $t = 0.0 \mu s$ to $t = 20 \mu s$ when the current through the target becomes zero in the case of $V_{pulse} = -4$ kV) and region 6 (after $t = -20.0 \mu s$ to the next pre-pulse at $t = 4$ ms.	107

LIST OF FIGURES

1.1	Schematic of PII process; the substrate is biased to a squared-shape high voltage in the order of 1 kV or 10 kV and duration orders of 1 or 10 μ s	3
2.1	The condition for a collisionless sheath within ion density of PII in ICP-2	11
2.2	(a) $V_{pulse} = -5$ kV smoothed voltage pulse input to a stainless steel target acquired earlier for this work, as generated by ICP-2 pulser; with 7.5 μ s duration. The voltage fluctuations in the grounded region are about 200 V. (b) Measured current density from Pearson model 150 Rogowski coil vs. predicted current by p2i code. The applied bias voltage is shown in figure 2.2a.	12
3.1	ICP-2 Plasma processing setup as of Spring 2018. (A. Gas and plasma control, B. Feed gas, C. Processing chamber, D. RF antenna and matching network, E. Transformer, F. Pulser, G. Pulser control)	14
3.2	ICP-2 stand rod without the sample holder, as used in the current project. The dimensions are given in the photo.	15
3.3	A schematic of ICP-2 Plasma processing chamber gas-flow controllers and pump-down systems. ARV, GV, FBV stand for Auxiliary Roughing Valve, Gate Valve, and Fore-line Block Valve, respectively.	16
3.4	(a) Photo of the assembled uncompensated Langmuir probe built and used to acquire data presented in appendix B in order to make possible the comparison of the RF-compensated and uncompensated probe measurements. (b) RF-compensated Langmuir probe with electrode used for acquiring data presented in chapter 5 and appendix A.	18
3.5	Schematic of the Langmuir probe control circuit. The Apex PA341 high voltage power operational amplifier amplifies the bias voltage from the DAQ by 10 \times before feeding it to the Langmuir probe. The current through the sense resistor R_5 is measured by the INA117 high common-mode voltage difference amplifier.	19
4.1	A sample I-V curve acquired by a Langmuir probe in RF-ICP Ar plasma for this work. . . .	21
4.2	A semi-logarithmic plot of electron current as a function of probe bias voltage from I-V curve acquired in RF-ICP plasma - similar to I-V curve shown in figure 4.1. The I-V curve is acquired in argon gas pressure $P_{Ar} = 1.5$ mTorr, $P_{RF} = 120$ W at the axial location of 21.7 cm above the stainless steel target.	23
4.3	An example of the floating potential V_f of an uncompensated probe in a RF-driven plasma. (a) Wave-pattern of the floating potential V_f of the uncompensated Langmuir probe measured directly by an oscilloscope. (b) Frequency spectrum of V_f obtained by FFT of the top figure.	25
4.4	The correct I-V curve is at the centre and the other two dashed curves have ± 5 V difference in their V_p measurements. This difference, i.e. shift in the plasma potential measurement is because of RF-oscillation effect of the plasma under study.	26
4.5	Measurement circuit to obtain transmission scattering vector (S_{21}) for RF-compensated Langmuir probe, as well as the RLC chokes individually.	27
4.6	Plot of voltage transfer function $S_{21} = \frac{v_2}{v_1}$ as a function of frequency, acquired from the final assembly of the RF-compensated Langmuir probe. The Impedance is less than 22 dB below 1 MHz and about 60.2 dB and 50.6 dB at 13.56 MHz and 27.12 MHz respectively.	27
4.7	The diagram shows the impact factor h and the closest approach point of the particles to the cylindrical Langmuir probe's tip, i.e. point g.	28

5.1	Steady state Ar plasma density as a function of RF-power in two different Argon gas pressures, on an axis location 21.7 cm above stainless steel target. Note that four different analysis methods (Druyvesteyn, Langmuir, ABR, and OML) were used to analyse each Langmuir probe curve as described in previous chapter 4. The spread on the power axis is artificial and just there to increase visibility of the data points.	33
5.2	Steady state Ar plasma density as a function of RF-power, on the axis location 8.7 cm above stainless steel target. Note that four different analysis methods (Druyvesteyn, Langmuir, ABR, and OML) were used to analyse each Langmuir probe curve as described in chapter 4. The spread on the power axis is artificial and just there to increase visibility of the data points.	34
5.3	Steady state Ar electron temperature as a function of RF-power at two different Argon gas pressures, on an axis location 21.7 cm above stainless steel target. Note that two different analysis methods (Druyvesteyn and Langmuir) were used to analyse each Langmuir probe curve as described in previous chapter 4. The spread on the power axis is artificial and just there to increase visibility of the data points.	35
5.4	Steady state Ar electron temperature as a function of RF-power at two different Argon gas pressures, on an axis location 8.7 cm above stainless steel target. Note that two different analysis methods (Druyvesteyn and Langmuir) were used to analyse each Langmuir probe curve as described in previous chapter 4. The spread on the power axis is artificial and just there to increase visibility of the data points.	35
5.5	Steady state Ar plasma density as a function of Argon gas pressure at two different RF-powers, on an axis location 21.7 cm above stainless steel target. Note that four different analysis methods (Druyvesteyn, Langmuir, ABR, and OML) were used to analyse each Langmuir probe curve as described in previous chapter 4. The spread on the pressure axis is artificial and just there to increase visibility of the data points.	37
5.6	Steady state Ar plasma density as a function of Argon gas pressure at two different RF-powers, on an axis location 8.7 cm above stainless steel target. Note that four different analysis methods (Druyvesteyn, Langmuir, ABR, and OML) were used to analyse each Langmuir probe curve as described in previous chapter 4. The spread on the pressure axis is artificial and just there to increase visibility of the data points.	37
5.7	Steady state Ar electron temperature as a function of Argon gas pressure at two RF-powers, on an axis location 21.7 cm above stainless steel target. Note that four different analysis methods (Druyvesteyn, Langmuir, ABR, and OML) were used to analyse each Langmuir probe curve as described in previous chapter 4. The spread on the pressure axis is artificial and just there to increase visibility of the data points.	38
5.8	Steady state Ar electron temperature as a function of argon gas pressure at two RF-powers, on an axis location 8.7 cm above stainless steel target. Note that two different analysis methods (Druyvesteyn and Langmuir) were used to analyse each Langmuir probe curve as described in previous chapter 4. The spread on the pressure axis is artificial and just there to increase visibility of the data points.	39
5.9	Ar plasma density radial profile, $z_p = 21.7$ cm above stainless steel target plate, $P_{RF} = 300$ W, Argon pressure $P_{Ar} = 25$ mTorr. The spread on the x-axis is artificial and just there to increase visibility of the data points.	40
5.10	Ar electron temperature radial profile, $z_p = 21.7$ cm above stainless steel target plate, $P_{RF} = 300$ W, Ar gas pressure $P_{Ar} = 25$ mTorr. The spread on the x-axis is artificial and just there to increase visibility of the data points.	41
5.11	(a) -1 kV and -4 kV high voltage pulse biased to a stainless steel target immersed in Ar plasma with pressure $P_{Ar} = 25$ mTorr and RF-power $P_{RF} = 120$ W. (b) A zoom in time of high voltage pulse, showing regions 2, 3, 4. (c) Shows the current going through the stand measured by Rogowski coil during each pulse. (d) A zoom in time of current through the target, showing the rise of the current in region 2, plateau of the current in region 3, and the fall in region 4 more clearly.	42

- 5.12 (a) Ar plasma floating potential V_f , during a single -4 kV, 5 μ s duration pulse (pulse repetition frequency, prf= 250 Hz). The probe position was 8.7 cm above the pulsed stainless steel target. Ar plasma with fixed RF-power P_{Ar} = 1.5 mTorr. Note that compared with figure 5.11, these data are plotted on a much longer ($\times 1000$) time scale. This was done in order to make plain the relatively long time required for the plasma to return to the initial state after the pulse. (b) The long time scale floating potential, normalised to the steady state floating potential before the pulse, showing the relative changes of each floating potential. (c) Shows a zoom in time of the same floating potential at a short time scale about the pulse within the range shown in figure 5.11, (d) shows the relative changes by normalising the floating potential to its steady state before the pulse. 45
- 5.13 (a) Ar plasma floating potential V_f , during a single -4 kV, 5 μ s duration pulse (pulse repetition frequency, prf= 250 Hz). The probe position was z_p = 21.7 cm above the pulsed stainless steel target. Ar plasma with fixed RF-power P_{RF} = 300 W. Note that compared with figure 5.11, these data are plotted on a much longer ($\times 1000$) time scale. This was done in order to make plain the relatively long time required for the plasma to return to the initial state after the pulse. (b) The long time scale floating potential, normalised to the steady state floating potential before the pulse, showing the relative changes of each floating potential. (c) Shows a zoom in time of the same floating potential at a short time scale about the pulse, (d) shows the relative changes by normalising the floating potential to its steady state before the pulse. 47
- 5.14 Variation of plasma floating potential V_f during a single -4 kV, 5 μ s duration pulse, for three different values of pressure. Probe location z_p = 21.7 cm above the pulsed stainless steel target. Ar plasma RF-power P_{RF} = 120 W. (b) The long time scale floating potential, normalised to the steady state floating potential before the pulse, showing the relative changes of each floating potential. (c) Shows a zoom in time of the same floating potential at a short time scale about the pulse, (d) shows the relative changes by normalising the floating potential to its steady state before the pulse. 48
- 5.15 (a) Ar plasma floating potential V_f , during a single -4 kV, 5 μ s duration pulse (pulse repetition frequency, prf= 250 Hz). The probe position was 8.7 cm above the pulsed stainless steel target. Ar plasma with fixed RF-power P_{RF} = 300 W. Note that compared with figure 5.11, these data are plotted on a much longer ($\times 1000$) time scale. This was done in order to make plain the relatively long time required for the plasma to return to the initial state after the pulse. (b) The long time scale floating potential, normalised to the steady state floating potential before the pulse, showing the relative changes of each floating potential. (c) Shows a zoom in time of the same floating potential at a short time scale about the pulse, (d) shows the relative changes by normalising the floating potential to its steady state before the pulse. 50
- 5.16 (a) Ar plasma floating potential V_f , during a single -4 kV, 5 μ s duration pulse (pulse repetition frequency, prf= 250 Hz). The probe position was 8.7 cm above the pulsed stainless steel target. Ar plasma with fixed RF-power P_{RF} = 120 W. Note that compared with figure 5.11, these data are plotted on a much longer ($\times 1000$) time scale. This was done in order to make plain the relatively long time required for the plasma to return to the initial state after the pulse. (b) The long time scale floating potential, normalised to the steady state floating potential before the pulse, showing the relative changes of each floating potential. (c) Shows a zoom in time of the same floating potential at a short time scale about the pulse, (d) shows the relative changes by normalising the floating potential to its steady state before the pulse. 52

5.17 (a) A comparison of Ar plasma floating potential for two different pulse magnitudes applied to the stainless steel target. Both pulses have 5 μ s duration pulse with the repetition rate of 250 Hz. The magnitudes are -1 kV during the plateau of the pulse (about 3 μ s) and -4 kV. The floating potentials are recorded 8.7 cm above the pulsed stainless steel target, Ar plasma pressure P_{Ar} = 1.5 mTorr. (b) The long time scale floating potential, normalised to the steady state floating potential before the pulse, showing the relative changes of each floating potential. (c) Shows a zoom in time of the same floating potential at a short time scale about the pulse, (d) Shows the relative changes by normalising the floating potential to its steady state before the pulse. (e) Shows the corresponding high voltage pulses, applied to the stainless steel target and (f) shows the current through the stainless steel target for both pulses, with Ar plasma pressure P_{Ar} = 1.5 mTorr and RF-power P_{RF} = 120 W.	54
5.18 (a) A comparison of Ar plasma floating potential for two different pulse duration applied to the stainless steel target. Both pulses have -4 kV magnitude during the plateau of the pulse, with the repetition rate of 250 Hz. The duration of the pulses are 5 μ s and 8 μ s. The floating potentials are recorded 21.7 cm above the pulsed stainless steel target, 25 mTorr plasma pressure, P_{RF} = 120 W. (b) Comparison of their relative changes with respect to the mean value of steady state floating potential between 20 to 10 μ s before the end of the pulses. (c) Shows the high voltage pulse and (d) shows the current through the stainless steel target measured by Rogowski coil.	56
5.19 (a) Floating potential for silicon and stainless steel targets during a -4kV with 5 μ s duration pulse. Argon gas pressure P_{Ar} = 1.5 mTorr, P_{RF} = 300 W. Axial probe location z_p = 21.7 cm above the targets. (b) Shows the normalised floating potentials, with respect to their steady state floating potential, a mean value of floating potentials between t = -15 μ s and t = -10 μ s. (c) Shows the floating potential, the short time scale around the pulse, δt = 10 μ s before the start of the pulse to δt = 30 μ s after the end of the pulse. (d) Shows the same short time scale floating potentials, normalised with respect to their steady state floating potentials. The spread on the vertical axis is artificial and just there to increase visibility of the data points.	58
5.20 (a) shows floating potential for silicon and stainless steel targets during a -4kV with 5 μ s duration pulse. Argon gas pressure P_{Ar} = 1.5 mTorr, P_{RF} = 120 W. Axial probe location z_p = 21.7 cm above the targets. (b) Shows the normalised floating potential, with respect to their steady state floating potential, a mean value of floating potentials between t = -15 μ s and t = -10 μ s. Figure (c) is measured currents through each target for both silicon and stainless plates.	60
5.21 The floating potential minima measurements for stainless steel and silicon pulsed targets during the high voltage pulse. Data acquired in the lower probe location z_p = 21.7 cm above each target. Each target was biased negatively to a 4 kV pulse with duration of 5 μ s and repetition frequency of 250 Hz.	62
5.22 The floating potential minima measurements for stainless steel and silicon pulsed targets during the high voltage pulse. Data acquired in the lower probe location z_p = 8.7 cm above each target. Each target was biased negatively to a 4 kV pulse with duration of 5 μ s and repetition frequency of 250 Hz.	63
5.23 First peak height measurements for stainless steel and silicon pulsed targets, occurring \sim 1 μ s after pulse ends. Data acquired in the lower probe location z_p = 21.7 cm above each target. Each target was biased negatively to a 4 kV pulse with duration of 5 μ s and repetition frequency of 250 Hz.	64
5.24 First peak height measurements for stainless steel and silicon pulsed targets, occurring \sim 1 μ s after pulse ends. Data acquired in the lower probe location z_p = 8.7 cm above each target. Each target was biased negatively to a 4 kV pulse with duration of 5 μ s and repetition frequency of 250 Hz.	65
5.25 The decay time constant of the floating potential, i.e. relaxation time constants for stainless steel and silicon pulsed targets after occurrence of the first peak after the pulse. Data acquired in the lower probe location z_p = 21.7 cm above each target. Each target was biased negatively to a 4 kV pulse with duration of 5 μ s and repetition frequency of 250 Hz.	66

5.26	The decay time constant of the floating potential, i.e. relaxation time constants for stainless steel and silicon pulsed targets after occurrence of the first peak after the pulse. Data acquired in the lower probe location $z_p= 8.7$ cm above each target. Each target was biased negatively to a 4 kV pulse with duration of $5 \mu s$ and repetition frequency of 250 Hz.	67
5.27	The second peak height measurements for stainless steel and silicon pulsed targets. Data acquired in the lower probe location $z_p= 21.7$ cm above each target. Each target was biased negatively to a 4 kV pulse with duration of $5 \mu s$ and repetition frequency of 250 Hz.	68
5.28	The second peak height measurements for stainless steel and silicon pulsed targets. Data acquired in the lower probe location $z_p= 8.7$ cm above each target. Each target was biased negatively to a 4 kV pulse with duration of $5 \mu s$ and repetition frequency of 250 Hz.	68
5.29	The decay time constant of the floating potential, i.e. relaxation time constants for stainless steel and silicon pulsed targets, after the second "smooth" peak of floating potential. Data acquired in the lower probe location $z_p= 21.7$ cm above each target. Each target was biased negatively to a 4 kV pulse with duration of $5 \mu s$ and repetition frequency of 250 Hz.	69
5.30	The decay time constant of the floating potential, i.e. relaxation time constants for stainless steel and silicon pulsed targets, after the second "smooth" peak of floating potential. Data acquired in the lower probe location $z_p= 8.7$ cm above each target. Each target was biased negatively to a 4 kV pulse with duration of $5 \mu s$ and repetition frequency of 250 Hz.	70
5.31	probe's collected current from Ar plasma during a single -4 kV pulse with $5 \mu s$ duration applied at 250Hz frequency to a stainless steel target 8.7 cm below the probe's tip. Plasma pressure was 1.5 mTorr with 120 W RF-power. 90 current curves during each pulse have been acquired from -35 V to 57 V with 1 V voltage steps. Only 6 curves are shown here as an example of the acquired data. Note that (b) is zoom in time range of figure (a).	71
5.32	Time-resolved constructed I-V curves in different times, argon plasma pressure $P_{Ar}= 1.5$ mTorr, RF-power $P_{RF}= 120$ W. The curves are acquired in different times during the cycle of a -4 kV with $5 \mu s$ duration pulse bias with repetition frequency of 250 Hz at probe location 8.7 cm above the stainless steel target. See figure 5.31 for the time reference. $t_1=-10 \mu s$ is acquired before pulse and after the relative recovery of plasma to the steady state. The constructed I-V curve has different characteristics to steady state, meaning plasma has not been quite recovered to steady state yet from the previous pulse. As expected, the I-V curve at the time of the highest floating potential has more deviation from steady state, with a high floating potential and colder electrons (less $V_p - V_f$).	72
5.33	Time-resolved plasma potentials, Argon plasma pressure $P_{Ar}= 1.5$ mTorr, RF-power $P_{RF}= 120$ W. The curves are acquired in different times during the cycle of a -4 kV with $5 \mu s$ duration pulse bias with repetition frequency of 250Hz at probe location 8.7 cm above the stainless steel target. See figure 5.31 for the time reference.	73
5.34	Time-resolved electron temperatures, Argon plasma pressure $P_{Ar}= 1.5$ mTorr, RF-power $P_{RF}= 120$ W. The curves are acquired in different times during the cycle of a -4 kV with $5 \mu s$ duration pulse bias with repetition frequency of 250 Hz at probe location 8.7 cm above the stainless steel target. See figure 5.31 for the time reference. $t_1=-10 \mu s$ is acquired before pulse and after the relative recovery of plasma to the steady state.	74
5.35	An un-smoothed curve acquired at time $t_7 = 3.4 \mu s$ right after the end of the pulse. The target is silicon. It can be hardly seen that based on the "knee" of this curve the plasma potential might be around $V_B = V_p \approx 30$ V, separating the exponential region from the linear electron saturation region. Given the high floating potential at this point (the I-V curve is acquired at the first post pulse floating potential peak). Additionally, it is better to use the electron saturation part of the curve for analysis, as the ion saturation is in the order of the oscilloscope voltage resolution limit.	74
5.36	Time-resolved plasma potentials, Argon plasma pressure $P_{Ar}= 1.5$ mTorr, RF-power $P_{RF}= 120$ W. The curves are acquired in different times during the cycle of a -4 kV with $5 \mu s$ duration pulse bias with repetition frequency of 250 Hz at probe location 21.7 cm above silicon and stainless steel targets. The pulse starts at $t=-5 \mu s$ and ends at $t=0 \mu s$	76

5.37	Time-resolved I-V characteristic curves, Argon plasma pressure $P_{Ar}= 1.5$ mTorr, RF-power $P_{RF}= 120$ W. The curves are acquired in different times during the cycle of a -4 kV with $5 \mu s$ duration pulse bias with repetition frequency of 250 Hz at probe location 8.7 cm above silicon and stainless steel targets. The pulse starts at $t=-5 \mu s$ and ends at $t=0 \mu s$	77
5.38	Time-resolved plasma potentials, Argon plasma pressure $P_{Ar}= 1.5$ mTorr, RF-power $P_{RF}= 120$ W. The curves are acquired in different times during the cycle of a -4 kV and -1 kV, both with $5 \mu s$ duration pulse bias with repetition frequency of 250 Hz at probe location 8.7 cm above the stainless steel target. The grey shade indicates the error boundaries.	78
5.39	Time-resolved plasma potentials, Argon plasma pressure $P_{Ar}= 1.5$ mTorr, RF-power $P_{RF}= 120$ W. The curves are acquired in different times during the cycle of a -4 kV and -1 kV, both with $5 \mu s$ duration pulse bias with repetition frequency of 250 Hz at probe location 8.7 cm above the silicon target. The grey shade indicates the error boundaries.	79
5.40	Time-resolved electron temperatures, Argon plasma pressure $P_{Ar}= 1.5$ mTorr, RF-power $P_{RF}= 120$ W. The curves are acquired in different times during the cycle of a -4 kV and -1 kV, both with $5 \mu s$ duration pulse bias with repetition frequency of 250 Hz at probe location 8.7 cm above the stainless steel target. The grey shade indicates the error boundaries.	80
5.41	Time-resolved electron temperature, Argon plasma pressure $P_{Ar}= 1.5$ mTorr, RF-power $P_{RF}= 120$ W. The curves are acquired in different times during the cycle of a -4 kV and -1 kV, both with $5 \mu s$ duration pulse bias with repetition frequency of 250 Hz at probe location 8.7 cm above the silicon target. The grey shade indicates the error boundaries.	82
5.42	Time-resolved electron densities, Argon plasma pressure $P_{Ar}= 1.5$ mTorr, RF-power $P_{RF}= 120$ W. The curves are acquired in different times during the cycle of a -4 kV and -1 kV, both with $5 \mu s$ duration pulse bias with repetition frequency of 250 Hz at probe location 8.7 cm above the stainless steel target. The grey shade indicates the error boundaries.	83
5.43	Time-resolved plasma densities, Argon plasma pressure $P_{Ar}= 1.5$ mTorr, RF-power $P_{RF}= 120$ W. The curves are acquired in different times during the cycle of a -4 kV and -1 kV, both with $5 \mu s$ duration pulse bias with repetition frequency of 250 Hz at probe location 8.7 cm above the silicon target. The grey shade indicates the error boundaries.	84
5.44	Time-resolved ion densities, Argon plasma pressure $P_{Ar}= 1.5$ mTorr, RF-power $P_{RF}= 120$ W. The curves are acquired in different times during the cycle of a -4 kV and -1 kV, both with $5 \mu s$ duration pulse bias with repetition frequency of 250 Hz at probe location 8.7 cm above the stainless steel target. The grey shade indicates the error boundaries.	85
5.45	Time-resolved ion densities, Argon plasma pressure $P_{Ar}= 1.5$ mTorr, RF-power $P_{RF}= 120$ W. The curves are acquired in different times during the cycle of a -4 kV and -1 kV, both with $5 \mu s$ duration pulse bias with repetition frequency of 250 Hz at probe location 8.7 cm above the silicon target. The grey shade indicates the error boundaries.	86
5.46	Time-resolved plasma potentials, Argon plasma pressure $P_{Ar}= 1.5$ mTorr. The curves are acquired in different times during the cycle of a -4 kV with $5 \mu s$ duration pulse bias with repetition frequency of 250 Hz at probe location 8.7 cm above the silicon target. The pulse starts at $t=-5 \mu s$ and ends at $t=0 \mu s$. The grey shade indicates the error boundaries.	87
5.47	Time-resolved electron temperatures, Argon plasma pressure $P_{Ar}= 1.5$ mTorr. The curves are acquired in different times during the cycle of a -4 kV with $5 \mu s$ duration pulse bias with repetition frequency of 250 Hz at probe location 8.7 cm above the silicon target. The pulse starts at $t=-5 \mu s$ and ends at $t=0 \mu s$	88
5.48	Time-resolved plasma potentials, Argon plasma pressure $P_{Ar}= 1.5$ mTorr. The curves are acquired in different times during the cycle of a -4 kV with $5 \mu s$ duration pulse bias with repetition frequency of 250 Hz at probe location 8.7 cm above the silicon target. The pulse starts at $t=-5 \mu s$ and ends at $t=0 \mu s$. The grey shade indicates the error boundaries.	89
5.49	Time-resolved ion densities, Argon plasma pressure $P_{Ar}= 1.5$ mTorr. The curves are acquired in different times during the cycle of a -4 kV with $5 \mu s$ duration pulse bias with repetition frequency of 250 Hz at probe location 8.7 cm above the silicon target. The pulse starts at $t=-5 \mu s$ and ends at $t=0 \mu s$. The grey shade indicates the error boundaries.	90

5.50	Time-resolved I-V characteristic curves, Argon plasma pressure $P_{Ar}= 25$ mTorr, RF-power $P_{RF}= 120$ W. The curves are acquired in different times during the cycle of a -4 kV with $5 \mu s$ duration pulse bias with repetition frequency of 250 Hz at probe location 21.7 cm above silicon and stainless steel targets. The pulse starts at $t=-5 \mu s$ and ends at $t=0 \mu s$. (a) A top view of the curves, showing plasma potential as a function of time. The colourbar determines the current going through the probe at each time-probe bias point in the plot. Colour-bar units are in mA. (b) A side view of the same family of curves. Notice the much lower I-V curves after the pulse. These curves don't reach electron saturation, thus plasma potential cannot be determined in their cases.	91
5.51	Time-resolved I-V characteristic curves, Argon plasma pressure $P_{Ar}= 1.5$ mTorr, RF-power $P_{RF}= 120$ W. The curves are acquired in different times during the cycle of a -4 kV with $5 \mu s$ duration pulse bias with repetition frequency of 250 Hz at probe location 21.7 cm above silicon and stainless steel targets. The pulse starts at $t=-5 \mu s$ and ends at $t=0 \mu s$	92
5.52	Time-resolved plasma potentials, Argon plasma pressure $P_{Ar}= 1.5$ mTorr, RF-power $P_{RF}= 120$ W. The curves are acquired in different times during the cycle of a -4 kV with $5 \mu s$ duration pulse bias with repetition frequency of 250 Hz at probe location 8.7 cm above silicon and stainless steel targets. The pulse starts at $t=-5 \mu s$ and ends at $t=0 \mu s$. The grey shade indicates the error boundaries.	93
5.53	Time-resolved electron temperatures, Argon plasma pressure $P_{Ar}= 1.5$ mTorr, RF-power $P_{RF}= 120$ W. The curves are acquired in different times during the cycle of a -4 kV with $5 \mu s$ duration pulse bias with repetition frequency of 250 Hz at probe location 21.7 cm above silicon and stainless steel targets. The pulse starts at $t=-5 \mu s$ and ends at $t=0 \mu s$. The grey shade indicates the error boundaries.	94
5.54	Time-resolved electron temperatures, Argon plasma pressure $P_{Ar}= 1.5$ mTorr, RF-power $P_{RF}= 120$ W. The curves are acquired in different times during the cycle of a -4 kV with $5 \mu s$ duration pulse bias with repetition frequency of 250 Hz at probe location 8.7 cm above silicon and stainless steel targets. The pulse starts at $t=-5 \mu s$ and ends at $t=0 \mu s$. The grey shade indicates the error boundaries.	95
5.55	Time-resolved plasma densities, Argon plasma pressure $P_{Ar}= 1.5$ mTorr, RF-power $P_{RF}= 120$ W. The curves are acquired in different times during the cycle of a -4 kV with $5 \mu s$ duration pulse bias with repetition frequency of 250 Hz at probe location 21.7 cm above silicon and stainless steel targets. The pulse starts at $t=-5 \mu s$ and ends at $t=0 \mu s$. The grey shade indicates the error boundaries.	96
5.56	Time-resolved ion densities, Argon plasma pressure $P_{Ar}= 1.5$ mTorr, RF-power $P_{RF}= 120$ W. The curves are acquired in different times during the cycle of a -4 kV with $5 \mu s$ duration pulse bias with repetition frequency of 250 Hz at probe location 21.7 cm above silicon and stainless steel targets. The pulse starts at $t=-5 \mu s$ and ends at $t=0 \mu s$. The grey shade indicates the error boundaries.	98
5.57	Time-resolved electron densities, Argon plasma pressure $P_{Ar}= 1.5$ mTorr, RF-power $P_{RF}= 120$ W. The curves are acquired in different times during the cycle of a -4 kV with $5 \mu s$ duration pulse bias with repetition frequency of 250 Hz at probe location 8.7 cm above silicon and stainless steel targets. The pulse starts at $t=-5 \mu s$ and ends at $t=0 \mu s$. The grey shade indicates the error boundaries.	99
5.58	Time-resolved ion densities, Argon plasma pressure $P_{Ar}= 1.5$ mTorr, RF-power $P_{RF}= 120$ W. The curves are acquired in different times during the cycle of a -4 kV with $5 \mu s$ duration pulse bias with repetition frequency of 250 Hz at probe location 8.7 cm above silicon and stainless steel targets. The pulse starts at $t=-5 \mu s$ and ends at $t=0 \mu s$. The grey shade indicates the error boundaries.	100
5.59	A comparison of the current through the stainless steel and silicon targets, as measured by Rogowski coil and simulated by p2i kinetic code which uses Lieberman's model to calculate fluence doped on the target. The measurements and simulations carried out with $V_{pulse} = -4$ kV, $5 \mu s$ duration pulse bias with repetition frequency of 250 Hz.	101

5.60	A comparison of the current through the stainless steel and silicon targets, as measured by Rogowski coil and simulated by p2i kinetic code which uses Lieberman model to calculate fluence doped on the target. The measurements and simulations carried out with $V_{pulse} = -1$ kV, $5 \mu s$ duration pulse bias with repetition frequency of 250 Hz.	102
5.61	(a) A schematic of the high voltage pulse shape, applied to the stainless steel and silicon targets for the PII experiments. The duration for most of the experiments were $5 \mu s$. The height of the pulse plateau was -4 kV and -1 kV. (b) A schematic of the corresponding current as a function of time shape going through the target during a $5 \mu s$ pulse.	108
5.62	Schematics of the general tendency of plasma parameters in the bulk plasma during a high voltage pulse in PII processing in different regions. The schematics are the visualisation of the tendencies of the plasma parameters from tables 5.3, 5.4 and 5.5. A cartoon of the corresponding applied pulse and the current through the targets are presented in figure 5.61a. (a) Floating potential tendency in a short range. (b) Plasma potential tendency in a short range. Plasma potential is flat in region 6. (c) Floating potential tendency in a long range; showing the second post-pulse-peak in floating potential happening in region 6. (d) Tendency of ion density through time. (e) Tendency of electron temperature in time; the small fluctuations shown during the pulse indicate a slightly higher electron temperature. (f) Tendency of electron density in time; the small fluctuations are shown throughout the pulse, indicating a slightly higher electron density during the pulse.	111
A.1	Steady state Ar plasma and floating potentials as a function of RF-power at two argon plasma pressures, on an axis location 21.7 cm above stainless steel target. Note that two different analysis methods (Druyvesteyn and Langmuir) were used to analyse each Langmuir probe curve as described in chapter 4.	122
A.2	Steady state Ar electron temperature calculated directly from the difference of potentials using equation A.1, as a function of RF-power at two argon plasma pressures, on an axis location 21.7 cm above stainless steel target. Note that two different analysis methods (Druyvesteyn and Langmuir) were used to analyse each Langmuir probe curve as described in chapter 4. Compare these figures to T_e measurements from the analysis, figure 5.3.	122
A.3	Steady state Ar plasma and floating potentials as a function of RF-power at two argon plasma pressures, on an axis location 8.7 cm above stainless steel target. Note that four different analysis methods (Druyvesteyn and Langmuir) were used to analyse each Langmuir probe curve as described in chapter 4.	123
A.4	Steady state Ar electron temperature calculated directly from the difference of potentials using equation A.1, as a function of RF-power at two argon plasma pressures, on an axis location 8.7 cm above stainless steel target. Note that four different analysis methods (Druyvesteyn and Langmuir) were used to analyse each Langmuir probe curve as described in chapter 4. Compare these figures to T_e measurements from the analysis, figure 5.4.	123
A.5	Steady state Ar plasma and floating potentials as a function of argon plasma pressure at two RF-powers, on an axis location 21.7 cm above stainless steel target. Note that two different analysis methods (Druyvesteyn and Langmuir) were used to analyse each Langmuir probe curve as described in chapter 4.	124
A.6	Steady state Ar plasma and floating potentials as a function of argon plasma pressure at two RF-powers, on an axis location 21.7 cm above stainless steel target. Note that two different analysis methods (Druyvesteyn and Langmuir) were used to analyse each Langmuir probe curve as described in chapter 4. Compare these figures to T_e measurements from the analysis, figure 5.7.	125
A.7	Steady state Ar electron temperature calculated directly from the difference of potentials using equation A.1, as a function of argon plasma pressure at two RF-powers, on an axis location 8.7 cm above stainless steel target. Note that two different analysis methods (Druyvesteyn and Langmuir) were used to analyse each Langmuir probe curve as described in chapter 4.	125

A.8	Steady state Ar electron temperature calculated directly from the difference of potentials using equation A.1, as a function of argon plasma pressure at two RF-powers, on an axis location 8.7 cm above stainless steel target. Note that two different analysis methods (Druyvesteyn and Langmuir) were used to analyse each Langmuir probe curve as described in chapter 4. Compare these figures to T_e measurements from the analysis, figure 5.8.	126
B.1	Steady state Ar plasma density as a function of RF-power in constant pressure and as a function of Argon gas pressure in constant RF-power, on an axis location 21.7 cm above stainless steel target acquired by uncompensated Langmuir probe. Note that four different analysis methods (Druyvesteyn, Langmuir, ABR, and OML) were used to analyse each Langmuir probe curve as described in chapter 4.	127
B.2	Steady state Ar plasma density as a function of RF-power in constant pressure and as a function of Argon gas pressure in constant RF-power, on an axis location 21.7 cm above stainless steel target acquired by RF-compensated probe. Note that four different analysis methods (Druyvesteyn, Langmuir, ABR, and OML) were used to analyse each Langmuir probe curve as described in chapter 4.	127
B.3	Steady state Ar plasma density as a function of RF-power in constant pressure and as a function of Argon gas pressure in constant RF-power, on an axis location 21.7 cm above stainless steel target obtained by uncompensated Langmuir probe. Note that four different analysis methods (Druyvesteyn, Langmuir, ABR, and OML) were used to analyse each Langmuir probe curve as described in chapter 4.	128
B.4	Steady state Ar plasma density as a function of RF-power in constant pressure and as a function of Argon gas pressure in constant RF-power, on an axis location 21.7 cm above stainless steel target, obtained by RF-compensated Langmuir probe. Note that four different analysis methods (Druyvesteyn, Langmuir, ABR, and OML) were used to analyse each Langmuir probe curve as described in chapter 4.	129
B.5	Steady state Ar electron temperature as a function of RF-power in constant pressure and as a function of Argon gas pressure in constant RF-power, on an axis location 21.7 cm above stainless steel target, acquired by uncompensated Langmuir probe. Note that two different analysis methods (Druyvesteyn and Langmuir) were used to analyse each Langmuir probe curve as described in chapter 4. Compare with values acquired by RF-compensated Langmuir probe, presented in figures B.7a and B.7b.	129
B.6	Steady state Ar electron temperature calculated directly from the difference of potentials using equation A.1, as a function of RF-power in constant pressure and as a function of Argon gas pressure in constant RF-power, on an axis location 21.7 cm above stainless steel target. Note that two different analysis methods (Druyvesteyn and Langmuir) were used to analyse each Langmuir probe curve as described in chapter 4. Compare with values acquired by RF-compensated Langmuir probe, presented in figures A.4b and A.8b.	130
B.7	Steady state Ar electron temperature as a function of RF-power in constant pressure and as a function of Argon gas pressure in constant RF-power, on an axis location 21.7 cm above stainless steel target acquired by RF-compensated Langmuir probe. Note that two different analysis methods (Druyvesteyn and Langmuir) were used to analyse each Langmuir probe curve as described in chapter 4. Compare with figure B.5, to see the overestimation of uncompensated probe comparing to the "correct" electron temperature values, measured by RF-compensated Langmuir probe.	130
C.1	The design for RF-compensated Langmuir probe without the reference electrode. The thin tungsten tip to be connected to the copper wire sticking out of the torr-sealed ceramic. The chokes should be as close as possible to the probe's tip, which is delivered in this design. . .	131
C.2	The RF-compensated probe's body made without the reference electrode. before and after the assembly.	132

C.3 RF-compensated Langmuir probe with electrode. (a) A 18 nF capacitor was used between the reference electrode and a series of 13.56 MHz and 27.12 MHz self-resonant chokes. (b) P1 is the tungsten probe tip (5.0 mm length, 1.0 mm diameter) and P2 is a copper ring ($A_2= 30\pi mm^2$) acting as the reference electrode. 132

LIST OF ABBREVIATIONS

UofS	University of Saskatchewan
PPL	Plasma Physics Laboratory
PII	Plasma Ion Implantation
PIII	Plasma Immersion Ion Implantation
RF	Radio Frequency
ICP	Inductively Coupled Plasma
prf	pulse repetition frequency
PIC	Particle In Cell
PPP	Post-Pulse Peak
Ar	Argon

1 INTRODUCTION

1.1 Plasma Ion Implantation

Plasma Ion Implantation (PII) is a materials processing technology in which ions are accelerated toward and implanted into a negatively biased target [1]. To reduce target heating and power load, the high voltage bias is usually pulsed. Pulses are applied with a pulse repetition frequency (prf) typically in the range of several hundred pulses per second. Each pulse implants a fixed number of ions into the target. The pulse duration determines this number and the voltage amplitude of the pulse determines the ion energy and therefore the implanted depth. In principle any steady state plasma source can be used for PII [1]. For the PII system operated in the University of Saskatchewan Plasma Physics Lab (UofS PPL) the plasma source is an Inductively Coupled Radio Frequency (ICP-RF) source operating at 13.56 MHz.

PII has many material applications. It is widely used for semiconductor device doping, as well as for improving corrosion and wear resistance properties of steel and other metal alloys. PII has applications for biomedical materials as well [2].

Figure 1.1 shows a schematic of the UofS PII system. The target to be implanted is immersed in the RF-ICP plasma and is biased with negative polarity high voltage pulses, typically ranging from 1 to 10 kV. During each high voltage pulse, a large electric field is pointing from the plasma toward the target; this accelerates positive ions from the plasma toward the target through a region referred to as the high voltage sheath. While the target shown is planar, (which is representative of a standard semiconductor wafer) non planar targets also can be uniformly implanted. In the case of non planar target immersed in the plasma, the ions are accelerated toward the target from all directions, leading to a uniform implantation. This is an advantage of PII compared with conventional ion beam implantation which would require complicated beam scanning and variable angle target fixturing to achieve the same uniformity as PII.

For users of PII, the most important parameter is the concentration of implanted ions vs. the depth of implantation. Different PII applications will require different dose vs. depth profiles and it is necessary for users of PII to be able to accurately predict these before carrying out PII. Therefore accurate models for PII are required. Development of such models is complicated because the plasma is not simply a stationary reservoir of ions with fixed density; instead the plasma density evolves dynamically during the applied high voltage pulse, due to a variety of effects, including secondary electrons ejected from the target and accelerated back into the plasma bulk [3]. This results in an increase or enhancement of the plasma density which can be experimentally observed and which can significantly modify the ion current going through the target [3]

and hence significantly increase the delivered ion dose.

A widely used model of pulsed PII processes is the Lieberman model [4]. This model has the advantage of being simple and computationally efficient, making it suitable for industrial applications. However when using Lieberman's model for dynamic sheath expansion of a high voltage biased target immersed in plasma, significant discrepancies with measurements arise, due to a number of effects.

Numerous groups have tried to quantify and accurately model plasma behaviour during PII pulses [5, 6, 7, 8, 9]. Each of these has a specific focus. Among those particle in cell (PIC) modelling of plasma is the most accurate method. However this comes with the nontrivial cost of being prohibitively time-consuming for most real-world applications. The post-pulse recovery of the plasma to a steady state has also been studied by Briel et al. in 2002 [7]. This recovery is an important factor for accurate ion fluence prediction since high voltage pulses may significantly deplete the plasma during the pulse with obvious effects on the subsequent pulse. This possibility is also not considered in Lieberman's model.

The role played by secondary electrons ejected from the target and accelerated back into the bulk plasma has been considered by different groups. Plasma density enhancement due to plasma heating as well as ionisation of neutrals by the secondary electron "beam" ejected from the target is known to play a significant role and has not been fully studied [3, 10].

The purpose of this thesis is to make a detailed study of plasma behaviour in a PII system before, during, and after each high voltage pulse. For this purpose a representative argon plasma was used. The use of the argon plasma avoided the unnecessary complexity associated with the molecular ion plasmas commonly used for real PII processing. Prior to the pulsed plasma studies, a comprehensive Langmuir probe study of the steady state RF-ICP argon plasma was carried out. This is described in detail in the first part of chapter 5. For this purpose a new high accuracy RF-compensated Langmuir probe was designed and built. This is described in chapter 4. The basic theory behind PII is briefly reviewed in chapter 2, while technical details of the UofS ICP-II PII apparatus are discussed in chapter 3.

After the steady state plasma characterisation, the time evolution of the electron temperature and plasma density of the plasma were measured during high voltage pulses applied to both semiconductor (silicon) and metal (stainless steel) targets, in order to investigate the effect of different secondary electron yield coefficients. Additionally, the recovery of the plasma steady state and the dependence of this on the RF-power and gas pressure was studied using direct measurements of the floating potential. From these data the plasma relaxation time was measured. The above comprehensive measurements of the plasma behaviour during PII provided a much deeper understanding of the dynamic plasma behaviour during PII pulses. From this I was able to identify a number of places where the real plasma behaviour deviated from the various PII models. This is discussed in the latter part of chapter 5 as well as the conclusion. Future possibilities for improving PII modelling in order to capture and more accurately model these previously ignored features are discussed in the conclusion.

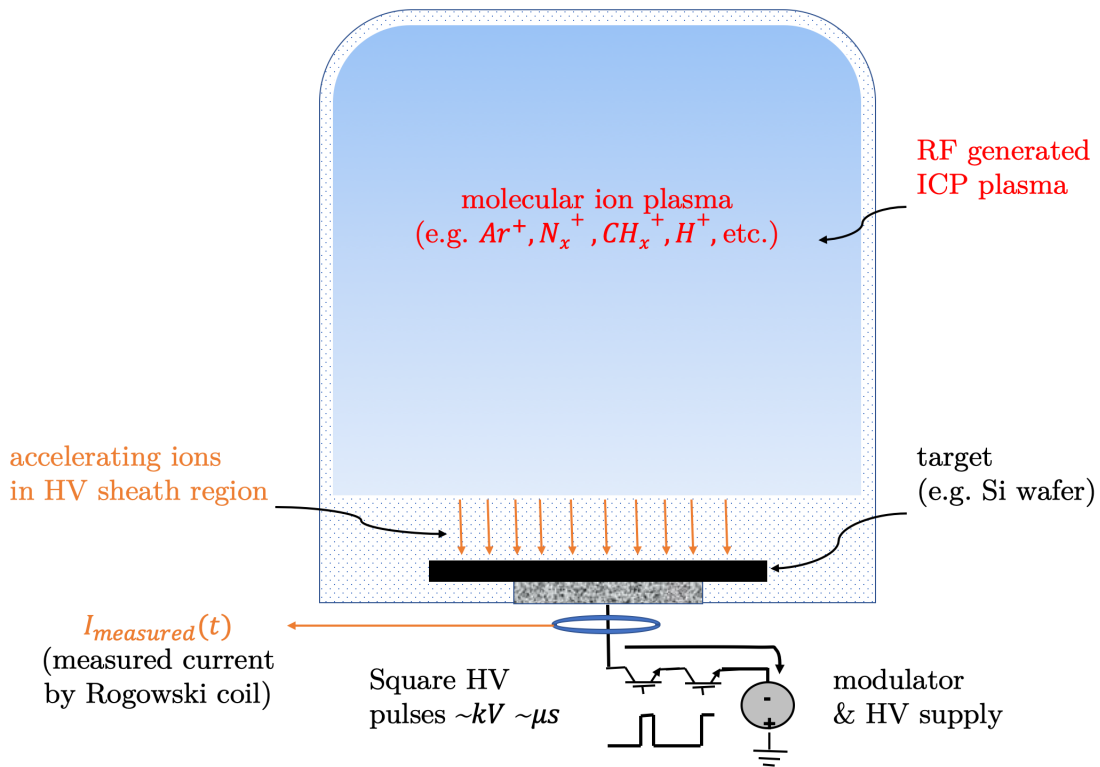


Figure 1.1: Schematic of PII process; the substrate is biased to a squared-shape high voltage in the order of 1 kV or 10 kV and duration orders of 1 or 10 μs . A high voltage sheath is formed around the target, which ions get accelerated from the generated plasma, through high voltage sheath toward the target with initial Bohm velocity u_B . The total current going through the substrate is measured by a Rogowski coil and the chamber is usually grounded (not the case for older glass chambers).

2 MODELLING PLASMA ION IMPLANTATION

Most applications of PII require that a certain ion fluence (usually quoted in ions per cm^2 of target area, and often colloquially referred to as ion *dose*) be delivered at a certain depth. The implantation depth is determined by the ion energy and hence the pulse voltage. Ion implantation depth increases monotonically but not linearly as the ion energy increases. Ion implantation depth has been extensively studied since the 1930s in the context of ion stopping power. Numerous computer codes accurately model the ion stopping process. The most commonly used code being SRIM (Stopping and Range of Ions in Matter [11]). To determine the total ion fluence F for a PII pulse we integrate the time varying ion flux $\Phi(t)$ as follows:

$$F = \int_0^{t_{on}} \Phi(t) dt \quad \left[\frac{\text{ions}}{\text{cm}^2} \right]. \quad (2.1)$$

For the ions with charge state Z_i (usually $+1$ for most PII applications), the ion flux can be determined from the ion current $I_i(t)$ extracted from plasma:

$$\Phi(t) = \frac{1}{A_T} \frac{I_i(t)}{Z_i e} \quad \left[\frac{\text{ions}}{\text{cm}^2 \text{s}} \right], \quad (2.2)$$

where A_T is the target area, and e is the elementary charge.

The ion current during a PII pulse can be obtained from a plasma model. A plasma is a quasi-neutral partially ionised gas containing free electrons, ions and neutral species. For PII plasmas the ionisation fraction is typically small meaning significant fraction of neutral gas atoms and/or molecules are present. The plasma formed in a chamber is in contact with a solid surface on its boundaries [12]. Plasma walls are grounded while the target is biased to a negative high voltage with respect to the grounded chamber during the voltage pulses.

Close to plasma boundaries, a Debye sheath arises because the electrons usually have a temperature more than one order of magnitude higher than that of the ions (see table 3.1), and are much lighter. Consequently, they are faster than the ions by at least a factor of $\sqrt{\frac{Z_i M_i}{m_e}}$, where M_i and m_e are ion and electron mass respectively. At the interface to the chamber walls or the substrate, plasma loses fast electrons to the surface, making the surface potential negative relative to the bulk plasma. Due to Debye shielding, the scale length of the transition region is Debye length $\lambda_{De} = \sqrt{\frac{\epsilon_0 k T_e}{n_e e^2}}$, in which k is Boltzmann constant, T_e is electron temperature and n_e is electron density. As the wall's potential decreases, more and more electrons are reflected by the sheath. An equilibrium is finally reached when the potential difference is a few times the electron temperature [12].

The electrostatic potential in the bulk plasma is constant. However, as the quasi-neutrality is broken when moving closer to the walls, the potential profile falls sharply near the boundaries. The electric field lines point from plasma bulk toward the confining walls. The force generated by the electric field in sheath region, repels the lower-energy electrons back to the plasma bulk. On the other hand, the ions entering the sheath region are accelerated toward the walls [1].

2.1 Lieberman’s Sheath Model

In this section I discuss Lieberman’s sheath model[4]. The mathematical treatment will closely follow that given in the previous reference. We start by the consideration of the plasma potential $V(x)$. This is given by Poisson’s equation:

$$\nabla^2 V(x) = \frac{e}{\epsilon_0} [n_e(x) - Z_i n_i(x)], \quad (2.3)$$

where $n_i(x)$ and $n_e(x)$ are ion and electron densities, respectively. Note that the right hand side term expresses charge imbalance. While plasmas are generally quasi-neutral, with $n_e \approx Z_i n_i$, significant charge imbalance can exist in plasma sheath.

Lieberman’s model treats the electrons statistically, i.e. as a gas, while treating the ions as moving ballistically. This is justified by the fact that the typical PII pulse duration is of the order of μ s which is much longer than electron thermalisation time scales but much shorter than ion response times. Modelling the electrons as a classical gas, the electron density can be assumed to follow a Maxwell-Boltzmann distribution:

$$n_e(x) = n_0 \cdot \exp\left(\frac{eV(x)}{kT_e}\right), \quad (2.4)$$

where $n_0 = n_e$ is the plasma density. The assumption of a Maxwell-Boltzmann distribution for the electrons in a steady state ICP-plasma is valid for pressures at or above a few mTorr [13, 14].

Lieberman’s model applies for the high voltage sheath which exists between the plasma and the negatively biased PII target. For the purposes of this model it is useful to replace the bulk plasma density n_0 with the density at the edge of the high voltage sheath which we will refer to as n_s .

To solve for the ion current and related quantities, we track the ions ballistically. Applying energy conservation for ions starting at the sheath edge and transiting through the sheath region gives [4, 5]

$$\frac{1}{2} M_i u_i^2 + e Z_i V(x) = \frac{1}{2} M_i u_B^2, \quad (2.5)$$

where u_i is the ion velocity. The leftmost term is the ion kinetic energy in the sheath region, and the second term is the ion potential energy in the sheath due to the sheath electric field. The right-hand side of the equation is the initial kinetic energy of the ions at the sheath edge entering the sheath from the bulk plasma with velocity u_B . u_B is known as the "Bohm velocity" and it will be discussed further in the following paragraphs.

From the ion continuity equation, assuming no ion loss due to neutralisation or charge exchange and no ion creation due to ionisation in the sheath, the flux of ions arriving at the grounded target or chamber wall must be equal to the flux of ions arriving at the sheath edge from the bulk plasma [1]:

$$n_s u_B = n_i u_i. \quad (2.6)$$

We can rearrange the conservation of energy equation 2.5 to find the ion drift speed in terms of the potential $V(x)$ at the ion location x [1, 15]:

$$u_i = (u_B^2 - \frac{2eZ_i V(x)}{M_i})^{1/2}. \quad (2.7)$$

To find the ion density at any location in the sheath we can substitute the above into the continuity equation to obtain [1]:

$$n_i(x) = n_s (1 - \frac{2eV(x)}{M_i u_B^2})^{-1/2}. \quad (2.8)$$

It is important to note that the sheath is non-neutral, so the electron density (equation 2.4) will differ from the ion density (equation 2.8). This will result in a variation of electric potential $V(x)$ across the sheath. To find this variation in potential we use Poisson's equation with the Boltzmann distributed electron density and the ballistic ion density to obtain:

$$\frac{d^2 V(x)}{dx^2} = \frac{en_s}{\epsilon_0} [\exp(\frac{V(x)}{k_B T_e}) - (1 - \frac{V(x)}{\epsilon_s})^{-1/2}], \quad (2.9)$$

where $e\epsilon_s = \frac{1}{2} M_i u_i^2$ is the kinetic energy of ions at sheath region [1]. This is the basic nonlinear equation which governs the spatial variation of sheath potential.

To proceed to a solution, we multiply the above equation by $dV(x)/dx$ and integrate over x . This gives the first integral, [1]

$$\int_0^V \frac{d}{dx} \frac{dV}{dx} (\frac{dV}{dx}) dx = \frac{en_s}{\epsilon_0} \int_0^V \frac{dV}{dx} [\exp(\frac{V(x)}{k_B T_e}) - (1 - \frac{V(x)}{\epsilon_s})^{-1/2}] dx. \quad (2.10)$$

Integration on both sides with respect to V , after cancelling dx from the two sides, we obtain the nonlinear differential equation:

$$\frac{1}{2} (\frac{dV}{dx})^2 = \frac{en_s}{\epsilon_0} [k_B T_e \exp(\frac{V}{k_B T_e}) - k_B T_e + 2\epsilon_s (1 - \frac{V}{\epsilon_s})^{-1/2} - 2\epsilon_s]. \quad (2.11)$$

For a solution to exist, the right hand side of the equation should be positive definite. From our previous discussion this means that the electron density must always be less than ion density in sheath region. Because of the exponential term, the right hand side will always be positive except possibly for small values of V . This corresponds to regions just past the sheath edge since we take the potential of the sheath edge to be zero (to see this consider equation 2.4 and see that $n_e = n_s$ when V is zero). We can derive a condition which will

guarantee the positivity of the right hand side term. By expanding the right hand term as a Taylor series to the second order, we obtain the following inequality [1]:

$$\frac{1}{2} \frac{V^2}{k_B T_e} - \frac{1}{4} \frac{V^2}{\varepsilon_s} \geq 0. \quad (2.12)$$

Cancelling V and substituting for the sheath kinetic energy ε_s , we obtain the famous *Bohm sheath criterion* [1]:

$$u_s \geq u_B = \sqrt{\frac{kT_e}{m_i}}. \quad (2.13)$$

The above calculation applies to the ordinary "low voltage" sheath which exist between a positive ion plasma and grounded chamber walls. When one wall of the chamber is replaced by a target biased to a large magnitude negative potential, a wider sheath is formed. This is referred to as the "high voltage sheath". In PII the ions entering the sheath from plasma bulk are then accelerated through a large potential drop in the high voltage sheath region and get implanted into the negatively biased target.

2.1.1 Transient Matrix Sheath

For a brief period after the application of the negative polarity step voltage pulse, the positive column of ions is exposed. This column of ions above the negatively biased target has ion density $n_i = n_0$. The electrons are pushed away from this region by the negative bias on a time scale which is of the order of the inverse plasma frequency, i.e. nanoseconds ω^{-1} . The matrix sheath is clearly non-neutral. It is also not a steady state sheath solution. The ions will move under the influence of the electric field with a time scale of the order of the ion acoustic speed. They will redistribute themselves to form a steady state Child-Langmuir high voltage sheath. A Matrix sheath occurs when a boundary of plasma, e.g. the substrate, is biased to a high negative voltage. Electrons are repelled quickly and the sheath only consists of ions, which are distributed uniformly. Solving Poisson's equation, equation 2.3 for constant $n_i = n_0$ and $n_e = 0$, gives the following parabolic potential distribution within the sheath [1]:

$$V(x) = -\frac{en_0}{\epsilon_0} \frac{x^2}{2}. \quad (2.14)$$

This is easily verified by direct substitution. This potential variation gives an electric field $E = -dV/dx$ which varies linearly with x . The matrix sheath edge is obtained from equation 2.14 by setting $V(s) = -V_0$. Rearranging and solving for sheath width s_M gives:

$$s_M = \lambda_D \sqrt{\frac{2eV_0}{kT_e}}, \quad (2.15)$$

where $\lambda_{De} = \sqrt{\frac{\epsilon_0 kT_e}{n_e e^2}}$ is the usual plasma Debye screening length. As a numerical example we consider a PII target immersed in a plasma with density $n_e = 1 \times 10^9 \text{ cm}^{-3}$ and the electron temperature of $kT_e = 4 \text{ eV}$ biased to $V_0 = -4 \text{ kV}$ (Debye length $\lambda_{De} = 470 \text{ }\mu\text{m}$) has a Matrix sheath width of $s_M = 45\lambda_{De} = 2.1 \text{ cm}$.

Biasing the target with a lower potential $V_0 = -1$ kV in same plasma conditions gives a Matrix sheath of $s_M = 1.05$ cm. The characteristic time scale to establish Matrix sheath is given by the time it takes an electron to go across the collisionless sheath with velocity of $u_{0,e} = \sqrt{\frac{2eV_0}{m_e}}$. This leads to the inverse of electron plasma frequency, as mentioned above:

$$\tau_e = \frac{s_M}{u_{0,e}} = \frac{\sqrt{2\epsilon_0 V_0 / en}}{\sqrt{2eV_0 / m_e}} = \sqrt{\frac{m_e \epsilon_0}{ne^2}} = \omega_e^{-1}. \quad (2.16)$$

For our Ar⁺ ICP plasma conditions used in this thesis (see Table 3.1) τ_e is in order of 0.1 ns.

2.1.2 Steady State High Voltage Sheath: The Child-Langmuir Sheath

The matrix sheath is only transient persisting for at most tens of nanoseconds. As noted previously the ions move under the influence of the sheath electric field until a steady state is achieved.

Lieberman's model for PII pulsed sheath evolution starts with the Child-Langmuir law for space charge limited current in vacuum diodes. By applying the Child-Langmuir law, for instantaneous sheath width and the Bohm current equal to the sum of the uncovered ion column plus the Bohm current, one can write the following equation for the sheath current [1]:

$$J = J_i = en \left(\frac{ds}{dt} + u_B \right) = \frac{4}{9} \epsilon_0 \sqrt{\frac{2e}{M_i}} \frac{V^{3/2}}{s^2}, \quad (2.17)$$

in which, $s = s(V, t)$ is the time-varying sheath width, ϵ_0 is the vacuum permittivity, and V is the potential difference between the bulk plasma and the negatively biased target. n is the bulk plasma density. Because n is typically reduced in presheath and also may increase during the ion implantation due to plasma heating driven by secondary electrons, it is useful to write $n = n(V, t)$. This is an extension beyond the standard Lieberman model which assumes $n = \text{constant}$ [16]:

$$n(V, t) = \begin{cases} 0.61 \cdot n_0 [1 + a \cdot V_B(t)] & \text{during PII} \\ 0.61 \cdot n_0 & \text{else} \end{cases}. \quad (2.18)$$

One of the main purposes of this thesis is to make detailed measurements to assess the correctness of this and other phenomenologically derived plasma enhancement terms. For the moment we restrict ourselves to the standard Lieberman model with the constant bulk plasma density. Rearranging equation 2.17 gives the following differential equation for the time varying sheath width, $s(t)$ [1]:

$$\frac{d}{dt} s(V, t) - \frac{4}{9} \epsilon_0 \sqrt{\frac{2e}{M_i}} V(t)^{\frac{3}{2}} \left(\frac{1}{s(V, t)^2} \right) = -\sqrt{\frac{kT_e}{M_i}} = -u_B \quad (2.19)$$

This nonlinear equation can be solved numerically to obtain the time evolution of the high voltage sheath from the initial matrix sheath through to the final steady state space-charge limited high voltage sheath governed by the Child-Langmuir law. The C code "p2i" (written by former UofS student, Marcel Risch, [16] and based on preliminary code by J. T. Steenkamp [17]) is a 4th order Runge-Kutta numerical integration of

Liebermans sheath model [4]. In addition to the basic Lieberman model with constant bulk plasma density it allows for phenomenologically determined plasma density variations of the form in equation 2.18. The Potential in Child-Langmuir sheath can be derived using conservation of energy and continuity equations, and equation 2.17 as [1]: The potential variation in the final steady state space-charge limited Child-Langmuir sheath can be derived using Poisson's equation 4.28 with $n_e = 0$ (the sheath is depleted of electrons) and an ion density n_i derived from the ion current J_i as follows:

$$\frac{d^2V}{dx^2} = \frac{e}{\epsilon_0} n_i = -\frac{J_i}{\epsilon_0} \left(-\frac{2eV}{M_i}\right)^{1/2}. \quad (2.20)$$

For the steady state solution we set V and $\frac{dV}{dx}$ equal to zero at the sheath edge $x = 0$. This leads to an expression for the potential in the sheath given by:

$$V(x) = -V_0 \left(\frac{x}{s_{CL}}\right)^{4/3}, \quad (2.21)$$

where s_{CL} is the Child Langmuir sheath thickness given by [1]:

$$s_{CL} = S_M \left(\frac{2u_{0,i}}{9u_B}\right)^{1/2} \quad (2.22)$$

where s_M is the transient matrix sheath thickness derived previously. $u_{0,i} = \sqrt{\frac{2eV_0}{m_i}}$ is the velocity of the ions when they reach the target and u_B is the Bohm velocity. Because $u_{0,i} \gg u_B$, $s_{CL} \gg s_M$ which we expect on physical grounds.

2.2 Validity of Lieberman's Assumptions

In Lieberman's sheath model, a variety of explicit and implicit assumptions are used. The important assumptions are delineated below [16]:

- Electrons are "inertialess" which means they respond instantaneously to the applied electric field.
- Because of the above the transient Matrix sheath forms instantaneously.
- The ion current is space-charge limited and therefore described by Child-Langmuir law during the sheath expansion.
- The bulk plasma is an infinite ion reservoir which is not depleted by the ion extraction.
- Ions arrive at the target instantly, i.e. transit time effects are ignored.
- The bulk plasma density is uniform.
- The ion flow is collisionless. (Lieberman did propose a modified version for collisional sheaths)
- The sheath edge is abrupt, i.e. no presheath.

- Ions are mono-atomic with a single charge state Z_i (usually $Z_i = 1$).
- One dimensional-planar geometry.
- The plasma density and the initial sheath width at the beginning of each applied pulse are the same, i.e. there are no memory effects.

Many of the above assumptions are reasonable for PII plasma conditions, but non are exact and some are very seriously violated during high voltage PII processes. We address these points below for parameters relevant for our PII system.

- The ratio of ion to electron response time in argon plasma ($Z_i(Ar^+) = 40$) is:

$$\frac{\tau_i}{\tau_e} = \frac{\omega_e}{\omega_i} = \sqrt{\frac{Z_i m_i}{m_e}} = 261 \quad (2.23)$$

which tells us that characteristic time scale in PII exceeds the electron response by far. Additionally, the ion transition time for small sheaths are negligible. Also, the change in electric field throughout the sheath region is minimal. Therefore, the electric field could be assumed frozen and quasi-static ion motion and sheath positions could be assumed.

- The Child-Langmuir law can be derived from Poisson's equation only when the electron temperature is small compared to the applied potential. This is generally true in PII. The discrepancy between measured and simulated current arises from the fact that at the beginning of the voltage pulse when the potential and sheath width rapidly increase, the quasi-static assumption is not valid anymore.
- Considering the size and the operating working pressure (> 1 mTorr) of ICP-2, the infinite ion reservoir is a fair assumption.
- The characteristic time scale of PII is set by the time that takes ions to travel through the Matrix sheath $\omega_i^{-1} < 40$ ns. 16 ns is the sampling time for oscilloscope, which means all ions arrive at the target within this time. Hence, the assumption of instant arrival of ions is valid.
- Uniform ion density can be assumed near the region of interest, i.e. the middle of chamber [16]. However the plasma ion density in discharges is distributed; This distribution is studied in detail in chapter 5.
- Collisionless ion flow condition is a valid assumption only if the mean free path of ions is greater than sheath width [1].

$$s_{CL,max} \approx \lambda_{De} \left(\frac{|V_0|}{T_e} \right)^{3/4}, \quad (2.24)$$

The mean free path of ions in plasma λ_{mfp} is given by [16]:

$$\lambda_{mfp} = \frac{a}{p}, \quad (2.25)$$

where a is a constant. (4.58 mTorr.cm for nitrogen) and p is the working pressure. Figure 2.1 shows graphical representation of the condition for a collisionless sheath.

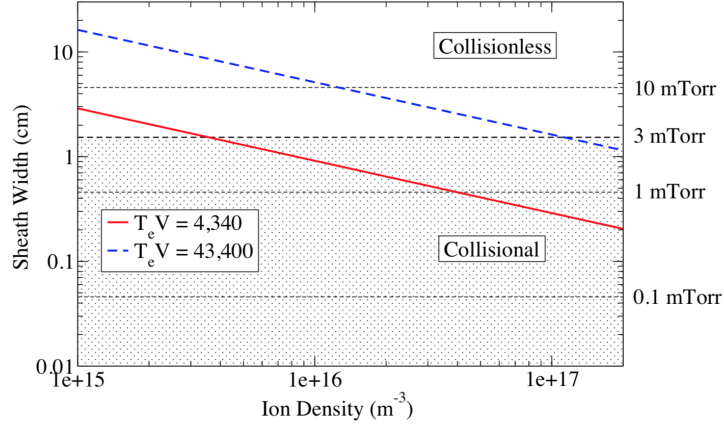


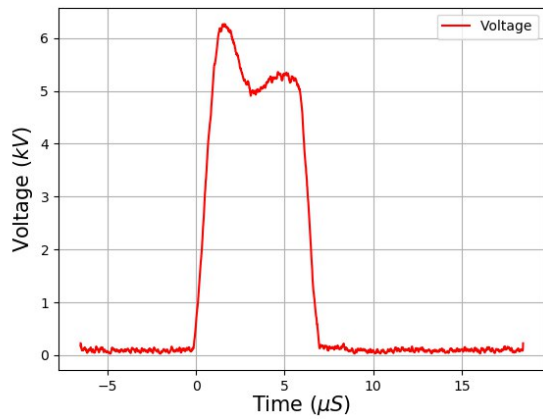
Figure 2.1: The condition for a collisionless sheath within ion density of PII in ICP-2, from Marcel Risch’s M.Sc. thesis [16]. The coloured lines represent the steady-state sheath width of ideal pulses for different electron temperatures T_e and voltage peaks V .

- Abrupt sheath is a valid assumption, due to the fact that Debye length is much smaller than the sheath width, which is the case when the biased voltage is much higher than electron temperature.
- For the last assumption to be valid, the sheath must collapse completely between pulses and the time between pulses must be large enough to let ions diffuse into former region and bring back the the density to its original level again. By calculating ion transition time with $\Delta t = \frac{s_{max}}{u_B}$. The sheath does not close if the pulse repetition rate is in order of μs for our working plasma density and electron temperature. These values are not reachable by our current high voltage pulser setup.

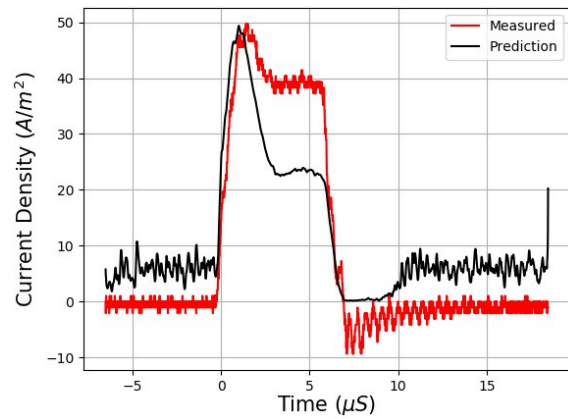
An example of -5 kV experimental voltage pulse is shown in figure 2.2a. Figure 2.2b shows the corresponding measured current and predicted current by p2i code with the same voltage pulse as an input parameter. The plot is calculated for the total area of a substrate holder with diameter of 15.0 cm.

Spikes before the pulse starts are the result of underestimation of minimal Matrix sheath width. The peaks at the end are by the minimal sheath width which collapses first and is close to the small pre-implantation steady-state while the voltage is high. The oscillations with high amplitude can be caused by the depletion, in the absence of ions, electrons are pouring into the void and go to the electrode almost instantly. The direction of this current should be opposite of the ion current, which is the case.

The measured current in figure 2.2b violates the assumption of plasma density enhancement made in this model. A hypothetical mechanism for plasma density enhancement must be dependent on the voltage as well as the shape of the voltage waveform.



(a) High voltage pulse



(b) Current through target.

Figure 2.2: (a) $V_{pulse} = -5$ kV smoothed voltage pulse input to a stainless steel target acquired earlier for this work, as generated by ICP-2 pulser; with $7.5 \mu s$ duration. The voltage fluctuations in the grounded region are about 200 V. (b) Measured current density from Pearson model 150 Rogowski coil vs. predicted current by p2i code. The applied bias voltage is shown in figure 2.2a.

3 PLASMA ION IMPLANTATION (PII) APPARATUS

The system used for PII at UofS Plasma Physics Laboratory (PPL) consists of the vacuum chamber holding the gas, pumping system, which includes fore-line pump and turbo pump, RF antenna and matching network which ionise the gas, a power supply to provide high voltage pulsed power to the sample holder and the diagnostics to monitor plasma parameters [16].

The setup for PII at U of S is shown in figure 3.1. Table 3.1 summarises the main parameters for ICP-2 which is used by our group for means of PII.

Table 3.1: Important parameters for ICP-2 chamber

Parameter	Range
RF power	$\leq 600\text{W}$
Radio frequency	13.56MHz
Plasma potential V_p	10 – 30V
Plasma bulk density (n_0)	$10^9 - 10^{11}\text{cm}^{-3}$
Electron temperature (T_e)	1 – 5eV
Ion temperature (T_i)	0.3 – 0.6eV
Base pressure	0.1 – $1\mu\text{Torr}$
Working pressure (P)	1 – 10mTorr
Typical pulse voltage	1 – 20kV
Typical pulse duration	1 – $100\mu\text{s}$

3.1 ICP II-600 Chamber

The Inductively Coupled Plasma (ICP) chamber was manufactured for plasma physics laboratory by Plasmaionique Inc., Varennes, QC, Canada. A photograph of chamber with current controllers and diagnostics devices is provided in figure 3.1. The chamber is cylindrical with 29.8 cm inner diameter and 46.0 cm height. The gas is ionised by induced Radio-Frequency (RF) electric field with 13.56 MHz frequency through a quartz window provided by a water-cooled planar coil on top of the processing chamber [16].

The stainless steel stand used for this project was used without the sample holder. The stainless steel part is disk-shape with dimensions given in figure 3.2. The sample holder can be mounted radially on a rod

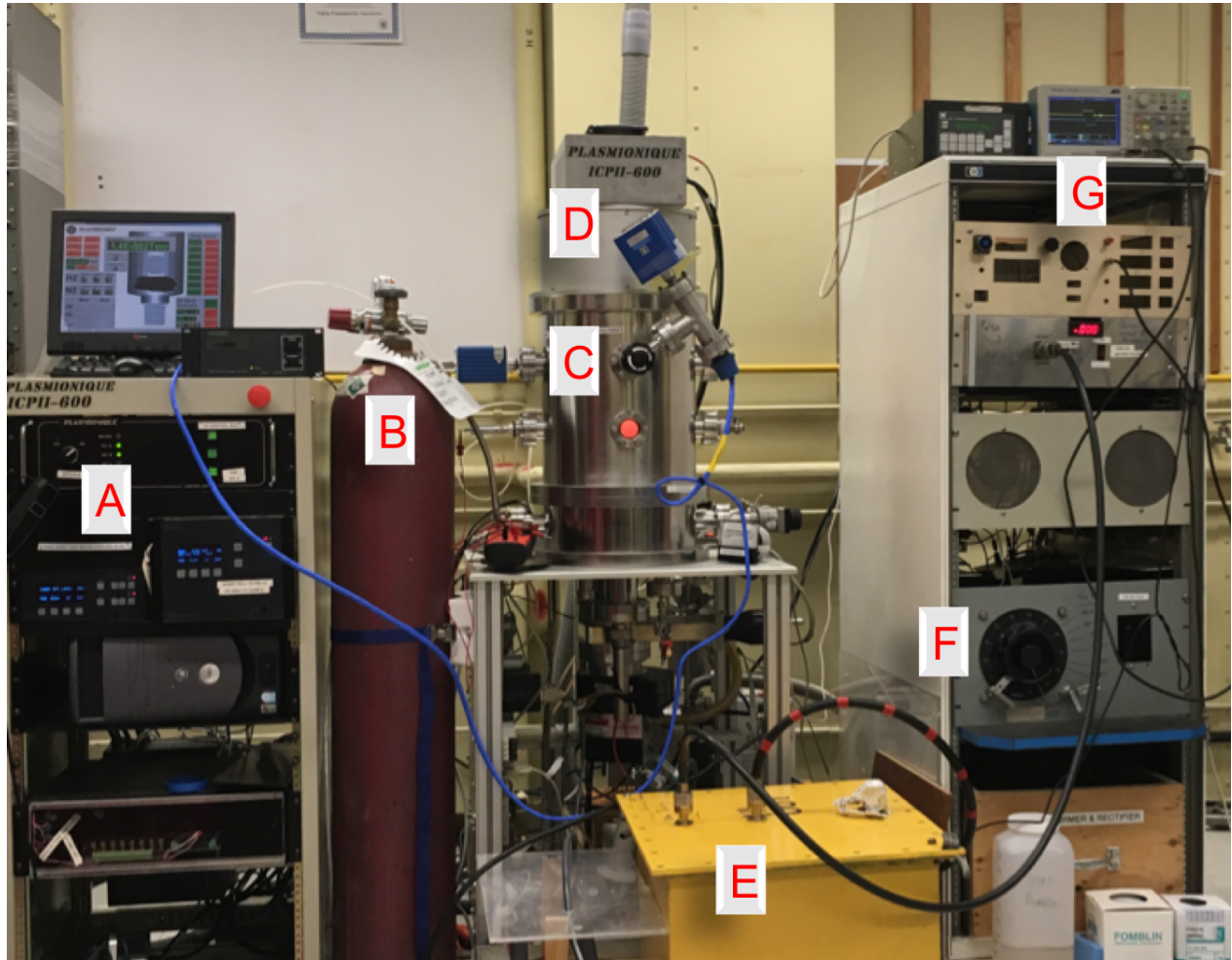


Figure 3.1: ICP-2 Plasma processing setup as of Spring 2018. (A. Gas and plasma control, B. Feed gas, C. Processing chamber, D. RF antenna and matching network, E. Transformer, F. Pulser, G. Pulser control)

which exits the chamber through the high-voltage feed-through. The stand without the sample holder is located about 35.0 cm below the quartz window.

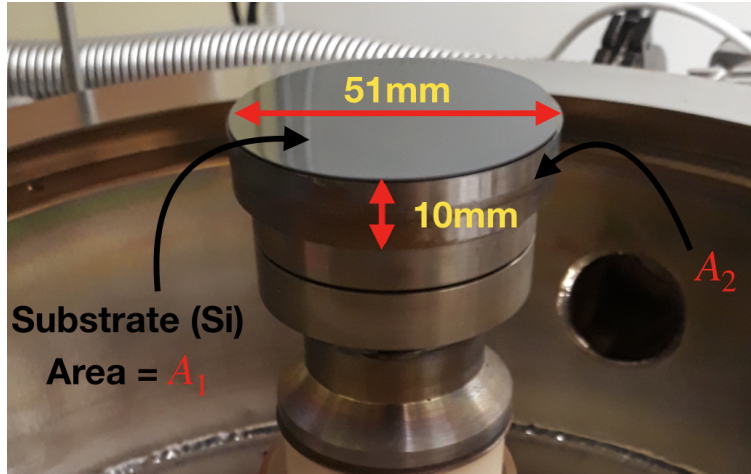


Figure 3.2: ICP-2 stand rod without the sample holder, as used in the current project. The dimensions are given in the photo. The total area of the disk-shape stainless steel part is $A_1 + A_2 = 20.43 \text{ cm}^2 + 16.02 \text{ cm}^2 = 36.45 \text{ cm}^2$. Note that A_1 is the area of the top circle, and A_2 is the area of the side ribbon. The silicon target fully covers the flat top of the stand.

3.2 Other Components

3.2.1 Gas and Pressure Controllers

The chamber is pumped down by an Alcatel Adixen 2010SD Pascal Dual Stage Rotary Vane Vacuum roughing pump down to ≈ 10 mTorr in a few minutes. After pumping down the pressure to $\lesssim 10$ mTorr by the roughing pump, using an air-cooled Leybold turbo-molecular high vacuum pump model Turbovac TW 200 N, the chamber's pressure is brought down to $\approx 1 \mu\text{Torr}$ in ≈ 6 hours. These times and conditions vary upon the condition of the chamber, e.g. chamber being clean and dry, humidity in the air, etc. The low base pressure is necessary to prevent contamination due to unwanted ions which will affect the quality of implanted substrates. The working pressure of e.g. 10 mTorr will have less than 1:10,000 ion contamination.

A Granville Philips Micro-Ion Plus gauge model 356-002 is connected to the chamber to read the working pressure. It is recommended not to let the fore-line pressure, i.e. the pressure between the roughing pump and the turbo pump, which is currently controlled by a KJLC 205 Series Thermocouple Gauge Controller, exceed ~ 200 mTorr, when the turbo pump is turned on and in line. The turbo pump should be isolated from the rough pump by turning off the fore-line air-controlled valve; and be isolated from the chamber, by fully closing the gate-valve, when the fore-line and chamber pressures are higher than the recommended values for the turbo pump. For a schematic of the valves and pumps see figure 3.3.

After each pump-down procedure and before filling the chamber with the working gas, it is always useful to

make sure that the base pressure is sufficiently low. Currently, the base pressure is monitored by a Granville Philips model 274 Bayard-Alpert ionisation gauge tube, controlled by a Veeco model RG-840 ionisation gauge controller.

The flow rate of gas into the chamber is controlled by a mass flow controller (MKS type M100B) and can be varied from 1 to 100 sccm. The chamber pressure is controlled the balance between the gas flow in and the pump out rate through the turbo pump. This rate can be adjusted by partially closing the gate valve (GV in figure 3.3). For a fixed value of the input flow rate, fine tuning of the pressure can be done by adjusting the gate valve until the desired pressure is reached. Figure 3.3 is the schematic of the vacuum and gas-flow system of the ICP-II 600 PII machine.

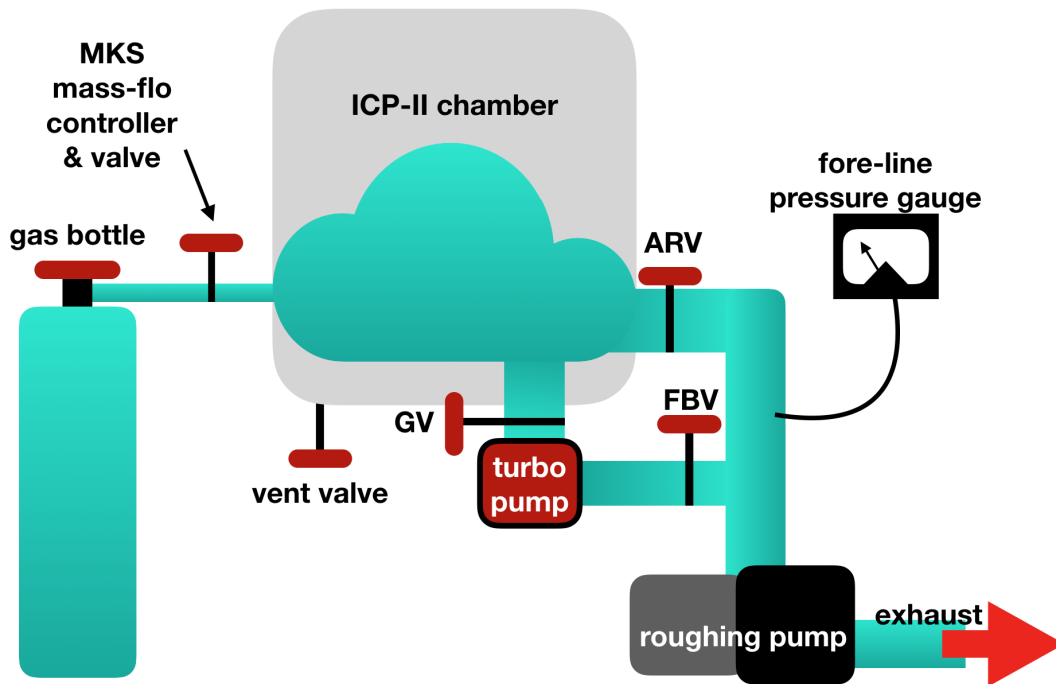


Figure 3.3: A schematic of ICP-2 Plasma processing chamber gas-flow controllers and pump-down systems. ARV, GV, FBV stand for Auxiliary Roughing Valve, Gate Valve, and Fore-line Block Valve, respectively.

3.2.2 Power Generator and Controller

The RF-power is obtained from a MKS ENI model OEM-650A RF-plasma generator, which is water cooled power source designed for the use in plasma and sputtering applications. The maximum continuous output power of this model is 650 W into a 50Ω impedance, matched with plasma by a Match Pro CPM-1000 matching network. The matching network consists of two parts, namely the tuning unit and the control unit. The tuning unit consists of the matching components, which include variable inductors and capacitors, and

RF sensors to provide feedback of the forward and reflected RF power.

3.2.3 The Marx High-Voltage Pulser

The high voltage pulses are supplied by stacks of custom built Marx stage modulators which were originally designed by J.T. Steenkamp [17] with successive upgrades. The peak voltage pulse amplitude is:

$$V = V_{DC} \times N_s \times \eta_t \quad (3.1)$$

V_{DC} is the voltage output of the direct current power supply (with max of ≈ 1 kV), this amount can be multiplied by number of the stages installed, N_s and the step-up ratio of the transformer η_t . The high voltage pulser system can be used in both Marx mode (no transformer) and transformer mode. In the transformer mode, a Westinghouse 610J647H01 step-up transformer (1:10 ratio) and a shunt resistor of 2 k Ω are connected between the pulse generator and the ICP-2 chamber's sample holder; providing the possibility of higher penetration of ions to the biased target in cost of wide spread in the ion energy distribution at the target. Narrower distribution is possible by eliminating the transformer and shunt resistor between Marx stage and chamber's stand, limiting the maximum pulse to about 1 kV. The standard operating mode used throughout this project is the transformer mode as it is commonly used to achieve greater ion penetration depth [16].

3.2.4 High-Voltage Monitoring

The pulse repetition frequency (prf) is fixed at 250 Hz, while the pulse duration can be varied from 2 μ s to hundreds of μ s using a custom-made pulse controller. The reason for such limitation at 2 μ s, is that each pulse needs a rising and falling time of ≈ 1 μ s. A Tektronix model P6015A is utilised to probe the voltage and the current is acquired using a Pearson model 150 Rogowski coil with 0.5 V/A ratio. More detailed discussion of the current high voltage pulser system can be reviewed in J.T. Steenkamp's M.Sc. thesis [17], Marcel Risch has discussed the changes he made to account for the pulser's limitations in his M.Sc thesis in detail [16].

3.2.5 Langmuir Probe

Langmuir probes are still the most widely used diagnostic devices for plasma characterisation due to their simplicity, practicality, and widely developed data analysis methods [12]. The basic Langmuir probe is a wire of known dimensions inserted into the plasma. Figure 3.4a shows an uncompensated probe made to acquire data presented in appendix B. The probe voltage is swept from a large negative value (typically -50 V) up to a positive value higher than the plasma potential. Analysis of the probe's I-V curve gives the main plasma parameters including the electron temperature T_e , plasma density n_0 , floating V_f and plasma potentials V_p . A new high-accuracy custom-made RF-compensated Langmuir probe was designed and built for the purposes

of this thesis. It was used to acquire the plasma data presented in chapter 5 as well as appendix A. Figure 3.4a shows this RF-compensated probe. Note this Langmuir probe has a removable tip. The theory of the Langmuir probe and design will be discussed in more detail in the chapter 4. Full details of the custom RF-compensated probe designed and built for this thesis is in appendix C.



(a) Uncompensated Langmuir probe.



(b) RF-compensated Langmuir probe.

Figure 3.4: (a) Photo of the assembled uncompensated Langmuir probe built and used to acquire data presented in appendix B in order to make possible the comparison of the RF-compensated and uncompensated probe measurements. The probe's tip is a tungsten wire immersed into the plasma. The final probe tip length is 1.0 cm, and the radius a for this probe tip is 0.155 mm. The design allows easy exchange of the tungsten probe tip. (b) RF-compensated Langmuir probe with electrode used for acquiring data presented in chapter 5 and appendix A.

3.3 Langmuir Probe Data Acquisition System

The Langmuir probe was controlled by a National Instrument data acquisition device (DAQ). Using Labview, the National Instruments DAQ was programmed to produce a voltage sweep from a minimum of -10V to a maximum of +10V, this signal is amplified 10 times by the Apex PA341 high-voltage power amplifier. A high-common voltage differential amplifier, Texas Instruments INA117, was utilised to measure the current acquired by the probe's tip. The voltage difference between the two ends of the measuring (Ohmic) resistor is then converted to current, using Ohm's law. The impedance of the probe at the given sweep frequency is taken into account at this stage. A schematic of the control circuit is shown in Figure 3.5. Note that the sense (measuring) resistor R_5 could be chosen at the time of measurement. Most of the measurements were done across a 150 Ω or 100 Ω sense resistor.

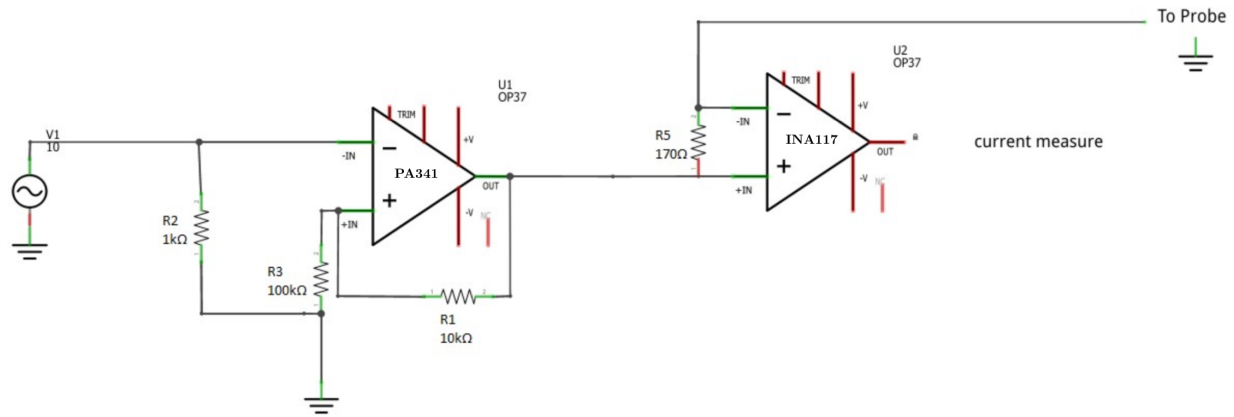


Figure 3.5: Schematic of the Langmuir probe control circuit. The Apex PA341 high voltage power operational amplifier amplifies the bias voltage from the DAQ by $10\times$ before feeding it to the Langmuir probe. The current through the sense resistor R_5 is measured by the INA117 high common-mode voltage difference amplifier.

3.3.1 The Data Acquisition Setup For Time-Resolved Measurements

Time-resolved measurements of Argon plasma during plasma ion implantation procedure were acquired using a steady DC power supply, a measuring resistor and TI INA117 differential amplifier. A four channel Tektronix model TBS2104 oscilloscope was used for measuring the current from the probe (INA117 out), the current going through the target measured by Rogowski coil, the applied high voltage pulse and the DC probe bias voltage from the power supply was directly measured on the scope. The Tektronix oscilloscope provides 20,000 data-points in each measured time window.

4 PLASMA DIAGNOSTICS: LANGMUIR PROBE

4.1 Langmuir Probe

Irving Langmuir used Langmuir probes for means of plasma diagnostics in early 20th century. The theoretical analysis of these probes has been done by Langmuir and Mott-Smith in 1926 [18]. A basic Langmuir probe is a wire inserted into the plasma [19]. This current-collecting wire/electrode can have different shapes, e.g. cylindrical, planar or spherical, to characterise plasmas with different geometries. Among those, cylindrical probes are most commonly used due to their manufacturing convenience and well-developed analysis [1].

The probe is biased both positively and negatively over a wide voltage range in order to measure a characteristic current-voltage curve for the plasma. When the probe is negatively biased, the current is mainly due to ions collected by the probe tip, thus usually referred to as ion saturation region $I_{i,sat}$. As the probe bias becomes more positive, the electron contribution to the collected current goes higher. The probe reaches the floating potential $V_B = V_f$ when the current from ions and more mobile electrons are the same. Increasing the bias voltage beyond this point, will draw more electrons to the probe, following an exponential curve, in a plasma with Maxwellian electron distribution. When the probe's bias voltage becomes equal to the local plasma potential $V_B = V_p$, the current drawn by the probe mostly comes from more mobile electrons. Increasing the bias voltage beyond this point results in electron saturation current, which is a constant current for planar probes and a growing linear function for cylindrical probes [19]. Figure 4.1 shows a typical I-V curve acquired by an RF-compensated probe in our Ar plasma. Due to the mobility of electrons, electron saturation current is a lot higher than ion saturation current, by the factor of $\approx (m_e/M_i)^{1/2}$ in a typical Langmuir probe I-V curve [19].

The basic theory for a biased plane electrode is already discussed in the sheath calculations in chapter 2. However the Langmuir probes are commonly made with a cylindrical geometry. The reason is the manufacturing convenience and to minimise the probe's surface [12]. It is better to make the probe's tip as small as possible, with the wire radius $a < \lambda_{De}$ to minimise plasma perturbation [19]. Ions and electrons hitting the probe's tip might deviate from their direct trajectories in the sheath created by the electrode [1].

The trajectories of charged particles in the sheath then become important in determining the collected current, as some particles will deviate from direct collision into the electrode. Thus the analysis becomes more complicated. As the voltage is raised, either to large positive or large negative values with respect to the plasma, the sheath thickness s increases according to Childs law (described in page 8), and also the collecting area around the probe increases [1].

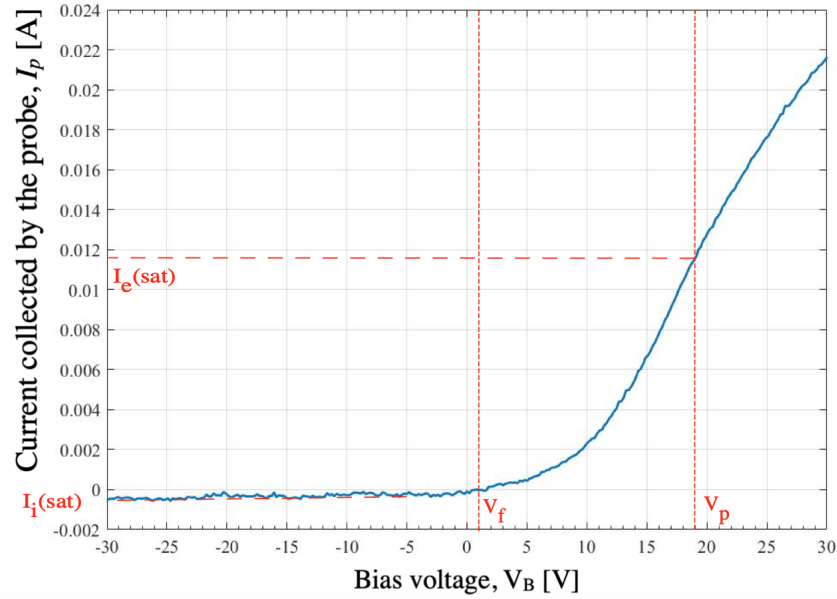


Figure 4.1: A sample I-V curve acquired by a Langmuir probe in RF-ICP Ar plasma for this work. The dimensions of the cylindrical tungsten tip used to acquire this curve was 1.0 cm length and 0.31 mm diameter. V_p is the plasma potential, also known as space potential, is near the "knee" of the curve. At the far negative bias, where all the electrons have been repelled from probe's tip, it's ion saturation current, I_{sat} . The floating potential V_f , is where the ion and electron currents are equal, and the net current going through probe's tip is zero. In the Transition Region, the ion current is negligible, and the electrons are partially repelled by the negative potential $V_B - V_p$. In a Maxwellian plasma, this part of the curve is exponential. When V_B reaches V_p , all of the random thermal flux of electrons is collected. In the Electron Saturation region, I_e grows more slowly because of the expansion of the sheath, the sheath expansion depends on the tip's geometry. From the I-V curve, the plasma density n_0 , electron temperature kT_e , and plasma potential V_p can be determined, but not the ion temperature.

In an RF-driven plasmas, e.g. RF-ICP, an additional complication arises which is the potential of the plasma oscillates with respect to ground. In order to accurately map our Argon plasma generated in an RF-ICP chamber, dealing with this issue by designing a RF-compensated Langmuir probe is the main focus of this chapter.

RF-discharges heat electrons in plasma, which results in a high temperature electron tail. Godyak et al. in 1993 [20] have modelled these plasmas with a bi-temperature Maxwellian distribution. They showed that in Langmuir probe analysis, if the electrons are modelled as a single temperature Maxwellian as their equilibrium-steady state distribution, it might lead to large errors in extracted plasma parameters from Langmuir probe I-V curves [21].

4.1.1 Maxwellian Electrons

Langmuir probe theory has generally been developed for plasmas in which the electron distribution can be approximated by a Maxwellian distribution, which ICP plasmas are considered to be fairly close to in their working pressure regimes [22]. Several groups [23, 24, 25] have studies electron distribution in ICP discharges recently. If the electrons are Maxwellian, the electron current in any time can be determined from [19]:

$$I_e = I_{es} \exp [e(V_B - V_p)/k_B T_e], \quad (4.1)$$

where electron saturation current I_{es} is determined by [19]:

$$I_{es} = eAn_e\bar{v}/4 = en_eA\left[\frac{k_B T_e}{2\pi m}\right]^{1/2} \quad (4.2)$$

m is electron's mass, e is its charge, n_e is the electron density. A is the probe's tip area in the equation. Equation 4.1 shows that the slope of the $(\ln I_p)V_B$ curve, figure 4.2, is $e/k_B T_e$ [19]. It is convenient and common in plasma community to write $k_B T_e$ as T_e , the electron temperature is given in eV . If the electron distribution can be assumed as Maxwellian, the electron energy distribution function (EEDF) $f(v_e)$ at a plasma potential V_p is given by the following [19]

$$f(v)d^3v = \left(\frac{m_e}{2\pi k_B T_e}\right)^{3/2} \exp\left(-\frac{e|V_p|}{k_B T_e}\right) \exp\left(-mv^2/2k_B T_e\right)d^3v \quad (4.3)$$

Remembering the I-V curve from figure 4.1, if the exponential part between floating and plasma potentials could be fitted with a straight line, when plotted as $\log(I_p)$ vs. V_B , i.e. semi-logarithmically, the electron distribution function can be assumed as Maxwellian. Figure 4.2 shows a measured electron characteristic and a straight-line fit to it.

4.1.2 Non-Maxwellian Electrons

If the electron energy distribution function (EEDF) is not Maxwellian, the electron energy distribution function (EEDF) $f(v_e)$ can be numerically determined from the shape of the curve shown in figure 4.2 [26].

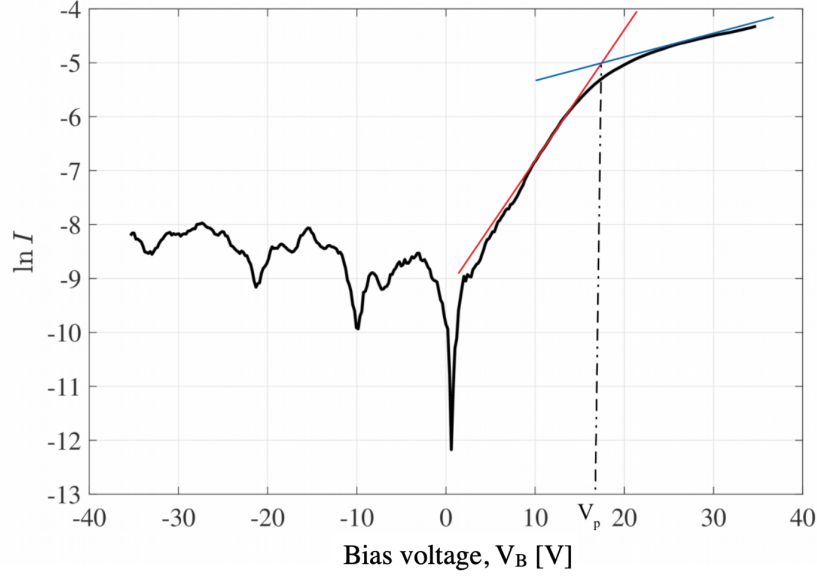


Figure 4.2: A semi-logarithmic plot of electron current as a function of probe bias voltage from I-V curve acquired in RF-ICP plasma - similar to I-V curve shown in figure 4.1. The I-V curve is acquired in argon gas pressure $P_{Ar} = 1.5$ mTorr, $P_{RF} = 120$ W at the axial location of 21.7 cm above the stainless steel target.

Plasmas generated in an RF-discharge tend to deviate from Maxwellian distribution in low pressures [13]. Recent studies are trying to model and approximate the electron energy probability with a bi-temperature Maxwellian distributions [14, 13]. In this subsection we focus on a non-Maxwellian but isotropic electron distribution in plasma. If the mean free path of electrons are larger than the probe's radius, Langmuir probe theory can be used with the consideration of the deviation from Maxwellian distribution. First we start with defining our polar coordinate system around the probe tip. Consider electrons having the z velocity component $v_z = v \cos \theta$ toward the probe tip, z direction is defined alongside the normal of the probe's tip surface. θ is the angle between electron's velocity vector and z axis. The general form of the current collected by the probe from electrons with an isotropic electron velocity distribution $f(v)$ is given as [12]:

$$I_e = eA \int f(\mathbf{v}) \mathbf{v} \cdot \mathbf{n}_e d^3v = eA \int f(v, \theta, \phi) v \cos \theta v^2 \sin \theta d\theta d\phi dv \quad (4.4)$$

Integrating over ϕ gives:

$$I_e = 2\pi eA \int_{v_{min}}^{\infty} \int_0^{\Theta_{max}} v^3 f(v, \theta) \cos \theta \sin \theta d\theta dv \quad (4.5)$$

in which v_{min} is defined as [27]:

$$v_{min} = \sqrt{\frac{2e}{m}(V_B - V_p)} \quad (4.6)$$

and Θ_{max} is defined as [27]:

$$\Theta_{max} = \cos^{-1}\left(\frac{v_{min}}{v}\right). \quad (4.7)$$

Using equations 4.6 and 4.7 to integrate equation 4.5 over θ leads to the followings [27]:

$$I_e = 2\pi eA \int_{v_{min}}^{\infty} v^3 f(v) dv \int_0^{\cos^{-1}\left(\frac{v_{min}}{v}\right)} \sin \theta \cos \theta d\theta \quad (4.8a)$$

$$I_e = \pi eA \int_{v_{min}}^{\infty} v^3 \left[1 - \left(\frac{2e(V_B - V_p)}{mv^2}\right)^2\right] f(v) dv. \quad (4.8b)$$

Defining energy distribution function $f(\epsilon)$ in which the kinetic energy of electrons are denoted as $\epsilon = \frac{1}{2}mv^2$:

$$f(\epsilon) = \sqrt{\frac{m^3}{2\epsilon}} v^2 f(v) \quad (4.9)$$

so that the electron density can be written in the form [12, 27]:

$$n_e = 4\pi \int f(\mathbf{v}) v^2 d\mathbf{v} = 4\pi \sqrt{\frac{2}{m^3}} \int f(\epsilon) \sqrt{\epsilon} d\epsilon. \quad (4.10)$$

Equation 4.9 would simplify equation 4.8b further [27]:

$$I_e = \frac{2\pi eA}{m^2} \int_{e\Delta V}^{\infty} f(\epsilon) (\epsilon - e\Delta V) d\epsilon. \quad (4.11)$$

in which $V = \Delta V = V_B - V_p$. getting the first derivative of equation 4.11 with respect to V gives [27]:

$$\frac{dI_e}{dV} = \frac{2\pi eA}{m^2} \int_{eV}^{\infty} \frac{d}{dV} [f(\epsilon) (\epsilon - eV)] d\epsilon \quad (4.12)$$

The second derivative of the equation, leads us to the Druyvesteyn formula [27]:

$$\frac{d^2 I_e}{dV^2} = \frac{2\pi e^3 A}{m^2} f(eV) = \frac{2\pi e^3 A}{m^2} f(\epsilon) \quad (4.13)$$

The above equation shows that the second derivation of a given I-V curve from a Langmuir probe measurement provides us with the distribution function of electrons in the plasma [27, 28]. The Druyvesteyn analysis of the plasma I-V curve is based on this, thus gives a more robust analysis than the Langmuir analysis generally, as it works for any isotropic distribution function, not only Maxwellian distributed electrons.

4.2 Potential Oscillation in RF Plasmas

Langmuir probe I-V curves for RF-driven plasmas are different from those for plasmas generated by DC or microwave discharges [1]. Plasma potential for radio frequency plasmas are oscillating at a frequency of $n\omega/2\pi$, in which n is the number of harmonic modes ($n = 1, 2, 3, \dots$) [29]. The potential of an RF-compensated Langmuir probe tip follows the plasma potential oscillation, i.e. in form of $\tilde{V}_{probe} = V_{DC} + \tilde{V}_p$ [1].

The wave-pattern of the floating potential, V_f of the uncompensated probe can be measured directly by connecting the Langmuir probe to an oscilloscope. Additionally, a fast Fourier transformation (FFT) of the signal can be acquired in order to determine the dominant frequency components of the plasma under study [29]. In the presented case, the RF-antenna of ICP-2 chamber is oscillating with 13.56 MHz frequency. As illustrated in figure 4.3, the dominant frequencies of such systems are the fundamental 13.56 MHz and the second harmonic which is 27.12 MHz. Therefore in order to design an efficient RF-compensated Langmuir probe, one should consider only to filter out these harmonics [30]. The ideal probe would be one with an extremely high impedance at these frequencies and near-zero impedance for the other frequencies, especially the ones which lay below 1 MHz as most plasma instabilities, (including the instabilities caused by 250 Hz high voltage pulser used for means of PII) occur in this regime [1].

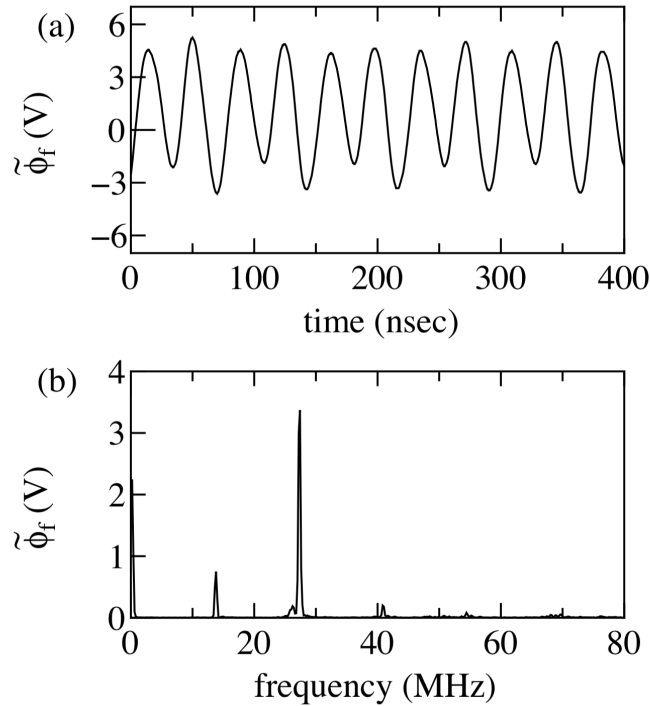


Figure 4.3: The image was taken from reference [29]. An example of the floating potential V_f of an uncompensated probe in a RF-driven plasma. (a) Wave-pattern of the floating potential V_f of the uncompensated Langmuir probe measured directly by an oscilloscope. (b) Frequency spectrum of V_f obtained by FFT of the top figure. As can be seen the first two harmonics are the most dominant ones.

4.2.1 Radio Frequency (RF) Compensation

Figure 4.4, shows the IV probe curves for various values of $V_p(t)$. The knee of the probe curve, marked with a vertical dashed line, gives the value of V_B where $V_p(t) = V_B$. As $V_p(t)$ oscillates in time as shown, the probe curve oscillates horizontally back and forth. The time average of this motion, indicated as the heavy

line, gives the apparent probe I-V curve. It is clear from the figure that the electron temperature determined from this curve will be much higher than the actual T_e [19].

Although it is possible to interpret the time-average current measurements [19], it is also possible to build filters for the dominant harmonics of the generated radio frequency so that the I-V curve obtained from the Langmuir probe can be analysed as it is acquired. Simple LC circuits with the self-resonance frequencies of the harmonics (see figure 4.3) can be placed in series with the probe's tip in order to act as passive filters for these frequencies [1]. Another collecting surface can be placed near the probe's tip as a local reference to get the oscillating frequency in the probe's tip area [19]. This reference electrode is connected in parallel between the series of LC circuits and the probe's tip. The LC circuits can be replaced with miniature choke coils in order to be placed close to the probe tip to get a more efficient RF compensation.

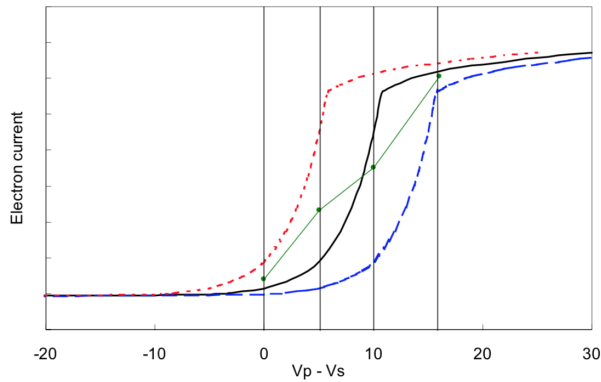


Figure 4.4: The image was reproduced from reference [19]. The correct I-V curve is at the centre and the other two dashed curves have ± 5 V difference in their V_p measurements. This difference, i.e. shift in the plasma potential measurement is because of RF-oscillation effect of the plasma under study. An I-V curve obtained by an uncompensated probe, looks like the green rebuilt of the I-V curve. The semi-log is fitted with a less steep line comparing to the correct one, leading to a higher electron temperature value as the electron temperature value increases with increase of the difference between floating and plasma potentials in the I-V curve (see equation A.1).

The probe circuit elements, the additional series inductive choke element built in LC circuits, and a large bypass capacitor C_{bypass} are shown in Figure C.3a.

4.3 Design of RF-compensated Langmuir Probe

4.3.1 Choke Coils Characterisation

Figure 4.5b shows the circuit used to characterise the choke coils and the circuitry inside the Langmuir probe's final assembly. A Rohde and Schwarz network analyser model ZH4 was used in order to acquire the transmission function S_{21} of the chokes in a wide range of frequency from a low of 100 kHz to a high of 55 MHz in order to cover the first three harmonics of RF-ICP system. See figure 4.6 for the S_{21} graph of the final probe's assembly.

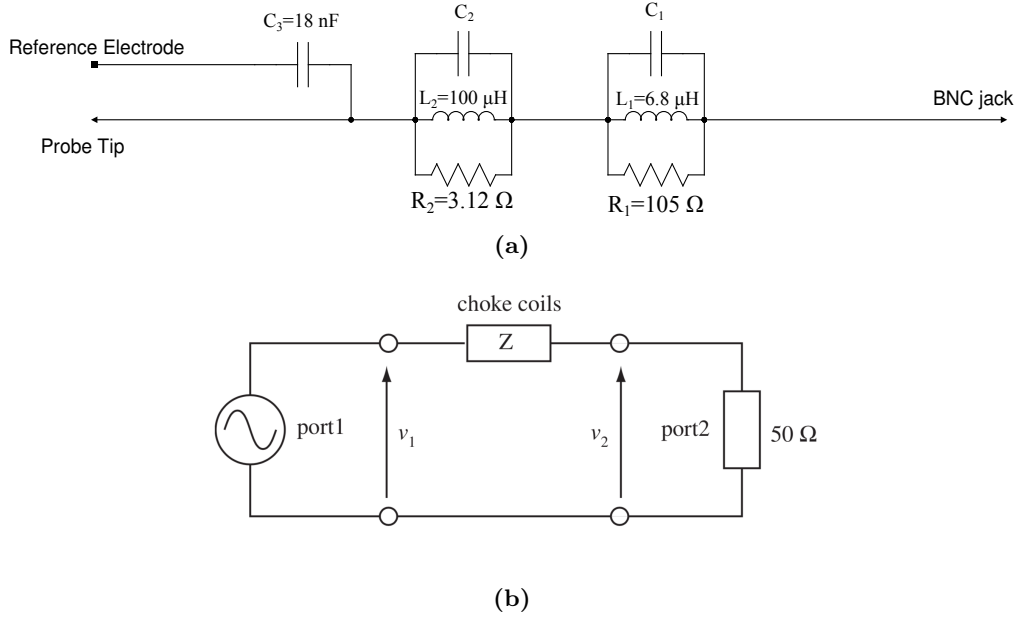


Figure 4.5: (a) The RF-compensated Langmuir probe circuit used in this work. The first and second RLC circuits represent the 27.12 MHz and 13.56 MHz self-resonant chokes respectively. Note that the self-capacitance values calculated from the choke parallel self-resonant frequencies are approximately $c_1 = 5.06$ pF and $c_2 = 1.38$ pF. (b) Measurement circuit to obtain the transmission S-parameter (S_{21}) for the RF-compensated Langmuir probe. **Note** that this figure has been reproduced from reference [29]. The S-parameter $S_{21} = v_2/v_1$ is the voltage transfer function.

Voltage Transfer Function S_{21} [dB]

Figure 4.6: Plot of voltage transfer function $S_{21} = \frac{v_2}{v_1}$ as a function of frequency, acquired from the final assembly of the RF-compensated Langmuir probe built to be used in this project. The transfer function S-parameter is less than -22 dB between 100 kHz to 1 MHz and about -60.2 dB and -50.6 dB at 13.56 MHz and 27.12 MHz respectively. The filtering of the third harmonic 54.24 MHz is about -45 dB which is not quite as important as the first two harmonics due to the low amplitude of the third harmonic frequency shown in figure 4.3.

4.4 Langmuir Probe Analysis Theories

4.4.1 Cylindrical Langmuir Probe With Collisionless Sheath - Orbital Motion Limit (OML) Theory

The early theory of ion analysis of a characteristic current-voltage curve done by Langmuir [18] was orbital motion limit theory, which was based on some simplifying assumptions making it not applicable to many working plasma conditions and probe geometries. Figure 4.7 shows a diagram of an approaching ion to a cylindrical Langmuir probe's tip. The ion assumed to come from infinity with a potential of 0, into a negative potential, through a space with a smooth variation of potential to the minimum of potential at probe's tip [19]. This assumption of sheath edge at infinity will leave out the sheath formation around probe's tip.

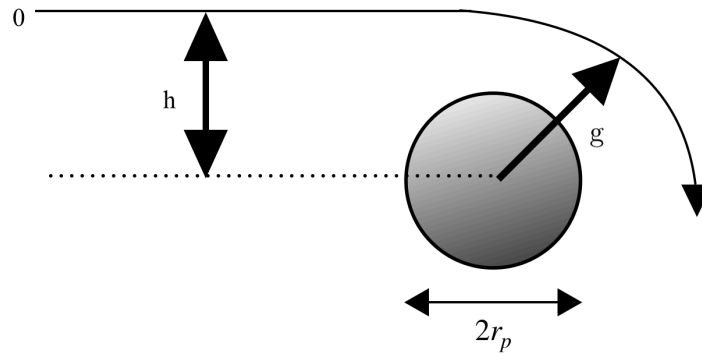


Figure 4.7: The image was reproduced from reference [31]. The diagram shows the impact factor h and the closest approach point of the particles to the cylindrical Langmuir probe's tip, i.e. point g .

We start by writing conservation of energy and angular momentum between point 0 and g shown in figure 4.7. The conservation of energy between the two points is as follows [19]:

$$\frac{1}{2}mv_0^2 = \frac{1}{2}mv_g^2 + eV_g = -eV_0, \quad (4.14)$$

where V_g is the potential at point g , eV_0 is the energy of particle at point 0. v_0 is the particle (e.g. ion) velocity at point 0 and v_g is the velocity at point g . The conservation of momentum between two points gives [19]:

$$mv_g r_g = mv_0 h, \quad (4.15)$$

where h is the radial distance between the particle trajectory and the axis of the cylindrical probe tip, shown in figure 4.7. r_g is the radial distance between the ion in location g and the probe's axis, at the critical limit of point g meeting the probe's surface $r_g = r_p$. Saying these, we are interested in the ions with a trajectory in the perpendicular plane to the probe's tip axis, and collected by the probe [31].

Rearranging the angular momentum conservation for h , and replacing the velocities by potentials using equation 4.14 gives [31]:

$$h = r_p \left(\frac{vg}{v_0} \right) = r_p \sqrt{1 + \frac{V_g}{V_0}}. \quad (4.16)$$

The ions with a velocity between v and $v + dv$ provide the following current to the probe's tip [31],

$$dI = 2lehv \left[1 + \frac{V_g}{V_0} \right]^{1/2} dn, \quad (4.17)$$

in which dn is given by the following in a plasma with the density of n_0 [31]:

$$dn = n_0 \left(\frac{m}{2\pi k_B T} \right) \exp\left(-\frac{mv^2}{2k_B T}\right) v dv, \quad (4.18)$$

in which $k_B T$ is the temperature of the particles. Integration over dI in equation 4.17 will provide us with the total current of the ions with trajectories in the planes perpendicular to the probe tip. Setting the following set of the parameters, will make the integration easier [31].

$$x^2 = \frac{mv^2}{2k_B T}, \quad (4.19a)$$

$$a^2 = \frac{eV_g}{k_B T}. \quad (4.19b)$$

The integration can now be written in the following form [31]:

$$I = \int dI = 4n_0 r_p l e \left(\frac{2k_B T}{m} \right) \int_0^\infty x e^{-x} (x^2 + a^2)^{1/2} dx. \quad (4.20)$$

Giving that the erf is 0 at 0 and 1 at infinity, and the values of m and $k_B T$ is always positive, solving the integration provides us with the following equation [31]:

$$I = 4\sqrt{\pi} n_0 r_p l e \left(\frac{k_B T}{2\pi m} \right)^{1/2} \left(1 + \frac{eV_g}{k_B T} \right)^{1/2}. \quad (4.21)$$

In the limit of $T \rightarrow 0$, the equation becomes [19]:

$$I \approx A_p n_0 e \frac{\sqrt{2}}{\pi} \left(\frac{eV_B}{m} \right)^{1/2}, \quad (4.22)$$

in which $A_p = 2\pi r_p l$ is defined as the probe's tip area. V_B is the probe bias. The equation above shows that if the sheath limit can be considered at infinity, a very rough estimation of the ions current to the probe in the limit of very cold ions will be proportional to the square root of the probe's bias potential [19]. As we already noted, OML has a lot of assumptions which makes the theory impractical in the case of the thicker probe tips.

4.4.2 Allen-Boyd-Reynolds (ABR) Theory

Allen, Boyd and Reynolds (ABR) constructed a theory for collecting ions by a Langmuir probe in 1957 [32]. Their theory simply solved Poisson equation from probe's tip to infinity, radially without taking into account the ions orbital motion around the probe's tip [19]. Later, in 1965, Francis F. Chen solved the same problem in cylindrical coordinates [33], to be used for cylindrical Langmuir probes [19]. As I used a cylindrical Langmuir probe to acquire argon plasma characteristics, Chen's generalisation for cylindrical probe will be presented in the following lines.

Having the probe tip at $r=0$ of the cylindrical coordinate, one can write Poisson's equation in the following form [19]:

$$\frac{1}{r} \frac{\partial}{\partial r} \left(r \frac{\partial \phi}{\partial r} \right) = \frac{e}{\epsilon_0} (n_e - n_i). \quad (4.23)$$

If I_i is set to be the total flux of ions collected by the probe, using current continuity, the flux at any radius r is given as [19]:

$$\Gamma = en_i v_i = \frac{I_i}{l2\pi r}, \quad (4.24)$$

where l is probe's tip length, and the velocity of ions, v_i is defined by the conservation of energy [19]:

$$\frac{1}{2} M v_i^2 = -e\Phi, \quad (4.25a)$$

rearranging for v_i :

$$v_i = \sqrt{\frac{-2e\phi}{M}}. \quad (4.25b)$$

Implementing the latter equation into equation 4.24 leads to the density of ions [19]:

$$n_i = \frac{\Gamma}{v_i} = \frac{I}{2\pi r l} \left(\frac{M}{-2e\Phi} \right)^{1/2}. \quad (4.26)$$

If we can assume that the electrons follow a Maxwellian distribution - which is a reasonable assumption for our RF-ICP plasma in steady state, from solving equation 4.10 for Maxwellian distribution:

$$f(v) d^3v = \left(\frac{m_e}{2\pi k_B T_e} \right)^{3/2} \exp\left(\frac{-e|\Phi|}{k_B T_e} \right) \exp\left(-\frac{mv^2}{2k_B T_e} \right) d^3v,$$

we can write [19]:

$$n_e = n_0 e^{e\Phi/k_B T_e}. \quad (4.27)$$

Now, by determining ion and electron densities, we can re-write the Poisson equation from equation 4.23 as [19]:

$$\frac{1}{r} \frac{\partial}{\partial r} \left(r \frac{\partial \phi}{\partial r} \right) = \frac{e}{\epsilon_0} \left[\frac{I}{l2\pi r} \left(\frac{M}{-2e\Phi} \right)^{1/2} - n_0 e^{e\Phi/k_B T_e} \right]. \quad (4.28)$$

This is the ABR relation between collected current, in a potential ϕ and the electron temperature and the density of the plasma. In the next chapter, the results of this analysis is presented and will be compared to the results obtained by OML and Langmuir analysis.

4.4.3 Bernstein-Rabinowitz-Laframboise (BRL) Theory

ABR theory does not take into account the sheath formation around the probe's tip. It assumes that the ions starting from infinity can hit the probe tip without feeling a potential barrier until hitting the probe's tip [32]. In 1959 Bernstein and Rabinowitz published a theory which included both sheath formation and ion orbital motion [34]. In BR theory the ions are assigned an energy E , and an angular momentum J . Based on J and E of the ions, a maximum radius is defined for collecting ions. The ions with the sufficient amount of energy and angular momentum can hit the probe, and those with insufficient energy or angular momentum are repelled by the sheath potential barrier and will not make it to the probe tip [19]. In 1966 Laframboise modified the theory by assuming a Maxwellian ion distribution function [35]. Before, BR theory assumed the ions to have zero temperature [19].

BRL method for cylindrical probes requires solving the following equation [19]:

$$\begin{aligned} \frac{1}{\xi} \frac{d}{d\xi} \left(\xi \frac{d\eta}{d\xi} \right) &= 1 - \frac{1}{\pi} \sin^{-1} \left(\frac{I/l\xi^2}{1+\eta/\beta} \right)^{1/2} & \xi > \xi_0 \\ &= \frac{1}{\pi} \sin^{-1} \left(\frac{I/l\xi^2}{1+\eta/\beta} \right)^{1/2} & \xi < \xi_0 \end{aligned} \quad (4.29)$$

where β is ion energy divided by $k_B T_e$, ξ_0 occurs when the argument of the \sin^{-1} is one, leading to $\sin^{-1}(1) = \pi/2$. We will not use the BRL analysis method as BRL predictions is more suitable for fully ionised plasmas rather than partially ionised ones such as ICP systems. One might think that BR results would be similar to ABR as one takes the ion temperature to be zero $T_i=0$; this is the case only in spherical probes and will not apply to our cylindrical probe [19].

5 EXPERIMENTAL RESULTS: STEADY STATE AND PULSED ARGON PLASMAS

- This is a story of migrating ions and electrons.

5.1 Steady State Plasma Characterisation

The RF-compensated Langmuir probe system described previously was used to characterise the steady state operation of the RF-ICP plasma system.

The purpose of these steady state measurements is to determine the key plasma properties which are, the plasma Density n_0 , the electron temperature T_e , in addition measurements were made of the plasma potential V_p as well as the floating potential V_f . Remembering $(V_p - V_f) \propto T_e$ [18], the results for plasma potential and floating potentials are presented in appendix A.

5.1.1 Measurements of Plasma Density at Constant Pressure

In this subsection I present measurements of the steady state plasma density in the RF-ICP system at two different locations on the axis of the cylindrical chamber, vertically separated by distance of 13.0 cm. Plasma density measurements were made at different values of RF-power, ranging from $P_{RF} = 80$ W to $P_{RF} = 300$ W. Measurements were done at three different pressures of Argon, namely 1.5 mTorr, 10 mTorr and 25 mTorr. Having accurate information of plasma in steady state, i.e. grounded target, is vital in order to study the pulsed argon plasma during plasma ion implantation. For instance, Lieberman's model assumes a steady state value for plasma parameters throughout the PII.

Plasma Density at Upper Probe Location

Figure 5.1 shows plasma densities in 21.7 cm above the stainless steel target plate. Figure 5.1a shows results for 1.5 mTorr Argon plasma, and 5.1b shows results for 25 mTorr. As expected, plasma density increases by applying more RF-power. Figure 5.1, shows an increase in plasma density in same power but higher gas pressure. The results for different pressure at constant RF-power will be analysed in detail in subsection 5.1.3. Note that densities are plotted in semi-logarithmic scale. Notice the plasma density overestimation of OML theory in comparison to Druyvesteyn, Langmuir and ABR theories. This overestimation is more noticeable in higher RF-powers. On the other hand, ABR theory underestimates plasma density in lower RF-powers,

however it agrees or exceeds the estimation of Druyvesteyn method at higher RF-powers. This results agree with previous works [19, 36, 37]. OML theory is generally more reliable in less dense plasmas while ABR is used for denser plasmas. A mean of the two can be used, and it is known to be in good agreement with other methods of density measurements, e.g. see reference [19] for a comparison of Langmuir probe theories to microwave interferometry measurements.

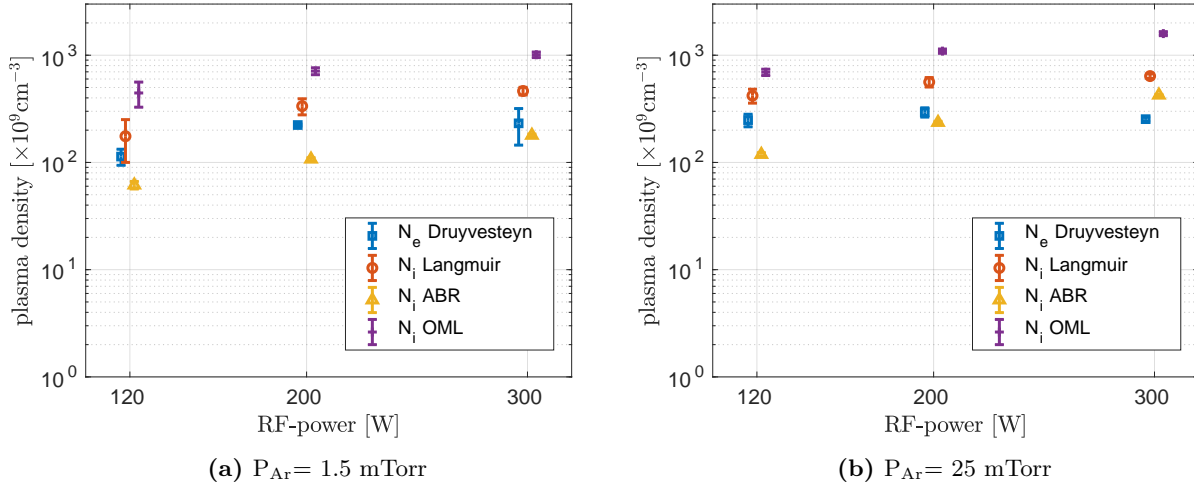


Figure 5.1: Steady state Ar plasma density as a function of RF-power in two different Argon gas pressures, on an axis location 21.7 cm above stainless steel target. Note that four different analysis methods (Druyvesteyn, Langmuir, ABR, and OML) were used to analyse each Langmuir probe curve as described in previous chapter 4. The spread on the power axis is artificial and just there to increase visibility of the data points.

Plasma Density at Lower Probe Location

Figure 5.2 shows plasma densities in 8.7 cm above the stainless steel target plate. Figure 5.2a shows results for 1.5 mTorr Argon plasma, and 5.2b shows results for 25 mTorr. Comparing these plots with the same pressure measurements from upper probe location, $\delta z_p = 13.0$ cm, shows that the plasma density is much lower (2-15 times) close to the target. This is a good check for our plasma density measurements, as it can be seen with naked eye that the upper location plasma which is closer to the RF-source is brighter.

5.1.2 Measurements of Electron Temperature at Constant Pressure

In this subsection I present measurements of the steady state electron temperature in the RF-ICP system at two different locations on the axis of the cylindrical chamber, and vertically separated by distance of 13.0 cm. Electron temperature measurements were made at a number of values of RF-power, ranging from a low of $P_{RF} = 80$ W to a high of $P_{RF} = 300$ W. Measurements were done at three different pressures of Argon, namely 1.5 mTorr, 10 mTorr and 25 mTorr. The following is a study of electron temperature evolution by changing RF-power in two constant pressures, namely 1.5mTorr and 25 mTorr.

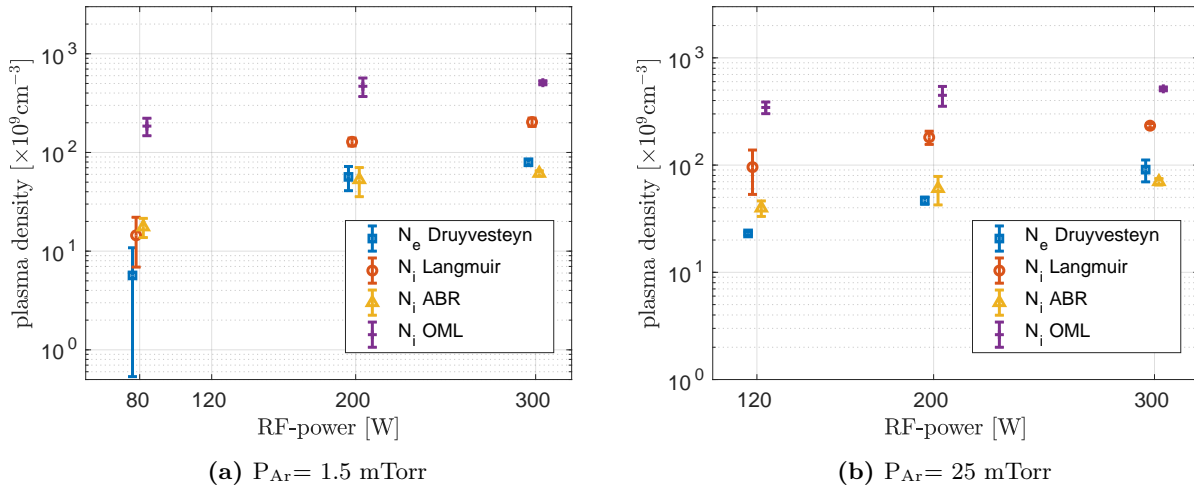


Figure 5.2: Steady state Ar plasma density as a function of RF-power, on the axis location 8.7 cm above stainless steel target. Note that four different analysis methods (Druyvesteyn, Langmuir, ABR, and OML) were used to analyse each Langmuir probe curve as described in chapter 4. The spread on the power axis is artificial and just there to increase visibility of the data points.

Electron Temperature at Upper Probe Location

Figure 5.3 shows electron temperatures in the higher of the two probe location (21.7 cm above the stainless steel target plate). Figure 5.3a shows results for 1.5 mTorr argon plasma, and 5.3b shows results for 25 mTorr gas pressure. In $P_{\text{Ar}} = 1.5 \text{ mTorr}$, the results from Druyvesteyn analysis show a raise, however the acquainted uncertainties are in the range that the electron temperature can be assumed to be unaffected by the power increase. The Langmuir analysis also suggest that although increasing RF-power might show a measurable raise in electron temperature, it is minimal within the measured error bars.

Electron Temperature at Lower Probe Location

Figure 5.4 show electron temperatures in 8.7 cm above the stainless steel target plate. Figure 5.4a shows results for 1.5 mTorr Argon plasma, and 5.4b shows results for 25 mTorr Argon gas pressure. Langmuir analysis shows almost no change in electron temperature, while Druyvesteyn results for 1.5 mTorr argon pressure shows an increase from $P_{\text{RF}} = 80 \text{ W}$ to $P_{\text{RF}} = 200 \text{ W}$ followed by decrease when increasing power from 120 W to 200 W for argon gas pressure of $P_{\text{Ar}} = 25 \text{ mTorr}$. As Druyvesteyn analysis identifies the plasma potential by zero-crossing the second derivative of the I-V curve, lesser accuracy of this analysis is expected for noisy I-V curves. Additionally, the RF-power source heats the electrons close to the RF-antenna. Comparing the lower with the upper probe location measurements, it can be seen that as expected electron temperature at fixed P_{RF} and P_{Ar} decreases with moving away from RF source.

In addition, by comparing electron temperatures in upper and lower probe locations at fixed RF-power but different pressures (figure 5.3b with figure 5.3a, and figure 5.4b with 5.4a), it can be seen that a higher pressure results in the decrease in electron temperature. The dependence of electron temperature to pressure

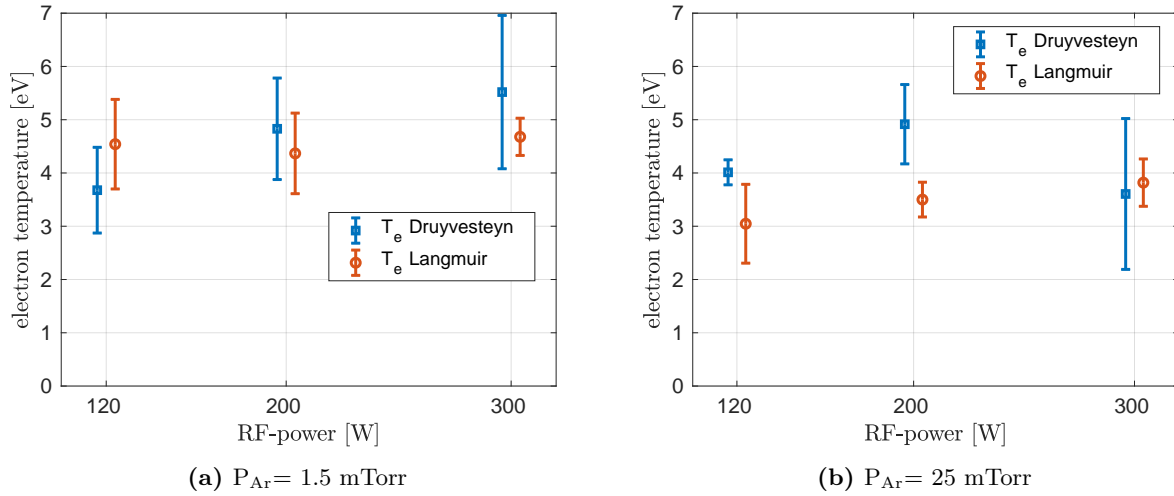


Figure 5.3: Steady state Ar electron temperature as a function of RF-power at two different Argon gas pressures, on an axis location 21.7 cm above stainless steel target. Note that two different analysis methods (Druyvesteyn and Langmuir) were used to analyse each Langmuir probe curve as described in previous chapter 4. The spread on the power axis is artificial and just there to increase visibility of the data points.

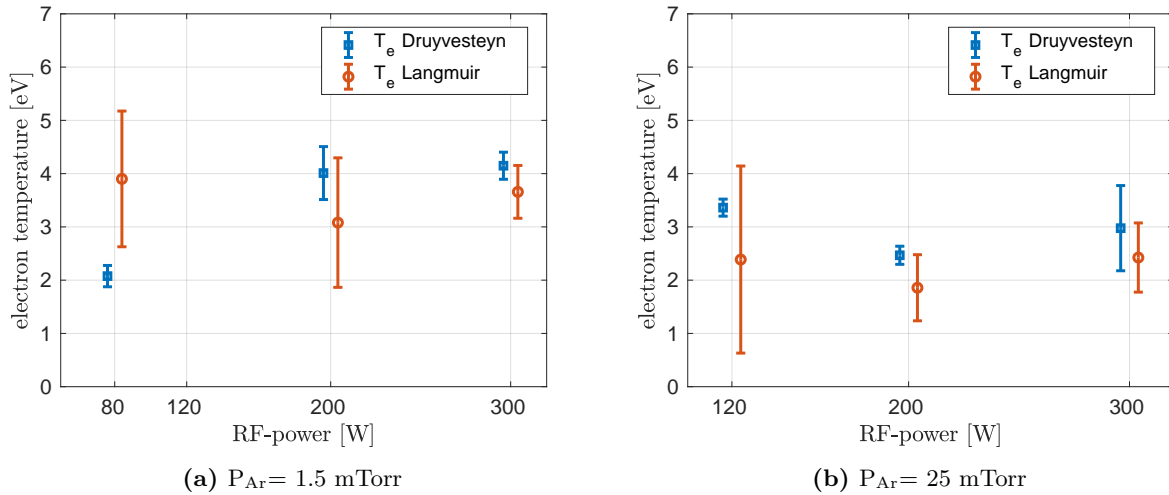


Figure 5.4: Steady state Ar electron temperature as a function of RF-power at two different Argon gas pressures, on an axis location 8.7 cm above stainless steel target. Note that two different analysis methods (Druyvesteyn and Langmuir) were used to analyse each Langmuir probe curve as described in previous chapter 4. The spread on the power axis is artificial and just there to increase visibility of the data points.

will be discussed in detail in the next subsection.

5.1.3 Measurements of Plasma Density at Constant RF-power

In this subsection I present measurements of the steady state plasma density in the RF-ICP system at two different locations on the axis of the cylindrical chamber, and vertically separated by distance of $\delta z_p = 13.0$ cm. Plasma density measurements presented here, were made at two different values of RF-power, $P_{RF} = 120$ W and $P_{RF} = 300$ W. Measurements were done at three different pressures of Argon, namely 1.5 mTorr, 10 mTorr and 25 mTorr. The evolution of electron temperature T_e as a function of pressure at constant P_{RF} is studied here.

Plasma Density at Upper Probe Location

Figure 5.5 show plasma densities in 21.7 cm above the stainless steel target plate. Figure 5.5a shows results for 200 W RF-power, and 5.5b shows results for 300 W RF-power. One can see the overestimation of densities especially in the case of more dense plasmas from OML analysis in here as well. ABR shows good agreement with Langmuir and Druyvesteyn analysis in the reported RF-powers. At both 200 W and 300 W powers, ABR, Langmuir, and OML analysis show increase in plasma density as argon gas pressure increases. This increase is within the order of 10^{11} cm⁻³ for ABR and Langmuir analysis, while OML predicts a higher plasma density closer to 10^{12} cm⁻³. On the other hand, Druyvesteyn analysis shows a decrease in plasma density in 200 W plasma power from 1.5 mTorr pressure to 10 mTorr argon pressure. By comparing figure 5.5a to figure 5.5b, OML, ABR and Langmuir theories predict higher values of plasma density for 300 W plasma. The density values predicted by Druyvesteyn analysis are the same within the errors for $P_{RF} = 300$ W vs. $P_{RF} = 200$ W.

Plasma Density at Lower Probe Location

Figure 5.6 show plasma densities in the lower of the two probe locations (8.7 cm above the stainless steel target plate).

Figure 5.6a shows results for 200 W RF-power, and 5.6b shows results for 300 W RF-power. All of the analysis methods show increase in plasma density increasing the gas pressure. All of the analysis methods report a stronger increase from 1.5 mTorr to 10 mTorr than from 10 to 25 mTorr. Druyvesteyn analysis follow ABR analysis closely in all cases. Also, notice the lower densities in comparison with upper probe location, plotted in figure 5.5. Additionally, while OML theory predicts the same plasma density for both 200 W and 300 W plasmas, the other theories correctly predict a slightly higher density value for 300 W plasma in same pressure. A combination of both ABR and OML theories would seem to give accurate results, close to Langmuir values, for plasma densities [19].

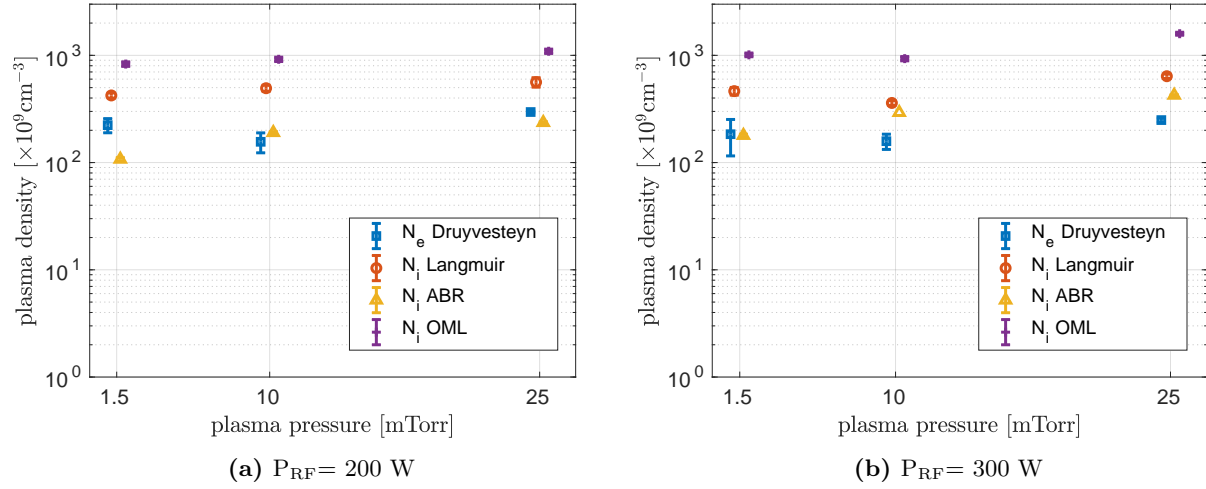


Figure 5.5: Steady state Ar plasma density as a function of Argon gas pressure at two different RF-powers, on an axis location 21.7 cm above stainless steel target. Note that four different analysis methods (Druyvesteyn, Langmuir, ABR, and OML) were used to analyse each Langmuir probe curve as described in previous chapter 4. The spread on the pressure axis is artificial and just there to increase visibility of the data points.

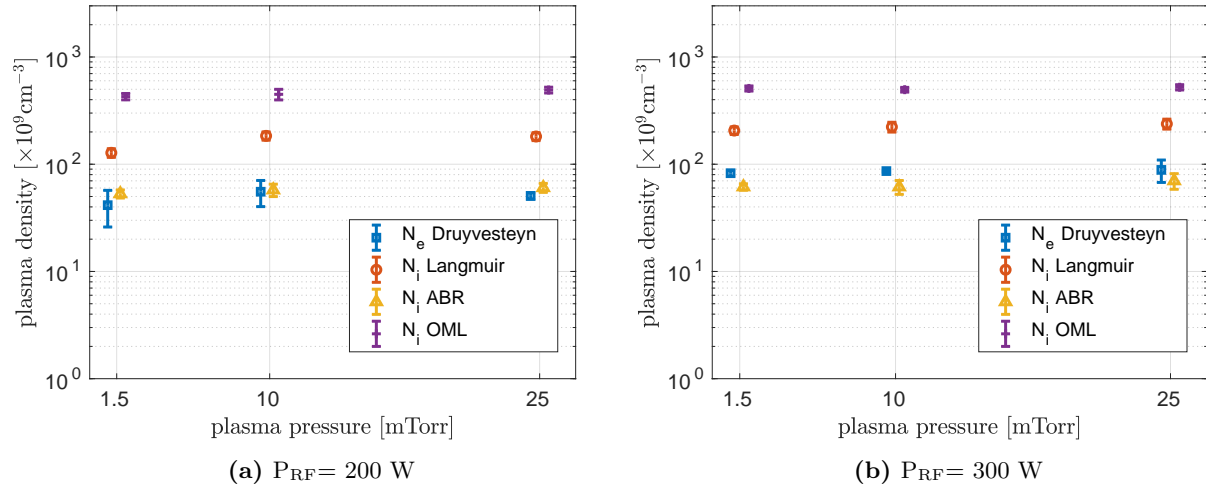


Figure 5.6: Steady state Ar plasma density as a function of Argon gas pressure at two different RF-powers, on an axis location 8.7 cm above stainless steel target. Note that four different analysis methods (Druyvesteyn, Langmuir, ABR, and OML) were used to analyse each Langmuir probe curve as described in previous chapter 4. The spread on the pressure axis is artificial and just there to increase visibility of the data points.

5.1.4 Measurements of Electron Temperature at Constant RF-power

In this subsection I present measurements of the steady state electron temperature in the RF-ICP system at two different locations on the axis of the cylindrical chamber, and vertically separated by distance of 13.0 cm. Electron temperature measurements presented here, were made at two different values of RF-power, $P_{RF}=120$ W and $P_{RF}=300$ W. Measurements were done at three different pressures of Argon, namely 1.5 mTorr, 10 mTorr and 25 mTorr. The evolution of electron temperature T_e as a function of pressure at constant P_{RF} is studied here.

Electron Temperature at Upper Probe Location

Figure 5.7 shows electron temperature in 21.7 cm above the stainless steel target plate. Figure 5.7a shows results for 200 W RF-power, and 5.7b shows results for 300 W RF-power. Both Druyvesteyn and Langmuir analysis show a decrease in electron temperature with increasing the gas pressure. Langmuir and Druyvesteyn are both showing close results to each other in a given condition. However, the Druyvesteyn analysis shows a higher electron temperature in every one of these cases.

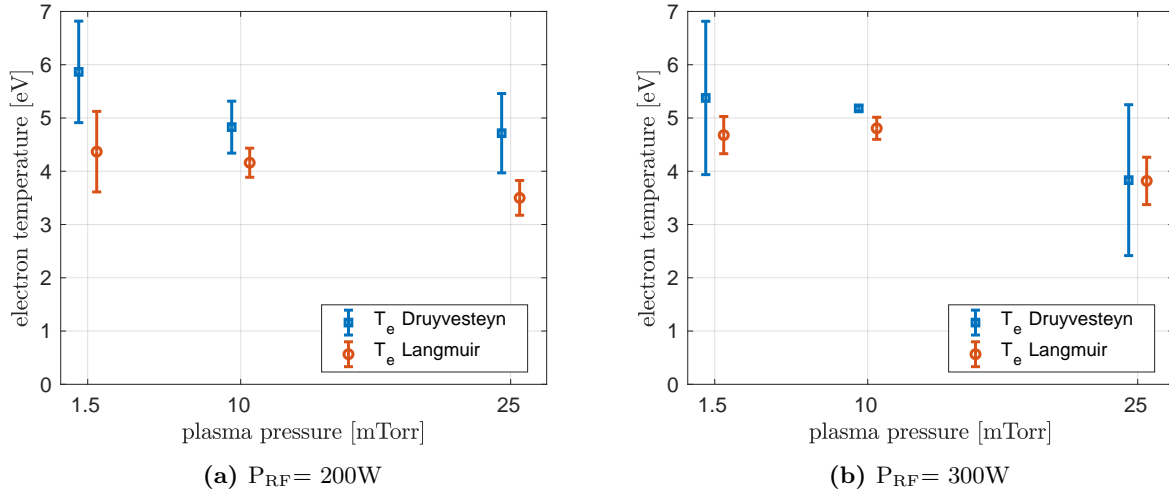


Figure 5.7: Steady state Ar electron temperature as a function of Argon gas pressure at two RF-powers, on an axis location 21.7 cm above stainless steel target. Note that four different analysis methods (Druyvesteyn, Langmuir, ABR, and OML) were used to analyse each Langmuir probe curve as described in previous chapter 4. The spread on the pressure axis is artificial and just there to increase visibility of the data points.

Electron Temperature at Lower Probe Location

Figure 5.8b show electron temperature 8.7 cm above the stainless steel target plate. Figure 5.34a shows results for 200 W RF-power, and 5.8b shows results for 300 W RF-power. As same as the upper-faster electrons, the lower electrons as well tend to cool down with increasing gas pressure.

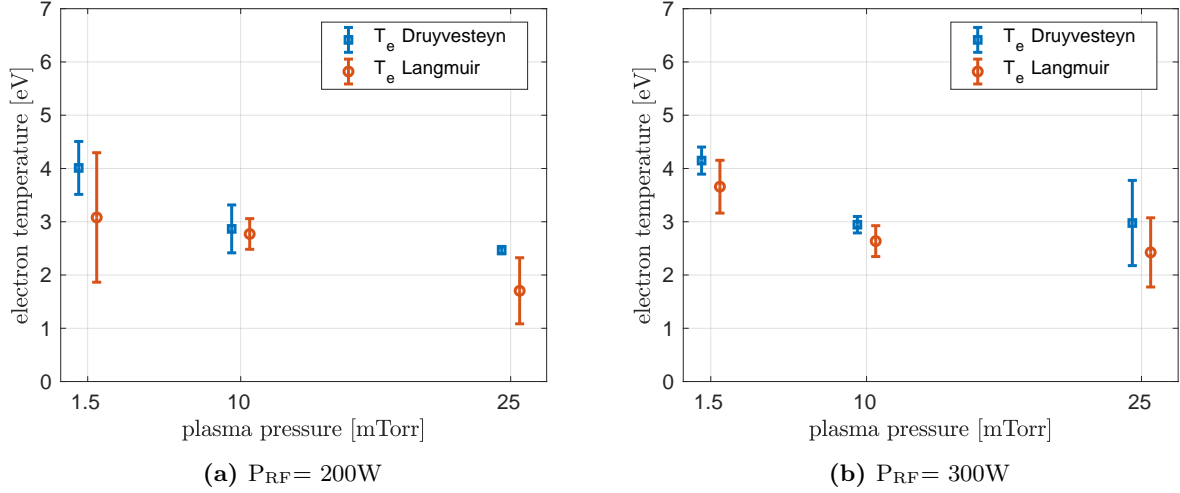


Figure 5.8: Steady state Ar electron temperature as a function of argon gas pressure at two RF-powers, on an axis location 8.7 cm above stainless steel target. Note that two different analysis methods (Druyvesteyn and Langmuir) were used to analyse each Langmuir probe curve as described in previous chapter 4. The spread on the pressure axis is artificial and just there to increase visibility of the data points.

Langmuir and Druyvesteyn analysis strongly agree with each other in lower probe location, both showing a stronger electron cool-down from 1.5 mTorr to 10 mTorr, than from 10 to 25 mTorr, same as plasma density increase dependency on gas pressure in the same location. The higher increase in the number of ions and the higher electron temperature changes in the plasma, while the source is producing the same power suggests that electrons tend to cool-down by having more collisions with the higher number of surrounding particles.

In next subsection, the radial profiles of electron’s temperature and plasma density at a single plasma condition will be analysed.

5.1.5 Radial profiles of Plasma Density and Electron Temperature

A complete characterisation of a steady state plasma would encompass measurements of plasma density and electron temperature at every point in plasma chamber. While this is usually impractical because of the volume of data required, selected profiles can be useful. In a cylindrical plasma chamber such as the RF-ICP chamber used in this work, the radial variation of the plasma from the central axis toward the chamber wall can be measured. Here, I present the measurements of radial variation of plasma density and electron temperature as a function of radial position, at a z_p 21.7 cm above the target plate. The data chosen to be presented here are acquired at 25 mTorr argon pressure and 300 W RF-power.

Radial Profile of Plasma Density at Upper Probe Location

Figure 5.9 shows the radial profile of plasma density in upper probe location of argon plasma with 25 mTorr pressure and 300 W RF-power. As can be seen the plasma density can be considered uniform radially. Several

groups have measured a radial profile close to a Bessel function in their ICP vessels. The measurements are done in a vessel with 15.0 cm radius, thus at least 4.0 cm away from the chamber’s wall. Druyvesteyn method analyses electron densities, while Langmuir analyses the ion densities. While Druyvesteyn method expects a small decrease in electron density while moving from chamber’s axis toward the wall. Comparing Druyvesteyn and Langmuir analysis results, it is safe to say that electrons are deviating from Maxwellian, and the small rise shown by Langmuir analysis is artificial. OML analysis predicts the raise of ion density close to the wall. Given that numerous earlier works have reported a bell-shaped radial profile of density in an ICP [38] with just a slightly lower density in the middle, OML fails to predict a correct radial profile for our plasma.

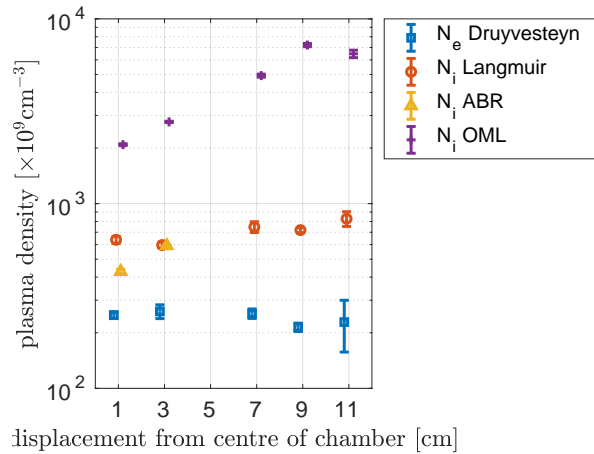


Figure 5.9: Ar plasma density radial profile, $z_p = 21.7$ cm above stainless steel target plate, $P_{RF} = 300$ W, Argon pressure $P_{RF} = 25$ mTorr. The spread on the x-axis is artificial and just there to increase visibility of the data points.

Radial Profile of Electron Temperature at Upper Probe Location

The radial profile for electron temperature in ICP plasma have been modelled previously by different groups [39]. Several groups have measured the radial profile of electron temperature in different kinds of plasma environments including RF-driven ICP plasmas [24, 40, 25, 41]. Reference [23] provides a measurement and characterisation of electrons as well as their bi-temperature distribution, discussed in chapter 4, in a very similar RF-ICP plasma in University of Saskatchewan.

The radial profile for electron temperature shown in figure 5.10 shows a relatively steady value within the error bars for electron temperature, moving away from the axis of the ICP-vessel. There is a small decrease moving toward the chamber’s wall, which might be due to moving away from the RF-power source. One should have more spacial resolution as well as a broader spacial coverage of radius in the measurements, in order to identify the distribution function for electron temperature radial profile in RF-ICP.

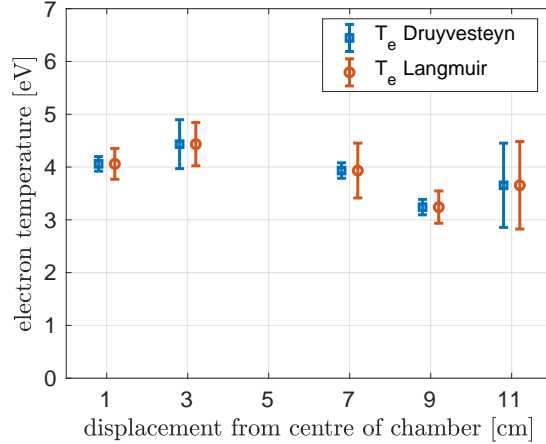


Figure 5.10: Ar electron temperature radial profile, $z_p = 21.7$ cm above stainless steel target plate, $P_{RF} = 300$ W, Ar gas pressure $P_{Ar} = 25$ mTorr. The spread on the x-axis is artificial and just there to increase visibility of the data points.

5.2 Pulsed Plasma Studies Using Stainless Steel Target Plate in Argon Plasma

The steady state plasma data acquired in previous section will provide the basis for the analysis of the plasma in a pulsed target regime. The steady state plasma density n_0 and electron temperature T_e can be used in various models to predict the response to a target biased for a short duration by a high voltage pulse. This thesis work concentrates on negative polarity pulses applied to 5 cm diameter disk targets made of silicon and stainless steel. The pulse voltage was in the range of 1 kV to 10 kV, as these are widely used in plasma ion implantation (PII) applications. Users of PII need a quantitative way to predict the effect of a particular pulse sequence and a variety of models have been used for this purpose. These range from the relatively simple semi-analytic approach of Lieberman et al. [5, 4] which is fast but makes many assumptions and does not capture many aspects of the physics, through to accurate particle in cell (PIC) simulations which take days to run and are therefore impractical [42, 43, 44]. One purpose of this work is to gain more insight into pulsed plasma processes in the PII regime in order to improve the modelling [45].

In order to gain a better understanding of the plasma parameters evolution during a pulse cycle, we divide each cycle into six different time regions. Figure 5.11 shows the high voltage pulse and the current through the target for -1 kV and -4 kV pulses, divided in these six regions.

- **Region 1:** Right before the pulse starts, when the plasma had enough time to rearrange its ions and electrons to a quasi-steady state.
- **Region 2:** During rise time of the pulse.
- **Region 3:** During the high voltage plateau.

- **Region 4:** During the fall of the voltage pulse.
- **Region 5:** When the pulse has ended and the Rogowski coil measures a negative current after the pulse.
- **Region 6:** Corresponds to the after pulse, after the negative current diminishes.

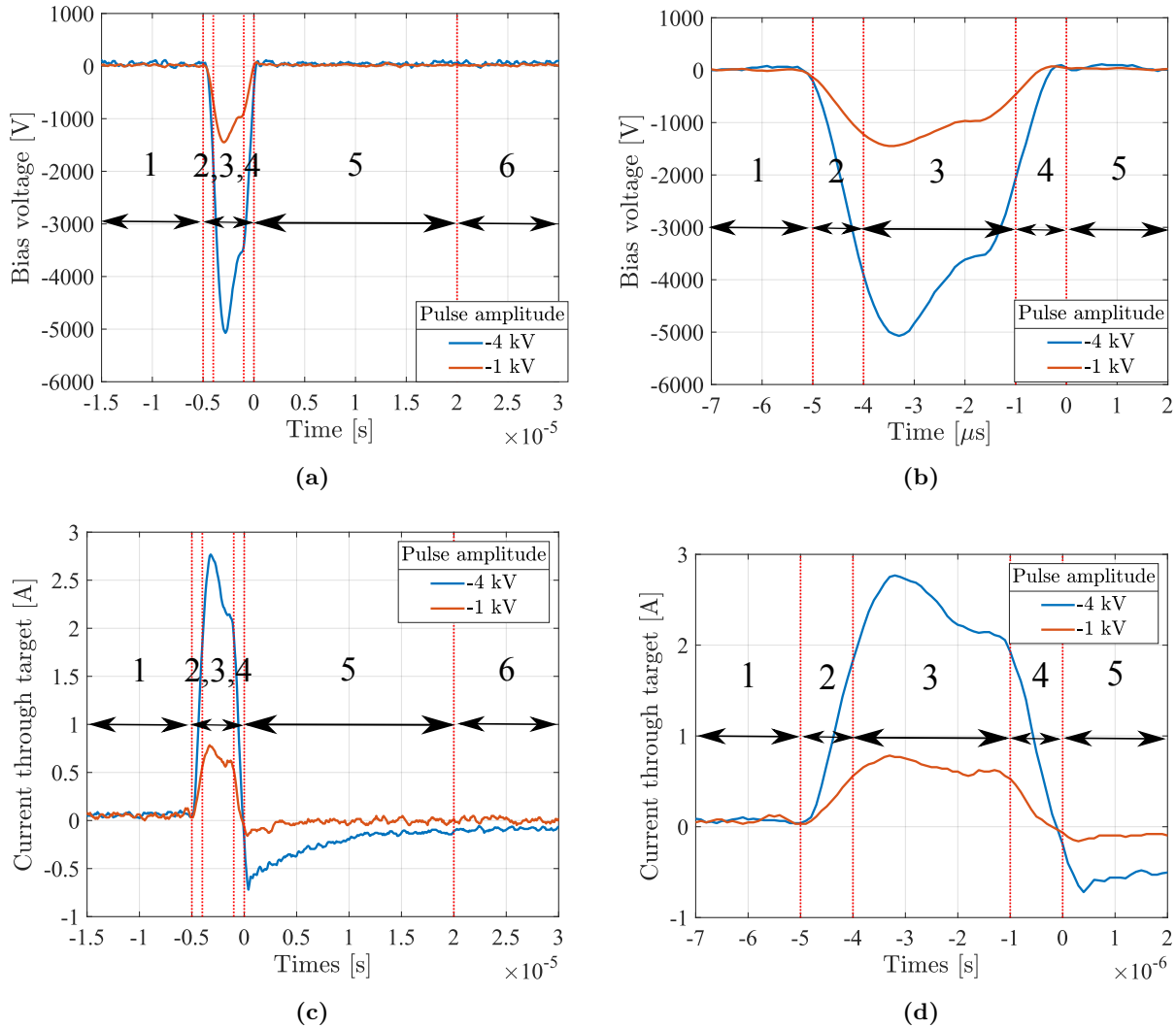


Figure 5.11: (a) -1 kV and -4 kV high voltage pulse biased to a stainless steel target immersed in Ar plasma with pressure $P_{Ar} = 25$ mTorr and RF-power $P_{RF} = 120$ W. (b) A zoom in time of high voltage pulse, showing regions 2, 3, 4. (c) Shows the current going through the stand measured by Rogowski coil during each pulse. (d) A zoom in time of current through the target, showing the rise of the current in region 2, plateau of the current in region 3, and the fall in region 4 more clearly.

5.2.1 Time-Resolved Measurements of Floating Potential in Pulsed Argon Plasma - Stainless Steel Target

Floating potential measurements during a single pulse period are done for several reasons. First, a direct measurement of the floating potential provides a good check for the analysis of the steady state data shown in previous section of this chapter. Also, knowing the floating potential during a pulse will help acquiring the current-voltage characteristic of the plasma during the pulse. Indeed having already measured the electron temperature, it will give us a good indication of the probe bias interval necessary to measure good characteristics. Remembering equation A.1, gaining an insight of the evolution of electron temperature in plasma requires knowing the difference between plasma potential and floating potential. At this point, we already have an estimation of the electron temperature, thus a rough idea about the difference between plasma potential and floating potential in our plasma. After acquiring the floating potential during the pulse, one can know the boundaries of the probe bias sweeps for each given plasma condition, in order to gain a full current-voltage characteristic curve which doesn't leave out plasma voltage "knee". In addition to these, measuring the floating potential during the high voltage pulse prior to acquiring its time-resolved current-voltage characteristic gives a valuable insight of plasma evolution during the pulse.

Measurements of Floating Potential at Constant Plasma Pressures

Figure 5.12 shows floating potential during a -4 kV pulse bias with duration of 5 μs in the lower of the two probe location (8.7 cm above the stainless steel target plate). This figure shows results for 1.5 mTorr argon gas pressure for three different RF-powers P_{RF} . Figures 5.12b and 5.12d show the normalised floating potentials to the pre pulse value of floating potential V_{of} . The pre-pulse value V_{of} is the mean value of floating potential between $t = -15 \mu\text{s}$ and $t = -10 \mu\text{s}$ before the end of the pulse.

Given that the high voltage pulses are applied at 250 Hz repetition frequency and they have $<10 \mu\text{s}$ duration, it is interesting to check if the plasma has the time for relative recovery after the pulse. The floating voltage acquired by the probe right before applying the pulse at each location can be checked against the steady state analysis. See appendix A for plasma and floating potentials in steady state. These voltages are slightly higher than the steady state measurements, which shows that even before the pulse the plasma might be still affected and might not have recovered to steady state yet.

Another interesting property of these graphs is the dependency of floating voltage on RF-power. The graphs show that increasing RF-power in same pressure, increases the floating potential. Remember the definition of floating potential, as well as the dependency of electron temperature to the difference of floating potential and plasma potential ($V_p - V_f$). Increasing RF-power increases the plasma potential (see section A.1.1 in appendix A), however with electron temperature's relative Independence on RF-power (see section 5.1.2), floating potential has to increase.

- **Region 1:** Right before the pulse, the floating potential is quasi-steady for the different RF-powers.

Higher RF-power exhibits a higher floating potential.

- **Region 2:** With the rise of the negative high voltage pulse, the floating potentials at all RF-powers are decreasing. Even though the relative changes might be different for different powers, different plasmas experience close drop in floating potential values in this region.
- **Region 3:** Floating potential shows a dip about 10-15% lower than the pre-pulse value in this region. The minimum of the dip happens in the middle of the region and then the floating potential starts to rise.
- **Region 4:** The floating potential experiences a steep rise to a value more than the pre-pulse value. This rise is steeper in lower RF-powers at constant pressure.
- **Region 5:** The rise from region 4 is continuing into this region to a high peak for every RF-power in about $t = 2 \mu s$. This peak is higher for lower RF-power values. The floating potential starts to relax to the steady state value. The relaxation time seems to be lower for plasmas with lower RF-powers.
- **Region 6:** After the partial relaxation of the first post-pulse-peak (first PPP) in floating potential, looking at long-range graphs, we see that the floating potential starts to increase slowly again to experience a peak between 0.5 to 1 ms. This floating potential enhancement, is occurring about $t = 0.5$ ms for 120 W plasma and at $t \approx 1$ ms in the 300 W plasma. The second post-pulse-peak (second PPP) is much lower than the first PPP in 120 W plasma, but higher than the first PPP for 300 W plasma. Further analysis of the peak values are done in next section.

5.2.2 Measurements of Floating Potential at Constant RF-powers

In this subsection I present measurements of the evolution of floating potential in the RF-ICP system during a -4 kV pulse with duration of $5 \mu s$, at two different locations on the axis of the cylindrical chamber, and vertically separated by distance of 13.0 cm. Floating potential measurements presented here, were made at two different values of RF-power, $P_{RF} = 120$ W and $P_{RF} = 300$ W. Measurements were done at three different pressures of Argon, namely 1.5 mTorr, 10 mTorr and 25 mTorr. The evolution of floating potential V_f during a pulse for three different pressures for RF-power $P_{RF} = 300$ W and 120 W are presented here.

Pulsed Data For Floating Potential at Upper Probe Location

Figure 5.13 shows floating potential during a pulse cycle for three different argon pressures at $P_{RF} = 300$ W.

- **Region 1:** The floating potential close to the beginning of the pulse is steady. The value of floating potential for $P_{RF} = 300$ W right before the pulse starts, gets higher with increasing the gas pressure. This higher value of floating potential for higher pressure is sustained during the full pulse cycle.

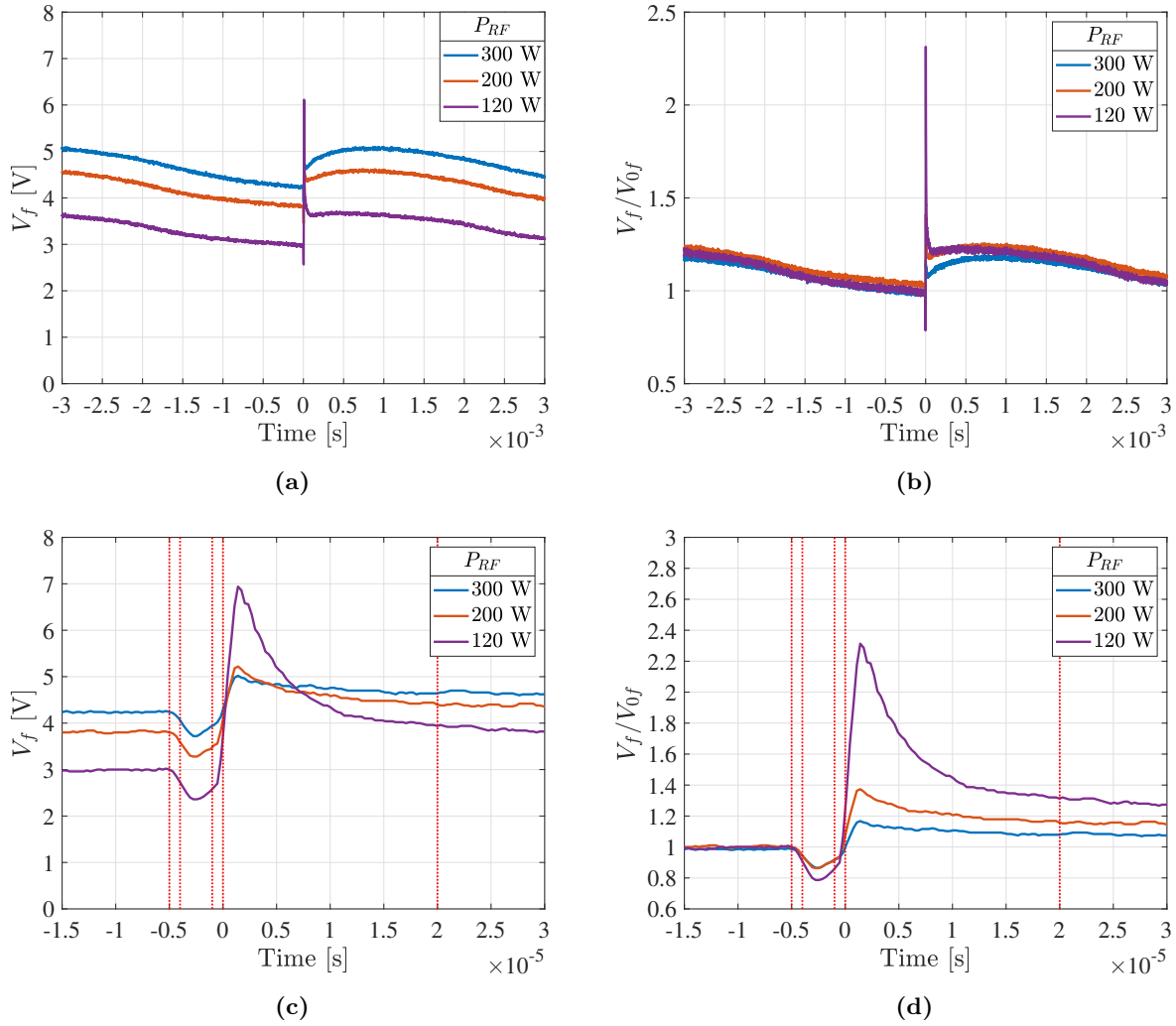


Figure 5.12: (a) Ar plasma floating potential V_f , during a single -4 kV, $5 \mu\text{s}$ duration pulse (pulse repetition frequency, $\text{prf} = 250$ Hz). The probe position was 8.7 cm above the pulsed stainless steel target. Ar plasma with fixed RF-power $P_{\text{Ar}} = 1.5$ mTorr. Note that compared with figure 5.11, these data are plotted on a much longer ($\times 1000$) time scale. This was done in order to make plain the relatively long time required for the plasma to return to the initial state after the pulse. (b) The long time scale floating potential, normalised to the steady state floating potential before the pulse, showing the relative changes of each floating potential. (c) Shows a zoom in time of the same floating potential at a short time scale about the pulse within the range shown in figure 5.11, (d) shows the relative changes by normalising the floating potential to its steady state before the pulse.

- **Region 2:** Floating potential starts to drop during the rise of the negative high voltage pulse in three argon pressures.
- **Region 3:** The floating potential experiences a dip in this region for the three pressures. The relative changes of the floating potential shows a slightly deeper dip of the floating potential during the high voltage pulse for the lower gas pressures. Note that the change in values of the dip measurements are in the resolution limit of the oscilloscope.
- **Region 4:** During the fall of the pulse, the floating potential is increasing similarly for every argon pressure value.
- **Region 5:** The floating potential continues to rise, and experiences the first PPP at about $2 \mu\text{s}$. Despite the higher value of floating potential for higher gas pressures, the relative peak is more intense in lower argon gas pressures for RF-power $P_{\text{RF}} = 300 \text{ W}$. After experiencing first PPP, the floating potential relaxes to pre-pulse value, the relaxation time seems to be shorter for lower gas pressure.
- **Region 6:** Floating potential at upper probe location experiences the second PPP 1 ms after the end of the pulse, for $P_{\text{RF}} = 300 \text{ W}$ and all three pressures. This peaks are very close to each other in different pressures. Their normalised changes seem to be identical to each other.

Figure 5.13 shows floating potential during a pulse cycle for three different argon pressures at $P_{\text{RF}} = 120 \text{ W}$.

- **Region 1:** The floating potential close to the beginning of the pulse is steady. Similar to the pre-pulse floating potential values for $P_{\text{RF}} = 300 \text{ W}$, (Figure 5.13), the value of floating potential for $P_{\text{RF}} = 120 \text{ W}$ right before the pulse starts, gets higher with increasing gas pressure.
- **Region 2:** During the rise of the pulse, the floating potential starts to drop to a slightly lower value.
- **Region 3:** The floating potential experiences a dip in this region for the three pressures.
- **Region 4:** During the fall of the pulse, the floating potential for three pressures start to rise. The initial rise of floating potential for different pressures are close to each other in this region.
- **Region 5:** After the pulse, the floating potential experiences a very intense first PPP in argon plasma with RF-power $P_{\text{RF}} = 120 \text{ W}$ at all pressures. The first PPP is increasing with increasing gas pressure. After reaching the peak values, the floating potentials relax back to near steady state values.
- **Region 6:** Floating potential at upper probe location experiences a second PPP between 0.5 to 1 ms after the end of the pulse, for $P_{\text{RF}} = 120 \text{ W}$ at all three pressures. This peaks are very close to each other in different pressures. Their normalised changes seem to be identical to each other. Also, the values of the second PPPs are close to $P_{\text{RF}} = 300 \text{ W}$ plasma.

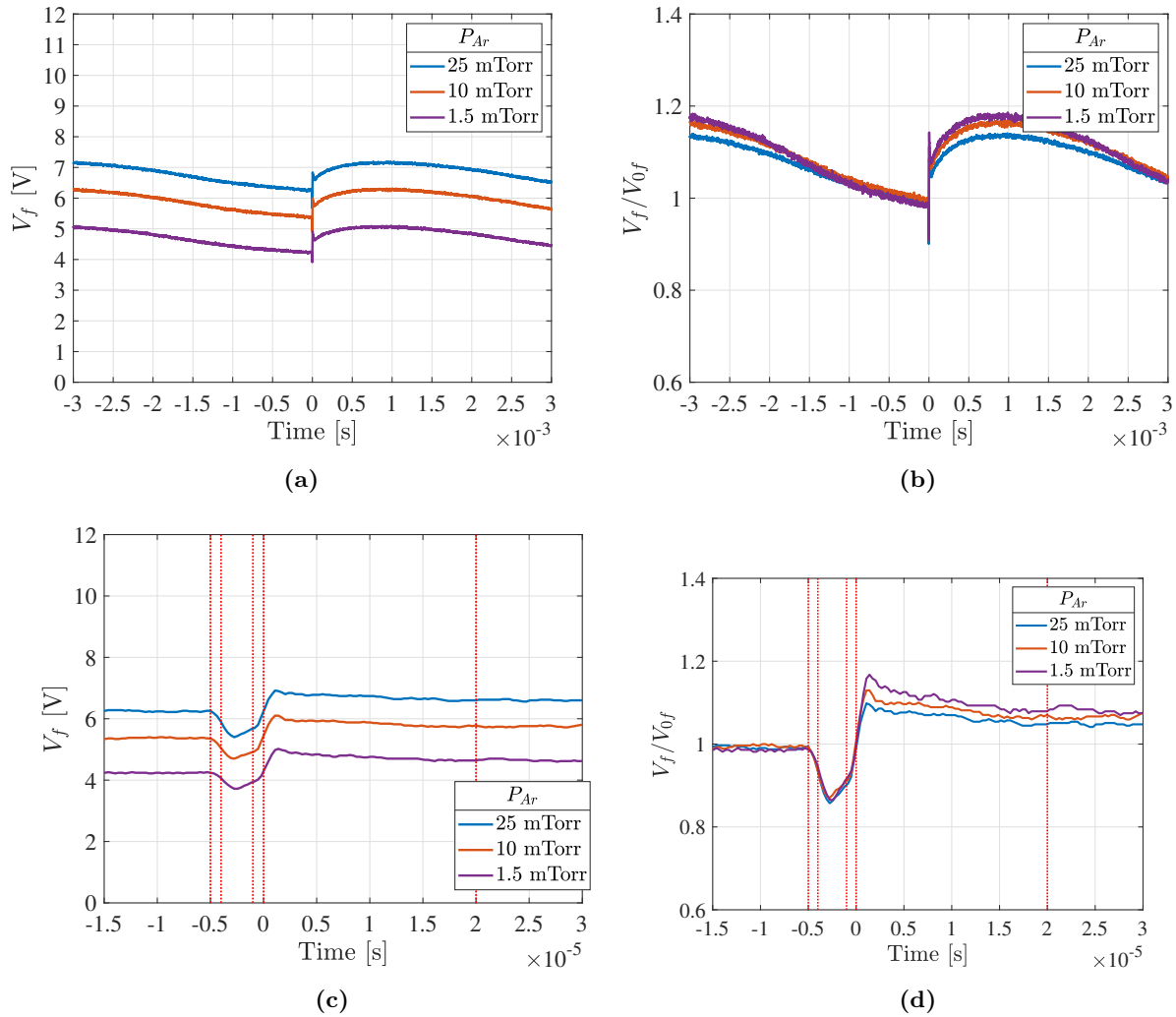


Figure 5.13: (a) Ar plasma floating potential V_f , during a single -4 kV, 5 μ s duration pulse (pulse repetition frequency, prf= 250 Hz). The probe position was $z_p = 21.7$ cm above the pulsed stainless steel target. Ar plasma with fixed RF-power $P_{RF} = 300$ W. Note that compared with figure 5.11, these data are plotted on a much longer ($\times 1000$) time scale. This was done in order to make plain the relatively long time required for the plasma to return to the initial state after the pulse. (b) The long time scale floating potential, normalised to the steady state floating potential before the pulse, showing the relative changes of each floating potential. (c) Shows a zoom in time of the same floating potential at a short time scale about the pulse, (d) shows the relative changes by normalising the floating potential to its steady state before the pulse.

Comparing the short range relative values of figure 5.14 to figure 5.13, in 300 W RF-power argon plasma, higher gas pressure results in damping the changes in floating potential, while in 120 W RF-power, the higher pressure corresponds to much higher first PPP.

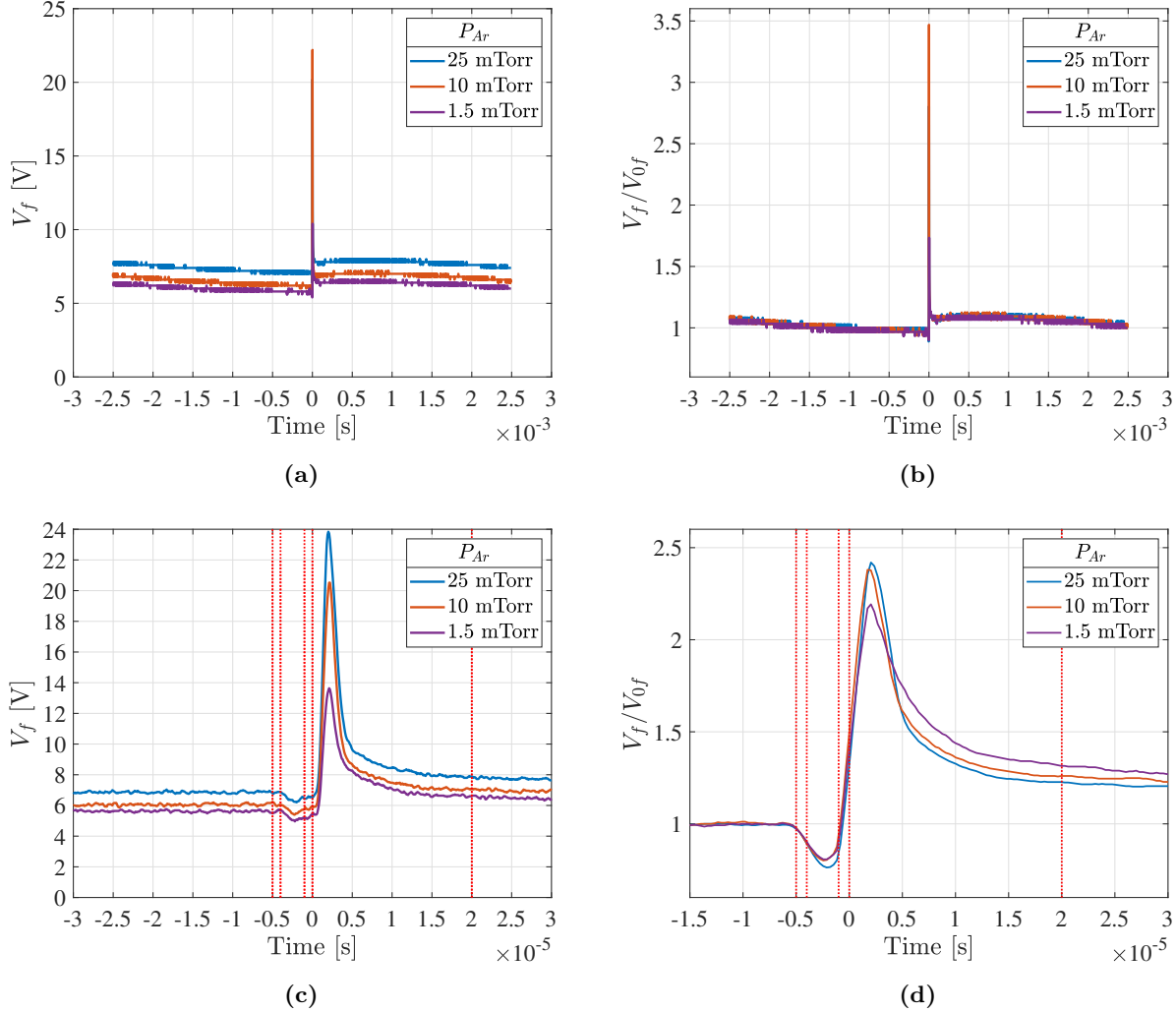


Figure 5.14: Variation of plasma floating potential V_f during a single -4 kV, 5 μ s duration pulse, for three different values of pressure. Probe location $z_p = 21.7$ cm above the pulsed stainless steel target. Ar plasma RF-power $P_{RF} = 120$ W. (b) The long time scale floating potential, normalised to the steady state floating potential before the pulse, showing the relative changes of each floating potential. (c) Shows a zoom in time of the same floating potential at a short time scale about the pulse, (d) shows the relative changes by normalising the floating potential to its steady state before the pulse.

Pulsed Data For Floating Potential at Lower Probe Location

Floating potential values for lower location are presented here to show how floating potential changes by moving away from the RF-antenna toward the pulsed target; where the plasma density becomes lower. The vertical distance between two points are $\delta z_p = 13.0$ cm. The lower point is 8.7 cm above the target, while the

upper is 21.7 cm, axial distance.

Figure 5.15 shows floating potential variations in lower probe location during -4 kV pulse with 5 μ s duration in argon plasma. The steady state floating potential for the same plasma parameters is higher at upper probe location $\delta z_p = 13.0$ cm. Comparing the long time range floating potentials of upper and lower plasma, this can be seen during the whole pulse cycle. Similar to the upper location, figure 5.15b shows that the floating potential experiences a higher relative second peak around 1 ms when the gas pressure is lower. The short time range values show smaller relative changes compared to the upper location floating potentials. However, the higher relative changes in the first PPP for lower pressure values can be seen here as well.

- **Region 1:** The floating potential close to the beginning of the pulse is steady. The value of floating potential for $P_{RF} = 300$ W right before the pulse starts, gets higher with increasing the gas pressure. This higher value of floating potential for higher pressure is sustained during the full pulse cycle. The values are slightly lower in lower probe location compared to the same plasma conditions in upper probe location. These tendencies are in agreement with the steady state measurements.
- **Region 2:** Floating potentials start to drop during the rise of the negative high voltage pulse.
- **Region 3:** The floating potential experiences a dip in this region for the three pressures. The relative changes of the floating potential shows identical dip of the floating potential during the high voltage pulse for all three gas pressures. The dip value seems to be similar to the upper probe location. Further investigation will be done in next section.
- **Region 4:** During the fall time of the pulse, the floating potential is increasing similarly for every argon pressure value.
- **Region 5:** The floating potentials continue to rise, and experience the first PPP at about 2 μ s. Despite the higher value of floating potential for high gas pressures, the relative peak is more intense in lower argon gas pressures for RF-power $P_{RF} = 300$ W. After experiencing first PPP, the floating potential relaxes to near the pre-pulse value, the relaxation time seems to be shorter for lower gas pressure. The first PPP floating potential value is lower in the lower probe location comparing to the upper probe location.
- **Region 6:** Floating potential at lower probe location experiences the second PPP between 0.8 to 1 ms after the end of the pulse, for $P_{RF} = 300$ W and all three pressures. This peaks are very close to each other in different pressures. However, their normalised values show a slightly higher peak for the plasmas with lower gas pressure.

Figure 5.16 shows floating potential variations of lower probe location. These measurements are close to the floating potential measurements in steady state and within their error limits, presented in appendix A. Comparing RF-power $P_{RF} = 120$ W results for upper and lower probe locations, the floating potential peak

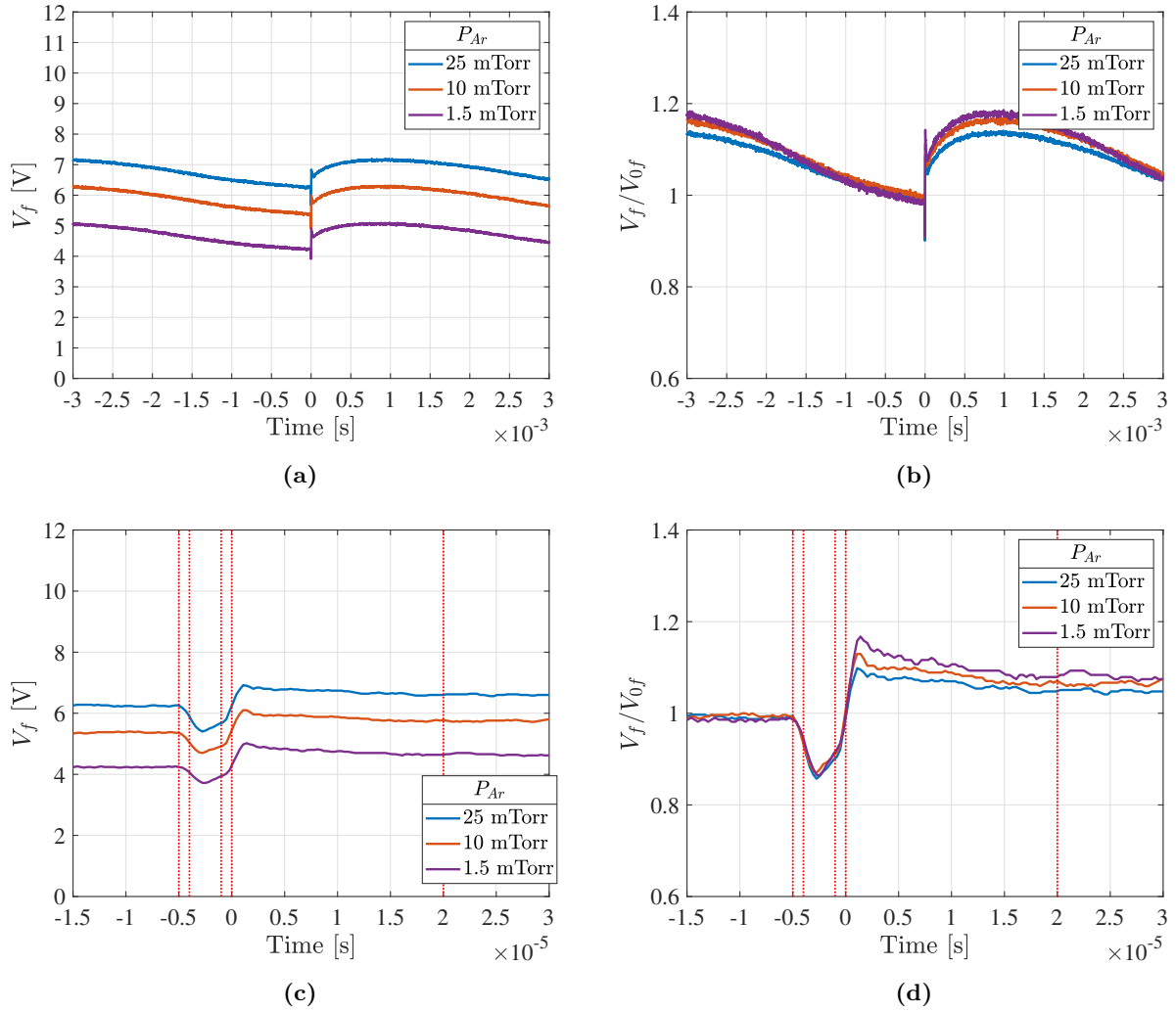


Figure 5.15: (a) Ar plasma floating potential V_f , during a single -4 kV, 5 μ s duration pulse (pulse repetition frequency, prf= 250 Hz). The probe position was 8.7 cm above the pulsed stainless steel target. Ar plasma with fixed RF-power $P_{RF}= 300$ W. Note that compared with figure 5.11, these data are plotted on a much longer ($\times 1000$) time scale. This was done in order to make plain the relatively long time required for the plasma to return to the initial state after the pulse. (b) The long time scale floating potential, normalised to the steady state floating potential before the pulse. (c) Shows a zoom in time of the same floating potential at a short time scale about the pulse, (d) shows the relative changes by normalising the floating potential to its steady state before the pulse.

in the probe location is much higher in the upper plasma. At RF-power $P_{RF} = 120$ W it can be seen that the change in floating potential right after the pulse is less in lower plasma.

- **Region 1:** The floating potential close to the beginning of the pulse is steady. Same as the pre-pulse floating potential values for $P_{RF} = 300$ W, (Figure 5.13), the value of floating potential for $P_{RF} = 120$ W right before the pulse starts, gets higher with increasing the gas pressure.
- **Region 2:** During the rise of the pulse, Floating potentials start to drop to a slightly lower value.
- **Region 3:** The floating potential experiences a dip in this region for the three pressures. The dips can be assumed to be the same for the three pressures.
- **Region 4:** During the fall of the pulse, the three pressures start to rise. The initial rise for different pressures are close to each other in this region.
- **Region 5:** After the pulse, the floating potential experiences a very intense first PPP in argon plasma with RF-power $P_{RF} = 120$ W in different pressures. The first PPP is increasing with increasing the gas pressure. After reaching the peak values, the floating potentials relax back to near the pre-pulse values.
- **Region 6:** Floating potential at upper probe location experiences the second PPP between 0.5 to 1 ms after the end of the pulse, for $P_{RF} = 120$ W and all three pressures. This peaks are very close to each other in different pressures. Their normalised changes show a slightly higher value of second PPP for lower pressure.

Floating Potential Study of Variable Pulse Magnitude: -1 kV vs. -4 kV

All data presented up to this point was for a fixed -4 kV pulse magnitude. PII processes use a range of pulses from -1 kV to several tens of kV. It is therefore of interest to study the effect of plasma pulsing for different pulse magnitudes. I present here some data taken with a lower pulse magnitude of -1 kV. Figure 5.17 compares the floating potential variations for the two pulse magnitudes. The graphs are acquired at two RF-powers, namely $P_{RF} = 120$ W and $P_{RF} = 300$ W, and one argon plasma pressure, $P_{Ar} = 1.5$ mTorr

- **Region 1:** The floating potentials are steady in pre-pulse region for both RF-powers $P_{RF} = 120$ W and $P_{RF} = 300$ W with -1 kV and -4 kV applied pulses. However the values of floating potential for the same plasma conditions but different applied voltage pulses, are different. Plasmas with a higher voltage pulse value have a higher plasma floating potential in same condition. Moreover, floating potential increases with increasing the RF-power.
- **Region 2:** Floating potential is steady for $P_{RF} = 300$ W in -1 kV applied pulse case. With -1 kV applied, $P_{RF} = 120$ W shows a slight decrease in the end of the pulse, very close to zero. However both plasmas shows a decrease in the case of -4 kV applied pulse.

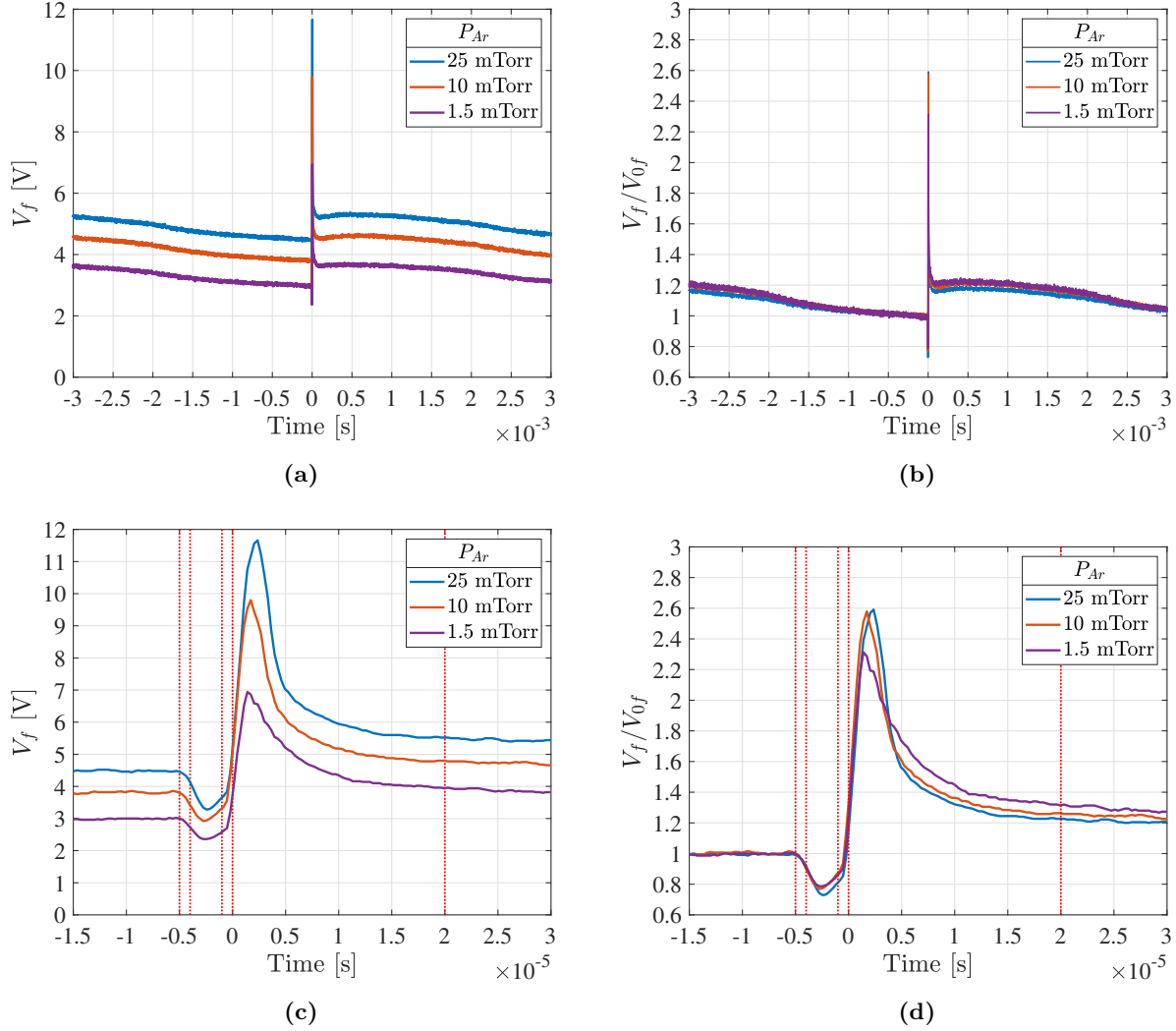


Figure 5.16: (a) Ar plasma floating potential V_f , during a single -4 kV, 5 μ s duration pulse (pulse repetition frequency, prf= 250 Hz). The probe position was 8.7 cm above the pulsed stainless steel target. Ar plasma with fixed RF-power $P_{RF}= 120$ W. Note that compared with figure 5.11, these data are plotted on a much longer ($\times 1000$) time scale. This was done in order to make plain the relatively long time required for the plasma to return to the initial state after the pulse. (b) The long time scale floating potential, normalised to the steady state floating potential before the pulse, showing the relative changes of each floating potential. (c) Shows a zoom in time of the same floating potential at a short time scale about the pulse, (d) shows the relative changes by normalising the floating potential to its steady state before the pulse.

- **Region 3:** During the high voltage plateau, the plasmas with -4 kV applied pulses to the stainless steel target show a dip to a value 10% less than their pre-pulse floating potentials. The plasmas with a -1 kV pulsed target show a similar to their pre-pulse floating potentials.
- **Region 4:** Argon plasma with -1 kV applied pulse target and RF-power $P_{RF}= 300$ W shows almost no change in the floating potential value. The other plasmas show a slight increase in their value of the floating potential in this region.
- **Region 5:** Argon plasma with -1 kV applied pulse target and RF-power $P_{RF}= 300$ W shows almost no change in the floating potential value throughout the first post-pulse region. Argon plasma with -1 kV applied pulse target and RF-power $P_{RF}= 120$ W RF-power shows the smallest first PPP, relative value is comparable with the -4 kV pulsed plasma with $P_{RF}= 300$ W RF-power, but the relaxation time is much shorter. The Plasma pulsed with -4 kV voltage and $P_{RF}= 120$ W RF-power shows a high first PPP, about 3.4 times its pre-pulse value. The relaxation time of the first PPP for this plasma is shorter than the same voltage pulse, but with $P_{RF}= 300$ W driving RF-power.
- **Region 6:** In this region, all the plasmas are experiencing the second PPP. The range shown here only shows the raise close to the peak value, but do not cover the peak. Thus the only comment can be made on this region is on the rise times. The rise time for 300 W plasmas seems to be slightly faster than the plasmas with 120 W RF power, with the same pulse. However, it can be seen that the pulse plays an important role in the magnitude of peak as well, higher pulse corresponds to a higher second PPP.

Figure 5.17e shows two applied pulses. Notice the overshoot of the voltage at the beginning of the pulse, 1 kV and 4 kV values refer to the plateau of the pulse afterwards, as the measurements are done for the low end of the pulse durations commonly used for PII, due to time consuming modellings. The low end of pulse duration on our plasma system is $3 \mu s$.

Figure 5.17f shows the current going through the stainless target target during a time-window of the applied voltage pulse. Note that as we have seen in steady state section plasma density does not enhance by far with a higher RF-power in a constant pressure. This can be confirmed by the target's current measurements. The main factor in getting more fluence to the target is by applying higher voltage. However applying higher voltage will affect the depth of the ion implantation. Thus in a desirable voltage height, higher pulse duration or higher plasma pressure can be both more effective than higher RF-power, in order to deliver more ions into a certain depth in the target. The pulse duration effect on floating potential variations is presented in the next subsection.

Study of Variable Pulse Duration: $8 \mu s$ vs. $5 \mu s$

All data presented up to this point was for a fixed $5 \mu s$ pulse duration. PII processes use a range of pulses from $1 \mu s$ to $100 \mu s$. It is therefore of interest to study the effect of plasma pulsing for different duration

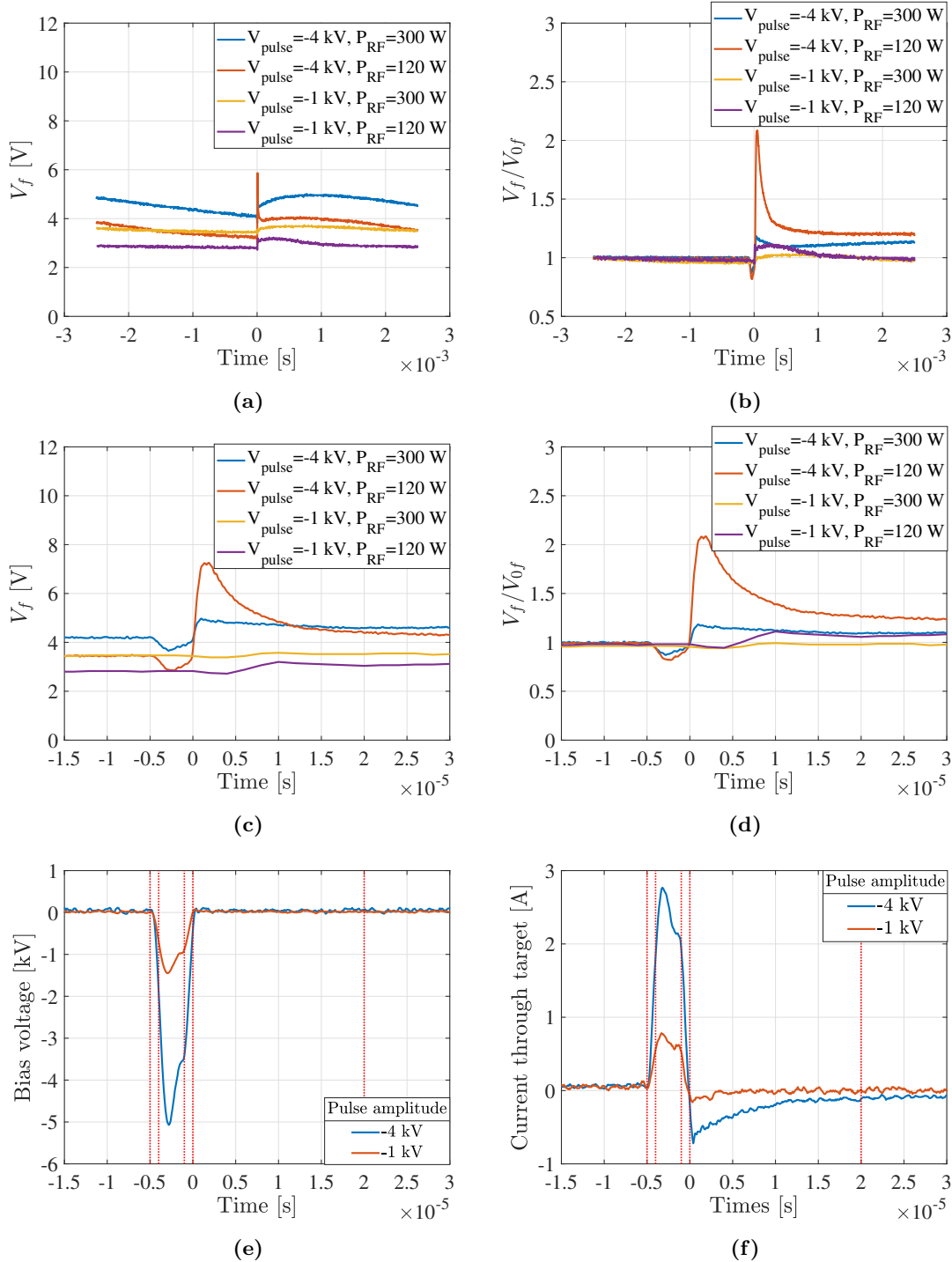


Figure 5.17: (a) A comparison of Ar plasma floating potential for two different pulse magnitudes applied to the stainless steel target. Both pulses have $5 \mu\text{s}$ duration pulse with the repetition rate of 250 Hz. The magnitudes are -1 kV during the plateau of the pulse (about $3 \mu\text{s}$) and -4 kV. The floating potentials are recorded 8.7 cm above the pulsed stainless steel target, Ar plasma pressure $P_{\text{Ar}} = 1.5$ mTorr. (b) The long time scale floating potential, normalised to the steady state floating potential before the pulse, showing the relative changes of each floating potential. (c) Shows a zoom in time of the same floating potential at a short time scale about the pulse, (d) Shows the relative changes by normalising the floating potential to its steady state before the pulse. (e) Shows the corresponding high voltage pulses, applied to the stainless steel target and (f) shows the current through the stainless steel target for both pulses, with Ar plasma pressure $P_{\text{Ar}} = 1.5$ mTorr and RF-power $P_{\text{RF}} = 120$ W.

pulses. I present here some data taken with a longer duration 8 μs pulse. It is useful to note that the pulse duration has the most effect on how long it takes to simulate plasma, therefore the focus of this thesis is on shortest possible pulse with a plateau that can be generated by our current setup for PII.

First two plots of figure 5.18 show a comparison of the floating potential variations during two -4 kV amplitude pulses with 250 Hz repetition frequency with 5 μs and 8 μs pulse durations.

Figure 5.18c shows the applied 5 μs and 8 μs pulses to the stainless steel target. Figure 5.18d compares the current through the stainless steel target, with 5 μs and 8 μs pulses. The current of the electrons after the pulse are the same for both pulses, indicating the Independence of the electron current through the target from the duration of the pulse.

- **Region 1:** Right before the pulse starts, the floating potentials are the same for the two plasmas.
- **Region 2:** During the rise of each pulse, both the floating potentials start to get lower in value.
- **Region 3:** during the high voltage plateau, both floating potentials are in their dip value. the dip value for both are the same.
- **Region 4:** At the end of this region, the floating potential starts to increase.
- **Region 5:** The magnitudes of the first post potential peaks (PPP) after the pulse are on par with each other. Additionally, they follow each other after the peak, suggesting the same relaxation time for both pulse durations.
- **Region 6:** The long range value are not recorded for the longer pulse duration due to their similarity. The existing data shows the same floating potential values for both pulse durations in this region.

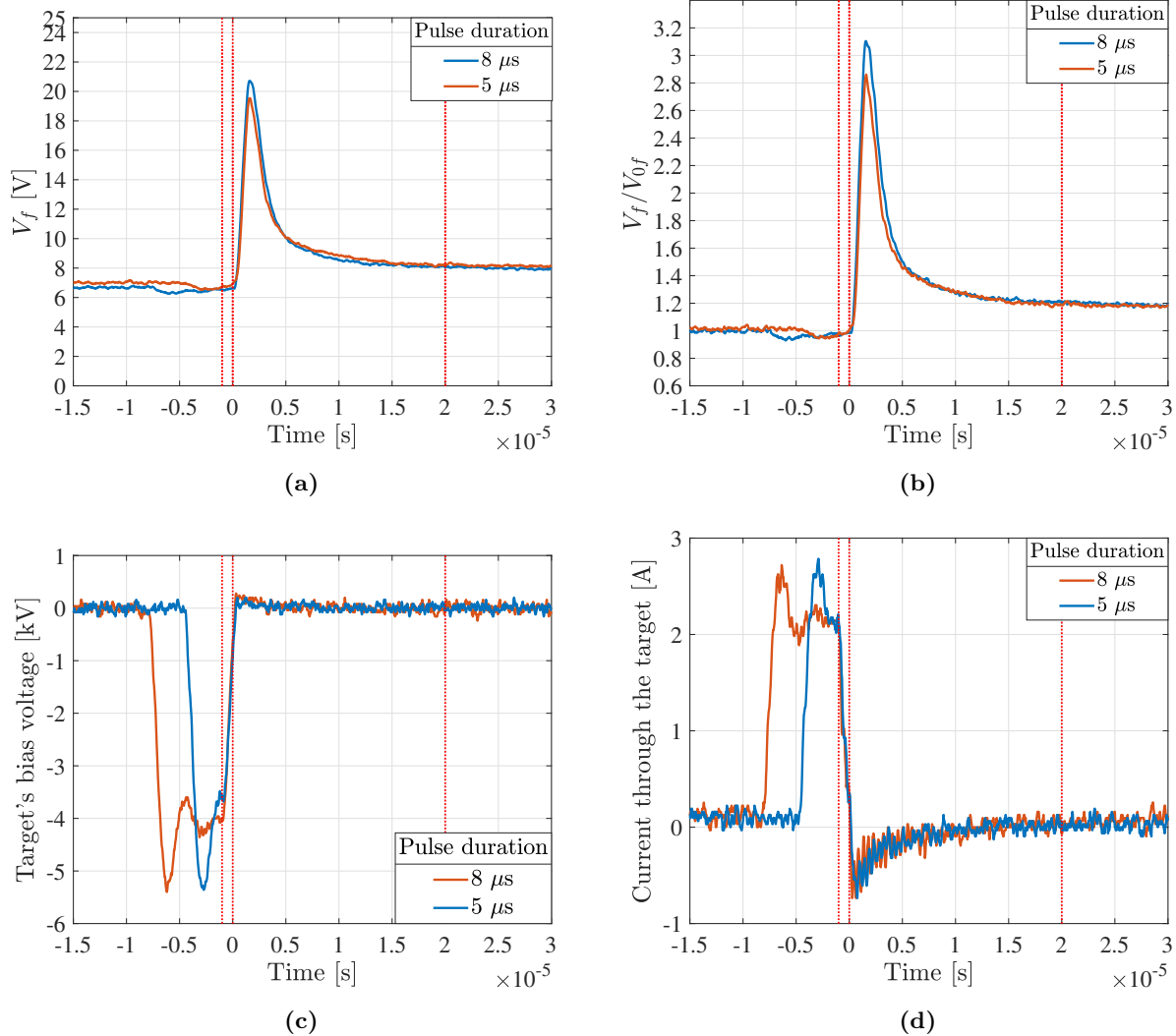


Figure 5.18: (a) A comparison of Ar plasma floating potential for two different pulse duration applied to the stainless steel target. Both pulses have -4 kV magnitude during the plateau of the pulse, with the repetition rate of 250 Hz. The duration of the pulses are 5 μs and 8 μs . The floating potentials are recorded 21.7 cm above the pulsed stainless steel target, 25 mTorr plasma pressure, $P_{\text{RF}} = 120$ W. (b) Comparison of their relative changes with respect to the mean value of steady state floating potential between 20 to 10 μs before the end of the pulses. (c) Shows the high voltage pulse and (d) shows the current through the stainless steel target measured by Rogowski coil.

5.3 Pulsed Plasma Studies Using Silicon Target Plate

In this section I present the data for silicon target in the same regime as used previously for the stainless steel target. There are several reasons which makes silicon a natural choice for study. Plasma processing accounts for approximately 70% of the processing steps used in fabricating chips for modern computing and mobile devices. despite of the advent of the semiconductors, silicon remains the backbone of the semiconductor device industry. One of the most common use for PII processes is fabricating semiconductor films like silicon nitride, gallium arsenide, etc. Thus engineering and scientists working in industry are keenly interested in results for silicon targets. Saying this, it is desirable to know how plasma react when the conductive plate has been exchanged by a semiconductor, e.g. silicon.

5.3.1 Time-Resolved Measurements of Floating Potential in Pulsed Argon Plasma - Silicon Target

Figure 5.19 shows a comparison of the floating potential of the -4 kV pulsed silicon target vs. the -4 kV pulsed stainless steel target. Both of them are pulsed in same discharge conditions, namely $P_{RF} = 300$ W and $P_{Ar} = 1.5$ mTorr. These data are measured in the upper probe location, i.e. $z_p = 21.7$ cm above the targets.

- **Region 1:** In the pre-pulse region, both plasmas have a steady value of floating potential. The values are very close to each other. The plotted short-range shows a slightly higher value for stainless steel, while the long range shows a slightly higher value of floating potential for silicon target case. This is due to error bars in discharge conditions for the two plasma, e.g. slightly different values for gas pressure or reflected RF-powers.
- **Region 2:** Both plasmas with silicon and stainless steel as targets, experience same decrease in floating potential, while the high voltage pulse starts.
- **Region 3:** The potential drop from the pre-pulse value, during the applied high voltage pulse are the same. Floating potential corresponding to silicon target has a slightly sharper dip and a slightly steeper rise.
- **Region 4:** Plasmas with different targets are experiencing an increase in their floating potential during the fall of the high voltage pulse. This increase is higher for the plasma with silicon target.
- **Region 5:** The floating potential value of the first PPP for silicon is about 1.3 times higher than its pre-pulse value, while the plasma with stainless steel target experiences only about 1.12 times higher floating potential. Despite the higher floating potential peak after the pulse, the relaxation to steady state floating potential value seems to be similar for both targets.

- **Region 6:** In this region, the second PPP is reached at about 1 ms after the end of the pulse. The values of floating potential seem to be very close to each other for both targets. This will be investigated further in next section.

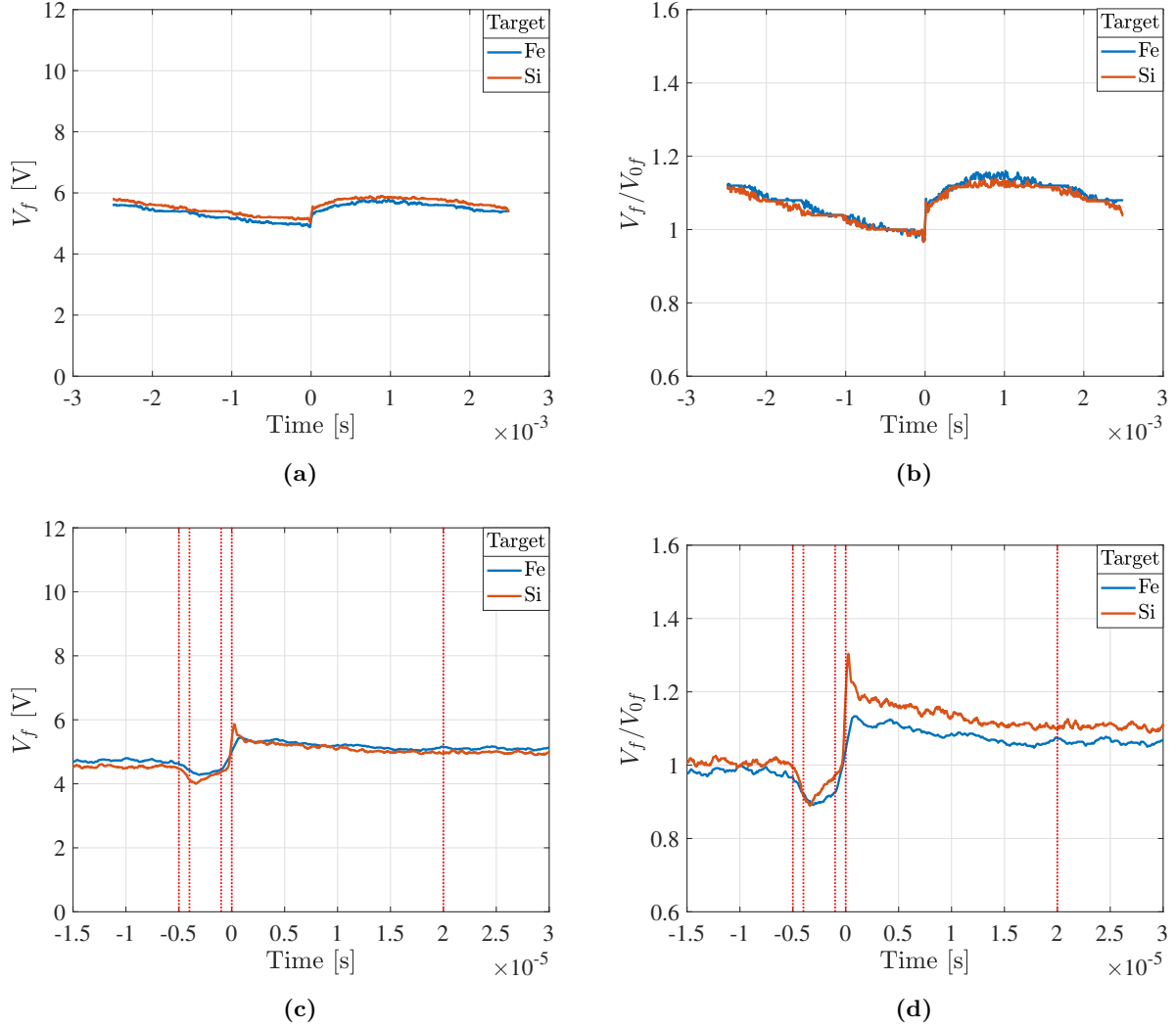


Figure 5.19: (a) Floating potential for silicon and stainless steel targets during a -4kV with 5 μ s duration pulse. Argon gas pressure P_{Ar} = 1.5 mTorr, P_{RF} = 300 W. Axial probe location z_p = 21.7 cm above the targets. (b) Shows the normalised floating potentials, with respect to their steady state floating potential, a mean value of floating potentials between $t=-15 \mu$ s and $t=-10 \mu$ s. (c) Shows the floating potential, the short time scale around the pulse, $\delta t= 10 \mu$ s before the start of the pulse to $\delta t= 30 \mu$ s after the end of the pulse. (d) Shows the same short time scale floating potentials, normalised with respect to their steady state floating potentials. The spread on the vertical axis is artificial and just there to increase visibility of the data points.

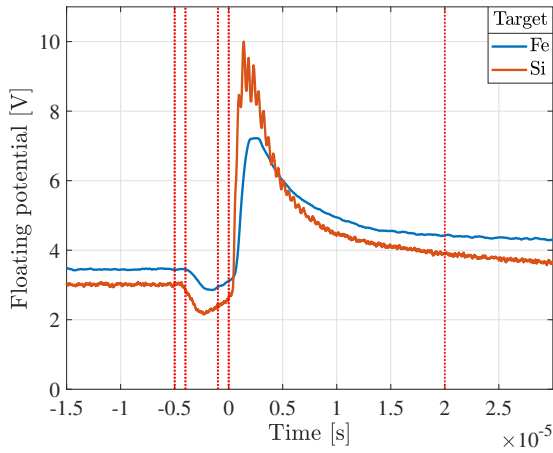
Figure 5.20 shows a comparison of the floating potential of the -4 kV pulsed silicon target vs. the -4 kV pulsed stainless steel target. Both of them are pulsed in same discharge conditions, namely P_{RF} = 120 W and P_{Ar} = 1.5 mTorr. The differences in the details of the floating potentials and the current through the targets

are the result of using different oscilloscopes with different resolutions. The data for silicon target has about 5.7 times more resolution than the data acquired for the stainless steel target.

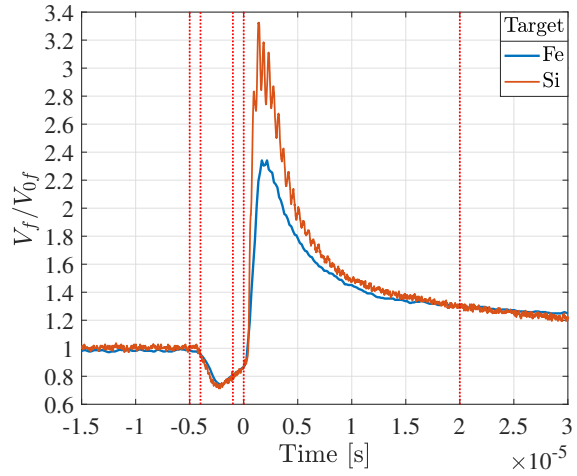
- **Region 1:** In the pre-pulse region, both plasmas have a steady value of floating potential. The plasma with stainless steel target immersed has a slightly higher value which might be due to their different discharge conditions, e.g. slightly different values for gas pressure or reflected RF-powers.
- **Region 2:** Both plasmas with silicon and stainless steel as targets, experience same decrease in floating potential, while the high voltage pulse starts.
- **Region 3:** The potential drop from the pre-pulse value, during the applied high voltage pulse are the same. Floating potential corresponding to silicon target has a slightly sharper dip and a slightly steeper rise to the after the pulse peak value.
- **Region 4:** Plasmas with different targets are experiencing a close increase in their floating potential during the fall of the high voltage pulse.
- **Region 5:** The floating potential value of the first PPP for silicon is about 3.3 times higher than its pre-pulse value, while the plasma with stainless steel target experiences only about 2.4 times higher floating potential. Despite the higher floating potential peak after the pulse, the relaxation to steady state floating potential value for silicon target seems to be faster than the plasma with stainless steel as a target.
- **Region 6:** In the plotted region, both plasmas experience relaxation from the first PPP. The second PPP is not reached in the acquired measurements.

Looking into the current going through each target during this pulse, despite the same pulse start time, the silicon's target experiences the peak of the current first and also experiences a slightly higher plateau than the stainless target. After the pulse, the negative electron current through the silicon target, dies out to zero faster than the current through stainless steel, in spite of their same initial amplitude.

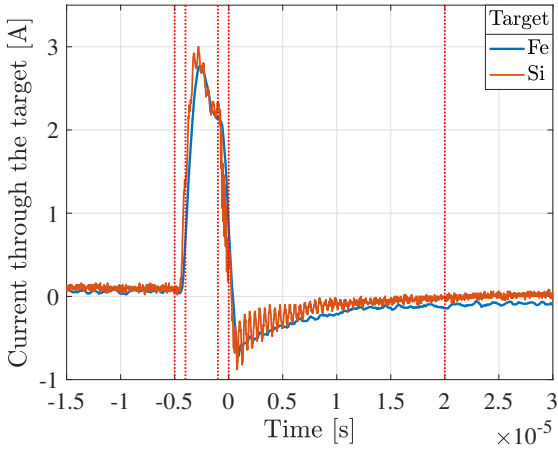
In next section, the floating potentials of both stainless steel and silicon targets are analysed for different gas pressures and RF-power values.



(a) Floating potential



(b) Floating potential ratio



(c) Currents through targets

Figure 5.20: (a) shows floating potential for silicon and stainless steel targets during a -4kV with $5\ \mu\text{s}$ duration pulse. Argon gas pressure $P_{\text{Ar}} = 1.5\ \text{mTorr}$, $P_{\text{RF}} = 120\ \text{W}$. Axial probe location $z_{\text{p}} = 21.7\ \text{cm}$ above the targets. (b) Shows the normalised floating potential, with respect to their steady state floating potential, a mean value of floating potentials between $t = -15\ \mu\text{s}$ and $t = -10\ \mu\text{s}$. Figure (c) is measured currents through each target for both silicon and stainless plates.

5.4 Floating Potential Analysis of Stainless Steel and Silicon Targets

The most important features of the presented floating potential measurements shown in figures 5.12 to 5.20, are the potential drop during the pulse, the evolution of the first and second peak of each curve, as well as their relaxation time to equilibrium. It would be interesting to study the dependence of these features to P_{RF} , plasma pressure, and the axial location of the probe. Moreover, I would like to focus on the recent discussion regarding the effect of a semiconductor plate as the target on the floating potential variation in plasma during PII. The two main features of the floating potential variations that are interesting for the study of plasma ion implantation are the ion relaxation time comparison of the two substrate, as well as the peak values of floating potential, occurring twice after the pulse, the first, more intense peak, $\sim 1 \mu s$ after the pulse ends and the later, smooth peak in the order of $\sim 100 \mu s$ after the end of the pulse.

These analysis is an attempt to characterise the plasma enhancement which affects the plasma from one pulse to the other. The first peak in the pulse is more intense, but does not have a long lasting effect and decays to the steady state potential. However the second enhancement, best seen in long-time ranges shown in figures 5.12 to figure 5.19, has a long lasting effect on plasma density and instabilities, until the next pulse is applied, thus its characterisation is important. The following subsections will focus on finding the minimum value, maximum peak, the second peak, and their corresponding relaxation times. The values for $P_{RF} = 120 \text{ W}$ and 300 W in lower and upper plasma for both silicon and stainless steel targets will be presented. Assuming that the peak follows an exponential decay, $V_f(t) = V_f(max) \exp(-\frac{t}{\tau})$, in which $V_f(max)$ is the peak's floating potential value. τ is extracted by numerically fitting a line to the $\ln[V_f(t)]$ vs. time.

5.4.1 Short Time Scale Analysis

The short range floating potential variations presented in the previous section, show a potential drop during the applied pulse, as well as a potential peak happening in less than $1 \mu s$ after the end of the pulse in both upper and lower plasmas. In this subsection, the analysis results for the potential drop during the pulse, the peak height right after the pulse and relaxation time constant of this instability for both silicon and stainless steel in the upper and lower probe locations, i.e. $z_p = 21.7 \text{ cm}$ and $z_p = 8.7 \text{ cm}$ above the pulsed targets are presented.

Floating Potential Dip During Pulse - Silicon and Stainless Steel Targets

A high voltage pulse with amplitude of -4 kV and duration of $5 \mu s$ and repetition frequency of 250 Hz is applied to both stainless steel and silicon targets. During the pulse, The Langmuir probe, located either at 8.7 cm or 21.7 cm above the pulsed targets, experiences a voltage drop. The maximum values of this voltage drop in different plasma conditions are presented here.

Figure 5.21 shows the floating potential minimum values subtracted by their steady state values, for different argon plasma pressures, namely 1.5 mTorr, 10 mTorr and 25 mTorr generated with 120 W and 300 W RF-powers for both stainless steel and silicon targets in upper probe location, i.e. 21.7 cm above the targets.

Comparing the same pressure results, the amplitude of the potential drop is higher in a lower RF-power value, except for stainless steel target immersed in 1.5 mTorr argon plasma, which reports a same drop in floating potentials for both 120 W and 300 W RF-powers. Comparing the same RF-powers in different pressures for both targets, would reveal a general tendency to higher potential drop with higher gas pressure. The exceptions are $P_{RF}= 300$ W from 10 to 25 mTorr in stainless steel target and $P_{RF}= 120$ W from 1.5 to 10 mTorr for silicon target, which show a slight increase in the potential drop values. This might be due to the noise of the oscilloscope. As further smoothing of the plots, results in removing or damping of the actual physical potential drops, a better analysis is only possible with acquiring data with higher resolution.

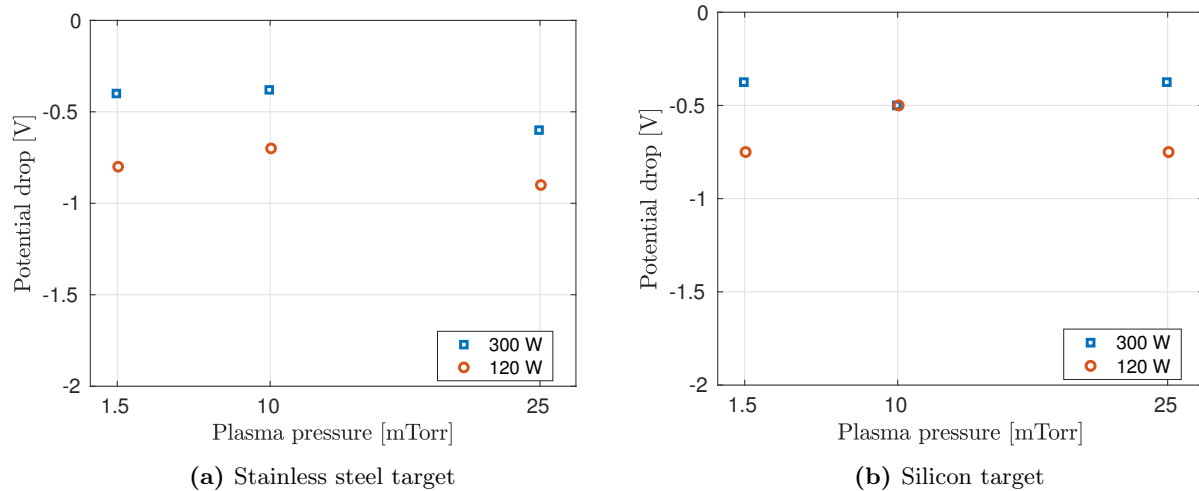


Figure 5.21: The floating potential minima measurements for stainless steel and silicon pulsed targets during the high voltage pulse. Data acquired in the lower probe location $z_p= 21.7$ cm above each target. Each target was biased negatively to a 4 kV pulse with duration of 5 μ s and repetition frequency of 250 Hz.

Figure 5.22 shows the floating potential minimum values subtracted by their steady state values, for different argon plasma pressures, namely 1.5 mTorr, 10 mTorr and 25 mTorr generated with 120 W and 300 W RF-powers for both stainless steel and silicon targets in lower probe location, i.e. 8.7 cm above the targets.

These results are close to the resolution limit of the oscilloscope, thus, within the error limits, they can be considered the same. Comparing the same pressure results, the amplitude of the potential drop is higher in a lower RF-power value, except for silicon target immersed in 10 mTorr argon plasma, which reports a same drop in floating potentials for both 120 W and 300 W RF-powers. Also, silicon target immersed in 1.5 mTorr argon plasma, reports a lower drop in floating potentials for 300 W RF-power. Comparing the same RF-powers in different pressures for both targets, does not show a trend for these three pressures.

Comparing the results for stainless steel to silicon target at both $P_{RF}= 300$ W and $P_{RF}= 120$ W, the plasma with silicon target, experiences a slightly higher potential drop, except for 25 mTorr argon gas pressure with $P_{RF}= 120$ W driving power, which a higher drop for stainless steel is reported. Again, the differences are minimal and within the background noise picked up by the oscilloscope.

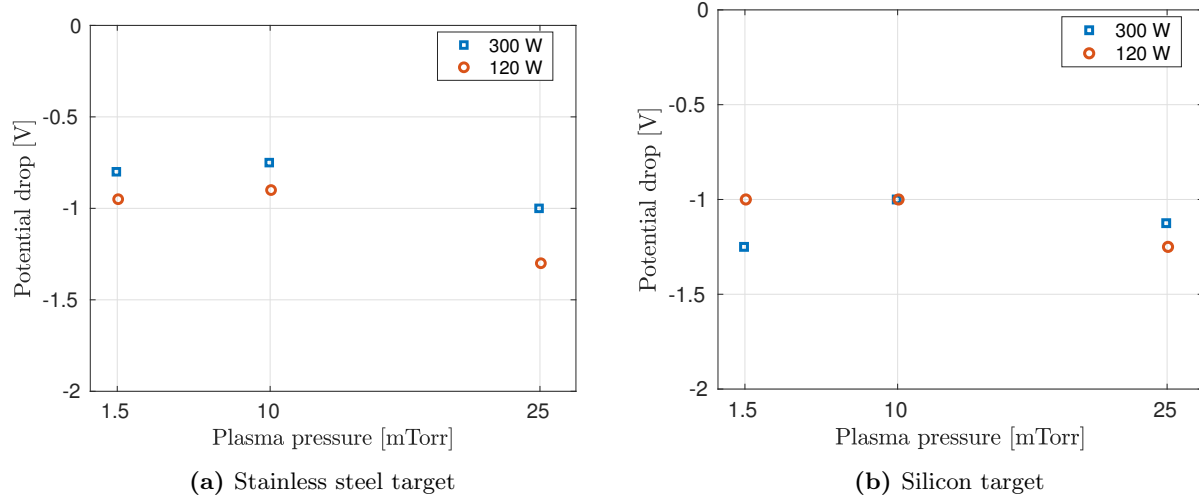


Figure 5.22: The floating potential minima measurements for stainless steel and silicon pulsed targets during the high voltage pulse. Data acquired in the lower probe location $z_p = 8.7$ cm above each target. Each target was biased negatively to a 4 kV pulse with duration of 5 μ s and repetition frequency of 250 Hz.

First Post-Pulse-Peak Height Analysis of Silicon and Stainless Steel Targets

Floating potential experiences an intense first peak at around ~ 1 μ s after the pulse ends which dies in the same time order. In this section the evolution of peak height as a function of RF-power analysis results for both silicon and stainless steel targets after this peak in floating potential are presented. Figure 5.23 shows the first peak heights at upper probe location $z_p = 21.7$ cm in argon plasma for both pulsed stainless steel and silicon targets. The results are presented in three values of argon gas pressure $P_{Ar} = 1.5$ mTorr, 10 mTorr and 25 mTorr and two RF-powers, namely $P_{RF} = 120$ W and 300 W.

Comparing the same pressure results, the amplitude of the maximum potential is higher in a lower RF-power value in every case. Comparing the same RF-powers in different pressures for both targets, shows a higher potential peak with higher gas pressure in every case, except for the case of $P_{RF} = 300$ W and 1.5 mTorr argon gas pressure, which is higher than $P_{Ar} = 10$ mTorr potential peak value. However their difference lies within the oscilloscope resolution value.

Comparing the results for stainless steel to silicon target at both $P_{RF} = 300$ W and $P_{RF} = 120$ W, the plasma with silicon target, experiences a higher potential maximum, is every case. The floating potential variations of the $P_{Ar} = 1.5$ mTorr with $P_{RF} = 120$ W, and $P_{Ar} = 1.5$ mTorr with $P_{RF} = 300$ W for both targets were shown in figures 5.20 and 5.19 in previous section.

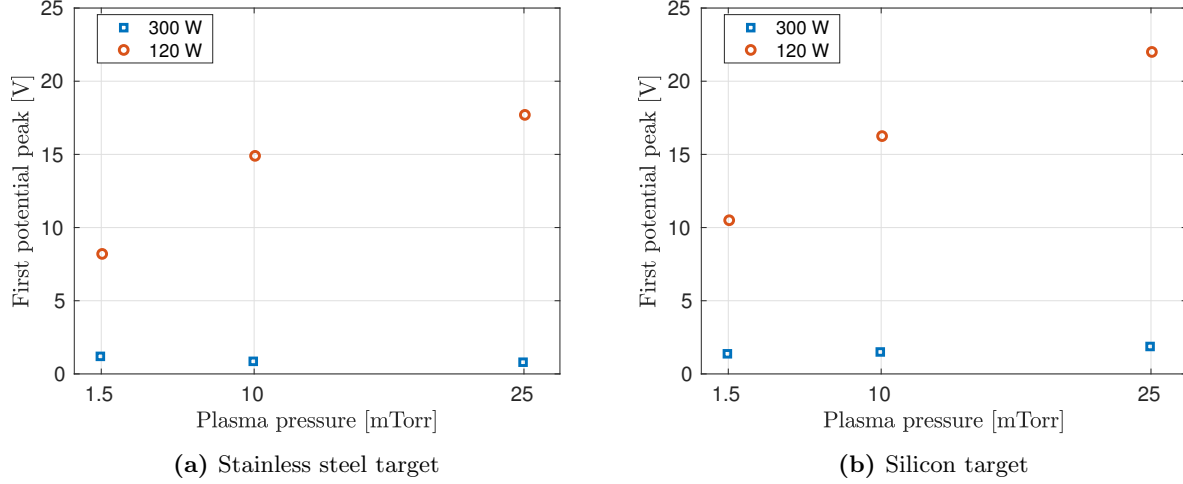


Figure 5.23: First peak height measurements for stainless steel and silicon pulsed targets, occurring $\sim 1 \mu\text{s}$ after pulse ends. Data acquired in the lower probe location $z_p = 21.7 \text{ cm}$ above each target. Each target was biased negatively to a 4 kV pulse with duration of $5 \mu\text{s}$ and repetition frequency of 250 Hz .

Figure 5.23 shows the first peak heights at lower probe location $z_p = 8.7 \text{ cm}$ in argon plasma for both pulsed stainless steel and silicon targets. The results are presented in three values of argon gas pressure $P_{Ar} = 1.5 \text{ mTorr}$, 10 mTorr and 25 mTorr and two RF-powers, namely $P_{RF} = 120 \text{ W}$ and 300 W , same as the upper location values.

Comparing the same pressure results, the amplitude of the maximum potential is higher in a lower RF-power value in every case. Comparing the same RF-powers in different pressures for both targets, shows a higher potential peak with higher gas pressure in every case with $P_{RF} = 120 \text{ W}$, while increasing the argon pressure in $P_{RF} = 300 \text{ W}$ results in no detectable change in potential peak value by our oscilloscope.

Comparing the results for stainless steel to silicon target at $P_{RF} = 300 \text{ W}$, both plasmas experience the same peak in the floating potential. In RF-power $P_{RF} = 120 \text{ W}$, while silicon target plasma have a highest first peak in floating potential, the plasma with pulsed stainless steel target experiences a slightly higher peak in both 1.5 mTorr and 25 mTorr argon pressures. However both of these peaks can be considered equal within the resolution limit of the oscilloscope. Also the data has been smoothed before the analysis. Given that the plasma with silicon target experiences a sharper first peak, the lower number of peak data points results in cutting off the peak point in smoothing some of the floating potential variations, especially in case of silicon.

Relaxation Time Analysis of First PPP For Silicon and Stainless Steel Targets

The recovery time for the first peak in floating potential has been analysed. The first instability in floating potential occurs early after the pulse ends, with a delay at the order of $\sim 1 \mu\text{s}$; it also has a short relaxation time constant. The time constant of these peaks are presented in this subsection.

Figure 5.26 shows relaxation time constant in lower argon plasma for both pulsed stainless steel and

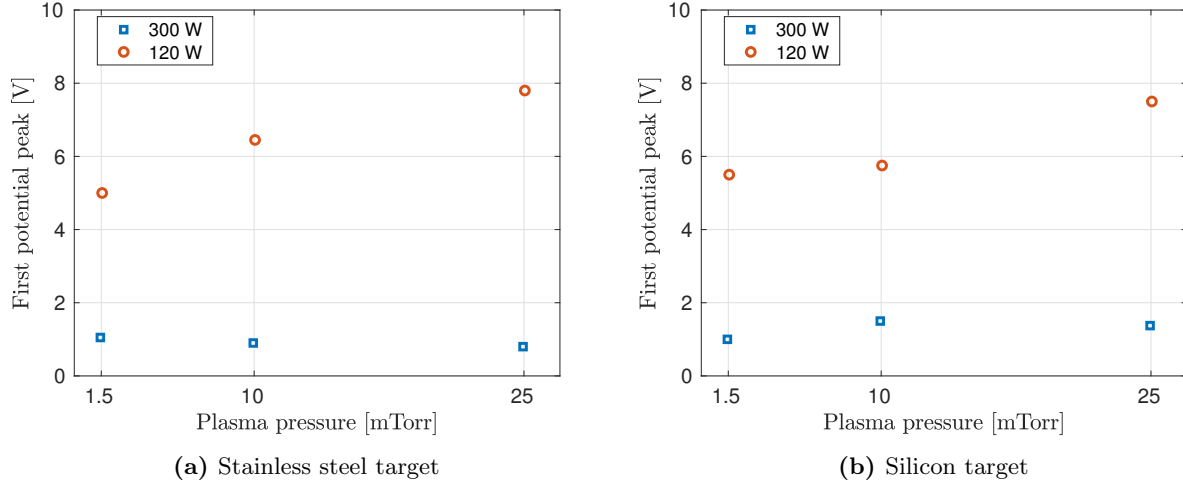


Figure 5.24: First peak height measurements for stainless steel and silicon pulsed targets, occurring $\sim 1 \mu\text{s}$ after pulse ends. Data acquired in the lower probe location $z_p = 8.7 \text{ cm}$ above each target. Each target was biased negatively to a 4 kV pulse with duration of $5 \mu\text{s}$ and repetition frequency of 250 Hz.

silicon targets. The results are presented in two values of constant RF-powers $P_{RF} = 300 \text{ W}$ and $P_{RF} = 120 \text{ W}$ as a function of argon gas pressure.

Comparing the same pressure analysis results, the plasma driven by $P_{RF} = 300 \text{ W}$ takes a lot longer to relax to steady state after experiencing the first peak in floating potential, for both silicon and stainless steel targets. This results are also backed by the the floating potential figure in the same pressure, shown in figures 5.12 and 5.17d.

Comparing the results at $P_{RF} = 300 \text{ W}$ with different pressures, in both targets cases the general tendency is that the relaxation time gets longer with higher pressure in the upper plasma. The exceptions are seen in the case of 1.5 mTorr to 10 mTorr for silicon target and 10 to 25 mTorr in the plasma with stainless steel target. In these cases the relaxation time is constant within the bigger error bars, caused by uncertainty in fitting. For $P_{RF} = 120 \text{ W}$, the relaxation time is getting shorter in higher plasma pressures, for every one of the cases in both silicon and stainless steel targets.

Figure 5.26 shows relaxation time constant in lower argon plasma for both pulsed stainless steel and silicon targets. The results are presented in two values of constant RF-powers $P_{RF} = 300 \text{ W}$ and $P_{RF} = 120 \text{ W}$ as a function of argon gas pressure.

Comparing the same pressure analysis results, the plasma driven by $P_{RF} = 300 \text{ W}$ takes a lot longer to relax to steady state after experiencing the first peak in floating potential, for both silicon and stainless steel targets. These results are comparable to the relaxation times for the upper plasma, except for 1.5 mTorr plasma with stainless steel target that shows a longer relaxation time in lower plasma, and 25 mTorr plasma with silicon target, also showing a longer relaxation time in lower plasma, which is closer to the pulsed target.

Comparing the results at $P_{RF} = 300 \text{ W}$ with different pressures in lower plasma, i.e. $z_p = 8.7 \text{ cm}$ above the pulsed target, in the plasma with a pulsed silicon target, analysis results show a higher relaxation time

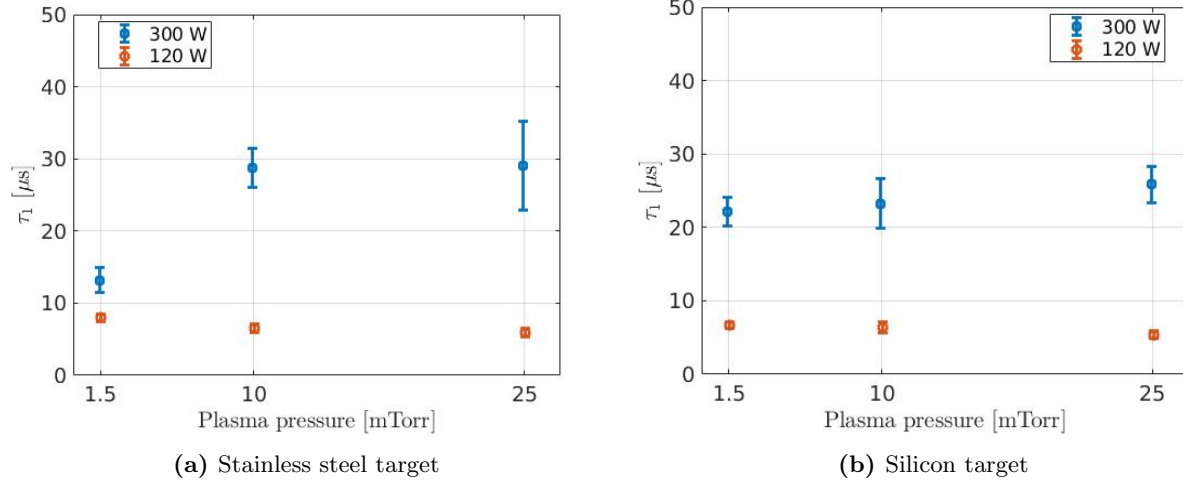


Figure 5.25: The decay time constant of the floating potential, i.e. relaxation time constants for stainless steel and silicon pulsed targets after occurrence of the first peak after the pulse. Data acquired in the lower probe location $z_p = 21.7$ cm above each target. Each target was biased negatively to a 4 kV pulse with duration of $5 \mu\text{s}$ and repetition frequency of 250 Hz.

in higher gas pressures. In the case of the pulsed stainless steel target, though the values are getting higher, the errors generated by the fitting method is too high to conclude the same. Similar to the upper plasma, for $P_{RF} = 120$ W, the relaxation time in lower plasma is getting shorter in higher plasma pressures, for every one of the cases in both silicon and stainless steel targets.

The results shown in figures 5.14 and 5.16, despite the bigger first peak after the pulse for higher pressures, it also takes them shorter to get to their steady state value. This means that the disturbed plasma time for all the pressures are on par with each other in the case of $P_{RF} = 120$ W for both silicon and stainless steel targets.

5.4.2 Long Time Scale Analysis

The long range floating potential variations presented in the previous section, show a second instability happening between 0.1 to 1 ms after the end of the pulse in both upper and lower plasmas. In this subsection, the analysis results for the peak height and relaxation time constant of this instability for both silicon and stainless steel targets in the upper and lower probe locations, i.e. $z_p = 21.7$ cm and $z_p = 8.7$ cm above the pulsed targets are presented.

Second Post-Pulse-Peak Height Analysis of Silicon and Stainless Steel Targets

Floating potential of plasma at probe's location experiences a second peaks at around $\sim 100 \mu\text{s}$ after the pulse ends which lasts until the next pulse. In this section the evolution of peak height as a function of RF-power analysis results for both silicon and stainless steel targets after this enhancement peak are presented. Figure 5.27 shows the second peak heights in upper argon plasma for both pulsed stainless steel and silicon targets.

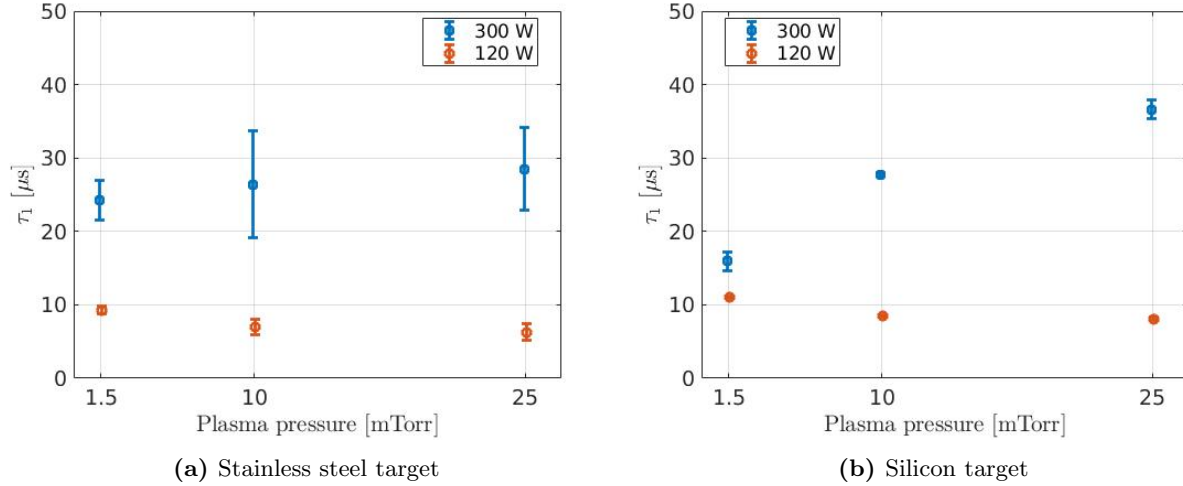


Figure 5.26: The decay time constant of the floating potential, i.e. relaxation time constants for stainless steel and silicon pulsed targets after occurrence of the first peak after the pulse. Data acquired in the lower probe location $z_p = 8.7$ cm above each target. Each target was biased negatively to a 4 kV pulse with duration of $5 \mu\text{s}$ and repetition frequency of 250 Hz.

Figure 5.28 shows the second peak heights in lower argon plasma for both pulsed stainless steel and silicon targets. The results are presented in three values of argon gas pressure $P_{\text{Ar}} = 1.5$ mTorr, 10 mTorr and 25 mTorr and two RF-powers, namely $P_{\text{RF}} = 120$ W and 300 W.

The graphs show that the second peak's height is about 1 V in every cases in the upper plasma which is 10 to 20 times lower than the first peak in same location with same plasma parameters. However, similar to the first peak, this peak also have a higher amplitude in more pressurised argon plasmas.

Comparing the results obtained for $P_{\text{RF}} = 120$ W plasmas to $P_{\text{RF}} = 300$ W in same pressure, 300 W plasmas experience a slightly higher second peak value for every pressure in both silicon and stainless steel, with a single exception of 25 mTorr plasma with pulsed silicon target.

Comparing the results obtained in the same RF-power, both of the RF-powers show higher second peak results for higher pressures. This results are consistent for both stainless steel and silicon pulsed targets. The results for 1.5 mTorr to 10 mTorr for stainless steel target, and 10 mTorr to 25 mTorr for silicon target are the same. The changes in the results are very close to the edge of the resolution in oscilloscope, which is the reason for the same results obtained in these transitions.

Comparing the silicon and stainless steel targets in both upper and lower plasma, the results are quite close to each other. With an exception of $P_{\text{Ar}} = 25$ mTorr and $P_{\text{RF}} = 120$ W, the second peak heights are similar for both targets within the resolution of the oscilloscope.

The graphs show a slight dependency of the height on plasma density, the height of the second maxima of the floating potential has a direct dependency on both RF-power and gas pressure. The interesting fact here is that, during steady state, the pulse time, and during the first floating peak until a while after the pulse, in same pressure, the floating potential is lowering with applying more RF-power in every case, see figure 5.12.

However a while, $\sim 0.1-1$ ms after the end of the pulse, more RF-power is in favour of a higher second peak in most cases.

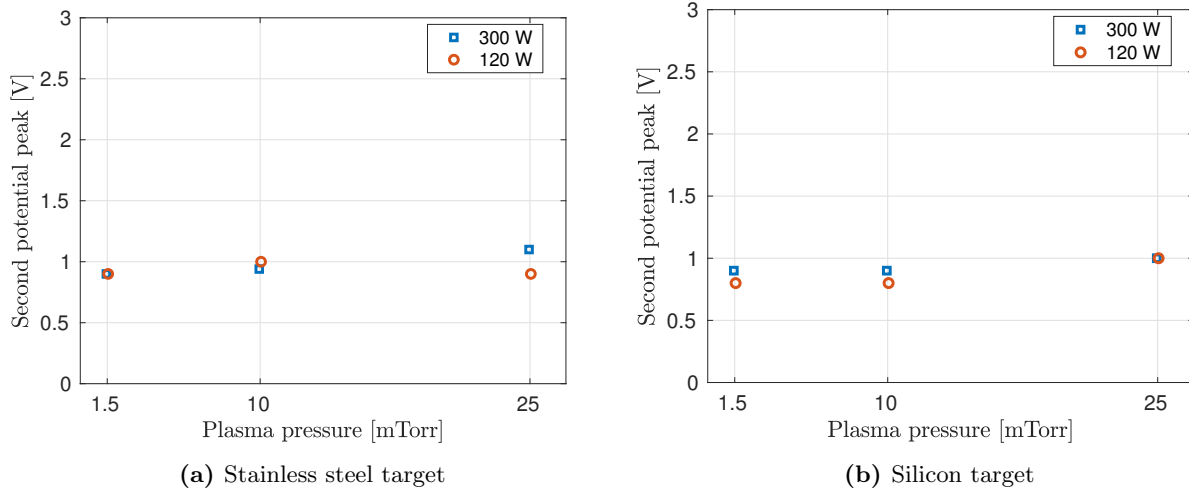


Figure 5.27: The second peak height measurements for stainless steel and silicon pulsed targets. Data acquired in the lower probe location $z_p = 21.7$ cm above each target. Each target was biased negatively to a 4 kV pulse with duration of $5 \mu\text{s}$ and repetition frequency of 250 Hz.

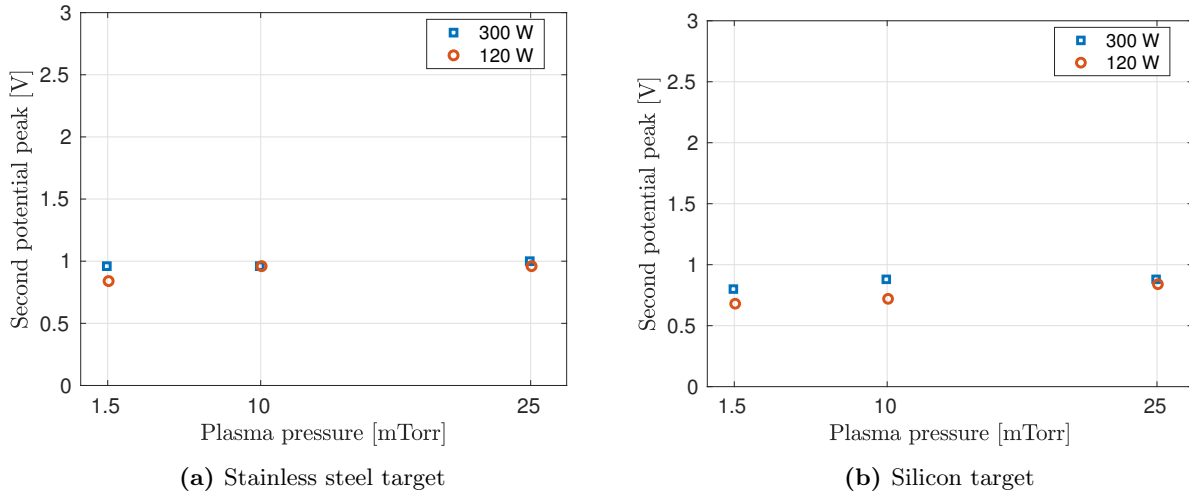


Figure 5.28: The second peak height measurements for stainless steel and silicon pulsed targets. Data acquired in the lower probe location $z_p = 8.7$ cm above each target. Each target was biased negatively to a 4 kV pulse with duration of $5 \mu\text{s}$ and repetition frequency of 250 Hz.

Relaxation Time Analysis of Second PPP For Silicon and Stainless Steel Targets

Plasma enhancement peaks sometime between $100 \mu\text{s}$ and 1 ms (based on plasma conditions) after the pulse ends and then continue to decay until the next pulse. In this section the relaxation time analysis results for both silicon and stainless steel targets after this enhancement peak are presented.

Figure 5.29 shows relaxation time constant in upper argon plasma for both pulsed stainless steel and silicon targets in the upper probe location, i.e. $z - p = 21.7$ cm. The results are presented in two values of constant RF-power $P_{RF} = 300$ W and $P_{RF} = 120$ W as a function of argon gas pressure.

Comparing the relaxation times in a constant pressure for the two values of RF-power, in upper plasma the instabilities corresponding to the $P_{RF} = 300$ W have longer relaxation times. Analysis of the peak showed a higher peak for higher value of RF-power, confirming the longer recovery time to their steady state in higher values of RF-power, in same pressure.

Comparing the relaxation times in a constant RF-power of 300 W, shows the increase of relaxation time constant in more pressurised plasmas. In the case of plasmas driven by 120 W RF-power, the relaxation time constant is getting shorter by increasing argon gas pressure in both silicon and stainless steel cases. Silicon shows a much more decrease between 1.5 to 10 mTorr than from 10 to 25 mTorr, while the plasma with pulsed stainless steel target shows more or less a consistent decrease increasing pressure. Additionally, comparing plasmas with silicon and stainless targets show that while the time constants are close to each other at 1.5 mTorr gas pressure for both 120 W and 300 W RF-powers, they become more and more spread apart increasing the gas pressure in plasma with silicon target, than pulsed stainless steel plasma.

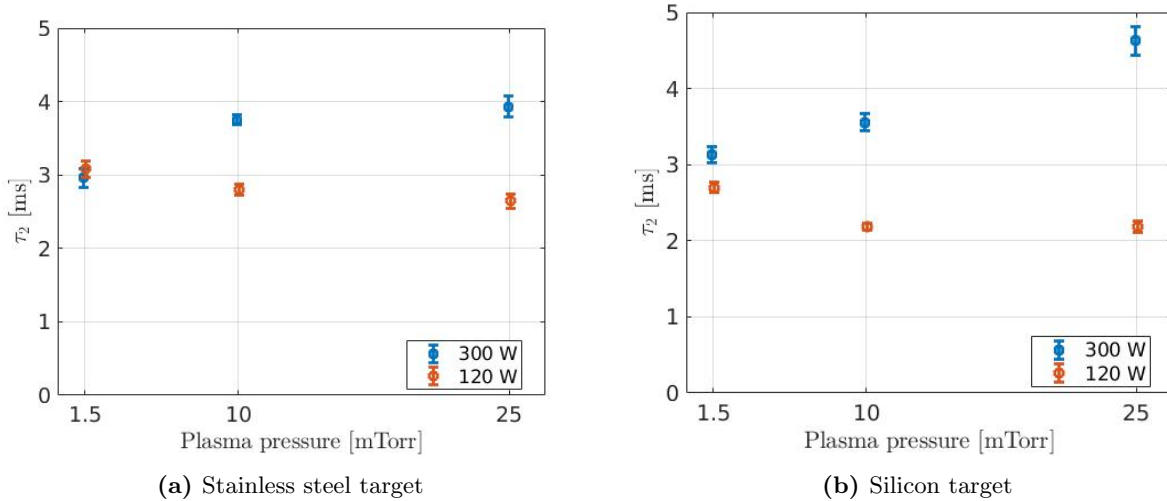


Figure 5.29: The decay time constant of the floating potential, i.e. relaxation time constants for stainless steel and silicon pulsed targets, after the second "smooth" peak of floating potential. Data acquired in the lower probe location $z_p = 21.7$ cm above each target. Each target was biased negatively to a 4 kV pulse with duration of 5 μ s and repetition frequency of 250 Hz.

Figure 5.30 shows relaxation time constant in upper argon plasma for both pulsed stainless steel and silicon targets in the upper probe location, i.e. $z - p = 8.7$ cm. The results are presented in two values of constant RF-power $P_{RF} = 300$ W and $P_{Ar} = 120$ W as a function of argon gas pressure.

Similar to the upper probe location, in the lower plasma both silicon and stainless steel targets show an increase of time relaxation value increasing pressure for $P_{Ar} = 300$ W. The results for stainless steel plasma at $P_{Ar} = 120$ W shows a decrease similar to the upper probe location, while the plasma with immersed silicon

target shows a small decrease from 1.5 mTorr to 10 mTorr, and no change in relaxation time from 10 to 25 mTorr.

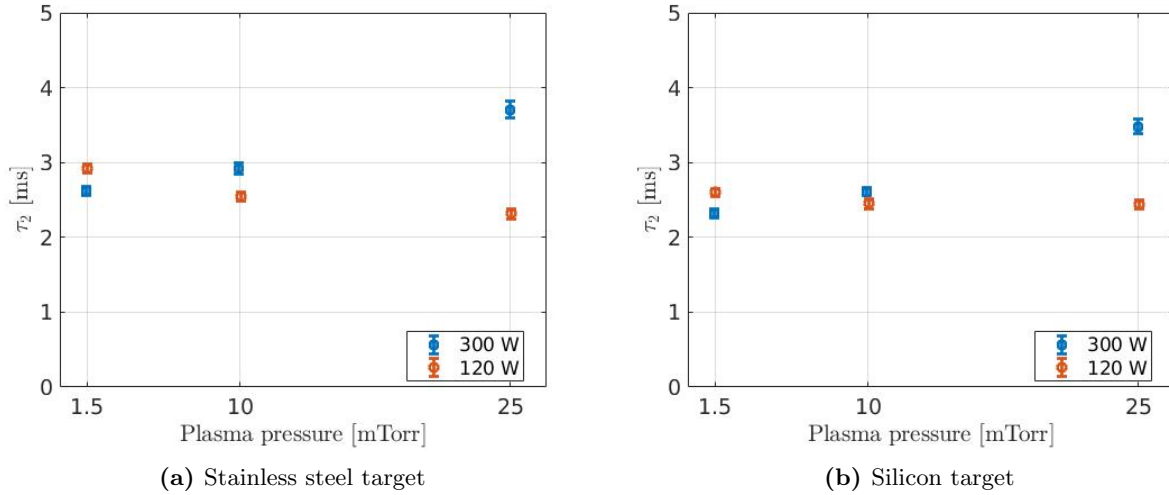


Figure 5.30: The decay time constant of the floating potential, i.e. relaxation time constants for stainless steel and silicon pulsed targets, after the second "smooth" peak of floating potential. Data acquired in the lower probe location $z_p = 8.7$ cm above each target. Each target was biased negatively to a 4 kV pulse with duration of 5 μ s and repetition frequency of 250 Hz.

5.5 Time-Resolved I-V Curve Analysis For Pulsed Stainless Steel and Silicon Targets

In this section I will present time-resolved I-V curve measurements for pulsed Argon plasma with different targets. These will provide important information about the time variation of the plasma properties during PII-relevant pulses. The generation of time-resolved I-V curves is a two step process which begins with the collection of time-resolved probe current data for a probe held at fixed bias voltage during a high-voltage target pulse. This is elaborated upon, in more detail in the following sections.

5.5.1 Measurement of Probe Current $I_p(t)$ During Pulsed Target Bias

All Time-Resolved data presented to this point have been measurements of floating potential V_f . While this is a relatively easy to measure with a fixed probe, many other measurements can be done with a RF-compensated Langmuir probe. In particular the time evolution of the probe current $I_p(t)$ can be measured for a fixed probe bias voltage V_B during a pulse. These data are presented at the figures below for both Silicon and stainless steel targets.

By rebuilding current $I_p(t)$ vs. probe bias V_B curves in different times, from the measurements of the probe's current during a single pulse period with a steady probe bias, valuable understanding of plasma

deviation from its equilibrium state during PII can be grasped. Figure 5.31 shows an example of probe's current during a PII cycle for different probe biases.

the peaks relation to the probe bias is another interesting feature of the graph. As ion current is a lot smaller than electron current, it starts to deviate from the acquired steady state current, by changing slowly. Then The dip in the current, exceeds zero at the peak for the floating potential. The growth of the peak, i.e. the deviation from steady state current, continues until it exceeds the plasma potential at the dip time. Afterwards, as the probe is biased with a higher voltage, the dip and the dip's deviation from the steady state value starts to shrink. Another interesting observation from these graphs are the increase of the time between the end of the pulse and the measured dip in the current. As the probe is biased with a more positive voltage, electrons tend to leave the attractive potential region slower.

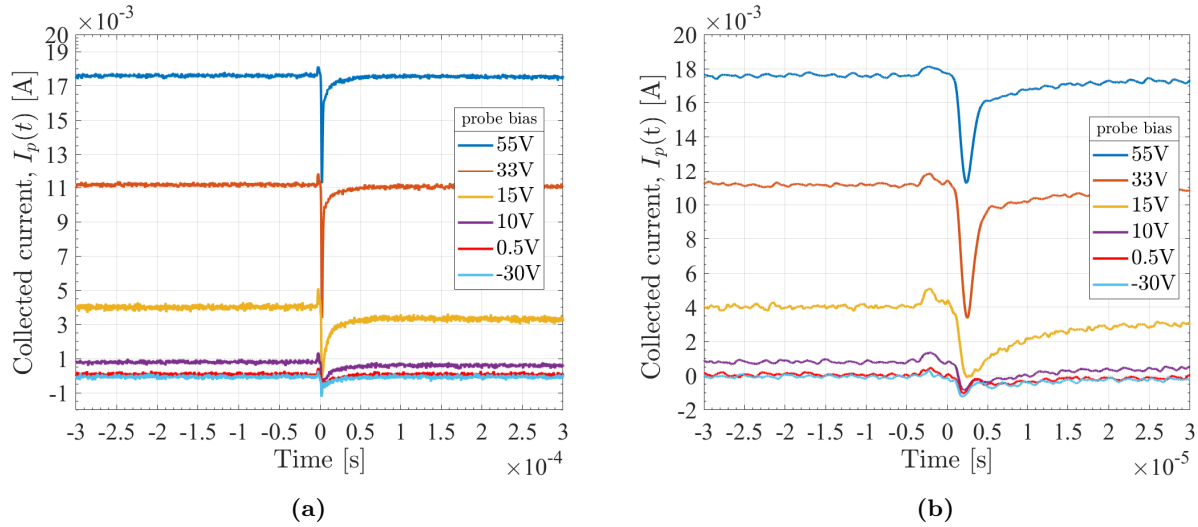


Figure 5.31: probe's collected current from Ar plasma during a single -4 kV pulse with 5 μ s duration applied at 250Hz frequency to a stainless steel target 8.7 cm below the probe's tip. Plasma pressure was 1.5 mTorr with 120 W RF-power. 90 current curves during each pulse have been acquired from -35 V to 57 V with 1 V voltage steps. Only 6 curves are shown here as an example of the acquired data. Note that (b) is zoom in time range of figure (a).

Constructing the current-voltage characteristics from these graphs will give yet a better idea of the plasma potential and floating potential at each time snapshot. The next section is an attempt to construct the I-V curves without losing their valuable inherent information.

5.5.2 Construction of Time-Resolved IV Curves From Probe Current Measurements In Pulsed Target Regime

Ten I-V curves have been rebuilt from the similar data sets shown in previous subsection. The time locations were chosen as follows. (1) Before the pulse begins, when the plasma had time to calm, semi-equilibrium state; acquired at $t=-10 \mu$ s.

(2) This curve is acquired at time= -1 μ s (see figure 5.31) when the electron population in plasma

start to rise during the rise of the negative high-voltage pulse. (3) During the pulse, when the pulse is at its highest negative bias and thus the current acquired by the probe is at its peak. ($t = 0 \mu s$ in figure 5.31) This momentarily rise in electron current collection during the pulse happens because the ions are drawn to the target, leaving the plasma around the probe tip with more electrons, causing a slightly more "positive" electron current to the probe. Plasma enhancement after the pulse, when electrons are drawn to the target, in order to fill in the depleted high-voltage sheath [see figure 2.2b, the Rogowski measurement of the electron current after the pulse.], the probe is left with more ion population and a "negative" ion current is recorded, comparing to the steady state. (4), (5) and (6) are acquired during the enhancement with $t_1 = (V_B(max) - V_B(min))/4$ time separation between them, (the rise of the floating voltage and the fall of probe's gathered current). (7) is acquired at the minimum of the first current curve (at time= $3.4 \mu s$). (8), (9), (10) are acquired at times t_1 , $3 \times t_1$, $12 \times t_1$ after the minima, respectively.

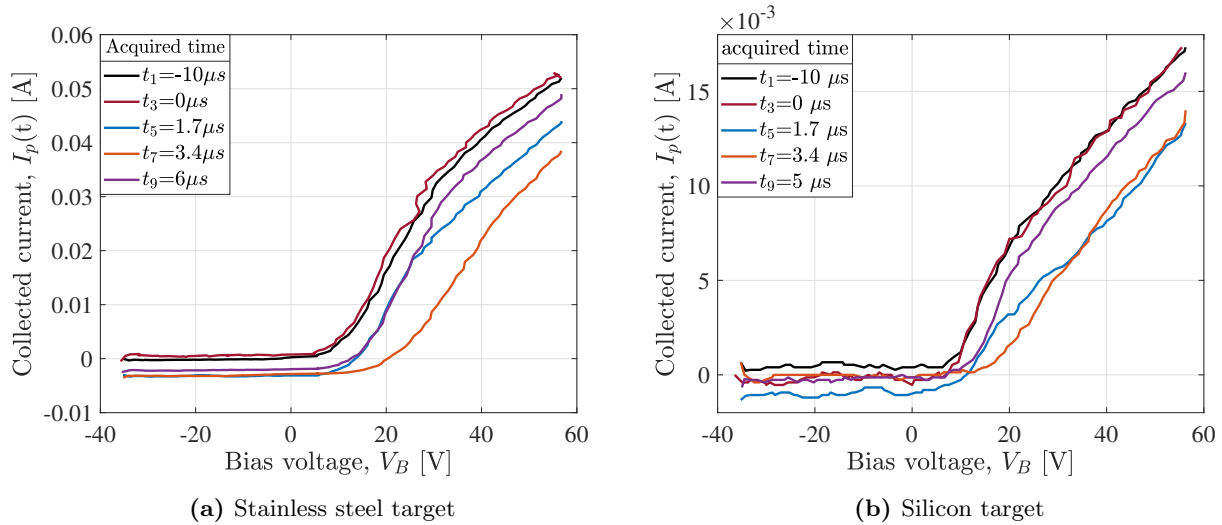


Figure 5.32: Time-resolved constructed I-V curves in different times, argon plasma pressure $P_{Ar} = 1.5$ mTorr, RF-power $P_{RF} = 120$ W. The curves are acquired in different times during the cycle of a -4 kV with $5 \mu s$ duration pulse bias with repetition frequency of 250 Hz at probe location 8.7 cm above the stainless steel target. See figure 5.31 for the time reference. $t_1 = -10 \mu s$ is acquired before pulse and after the relative recovery of plasma to the steady state. The constructed I-V curve has different characteristics to steady state, meaning plasma has not been quite recovered to steady state yet from the previous pulse. As expected, the I-V curve at the time of the highest floating potential has more deviation from steady state, with a high floating potential and colder electrons (less $V_p - V_f$).

The following is the analysis results of these curves during -4 kV pulsed stainless steel and silicon targets in RF-power $P_{RF} = 120$ W and argon gas pressure $P_{Ar} = 15$ mTorr.

5.5.3 Analysis of Time-Resolved IV Curves in Pulsed Target Regime

Figures 5.33 show the time-resolved Plasma and floating potential results for both stainless steel and silicon targets. The floating potential for silicon target is in good agreement with the direct measurements from the probe, presented in previous section. At time $t_1 = 0$ s, when the pulse has just ended and the floating

potential at lower probe location $z_p = 8.7$ cm is just below the steady state, plasma potential stays the same within the error bars, based on Langmuir analysis. For silicon substrate, Druyvesteyn method measures the plasma potential to be lower and for stainless measures a higher value of plasma potential relative to their each steady state. As expected, both plasma potential and floating potentials show a rise after the pulse ends. After reaching a peak for both plasma and floating potentials, they start to relax to the steady state. Both theories are in agreement in measuring the plasma potentials. Eyeballing the separation of the potentials, by remembering equation A.1, we would expect that the electron temperatures are warmest in the peak $t_7 = 3.4 \mu\text{s}$ and lowest during the rise and fall times of the floating potential, namely, $t_5 = 1.7 \mu\text{s}$ and $t_9 = 5 \mu\text{s}$.

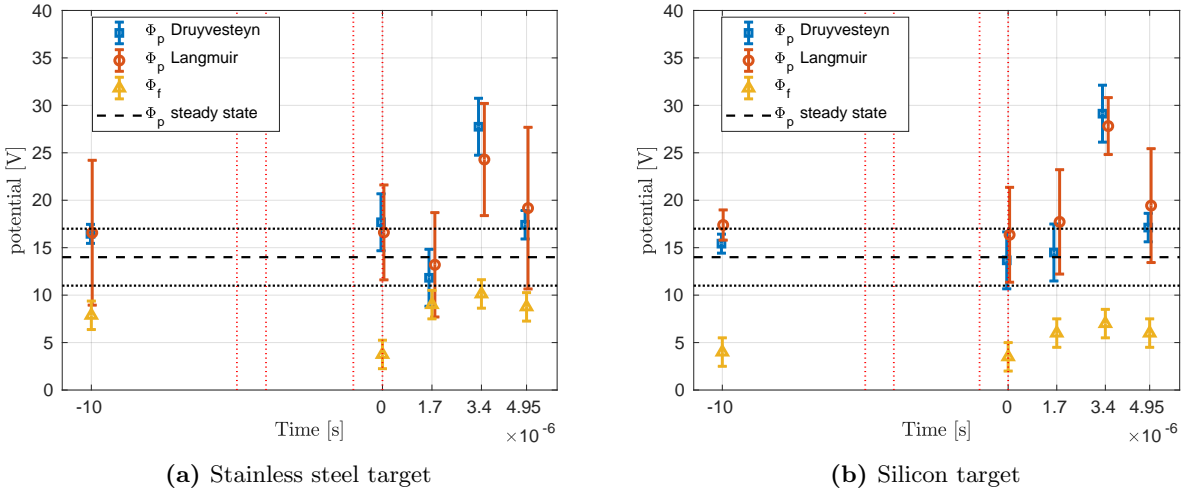


Figure 5.33: Time-resolved plasma potentials, Argon plasma pressure $P_{\text{Ar}} = 1.5\text{mTorr}$, RF-power $P_{\text{RF}} = 120$ W. The curves are acquired in different times during the cycle of a -4 kV with $5 \mu\text{s}$ duration pulse bias with repetition frequency of 250Hz at probe location 8.7 cm above the stainless steel target. See figure 5.31 for the time reference.

Figures 5.34 show the time-resolved electron temperature results for both stainless steel and silicon targets immersed in argon plasma.

Based on our expectations from the plasma potential and floating potential measurements, Langmuir probe analysis seem to be more accurate. The very high electron temperature results in $t_3 = 0$ s as well as the semi-steady state electron temperature discrepancies for stainless steel target, raise questions about the reliability of Druyvesteyn method in analysing the acquired time-resolved Langmuir probe I-V curves.

The reason for overestimation of the electron temperatures and unreliability of Druyvesteyn analysis method is coming from the difficulty regarding numerical derivation of a low resolution time resolved I-V curve. The most reliable method seems to be Langmuir analysis, if carefully carried out by the analyser, as the analyser fits the different lines to the electron and pre-electron saturation regimes. One should be careful in using Langmuir analysis, as it has the limitation of applicability to non-Maxwellian plasmas. See figure 5.35 for a raw I-V curve. The large separation between the acquired data points ~ 1 V made the smoothing

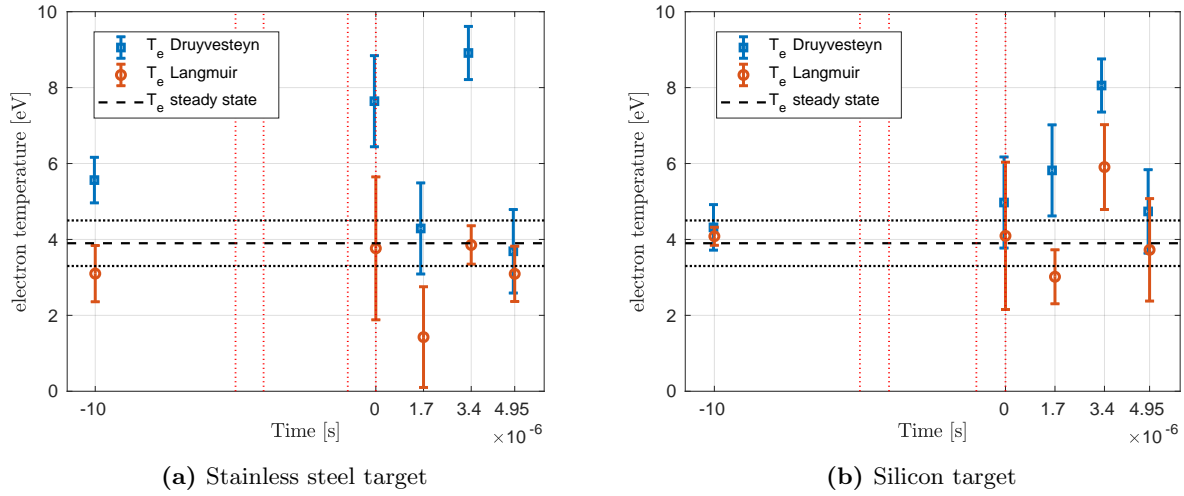


Figure 5.34: Time-resolved electron temperatures, Argon plasma pressure $P_{Ar} = 1.5$ mTorr, RF-power $P_{RF} = 120$ W. The curves are acquired in different times during the cycle of a -4 kV with $5 \mu s$ duration pulse bias with repetition frequency of 250 Hz at probe location 8.7 cm above the stainless steel target. See figure 5.31 for the time reference. $t_1 = -10 \mu s$ is acquired before pulse and after the relative recovery of plasma to the steady state.

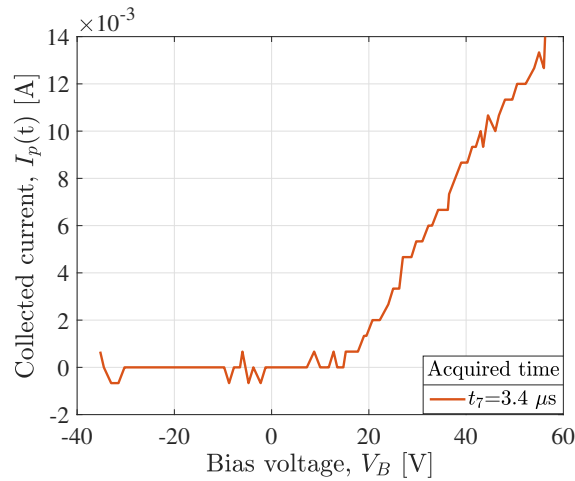


Figure 5.35: An un-smoothed curve acquired at time $t_7 = 3.4 \mu s$ right after the end of the pulse. The target is silicon. It can be hardly seen that based on the "knee" of this curve the plasma potential might be around $V_B = V_p \approx 30$ V, separating the exponential region from the linear electron saturation region. Given the high floating potential at this point (the I-V curve is acquired at the first post pulse floating potential peak). Additionally, it is better to use the electron saturation part of the curve for analysis, as the ion saturation is in the order of the oscilloscope voltage resolution limit.

inaccurate, thus the main features of the curve were lost in the first and second numerical derivations of the smoothed function. A rough estimation using the equation A.1, using the values of $V_p = 40$ V detecting the knee of the smoothed I-V curve from figure 5.32, and finally the direct measurement of the floating potential in $t_7 = 3.4 \mu\text{s}$, $V_f = 9$ V (See figure 5.20), one can have a rough estimation of 5.5 eV of the electron temperature in this time. This is quite in agreement with the Langmuir analysis. Additionally, OML analysis can be done to acquire the ion densities, as they might locally deviate from the electron densities during PII.

5.5.4 Langmuir Analysis of Time-Resolved IV Curves in Pulsed Target Regime

Determining the Langmuir analysis to be the more reliable analysis for our time-resolved Langmuir probe I-V curve measurements, the comprehensive analysis of the plasma with silicon and stainless steel pulsed targets in different argon gas pressures, namely $P_{\text{Ar}} = 1.5$ mTorr and 25 mTorr, two values of RF power, $P_{\text{RF}} = 300$ W and 120 W, with both silicon and stainless steel targets pulsed with -4 kV and -1 kV pulse amplitudes. The measurements were done in two probe locations above the pulsed targets, 13 cm separated vertically. 20000 I-V curves have been rebuilt and analysed for each one of the plasma conditions presented in the following. These analysis require a selection of the I-V curve from its exponential region to the electron saturation region. Different selections of this region in different plasma conditions would provide one with a slightly (or in some cases hugely) different analysis results. This, adds to the error boundaries of the analysis presented here, in addition to the presented error bars.

Figure 5.36 shows a family of I-V curves acquired in $P_{\text{Ar}} = 1.5$ mTorr argon pressure and RF-power of $P_{\text{RF}} = 120$ W recorded at the upper probe location with $z_p = 21.7$ cm vertical distance from the pulsed stainless steel and silicon targets. The probe was biased in a range from -35 V to 55 V with less than 1 V potential steps. 20000 I-V curves were acquired from 320 μs before the end of the pulse to 320 μs after the end of the pulse.

The colour bar shows the values for the current drawn to the probe's tip (1.0 mm diameter and 5.0 mm length). The dark blue region indicates the ion saturation region, the yellow and orange colours are corresponding to the electron saturation and the colours in between roughly show the exponential part of the curves. Notice a higher ion density, indicated by a darker shade of blue in probe's location occurring before 2 μ after the pulse ends. In addition to that, notice the electron temperature rise, indicated by an extended light blue and green colour into the electron saturation region. This spread of the I-V curve, shows a higher value for $V_p - V_f$, thus a higher temperature for electrons. The interesting observation from both of the curve families is the delay of the electron temperature rise compared to the rise of the ion density. This happens while the electrons are expected to have a faster response to the pulse due to their much higher mobility compared to the ions.

Figure 5.37 shows the same families of curves for the lower probe location, namely $z_p = 8.7$ cm above the pulsed targets. We notice a generally lower current drawn by the probe compared to the upper plasma in a given probe bias, due to the lower density of the plasma in lower probe location. Moreover, the electron

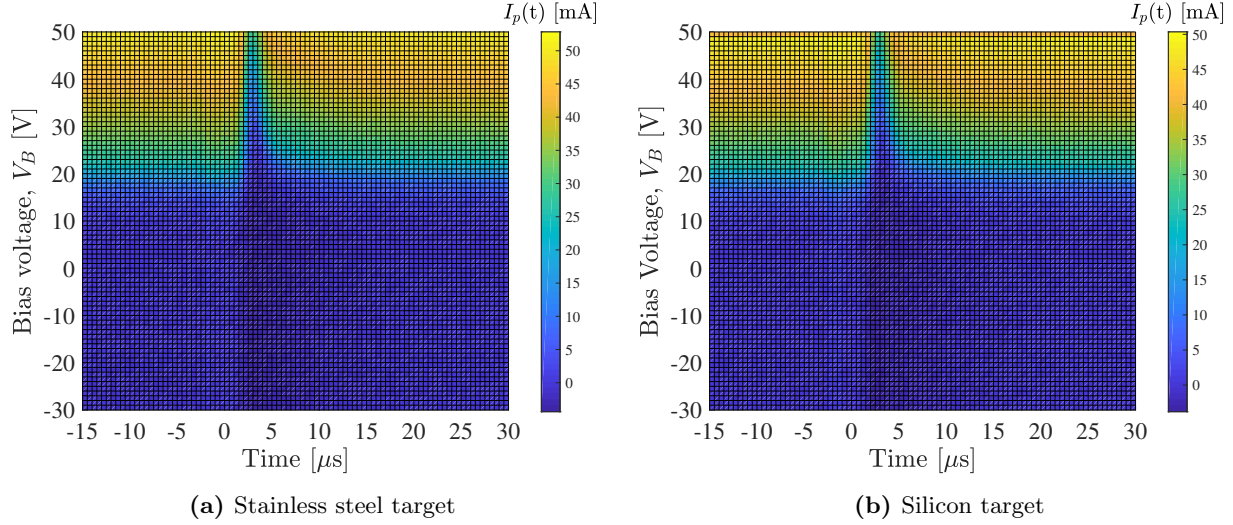


Figure 5.36: Time-resolved plasma potentials, Argon plasma pressure $P_{Ar}= 1.5$ mTorr, RF-power $P_{RF}= 120$ W. The curves are acquired in different times during the cycle of a -4 kV with $5 \mu s$ duration pulse bias with repetition frequency of 250 Hz at probe location 21.7 cm above silicon and stainless steel targets. The pulse starts at $t=-5 \mu s$ and ends at $t=0 \mu s$.

temperature in this region seems to be higher than the upper plasma. However, the ion density and plasma potential changes after the pulse seems to be less in this location, indicated by the smoother changes in the colour shades while moving in time direction. A slightly higher change in ion density and plasma and floating potentials can be seen in the plasma with pulsed silicon target compared to the pulsed stainless steel. Additionally, the same delay of the electron temperature rise is seen in the lower graphs for both silicon and stainless steel targets.

Looking at the figure 5.37b, note that after the pulse, the plasma potential might not be reached for the silicon target. The plasma with stainless steel target immersed, shows about the same peak as the upper location, about 40 V. Plasma with pulsed silicon target however, experiences a potential peak between 40 - 50 V, which is at the higher end of the sweep bias voltage of the probe. This value is subject to change with different analysis schemes of the data, but will either remain within this error boundary or will be out of the reach due to the hardware limitation in data acquisition. A hot-wire emissive Langmuir probe can be used in order to acquire a precise measurement of the high values of plasma potential during PII.

5.5.5 Study of Variable Pulse Magnitude: -1 kV vs. -4 kV

PII processes use a range of pulses from -1 kV to several tens of kV. It is therefore of interest to study the effect of plasma pulsing for different pulse magnitudes. I present here a comparison of plasma potential, electron temperature and plasma density values between -4 kV and a lower pulse magnitude of -1 kV, applied to both silicon and stainless steel targets. The following presented measurements are acquired in the lower probe location $z_p= 8.7$ cm in order to be closer to the pulsed target.

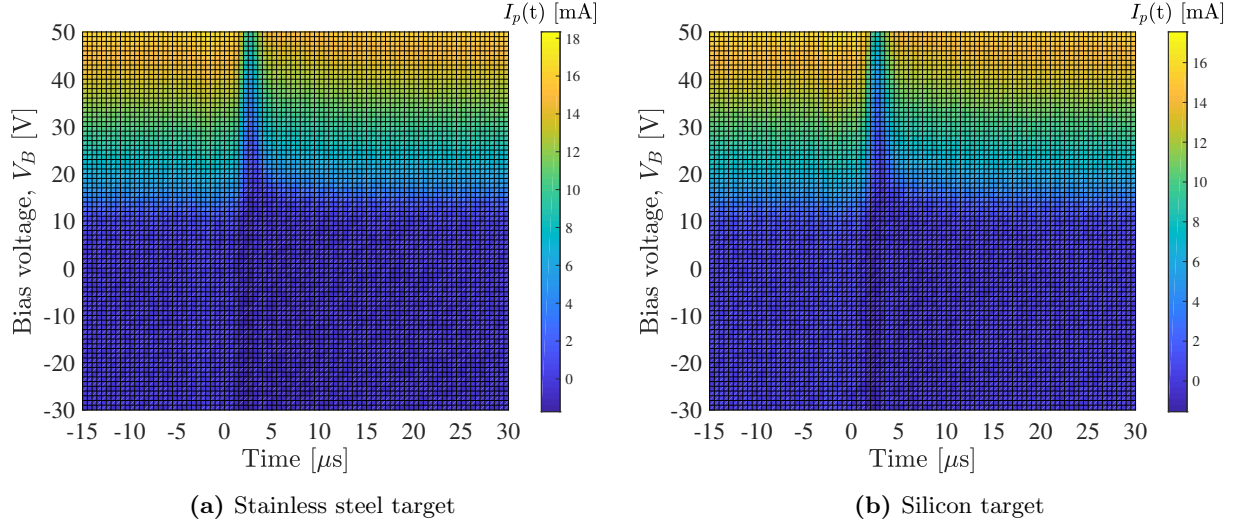


Figure 5.37: Time-resolved I-V characteristic curves, Argon plasma pressure $P_{Ar} = 1.5$ mTorr, RF-power $P_{RF} = 120$ W. The curves are acquired in different times during the cycle of a -4 kV with $5 \mu s$ duration pulse bias with repetition frequency of 250 Hz at probe location 8.7 cm above silicon and stainless steel targets. The pulse starts at $t = -5 \mu s$ and ends at $t = 0 \mu s$.

Plasma Potential Study of Variable Pulse Magnitude: -1 kV vs. -4 kV

Figure 5.38 compares the evolution of plasma potential during a -4 kV pulse and a -1 kV pulse applied to a stainless steel target in an argon plasma with 1.5 mTorr gas pressure and $P_{RF} = 120$ W driving RF-power. Both pulses start at $-5 \mu s$ and end at $0.0 \mu s$. For a comparison of the pulses and the currents going through the target during each pulse, see figure 5.17.

- **Region 1:** Before the pulse starts, The plasma potential is steady in both applied pulses. Considering the error bars, the plasma with -4 kV applied pulse is in a higher plasma potential than the plasma with -1 kV applied pulse. Remembering from section 5.2.2, the floating potential was also higher for -4 kV pulsed target.
- **Region 2:** During rise time of the pulse, the plasma potential stays steady for both -4 kV and -1 kV pulses.
- **Region 3:** Langmuir method analysis show a constant plasma potential during the -1 kV pulse in lower probe location within the corresponding error at each time. However, the plasma with -4 kV pulse, show a slight potential dip during the pulse.
- **Region 4:** During the pulse drop, the plasma potential experiences a slight increase in the plasma with -4 kV pulsed target. The plasma potential in -1 kV pulsed target case, stays steady.
- **Region 5:** The plasma potential experiences a peak at about $2 \mu s$ after the pulse ends. The plasma potential gets to a high point about 40 V, and then starts to relax back to its steady state value of 19

V. In the shown time window, the relaxation is not 100% but gets very close to the steady value after $\sim 15 \mu\text{s}$, in the order of the relaxation time constant we got for the floating potential, in the First PPP relaxation time analysis section.

- **Region 6:** The plasma potential continues the relaxation back to its steady state in this region for -4 kV applied pulse. -1 kV stays the same steady state during the whole pulse cycle.

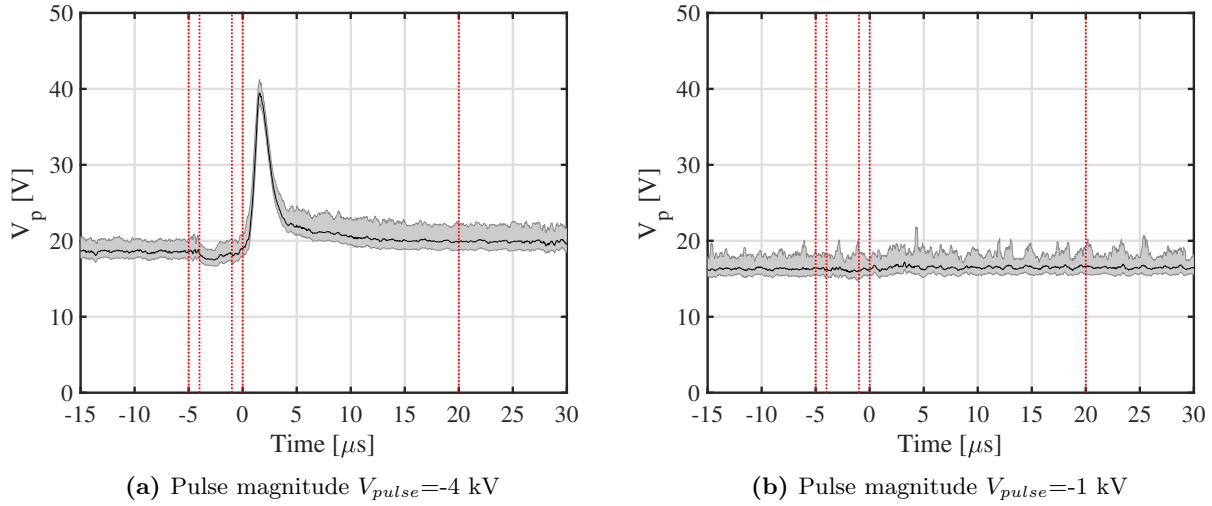


Figure 5.38: Time-resolved plasma potentials, Argon plasma pressure $P_{Ar} = 1.5$ mTorr, RF-power $P_{RF} = 120$ W. The curves are acquired in different times during the cycle of a -4 kV and -1 kV, both with $5 \mu\text{s}$ duration pulse bias with repetition frequency of 250 Hz at probe location 8.7 cm above the stainless steel target. The grey shade indicates the error boundaries.

Figure 5.39 shows the evolution of plasma potential during a -4 kV and a -1 kV magnitude pulse applied to a silicon target in the argon plasma with 1.5 mTorr gas pressure and $P_{RF} = 120$ W. Both pulses start at $-5 \mu\text{s}$ and end at $0.0 \mu\text{s}$.

- **Region 1:** Before the pulse starts, The plasma potential is steady in both applied pulses. Considering the error bars, the plasma with -4 kV applied pulse is in a higher plasma potential than the plasma with -1 kV applied pulse. Remembering from section 5.2.2, the floating potential was also higher for -4 kV pulsed target.
- **Region 2:** During rise time of the pulse, the plasma potential stays steady for both -4 kV and -1 kV pulses.
- **Region 3:** Langmuir method analysis show a constant plasma potential during the -1kV pulse in lower probe location within the corresponding error at each time. However, the plasma with -4 kV pulse, show a slight potential dip during the pulse.
- **Region 4:** During the pulse drop, the plasma potential experiences a slight increase in the plasma with -4 kV pulsed target. The plasma potential in -1 kV pulsed target case, stays steady.

- **Region 5:** The plasma potential experiences a peak at about $2 \mu\text{s}$ after the pulse ends. The plasma potential gets to a high point between 40 V to 50 V, and then starts to relax back to its steady state value of 19 V. In the shown time window, the relaxation is not 100% but gets very close to the steady state value after $\sim 15 \mu\text{s}$, in the order of the relaxation time constant we got for the floating potential, in the First PPP relaxation time analysis section.
- **Region 6:** The plasma potential continues the relaxation back to its steady state in this region for -4 kV applied pulse. -1 kV stays the same steady state during the whole pulse cycle.

The plasma potential is not affected by the pulse during the -1 kV pulse. Langmuir method analysis show a constant plasma potential during the -1kV pulse in lower probe location within the corresponding error at each time. However, the plasma with -4 kV pulse, show a slight potential drop during the pulse, The plasma potential then experiences a higher and sharper post pulse peak for silicon target compared to pulsed stainless steel target plasma at the same time $t= 2 \mu\text{s}$, after the pulse ends.

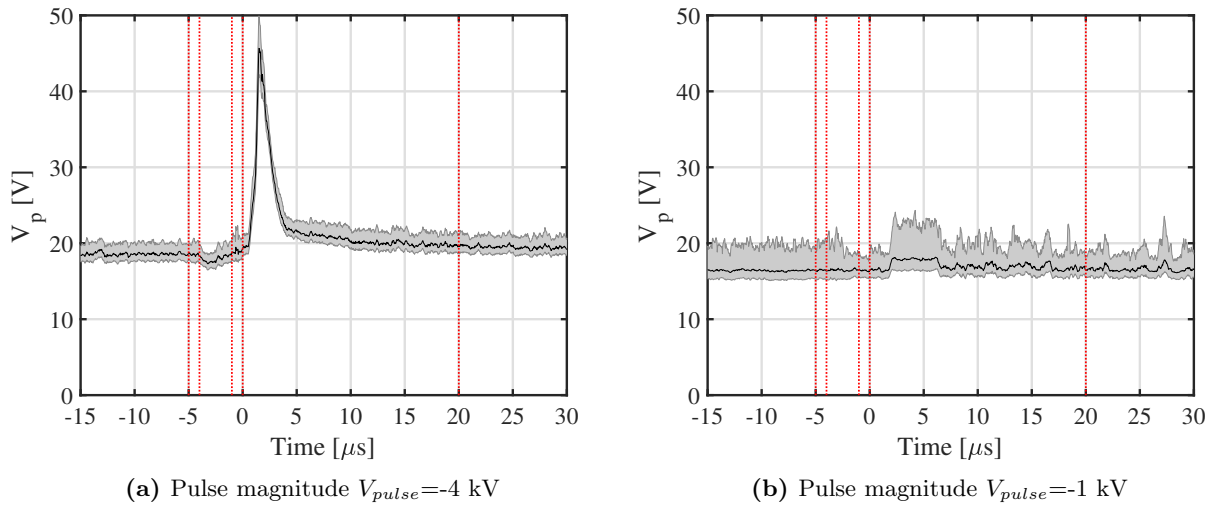


Figure 5.39: Time-resolved plasma potentials, Argon plasma pressure $P_{Ar} = 1.5 \text{ mTorr}$, RF-power $P_{RF} = 120 \text{ W}$. The curves are acquired in different times during the cycle of a -4 kV and -1 kV, both with $5 \mu\text{s}$ duration pulse bias with repetition frequency of 250 Hz at probe location 8.7 cm above the silicon target. The grey shade indicates the error boundaries.

Electron Temperature Study of Variable Pulse Magnitude: -1 kV vs. -4 kV

Figure 5.40 compares the evolution of electron temperature during a -4 kV pulse and a -1 kV pulse applied to a stainless steel target in an argon plasma with 1.5 mTorr gas pressure and $P_{RF} = 120 \text{ W}$ driving RF-power. Both pulses start at $-5 \mu\text{s}$ and end at $0.0 \mu\text{s}$.

Similar to the plasma potential, electron temperature is not affected by the pulse during the -1 kV pulse. Langmuir method analysis show a constant electron temperature during the -1kV pulse in lower probe location

within the corresponding error during a cycle. While the plasma with -4 kV pulsed target experiences a rise in electron temperature in the lower probe location after the pulse ends.

- **Region 1:** Before the pulse starts, the electron temperature is steady in both applied pulses. Considering the error bars, both plasmas have the same electron temperature.
- **Region 2:** During rise time of the pulse, the electron temperature stays steady for both -4 kV and -1 kV pulses.
- **Region 3:** During the pulse plateau, Langmuir method analysis shows a constant electron temperature during both applied pulses in lower probe location within the corresponding error at each time.
- **Region 4:** During the drop of the high voltage pulse, electron temperatures in both pulse cases, remain steady.
- **Region 5:** The electrons experience a high temperature of about 12-13 eV at 2 μs after the end of the -4 kV voltage pulse applied to the stainless steel target. The electron temperature then cools down to the steady value between 4-6 eV in lower plasma at about 5 μs after the end of the pulse. The plasma with -1 kV pulsed target shows no change in electron temperature in this region.
- **Region 6:** The electron temperature is steady in both applied pulses in this region. Considering the error bars, both plasmas have the same electron temperature.

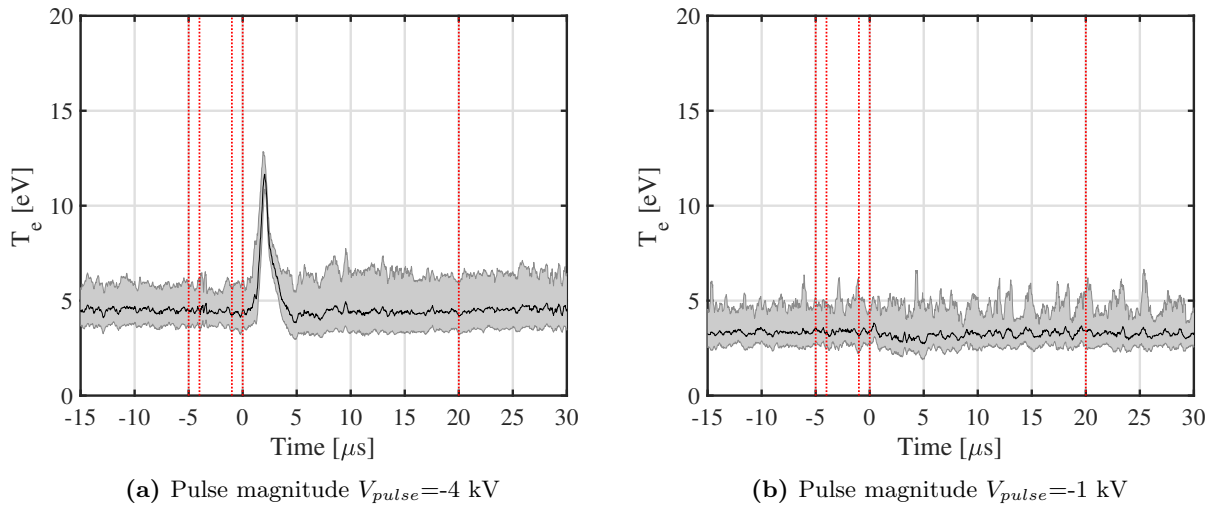


Figure 5.40: Time-resolved electron temperatures, Argon plasma pressure $P_{Ar} = 1.5$ mTorr, RF-power $P_{RF} = 120$ W. The curves are acquired in different times during the cycle of a -4 kV and -1 kV, both with 5 μs duration pulse bias with repetition frequency of 250 Hz at probe location 8.7 cm above the stainless steel target. The grey shade indicates the error boundaries.

Figure 5.41 compares the evolution of electron temperature during a -4 kV pulse and a -1 kV pulse applied to a silicon target immersed in argon plasma with 1.5 mTorr gas pressure and $P_{RF} = 120$ W driving RF-power. Both pulses start at -5 μs and end at 0.0 μs .

- **Region 1:** Before the pulse starts, the electron temperature is steady in both applied pulses. Considering the error bars, both plasmas have the same electron temperature.
- **Region 2:** During rise time of the pulse, the electron temperature stays steady for both -4 kV and -1 kV pulses.
- **Region 3:** During the pulse plateau, Langmuir method analysis shows a constant electron temperature during both applied pulses in lower probe location within the corresponding error at each time.
- **Region 4:** During the drop of the high voltage pulse, electron temperatures in both pulse cases, remain steady.
- **Region 5:** The electrons experience a high temperature of about 15-17 eV at 2 μ s after the end of the -4 kV voltage pulse applied to the silicon target. The electron temperature then cools down to the steady value between 4-6 eV in lower plasma at about 5 μ s after the end of the pulse. The plasma with -1 kV pulsed target shows no change in electron temperature in this region.
- **Region 6:** The electron temperature is steady in both applied pulses in this region. Considering the error bars, both plasmas have the same electron temperature.

Similar to the plasma potential, electron temperature is not affected by the pulse during the -1 kV pulse in the case of silicon target as well. While the electrons experience a high temperature of about 15-17 eV at 2 μ s after the end of the high voltage pulse applied to the target. This temperature is more than what we measured earlier for stainless steel target for the same -4 kV pulse, however the timing seems the same in the range of the oscilloscope's data acquisition rate (1 data point in each 0.02 μ s time step). Additionally, in the steady state region, Langmuir analysis generally predicts slightly colder electrons in -1 kV pulse steady state than the plasma with -4 kV applied pulse, however the error bars have a common region of temperature here as well, meaning they can be assumed as equal within their error limits.

Plasma Density Study of Variable Pulse Magnitude: -1 kV vs. -4 kV

Figure 5.42 compares the evolution of electron density during a -4 kV pulse and a -1 kV pulse applied to a stainless steel target in an argon plasma with 1.5 mTorr gas pressure and $P_{RF} = 120$ W driving RF-power. Both pulses start at -5 μ s and end at 0.0 μ s.

- **Region 1:** Before the pulse starts, the electron density is steady in both applied pulses. Considering the error bars, both plasmas have the same electron density.
- **Region 2:** During rise time of the pulse, the electron density stays steady for both -4 kV and -1 kV pulses.
- **Region 3:** During the pulse plateau, Langmuir method analysis shows a constant electron density during both applied pulses in lower probe location within the corresponding error at each time.

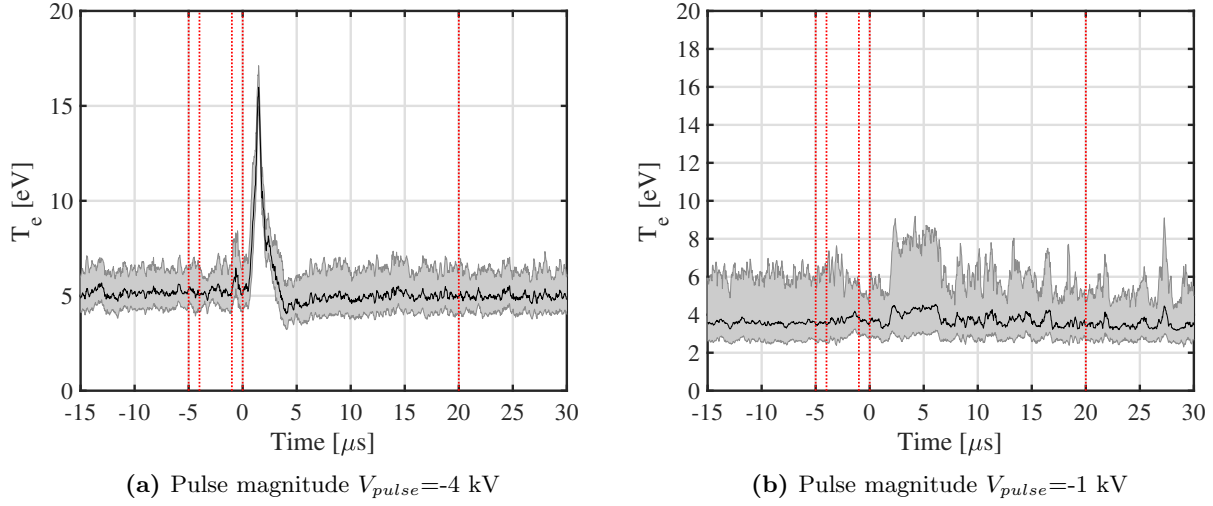


Figure 5.41: Time-resolved electron temperature, Argon plasma pressure $P_{Ar} = 1.5$ mTorr, RF-power $P_{RF} = 120$ W. The curves are acquired in different times during the cycle of a -4 kV and -1 kV, both with 5μ s duration pulse bias with repetition frequency of 250 Hz at probe location 8.7 cm above the silicon target. The grey shade indicates the error boundaries.

- **Region 4:** During the drop of the high voltage pulse, electron density in both pulse cases, remain steady.
- **Region 5:** At the same time that electron temperature rise, plasma density experiences a lower value in the case of -4 kV pulse magnitude. Plasma density drops to $3-4 \times 10^9 \text{ cm}^{-3}$ in its lowest point, occurs 2μ s after the pulse ends. The plasma density recovers to the steady state value at 5μ s after the end of the pulse, keeping the value until the next pulse. In the case of the -1 kV pulsed stainless steel target, the electron density remains the same through this region as well as the rest.
- **Region 6:** The electron density is steady in both applied pulses in this region. Considering the error bars, both plasmas have the same electron density.

Figure 5.43 compares the evolution of electron density during a -4 kV pulse and a -1 kV pulse applied to a stainless steel target in an argon plasma with 1.5 mTorr gas pressure and $P_{RF} = 120$ W driving RF-power. Both pulses start at -5μ s and end at 0.0μ s.

- **Region 1:** Before the pulse starts, the electron density is steady in both applied pulses. Considering the error bars, both plasmas have the same electron density.
- **Region 2:** During rise time of the pulse, the electron density stays steady for both -4 kV and -1 kV pulses.
- **Region 3:** During the pulse plateau, Langmuir method analysis shows a constant electron density during both applied pulses in lower probe location within the corresponding error at each time.

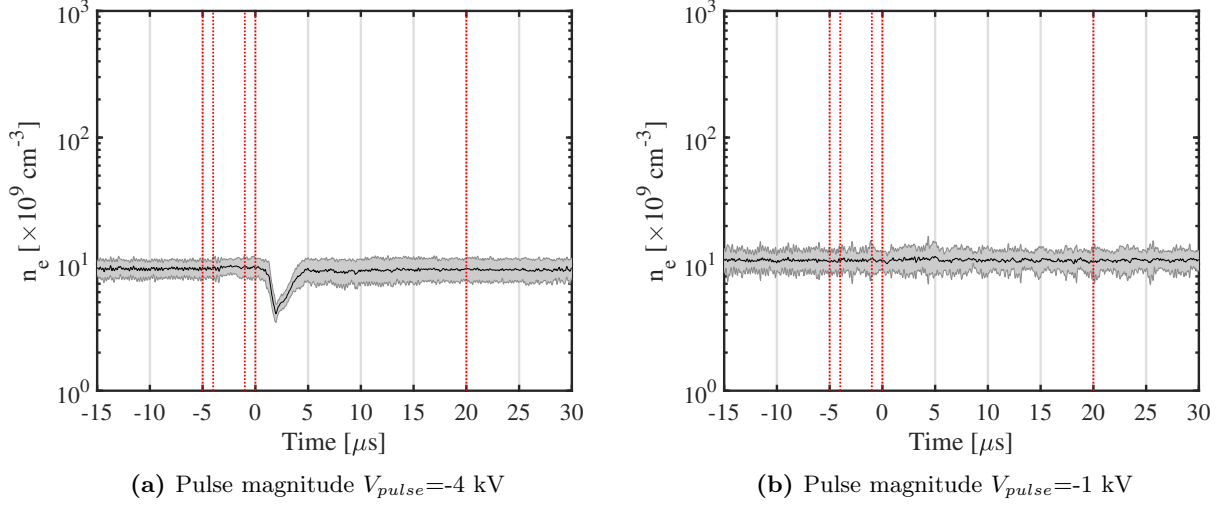


Figure 5.42: Time-resolved electron densities, Argon plasma pressure $P_{Ar} = 1.5$ mTorr, RF-power $P_{RF} = 120$ W. The curves are acquired in different times during the cycle of a -4 kV and -1 kV, both with $5 \mu s$ duration pulse bias with repetition frequency of 250 Hz at probe location 8.7 cm above the stainless steel target. The grey shade indicates the error boundaries.

- **Region 4:** During the drop of the high voltage pulse, electron density in both pulse cases, remain steady.
- **Region 5:** At the same time that electron temperature rise, plasma density experiences a lower value in the case of -4 kV pulse magnitude. Plasma density drops to $2-4 \times 10^9 \text{ cm}^{-3}$ in its lowest point, occurs $2 \mu s$ after the pulse ends. The plasma density recovers to the steady state value at $5 \mu s$ after the end of the pulse, keeping the value until the next pulse. In the case of the -1 kV pulsed silicon target, the electron density remains the same through this region as well as the rest.
- **Region 6:** The electron density is steady in both applied pulses in this region. Considering the error bars, both plasmas have the same electron density.

Similar to the plasma potential and electron temperature, plasma density is not affected by the pulse during the -1 kV pulse cycle, for both silicon and stainless steel targets. Langmuir method analysis show a constant electron density during the -1kV pulse cycle in lower probe location within the corresponding error at each time.

Figure 5.44 compares the evolution of ion density during a -4 kV pulse and a -1 kV pulse applied to a stainless steel target in an argon plasma with 1.5 mTorr gas pressure and $P_{RF} = 120$ W driving RF-power. Both pulses start at $-5 \mu s$ and end at $0.0 \mu s$.

- **Region 1:** Before the pulse starts, the ion density is steady in both applied pulses. Considering the error bars, both plasmas have the same ion density.
- **Region 2:** During rise time of the pulse, the ion density stays steady for both -4 kV and -1 kV pulses.

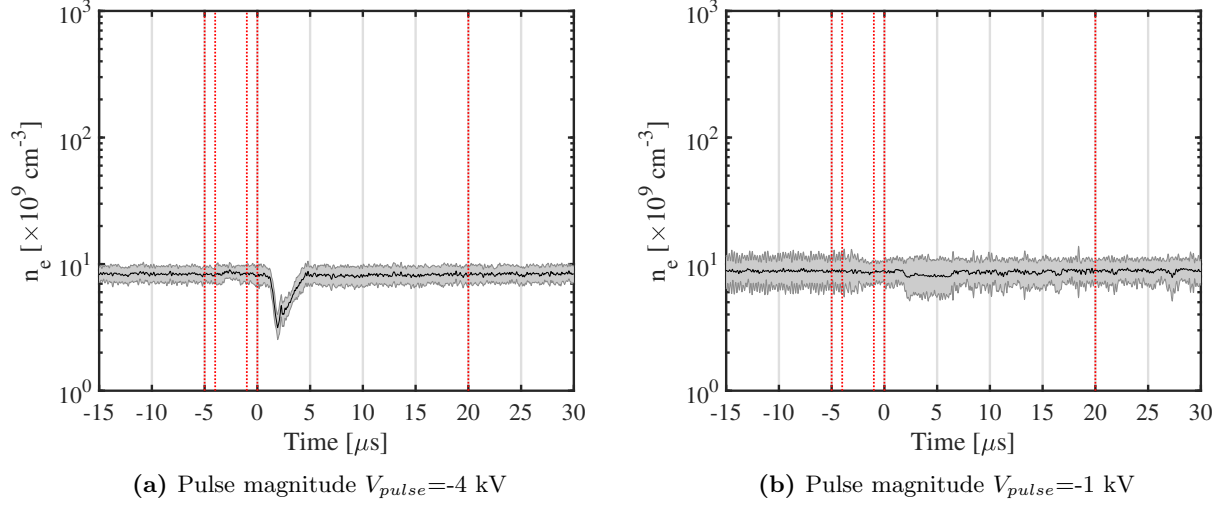


Figure 5.43: Time-resolved plasma densities, Argon plasma pressure $P_{Ar} = 1.5$ mTorr, RF-power $P_{RF} = 120$ W. The curves are acquired in different times during the cycle of a -4 kV and -1 kV, both with $5 \mu s$ duration pulse bias with repetition frequency of 250 Hz at probe location 8.7 cm above the silicon target. The grey shade indicates the error boundaries.

- **Region 3:** During the pulse plateau, Langmuir method analysis shows a drop in the ion density during both applied pulses in lower probe location within the corresponding error at each time. The dip for the -4 kV pulse is more intense than the -1 kV pulse. The local ion density barely changes in the case of -1 kV pulse.
- **Region 4:** During the drop of the high voltage pulse, ion density in both pulse cases, have their pre-pulse values.
- **Region 5:** At the same time that electron density dips, the ion density experiences a higher value in both cases. Ion density rise up to $2 \times 10^{10} \text{ cm}^{-3}$ in its highest point, occurs $2 \mu s$ after the pulse ends. The ion density recovers to the steady state value at the end of the region after the end of the pulse, keeping the value until the next pulse. In the case of the -1 kV pulsed stainless steel target, the electron density remains the same through this region as well as the rest.
- **Region 6:** The ion density is steady in both applied pulses in this region. Considering the error bars, both plasmas have the same ion density.

Figure 5.45 compares the evolution of ion density during a -4 kV pulse and a -1 kV pulse applied to a silicon target in an argon plasma with 1.5 mTorr gas pressure and $P_{RF} = 120$ W driving RF-power. Both pulses start at $-5 \mu s$ and end at $0.0 \mu s$.

- **Region 1:** Before the pulse starts, the ion density is steady in both applied pulses. Considering the error bars, both plasmas have the same ion density.
- **Region 2:** During rise time of the pulse, the ion density stays steady for both -4 kV and -1 kV pulses.

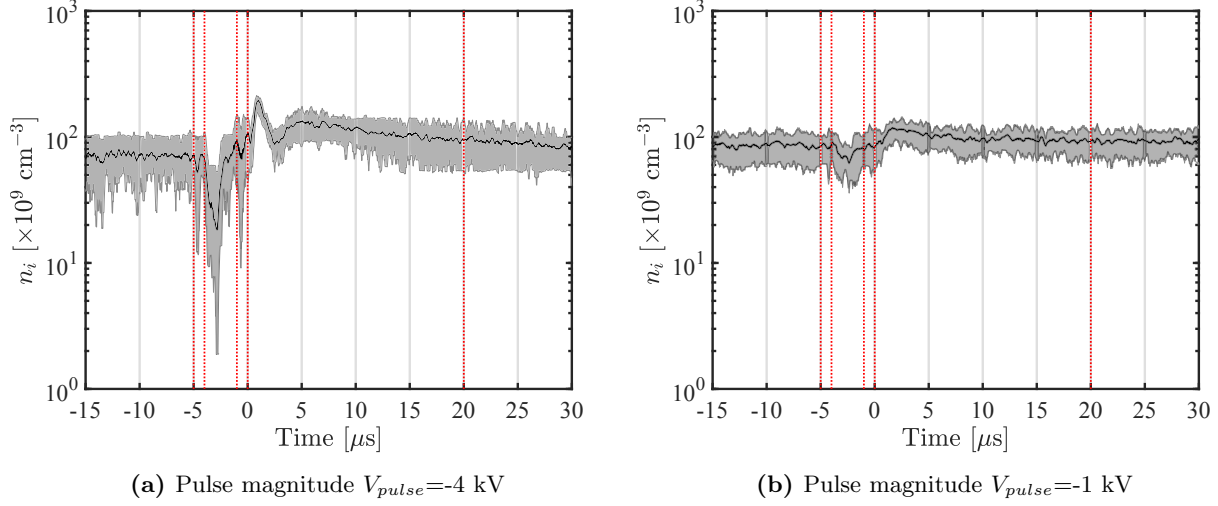


Figure 5.44: Time-resolved ion densities, Argon plasma pressure $P_{Ar} = 1.5$ mTorr, RF-power $P_{RF} = 120$ W. The curves are acquired in different times during the cycle of a -4 kV and -1 kV, both with $5 \mu s$ duration pulse bias with repetition frequency of 250 Hz at probe location 8.7 cm above the stainless steel target. The grey shade indicates the error boundaries.

- **Region 3:** During the pulse plateau, Langmuir method analysis shows a drop in the ion density during both applied pulses in lower probe location within the corresponding error at each time. The dip for the -4 kV pulse is more intense than the -1 kV pulse. The local ion density barely changes in the case of -1 kV pulse.
- **Region 4:** During the drop of the high voltage pulse, ion density in both pulse cases, have their pre-pulse values.
- **Region 5:** At the same time that electron density dips, the ion density experiences a higher value in both cases. Ion density rise up to $2 \times 10^{10} \text{ cm}^{-3}$ in its highest point, occurs $2 \mu s$ after the pulse ends. The ion density recovers to the steady state value at the end of the region after the end of the pulse, keeping the value until the next pulse.
- **Region 6:** The ion density is steady in both applied pulses in this region. Considering the error bars, both plasmas have the same ion density.

5.5.6 Study of Variable RF-Power: 120 W vs. 300 W

I present here a comparison of plasma potential, electron temperature and plasma density values between RF-powers $P_{RF} = 300$ W and a lower RF-power value of $P_{RF} = 120$ W, at a constant argon pressure of 1.5 mTorr. A -4 kV magnitude pulse with repetition frequency of 250 Hz and duration of $5 \mu s$ is applied to silicon target. The following presented measurements are acquired in the lower probe location $z_p = 8.7$ cm in order to be closer to the pulsed target.

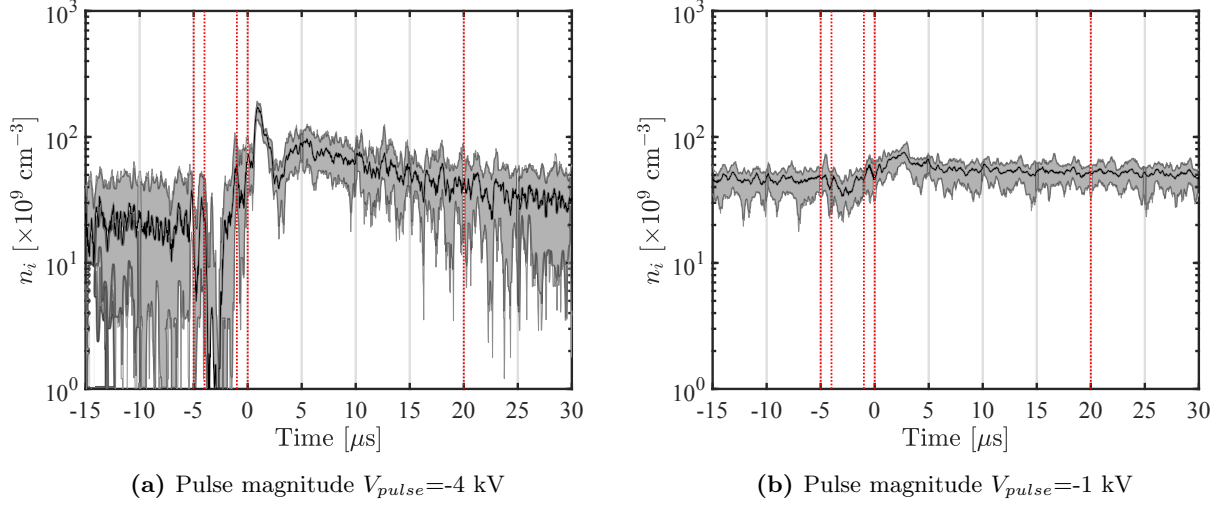


Figure 5.45: Time-resolved ion densities, Argon plasma pressure $P_{Ar} = 1.5$ mTorr, RF-power $P_{RF} = 120$ W. The curves are acquired in different times during the cycle of a -4 kV and -1 kV, both with 5 μ s duration pulse bias with repetition frequency of 250 Hz at probe location 8.7 cm above the silicon target. The grey shade indicates the error boundaries.

Plasma Potential Study of Variable RF-Power

Figure 5.46 compares the evolution of plasma potential during the cycle of -4 kV pulse applied to a silicon target between -5 μ s and 0 μ s in an argon plasma with 1.5 mTorr gas pressure and $P_{RF} = 300$ W and $P_{RF} = 120$ W driving values of RF-power.

- **Region 1:** Before the pulse starts, The plasma potential is steady in both RF-powers. Considering the error bars, the $P_{RF} = 120$ W argon plasma is in a higher plasma potential $V_p = 18$ V than the $P_{RF} = 300$ W plasma with $V_p = 16$ V plasma potential.
- **Region 2:** During rise time of the pulse, the plasma potential stays steady for both $P_{RF} = 300$ W and $P_{RF} = 120$ W plasmas.
- **Region 3:** Both plasmas, show a dip in plasma potential during the applied pulse. The dip is slightly more in the plasma with RF-power $P_{RF} = 120$ W.
- **Region 4:** During the pulse drop, the plasma potential experiences a slight increase in both cases.
- **Region 5:** The plasma potentials for both RF-power values experience a peak at about 2 μ s after the pulse ends. The plasma potential gets to a high point between 40 V to 50 V for $P_{RF} = 120$ W, and then starts to relax back to its steady state value of 19 V. In the shown time window, the relaxation is not 100% but gets very close to the pre-pulse value after ~ 15 μ s. The increase for the first post pulse peak in plasma potential is about 1 V with respect to its pre-pulse value. The relaxation time is in the order of the length of this region.

- **Region 6:** The plasma potential continues the relaxation back to its steady state in this region for 120 W RF-power. The plasma potential in the case of 300 W driving RF-power stays in the recovered pre-pulse value in this region.

To summarise, the plasma potential is affected minimally by the pulse in $P_{RF} = 300$ W. Langmuir method analysis shows a slight reduction of the plasma potential during the applied pulse and then a slightly higher plasma potential after the pulse which relaxes to the steady state with a smooth slope until $\sim 10 \mu s$. The plasma driven by 120 W RF-power, shows a much higher potential drop during the pulse, and also a 20 to 30 V plasma potential enhancement compared to >1 V enhancement in $P_{RF} = 300$ W plasma.

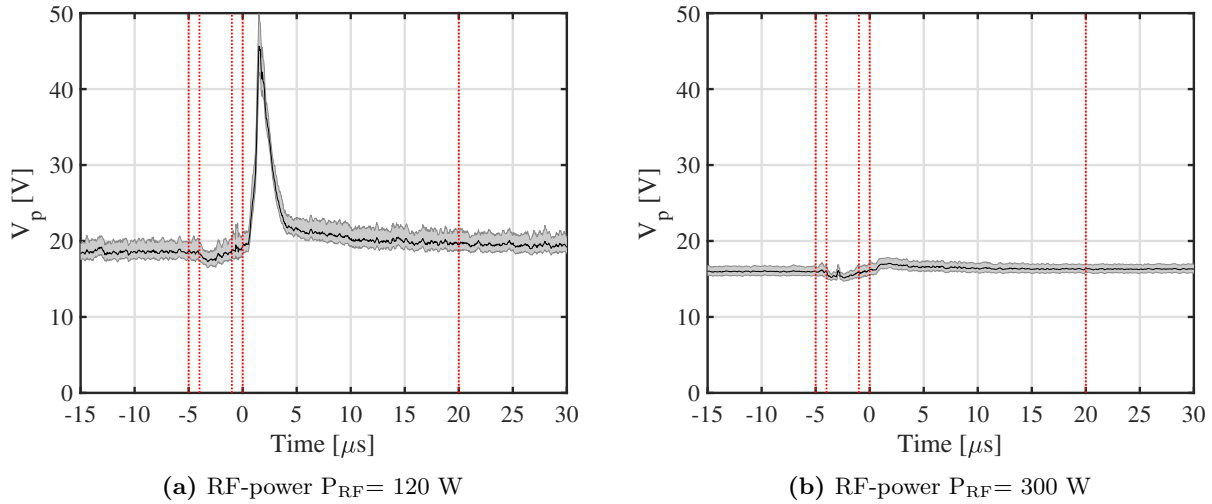


Figure 5.46: Time-resolved plasma potentials, Argon plasma pressure $P_{Ar} = 1.5$ mTorr. The curves are acquired in different times during the cycle of a -4 kV with $5 \mu s$ duration pulse bias with repetition frequency of 250 Hz at probe location 8.7 cm above the silicon target. The pulse starts at $t = -5 \mu s$ and ends at $t = 0 \mu s$. The grey shade indicates the error boundaries.

Electron Temperature Study of Variable RF-Power

Figure 5.47 compares the evolution of electron temperature during the cycle of -4 kV pulse applied to a silicon target between $-5 \mu s$ and $0 \mu s$ in an argon plasma with 1.5 mTorr gas pressure and $P_{RF} = 300$ W and $P_{RF} = 120$ W driving values of RF-power.

- **Region 1:** Before the pulse starts, The electron temperature is steady in both RF-powers. Considering the error bars, the $P_{RF} = 120$ W argon plasma is in a higher electron temperature $T_e = 4-6$ eV than the $P_{RF} = 300$ W plasma with $T_e \approx 3-4$ eV electron temperature.
- **Region 2:** During rise time of the pulse, the electron temperature stays steady for both $P_{RF} = 300$ W and $P_{RF} = 120$ W plasmas.
- **Region 3:** Both plasmas, have the same electron temperatures as their steady states considering the error bars.

- **Region 4:** During the pulse drop, the electron temperatures remains the same in both plasmas.
- **Region 5:** The electron temperature for $P_{\text{RF}}= 120$ W RF-power experiences a peak at about $2 \mu\text{s}$ after the pulse ends. The electron temperature gets to a high point between 15-17 eV for $P_{\text{RF}}= 120$ W, and then starts to relax back to its steady state value of 4-6 eV. This value relaxes back to the pre-pulse value at $t=5 \mu\text{s}$. In the plasma driven by $P_{\text{RF}}= 300$ W RF-power, the electron temperature shows no change in value through this region.
- **Region 6:** Both plasmas have the same pre-pulse electron temperatures in this region and will remain the same until next pulse.

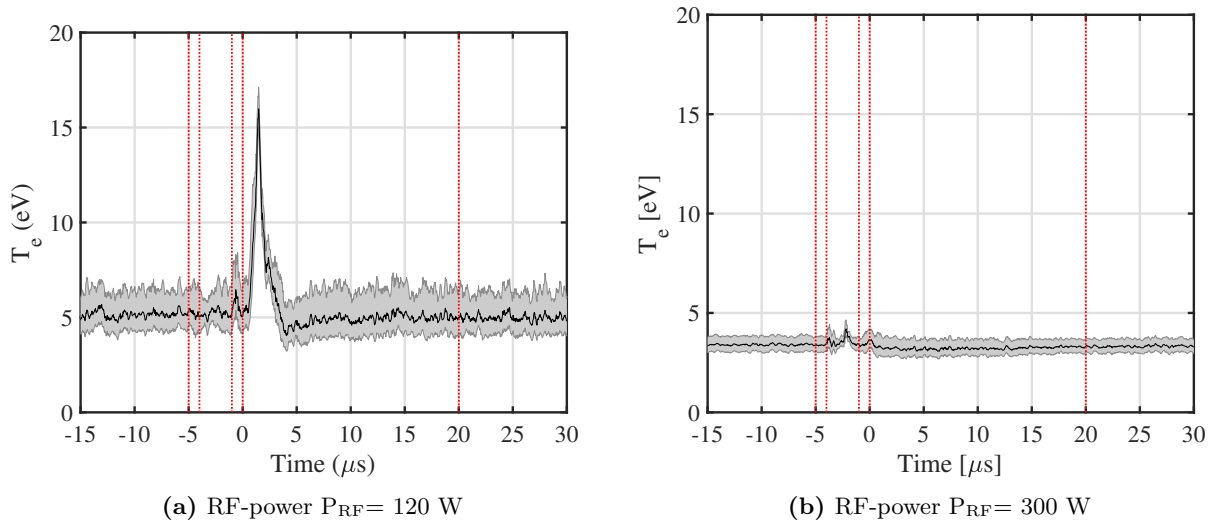


Figure 5.47: Time-resolved electron temperatures, Argon plasma pressure $P_{\text{Ar}}= 1.5$ mTorr. The curves are acquired in different times during the cycle of a -4 kV with $5 \mu\text{s}$ duration pulse bias with repetition frequency of 250 Hz at probe location 8.7 cm above the silicon target. The pulse starts at $t=-5 \mu\text{s}$ and ends at $t=0 \mu\text{s}$.

Plasma Density Study of Variable RF-Power

Figure 5.48 compares the evolution of electron density during the cycle of -4 kV pulse applied to a silicon target between $-5 \mu\text{s}$ and $0 \mu\text{s}$ in an argon plasma with 1.5 mTorr gas pressure and $P_{\text{RF}}= 300$ W and $P_{\text{RF}}= 120$ W driving values of RF-power.

- **Region 1:** Before the pulse starts, Langmuir method analysis show a constant plasma density during the pulse in lower probe location within the corresponding error at each time. The density value of the $P_{\text{RF}}= 300$ W plasma in the pre-pulse region is about $3 \times 10^{10} \text{ cm}^{-3}$, more than 3 times higher than the electron density of the $P_{\text{RF}}= 120$ W plasma.
- **Region 2:** During rise time of the pulse, the electron density stays steady for both $P_{\text{RF}}= 300$ W and $P_{\text{RF}}= 120$ W plasmas.

- **Region 3:** Both plasmas, have the same electron densities as their pre-pulse values considering the error bars.
- **Region 4:** During the pulse drop, the electron densities remains the same in both plasmas.
- **Region 5:** The electron density for $P_{\text{RF}}=120$ W RF-power experiences a drop at about $2 \mu\text{s}$ after the pulse ends. The electron density gets to a low point of $2\text{-}4 \times 10^9 \text{ cm}^{-3}$ for $P_{\text{RF}}=120$ W plasma, and then relaxes back to its pre-pulse value at $t=5 \mu\text{s}$. In the plasma driven by $P_{\text{RF}}=300$ W RF-power, the electron density shows no change in value through this region.
- **Region 6:** Both plasmas have the same pre-pulse electron density values in this region.

Unlike the minimal affect of the pulse on the plasma potential and electron temperature with 300 W RF-drive, plasma density is not affected by the pulse in this RF-power. Langmuir method analysis show a constant plasma density during the pulse in lower probe location within the corresponding error at each time. The density value of the $P_{\text{RF}}=300$ W plasma in the pre-pulse region is more than 3 times higher than the electron density in the steady state of the $P_{\text{RF}}=120$ W plasma. This higher plasma density shields the effects of the high voltage pulse in the plasma bulk.

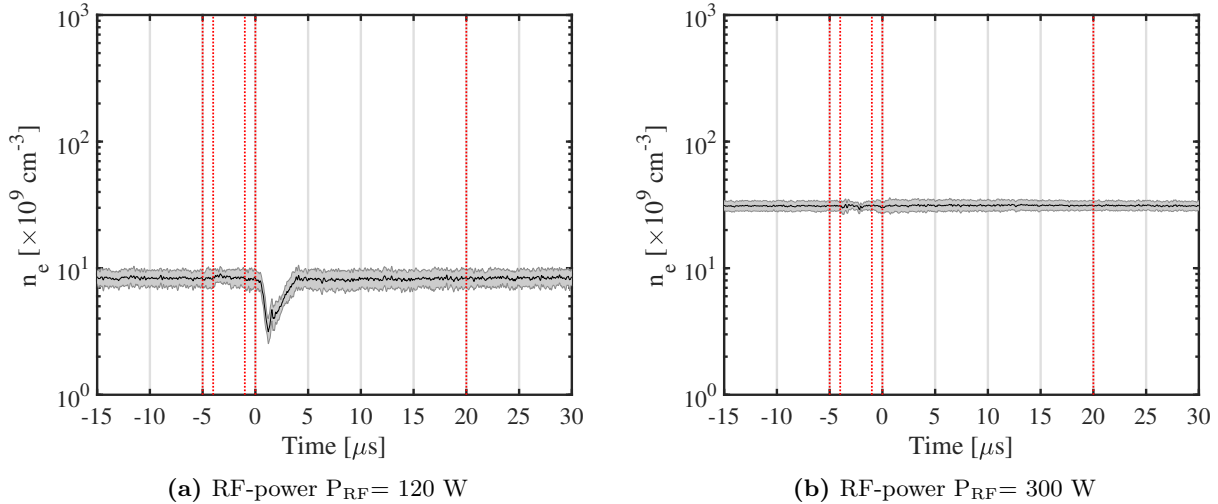


Figure 5.48: Time-resolved plasma potentials, Argon plasma pressure $P_{\text{Ar}}=1.5$ mTorr. The curves are acquired in different times during the cycle of a -4 kV with $5 \mu\text{s}$ duration pulse bias with repetition frequency of 250 Hz at probe location 8.7 cm above the silicon target. The pulse starts at $t=-5 \mu\text{s}$ and ends at $t=0 \mu\text{s}$. The grey shade indicates the error boundaries.

Figure 5.49 compares the evolution of ion density during the cycle of -4 kV pulse applied to a silicon target between $-5 \mu\text{s}$ and $0 \mu\text{s}$ in an argon plasma with 1.5 mTorr gas pressure and $P_{\text{RF}}=300$ W and $P_{\text{RF}}=120$ W driving values of RF-power.

- **Region 1:** Before the pulse starts, OML method analysis show a constant ion density during the pulse in lower probe location within the corresponding error at each time. The density value of the $P_{\text{RF}}=$

300 W plasma in the pre-pulse region is more than the plasma driven by 120 W RF-power.

- **Region 2:** During rise time of the pulse, the ion density stays steady for both $P_{\text{RF}}= 300$ W and $P_{\text{RF}}= 120$ W plasmas.
- **Region 3:** During the pulse plateau, Langmuir method analysis shows a drop in the ion density during the applied pulses in lower probe location within the corresponding error at each time. Though the ion saturation current recorded is in the resolution limit of the oscilloscope, thus the values are not reliable in this region.
- **Region 4:** During the drop of the high voltage pulse, ion density in $P_{\text{RF}}= 300$ W plasma, shows a rise in this region, however the $P_{\text{RF}}= 120$ W plasma has the same ion density as the pre-pulse value within the error bars.
- **Region 5:** At the same time that electron density dips, the ion density experiences a higher value in both cases. Ion density rise up to a value between $1\text{-}2 \times 10^{10} \text{ cm}^{-3}$ in its highest point, occurs $2 \mu\text{s}$ after the pulse ends. The ion density recovers to the steady state value at the end of the region after the end of the pulse, keeping the value until the next pulse.
- **Region 6:** The ion density is steady in both applied pulses in this region. Considering the error bars, both plasmas have the same ion density.

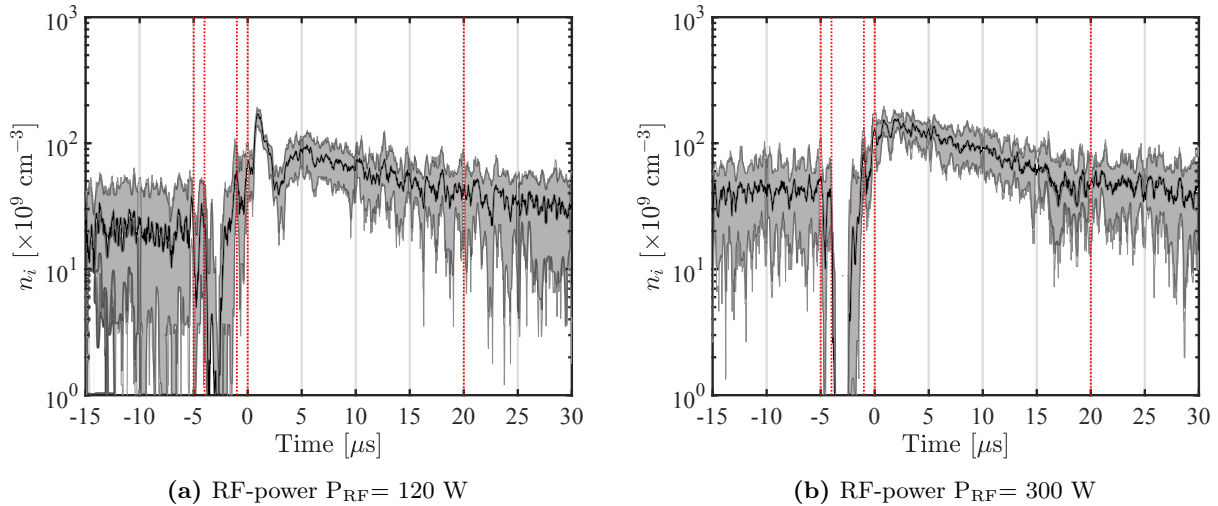


Figure 5.49: Time-resolved ion densities, Argon plasma pressure $P_{\text{Ar}}= 1.5$ mTorr. The curves are acquired in different times during the cycle of a -4 kV with $5 \mu\text{s}$ duration pulse bias with repetition frequency of 250 Hz at probe location 8.7 cm above the silicon target. The pulse starts at $t=-5 \mu\text{s}$ and ends at $t=0 \mu\text{s}$. The grey shade indicates the error boundaries.

5.5.7 Study of Variable Argon Gas Pressure: 1.5 mTorr vs. 25 mTorr

Figure 5.50 shows a family of I-V curves acquired in $P_{Ar} = 25$ mTorr argon pressure and RF-power of $P_{RF} = 120$ W. Notice that the plasma potential is not reached after the pulse ends. The highest sweep bias voltage was 50V due to several limitations. The RF-compensated probe had a limitation of 120 mA current saturation for the components. Additionally, at 5 V above this value, the probe's tip was starting to glow. The probe should not be operated in electron saturation regime for a long time, as the tip might get damaged [19]. As the values obtained for plasma potential, electron temperature and electron density are not reliable in this region, they will not be presented.

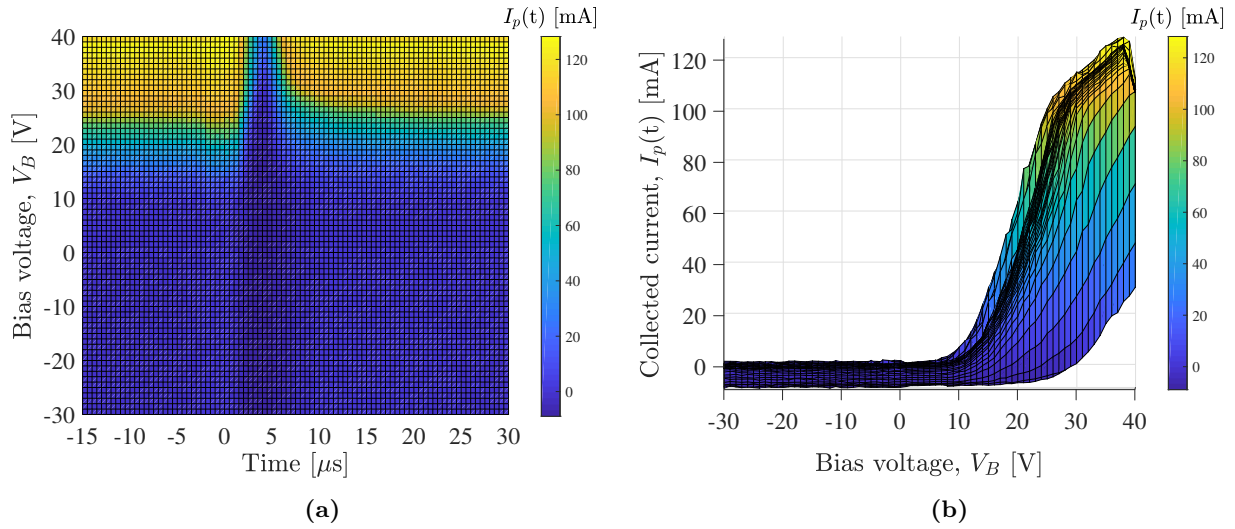


Figure 5.50: Time-resolved I-V characteristic curves, Argon plasma pressure $P_{Ar} = 25$ mTorr, RF-power $P_{RF} = 120$ W. The curves are acquired in different times during the cycle of a -4 kV with 5 μ s duration pulse bias with repetition frequency of 250 Hz at probe location 21.7 cm above silicon and stainless steel targets. The pulse starts at $t = -5$ μ s and ends at $t = 0$ μ s. (a) A top view of the curves, showing plasma potential as a function of time. The colourbar determines the current going through the probe at each time-probe bias point in the plot. Colour-bar units are in mA. (b) A side view of the same family of curves. Notice the much lower I-V curves after the pulse. These curves don't reach electron saturation, thus plasma potential cannot be determined in their cases.

5.5.8 Case Study of Silicon and Stainless Steel Targets - $P_{Ar} = 1.5$ mTorr, $P_{RF} = 120$ W

In this subsection a full Langmuir analysis of argon plasma during a -4 kV pulse with duration of 5 μ s and the repetition frequency of 250 Hz applied to silicon and stainless steel targets will be presented. The time resolved Langmuir analysis results for plasma potential, electron temperature and electron density presented here are acquired in two probe locations on the axis of the chamber, vertically separated by $\delta z_p = 13.0$ cm.

Plasma Potentials - Upper Probe Location

Figure 5.51 compares the plasma potentials in the upper probe location for two targets.

- **Region 1:** The plasma potentials in the upper location have the same 21-22 V value within their error bars before the pulse.
- **Region 2:** During rise time of the pulse, the plasma potential for both targets remain the same.
- **Region 3:** During the high voltage plateau, the potential drops slightly for both plasmas.
- **Region 4:** During fall time of the pulse, the plasma potential for stainless steel is still in its dip, while the plasma potential in the plasma with silicon target starts to increase slightly.
- **Region 5:** After the pulse, the plasma potential peaks to a value about 39-42 V for both plasmas at about $t= 2 \mu s$, and then start to relax back to their pre-pulse values. The relaxation is not 100% in this region for both targets.
- **Region 6:** In this region, both plasmas are still in the relaxation of their post-pulse-peak in the potentials. The values are the same in each time for both plasmas, within their error bars.

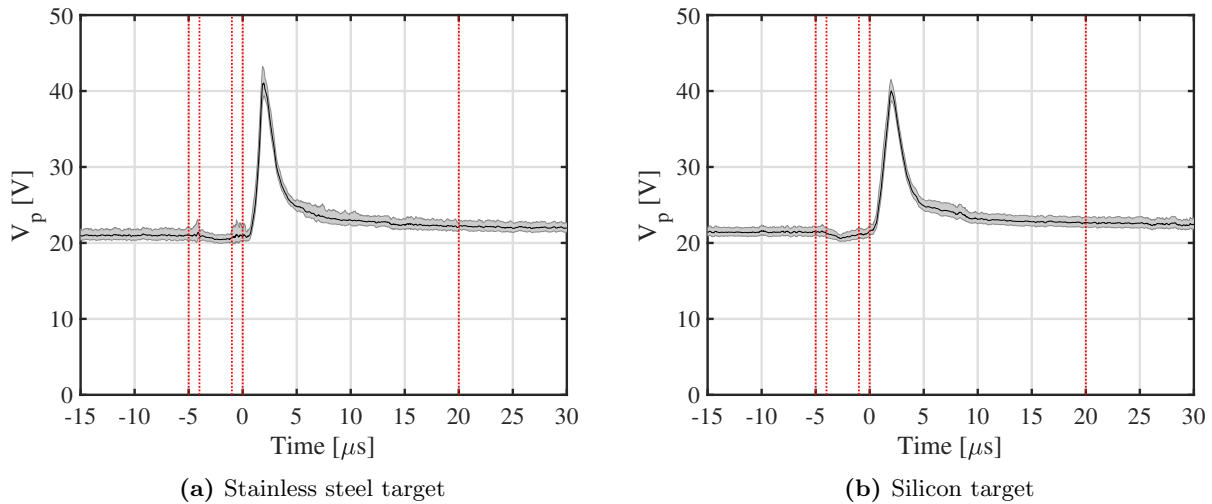


Figure 5.51: Time-resolved I-V characteristic curves, Argon plasma pressure $P_{Ar} = 1.5$ mTorr, RF-power $P_{RF} = 120$ W. The curves are acquired in different times during the cycle of a -4 kV with 5 μs duration pulse bias with repetition frequency of 250 Hz at probe location 21.7 cm above silicon and stainless steel targets. The pulse starts at $t = -5 \mu s$ and ends at $t = 0 \mu s$.

Plasma Potentials - Lower Probe Location

Figure 5.52 compares the plasma potentials in the lower probe location for silicon and stainless steel targets. The plasma potentials in the lower location are the same within their errors before the pulse, in their steady

state with a value slightly lower than 20 V and during the pulse, when the potential drops slightly for both plasmas. However, unlike the upper plasma,

- **Region 1:** The plasma potentials in the lower location have the same 21-22 V value within their error bars before the pulse.
- **Region 2:** During rise time of the pulse, the plasma potential for both targets remain the same.
- **Region 3:** During the high voltage plateau, the potential drops slightly for both plasmas.
- **Region 4:** During fall time of the pulse, the plasma potential for stainless steel is still in its dip, while the plasma potential in the plasma with silicon target starts to increase slightly.
- **Region 5:** After the pulse, the plasma potential peaks differently for two targets. The plasma with stainless steel target immersed, shows about the same peak as the upper location, about 40 V. Plasma with pulsed silicon target however, experiences a potential peak between 39-50 V, which is at the higher end of the sweep bias voltage of the probe.
- **Region 6:** In this region, both plasmas are still in the relaxation of their post-pulse-peak in the potentials. The values are the same in each time for both plasmas, within their error bars.

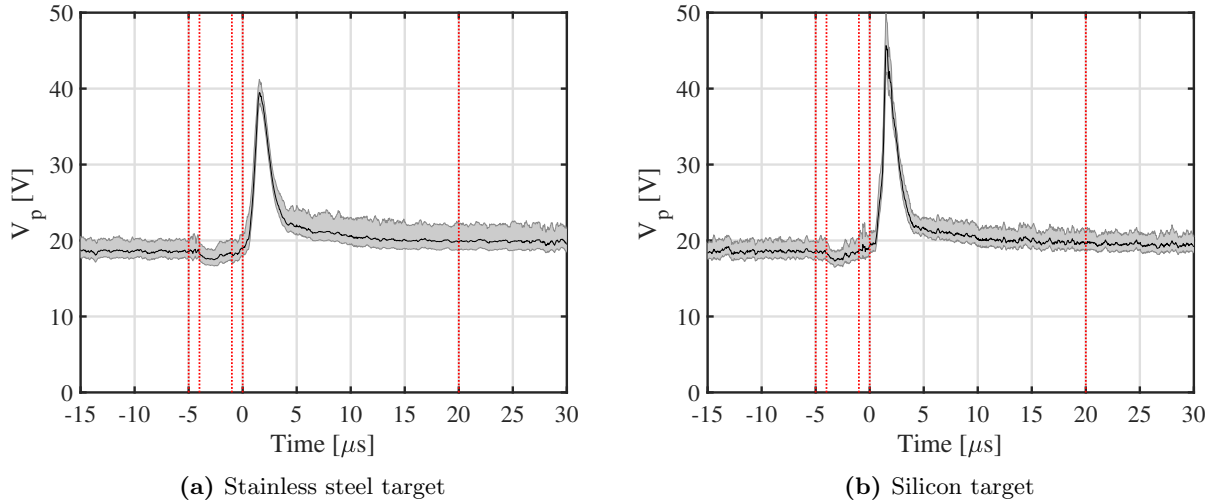


Figure 5.52: Time-resolved plasma potentials, Argon plasma pressure $P_{Ar} = 1.5$ mTorr, RF-power $P_{RF} = 120$ W. The curves are acquired in different times during the cycle of a -4 kV with 5 μ s duration pulse bias with repetition frequency of 250 Hz at probe location 8.7 cm above silicon and stainless steel targets. The pulse starts at $t = -5$ μ s and ends at $t = 0$ μ s. The grey shade indicates the error boundaries.

Electron Temperature - Upper Probe Location

Figure 5.53 compares electron temperatures in the upper probe location for two targets.

- **Region 1:** The electron temperatures at the upper location have the same 3.5-5 eV value within their error bars before the pulse.
- **Region 2:** During rise time of the pulse, the electron temperature for both targets remain the same.
- **Region 3:** During the high voltage plateau, the electron temperature for both targets remain the same within the error bars. In the middle of the pulse, the silicon target shows a slight increase in electron temperature, which can still be considered to be as same as pre-pulse value within the error bars.
- **Region 4:** During rise time of the pulse, the electron temperatures for both targets remain the same within the error bars.
- **Region 5:** After the pulse, the electron temperatures peak for two targets at about $t= 2 \mu\text{s}$. The plasma with stainless steel target immersed, shows an electron temperature PPP value of about 11-14 eV. Electrons in the plasma with pulsed silicon target however, experiences a temperature peak between 10.5-13 eV. The peak values can be assumed the same for both targets. This high temperature electrons are cooling down to the pre-pulse electron temperature values at about $t=5 \mu\text{s}$ after the end of the pulse.
- **Region 6:** In this region, both plasmas have the same steady, pre-pulse electron temperature values.

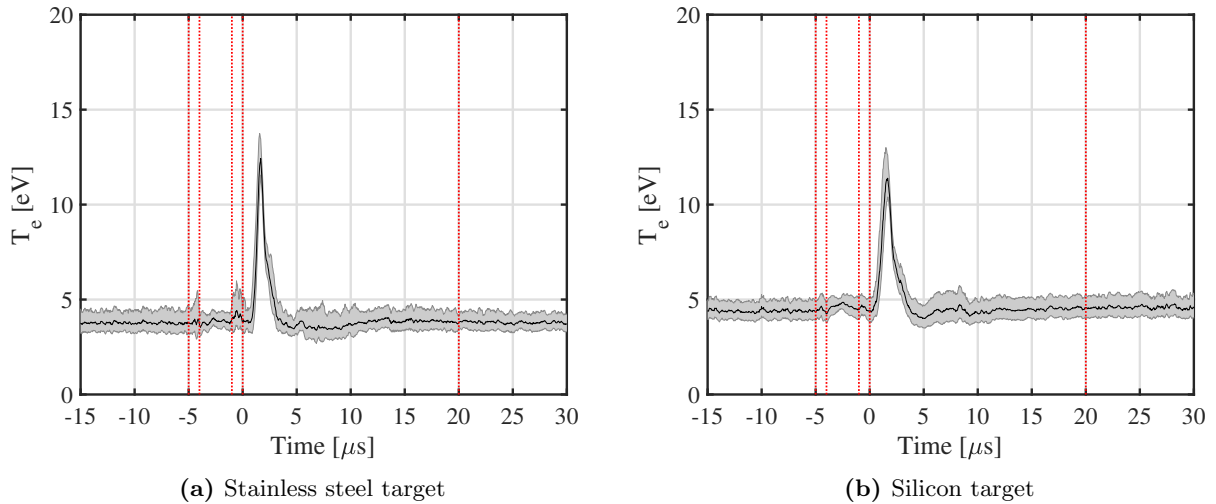


Figure 5.53: Time-resolved electron temperatures, Argon plasma pressure $P_{Ar} = 1.5 \text{ mTorr}$, RF-power $P_{RF} = 120 \text{ W}$. The curves are acquired in different times during the cycle of a -4 kV with $5 \mu\text{s}$ duration pulse bias with repetition frequency of 250 Hz at probe location 21.7 cm above silicon and stainless steel targets. The pulse starts at $t = -5 \mu\text{s}$ and ends at $t = 0 \mu\text{s}$. The grey shade indicates the error boundaries.

Electron Temperature - Lower Probe Location

- **Region 1:** The electron temperatures at the lower location have the same 4-6 eV value within their error bars before the pulse.
- **Region 2:** During rise time of the pulse, the electron temperature for both targets remain the same.
- **Region 3:** During the high voltage plateau, the electron temperature for both targets remain the same within the error bars. In the middle of the pulse, the silicon target shows a slight increase in electron temperature, which can still considered to be as same as pre-pulse value within the error bars.
- **Region 4:** During rise time of the pulse, the electron temperatures for both targets remain the same within the error bars.
- **Region 5:** After the pulse, the electron temperatures peaks for two targets at about $t = 2 \mu\text{s}$. The plasma with stainless steel target immersed, shows an electron temperature PPP value of about 11-13 eV, almost the same as its upper location PPP value. Electrons in the lower location plasma with pulsed silicon target however, experiences a higher temperature peak between 14-17 eV. Note that because of the limitation in determining plasma potential values above 40 V, this value cannot be trusted 100%.
- **Region 6:** In this region, both plasmas have the same steady, pre-pulse electron temperature values.

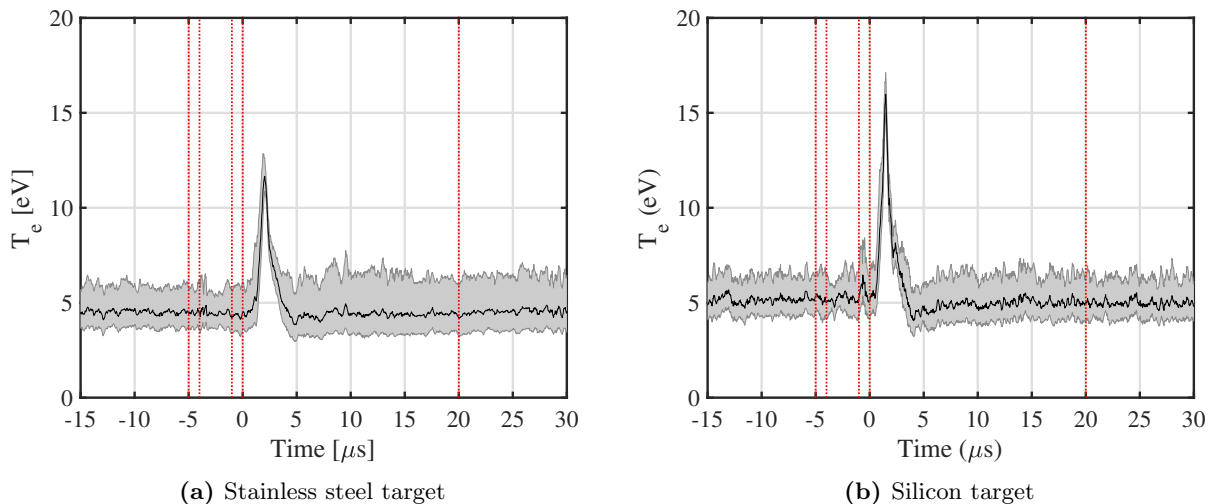


Figure 5.54: Time-resolved electron temperatures, Argon plasma pressure $P_{Ar} = 1.5$ mTorr, RF-power $P_{RF} = 120$ W. The curves are acquired in different times during the cycle of a -4 kV with $5 \mu\text{s}$ duration pulse bias with repetition frequency of 250 Hz at probe location 8.7 cm above silicon and stainless steel targets. The pulse starts at $t = -5 \mu\text{s}$ and ends at $t = 0 \mu\text{s}$. The grey shade indicates the error boundaries.

Plasma Density - Upper Probe Location

Figure 5.55 shows electron density evolution for both plasmas with pulsed silicon and pulsed stainless steel targets in the upper probe location.

- **Region 1:** The electron densities at the upper location have the same $3\text{-}4 \times 10^{10} \text{ cm}^{-3}$ value within their error bars before the pulse.
- **Region 2:** During rise time of the pulse, the electron density for both targets remain the same.
- **Region 3:** During the high voltage plateau, the electron density for both targets remain the same within the error bars.
- **Region 4:** During rise time of the pulse, the electron density for both targets remains the same within the error bars.
- **Region 5:** After the pulse, the electron density experiences a dip for two targets at about $t = 2 \mu\text{s}$. The plasma with stainless steel and silicon targets immersed, show an electron density drop to about $0.9\text{-}1 \times 10^{10} \text{ cm}^{-3}$ value. The electron densities are recovered to the pre-pulse value at $5 \mu\text{s}$ after the pulse.
- **Region 6:** In this region, both plasmas have the same steady, pre-pulse electron density values.

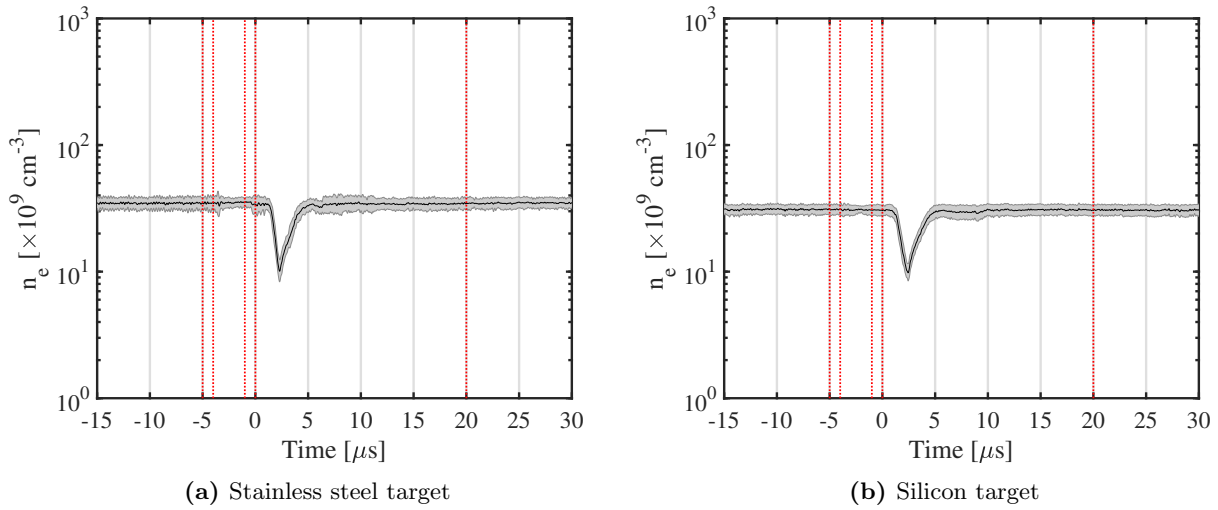


Figure 5.55: Time-resolved plasma densities, Argon plasma pressure $P_{\text{Ar}} = 1.5 \text{ mTorr}$, RF-power $P_{\text{RF}} = 120 \text{ W}$. The curves are acquired in different times during the cycle of a -4 kV with $5 \mu\text{s}$ duration pulse bias with repetition frequency of 250 Hz at probe location 21.7 cm above silicon and stainless steel targets. The pulse starts at $t = -5 \mu\text{s}$ and ends at $t = 0 \mu\text{s}$. The grey shade indicates the error boundaries.

Figure 5.56 shows ion density evolution for both plasmas with pulsed silicon and pulsed stainless steel targets in the upper probe location.

- **Region 1:** Before the pulse starts, OML method analysis show a constant ion density during the pulse in lower probe location within the corresponding error at each time. The density value of the plasma with stainless steel target is slightly higher than the plasma with immersed silicon target, in the pre-pulse region, but also can be considered as equal within the error limits, having the density between $9-10 \times 10^9 \text{ cm}^{-3}$.
- **Region 2:** During rise time of the pulse, the ion density remains the same for both targets.
- **Region 3:** During the pulse plateau, Langmuir method analysis shows a drop in the ion density during both applied pulses in lower probe location within the corresponding error at each time. Though due to the resolution limit of the oscilloscope, the ion densities are recorded very close to zero in the plasma with silicon target, showing a value less than $2 \times 10^9 \text{ cm}^{-3}$. However, the values are not reliable in this region. The ion density for stainless steel target is down to a value between $0.1-3.5 \times 10^9 \text{ cm}^{-3}$ in this region.
- **Region 4:** During the drop of the high voltage pulse, ion densities are rising, but still lower than the pre-pulse values in both plasmas.
- **Region 5:** At the same time that electron density dips, the ion density experiences a higher value in both cases. Ion density rise up to a value of $4 \times 10^{10} \text{ cm}^{-3}$ in its highest point, occurs $2 \mu\text{s}$ after the pulse ends. The ion density recovers to the steady state value at the end of the region, and then keeping the pre-pulse value until the next pulse.
- **Region 6:** The ion density is steady in both applied pulses in this region. Considering the error bars, both plasmas have the same ion density.

Plasma Density - Lower Probe Location

Figure 5.57 shows electron density evolution for both plasmas with pulsed silicon and pulsed stainless steel targets in the lower probe location.

- **Region 1:** The electron densities at the lower location have the same $9-10 \times 10^9 \text{ cm}^{-3}$ value within their error bars before the pulse. This value is about 4 times lower than their upper plasma electron densities.
- **Region 2:** During rise time of the pulse, the electron density for both targets remain the same.
- **Region 3:** During the high voltage plateau, the electron density for both targets remain the same within the error bars.
- **Region 4:** During rise time of the pulse, the electron density for both targets remains the same within the error bars.

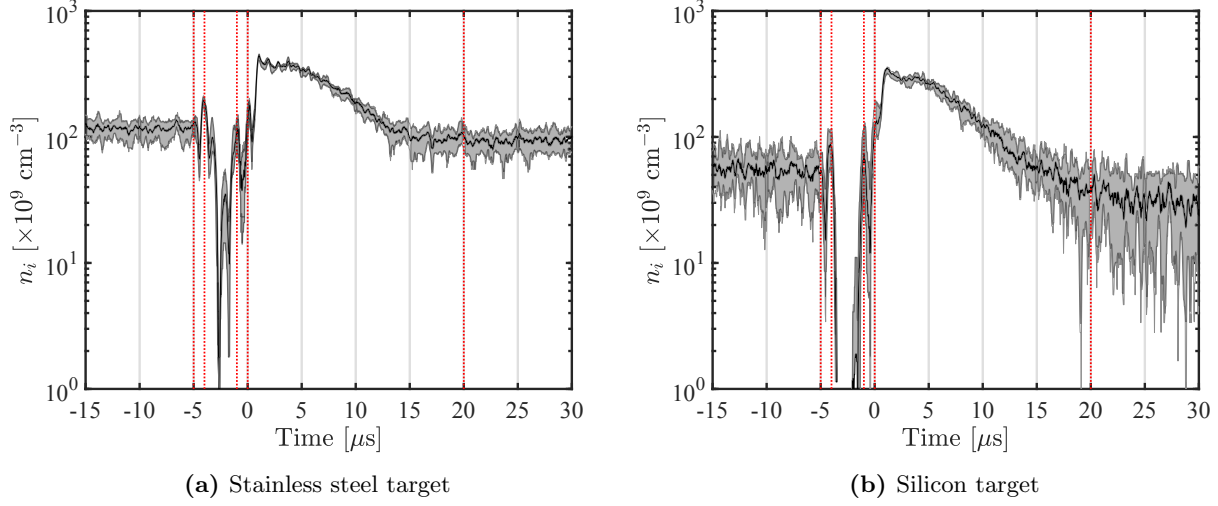


Figure 5.56: Time-resolved ion densities, Argon plasma pressure $P_{Ar} = 1.5$ mTorr, RF-power $P_{RF} = 120$ W. The curves are acquired in different times during the cycle of a -4 kV with $5 \mu s$ duration pulse bias with repetition frequency of 250 Hz at probe location 21.7 cm above silicon and stainless steel targets. The pulse starts at $t = -5 \mu s$ and ends at $t = 0 \mu s$. The grey shade indicates the error boundaries.

- **Region 5:** After the pulse, the electron density experiences a dip for two targets at about $t = 2 \mu s$. However, unlike the upper plasma the drop values for different targets cannot be assumed the same within their analysis error boundaries. Plasma with pulsed stainless target experiences a drop to a value between $4-5 \times 10^9 \text{ cm}^{-3}$ while the plasma with pulsed silicon target shows a drop to a value between $2-4 \times 10^9 \text{ cm}^{-3}$ in their electron density. The electron densities recover to the pre-pulse values at about $t = 5 \mu s$ after the pulse ends.
- **Region 6:** In this region, both plasmas have the same steady, pre-pulse electron density values.

Figure 5.58 shows ion density evolution for both plasmas with pulsed silicon and pulsed stainless steel targets in the lower probe location.

- **Region 1:** Before the pulse starts, OML method analysis show a constant ion density during the pulse in lower probe location within the corresponding error at each time. The density value of the plasma with stainless steel target is slightly higher than the plasma with immersed silicon target, in the pre-pulse region, but also can be considered as equal within the error limits, having the density between $3-5 \times 10^9 \text{ cm}^{-3}$.
- **Region 2:** During rise time of the pulse, the ion density remains the same for both targets.
- **Region 3:** During the pulse plateau, Langmuir method analysis shows a drop in the ion density during both applied pulses in lower probe location within the corresponding error at each time. Though due to the resolution limit of the oscilloscope, the ion densities are recorded very close to zero in the plasma

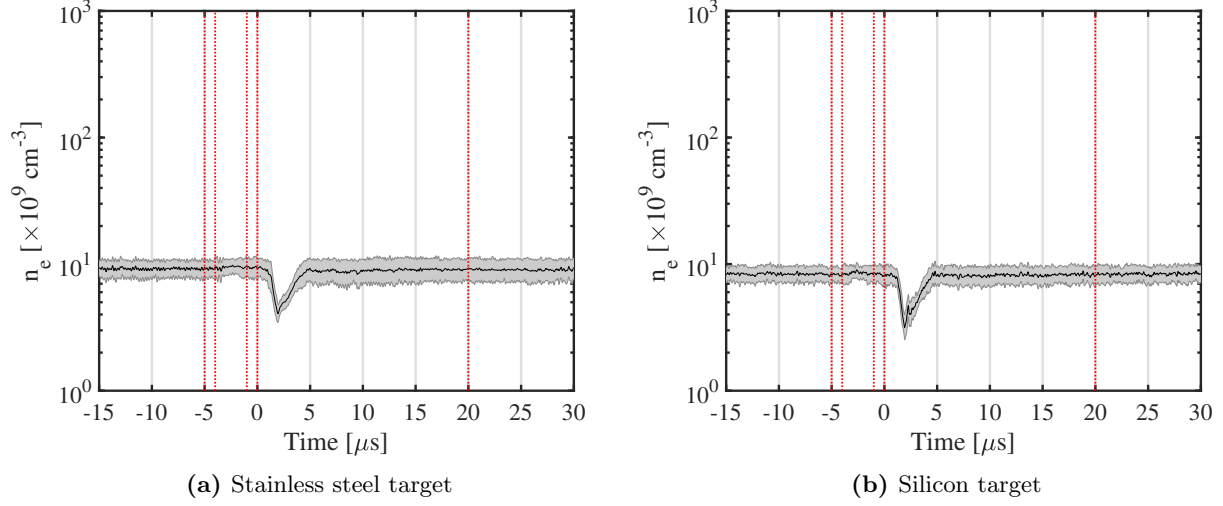


Figure 5.57: Time-resolved electron densities, Argon plasma pressure $P_{Ar} = 1.5$ mTorr, RF-power $P_{RF} = 120$ W. The curves are acquired in different times during the cycle of a -4 kV with $5 \mu s$ duration pulse bias with repetition frequency of 250 Hz at probe location 8.7 cm above silicon and stainless steel targets. The pulse starts at $t = -5 \mu s$ and ends at $t = 0 \mu s$. The grey shade indicates the error boundaries.

with silicon target, showing a value less than $2 \times 10^9 \text{ cm}^{-3}$. However, the values are not reliable in this region. The ion density for stainless steel target is down to a value between $0.1\text{-}3.5 \times 10^9 \text{ cm}^{-3}$ in this region.

- **Region 4:** During the drop of the high voltage pulse, ion densities are rising, but still lower than the pre-pulse values in both plasmas.
- **Region 5:** At the same time that electron density dips, the ion density experiences a higher value in both cases. Ion density rise up to a value between $1\text{-}2 \times 10^{10} \text{ cm}^{-3}$ in its highest point, occurs $2 \mu s$ after the pulse ends. The ion density recovers to the steady state value at the end of the region, and then keeping the pre-pulse value until the next pulse.
- **Region 6:** The ion density is steady in both applied pulses in this region. Considering the error bars, both plasmas have the same ion density.

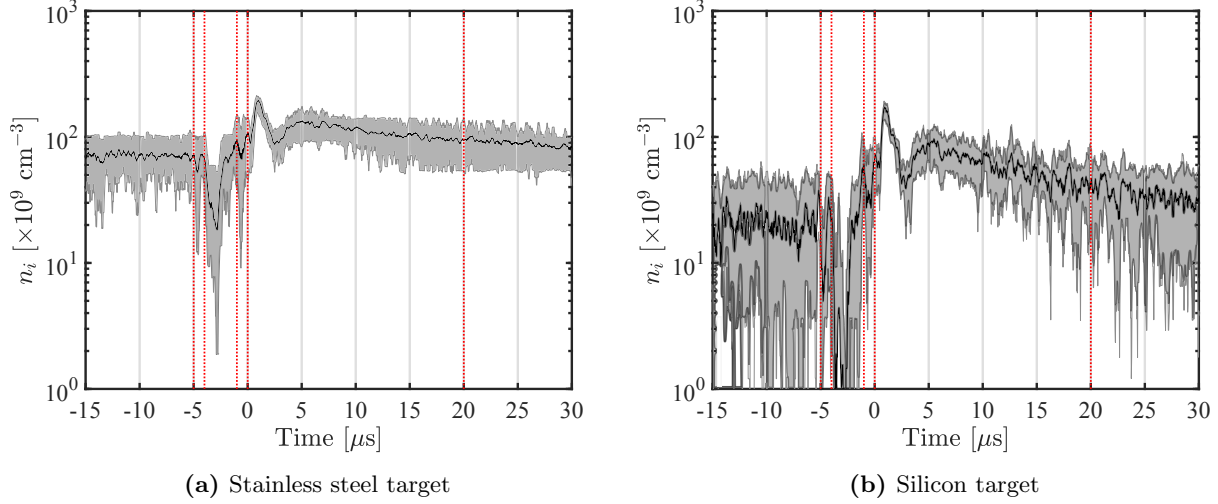
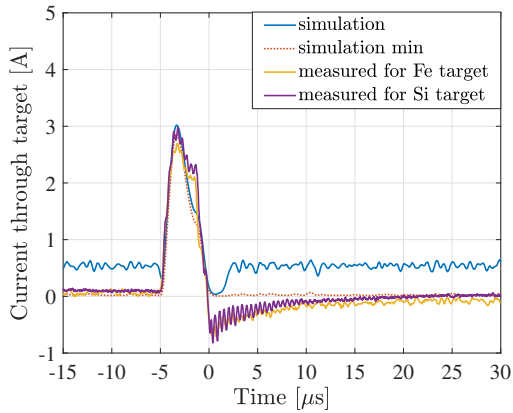


Figure 5.58: Time-resolved ion densities, Argon plasma pressure $P_{Ar} = 1.5$ mTorr, RF-power $P_{RF} = 120$ W. The curves are acquired in different times during the cycle of a -4 kV with $5 \mu s$ duration pulse bias with repetition frequency of 250 Hz at probe location 8.7 cm above silicon and stainless steel targets. The pulse starts at $t = -5 \mu s$ and ends at $t = 0 \mu s$. The grey shade indicates the error boundaries.

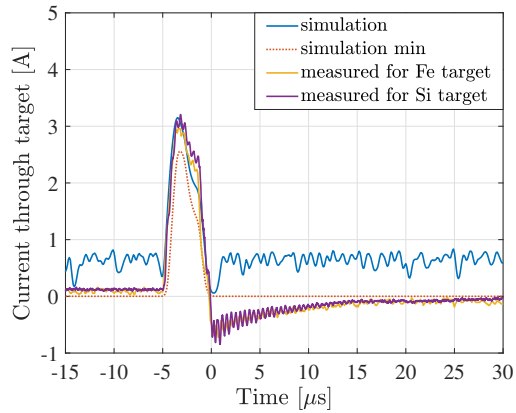
5.6 Plasma Density-Enhancement Effect on Dosimetry

p2i code, used for predicting fluence (dose) implanted on the target during PII is based on Lieberman’s model [4, 5]. The p2i code is written by Marcel Risch [16]. Figures 5.59 and 5.60 show comparisons of the measured current through the stainless steel and silicon targets by Rogowski coil and the predicted current by the p2i code, with the steady state argon plasma information of density, plasma potential and electron temperatures as well as the negative high voltage bias as an input. Figure 5.59 shows the results for -4 kV pulse bias, while figure 5.60 shows the measured and simulation results for -1 kV pulse bias to the targets. The data are acquired with the Pearson model 150 Rogowski coil with a low frequency cut-off of 1 Hz [46]. This cut-off frequency is not applied to the simulations, resulting in a net Bohm current in the grounded time region of the simulations which cannot be measured by the Rogowski coil.

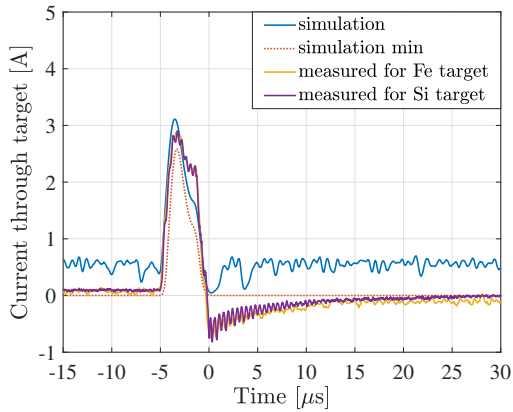
Comparing the time-resolved experimental results to the Lieberman’s model, which assumes the plasma to be in a stationary state with the steady electron temperature and static electron and ion densities, as well as stationary plasma potential during PII, we can notice several discrepancies. The model neglects the electron current through the target. This results in the wrong current prediction while the target is grounded between pulses. During the pulse, p2i code predicts a higher overshoot at first for most discharge conditions. Additionally, p2i fails to simulate the plateau magnitude of the pulse correctly, leading to prediction of a less value even in a short pulse; see figure 2.2b for the discrepancy during a longer duration pulse. These discrepancies leading to the overall lower fluence prediction for PII in all plasma discharges.



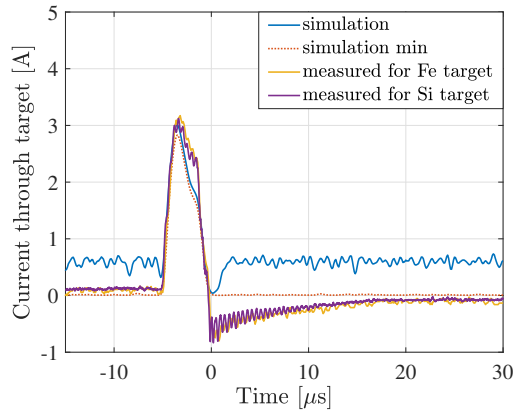
(a) $P_{Ar} = 1.5$ mTorr, $P_{RF} = 120$ W.



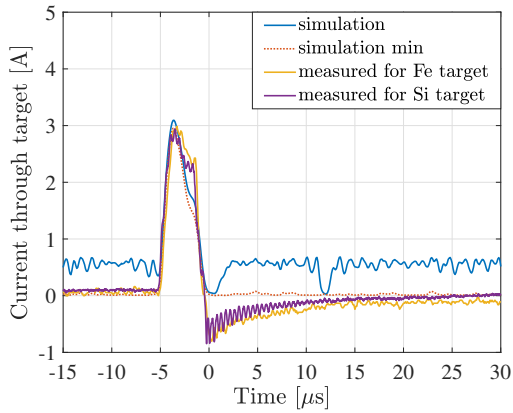
(b) $P_{Ar} = 1.5$ mTorr, $P_{RF} = 300$ W.



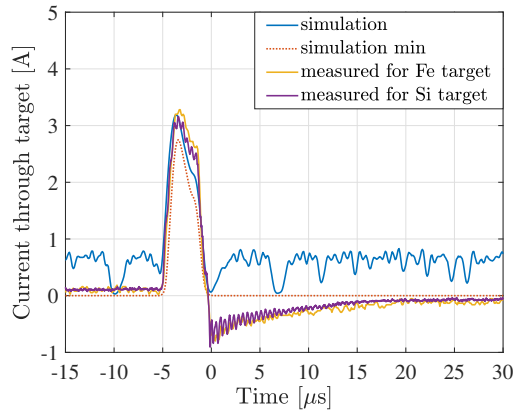
(c) $P_{Ar} = 10$ mTorr, $P_{RF} = 120$ W.



(d) $P_{Ar} = 10$ mTorr, $P_{RF} = 300$ W.



(e) $P_{Ar} = 25$ mTorr, $P_{RF} = 120$ W.



(f) $P_{Ar} = 25$ mTorr, $P_{RF} = 300$ W.

Figure 5.59: A comparison of the current through the stainless steel and silicon targets, as measured by Rogowski coil and simulated by p2i kinetic code which uses Lieberman's model [4] to calculate fluence doped on the target. The measurements and simulations carried out with $V_{pulse} = -4$ kV, $5 \mu s$ duration pulse bias with repetition frequency of 250 Hz. The simulated maximum is too high to be plotted in this figure.

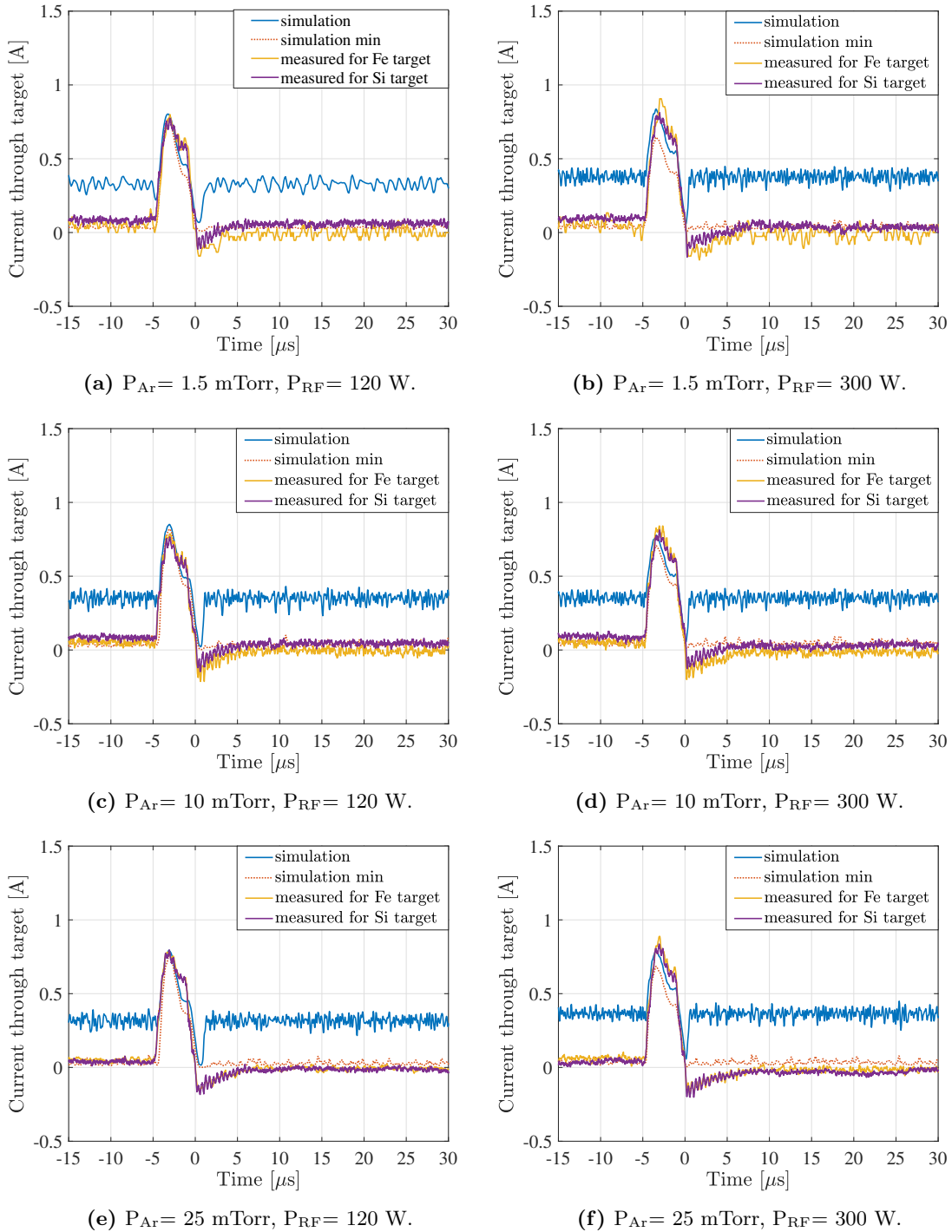


Figure 5.60: A comparison of the current through the stainless steel and silicon targets, as measured by Rogowski coil and simulated by p2i kinetic code which uses Lieberman model [4] to calculate fluence doped on the target. The measurements and simulations carried out with $V_{pulse} = -1 \text{ kV}$, $5 \mu\text{s}$ duration pulse bias with repetition frequency of 250 Hz. The simulated maximum is too high to be plotted in this figure.

5.7 Physical Interpretation of the Results

Table 5.1 summarises the Langmuir analysis results for steady state plasma parameters in the upper probe location, i.e. $z_p = 21.7$ cm above the grounded stainless target.

Table 5.2 summarises the Langmuir analysis results for plasma parameters in the lower probe location, i.e. $z_p = 8.7$ cm above the grounded stainless target.

- Plasma density: Plasma density increases with increasing RF-power and gas pressure. Additionally, the plasma density is higher in the upper probe location, which is closer to the RF-source. Higher RF-power, corresponds to higher energy delivered to the electrons in plasma, thus ionising yet more neutrals. Higher gas pressure means higher number of molecules, thus higher ion and electron density.
- Electron temperature: Electron temperature remains the same in different RF-powers. However, electron temperature and gas pressure have an inverse relation. Also, electrons are warmer in the higher probe location. The RF-source is delivering power to the electrons. Being closer to the source trivially corresponds to higher electron temperature. However, in a fixed location, applying the higher RF-power plasma have the same electron temperature within error boundaries. Despite the higher applied power, the electron temperature stays the same or lowers slightly because of the same absorbed power by the electrons P_{abs} through both Ohmic dissipation and collisionless heating which has an inverse square root relation with plasma density $P_{\text{abs}} \propto n_0^{-1/2} I_{\text{RF}}^2$ in inductively coupled RF discharges [1]. In this relation I_{RF} is the RF source current. Higher gas pressure corresponds to higher number of neutrals, thus electrons in higher pressure cool down by the higher collisions.
- Plasma and floating potentials: Floating potential does not show a tendency within the error bars for different pressure and RF-powers. Remembering $V_p - V_f \propto T_e$ relation [18], plasma potential should follow the electron temperature relations; meaning that plasma potential should remain the same in different RF-powers, while lower with increasing gas pressure. Checking the results obtained for floating and plasma potentials in appendix A, the results for potentials are following the electron temperature results in steady state argon plasma.

Table 5.3 to 5.5 show the tendencies of the evolution of plasma parameters in the bulk plasma during a -1 kV and a -4 kV pulse with the repetition frequency of 250 Hz and pulse duration of 5 μs . The general shape for the high voltage pulse and current going through the targets are shown in figure 5.61.

Table 5.1: Steady state plasma parameters in upper probe location, i.e. $z_p = 21.7$ cm above the stainless steel target

Upper Probe Location					
Argon gas pressure [mTorr]	RF-power [W]	n_0 [$\times 10^9$ cm $^{-3}$]	T_e [eV]	V_p [V]	V_f [V]
1.5	120 W	200 ± 100	4.6 ± 0.8	17.5 ± 2	2.6 ± 0.9
	200 W	350 ± 70	4.4 ± 0.7	18.5 ± 4	2.5 ± 0.4
	300 W	470 ± 60	4.7 ± 0.3	17.8 ± 2.3	2.4 ± 0.8
10	120 W	310 ± 60	4.3 ± 0.5	13.9 ± 0.6	2.3 ± 0.5
	200 W	490 ± 80	4.1 ± 0.2	15 ± 4	1.8 ± 0.1
	300 W	360 ± 60	4.8 ± 0.2	19.1 ± 3.8	2.3 ± 0.1
25	120 W	420 ± 100	3.1 ± 0.8	12.2 ± 1.6	2.9 ± 0.3
	200 W	550 ± 100	3.5 ± 0.4	14.3 ± 1.2	2.8 ± 0.3
	300 W	660 ± 90	3.9 ± 0.5	14 ± 1.5	3.0 ± 0.2

Table 5.2: Steady state plasma parameters in lower probe location, i.e. $z_p = 8.7$ cm above the stainless steel target

Lower Probe Location					
Argon gas pressure [mTorr]	RF-power [W]	n_0 [$\times 10^9$ cm $^{-3}$]	T_e [eV]	V_p [V]	V_f [V]
1.5	80 W	15 ± 6	3.9 ± 1.2	16 ± 7	2.6 ± 0.8
	200 W	130 ± 40	3.1 ± 1.2	14.5 ± 5	4.8 ± 0.7
	300 W	200 ± 50	3.7 ± 0.6	15 ± 2	2.9 ± 0.5
10	200 W	190 ± 40	2.9 ± 0.3	15 ± 4	1.8 ± 0.1
	300 W	220 ± 50	3.0 ± 0.3	19.1 ± 3.8	2.3 ± 0.1
25	120 W	100 ± 50	2.3 ± 1.5	9.9 ± 4.2	5.3 ± 1.8
	200 W	190 ± 40	1.9 ± 0.7	10.6 ± 3.1	6.7 ± 1.7
	300 W	240 ± 30	2.4 ± 0.7	12 ± 2.7	4.6 ± 0.9

Table 5.3: A summary of the general tendency of the plasma parameters in ICP, for both upper and lower probe locations. The results are shown for region 1 (before the pulse starts at $t=-5.0 \mu\text{s}$) and region 2 (coincides with the rise of the pulse between $t=-5.0 \mu\text{s}$ to $t=-4.0 \mu\text{s}$).

		Region 1					Region 2				
		in time	increasing z_p	increasing P_{Ar}	increasing P_{RF}	time	increasing z_p	increasing P_{Ar}	increasing P_{RF}		
-1 kV	n_i	steady	increasing	increasing	increasing	steady	increasing	increasing	increasing	increasing	
	n_e	steady	increasing	increasing	increasing	steady	increasing	increasing	increasing	increasing	
	T_e	steady	inc/steady	decreasing	steady	steady	inc/steady	decreasing	steady	steady	
	V_p	steady	increasing	increasing	increasing	steady	increasing	increasing	increasing	increasing	
	V_f	steady	increasing	increasing	increasing	steady	increasing	increasing	increasing	increasing	
-4 kV	n_i	steady	increasing	increasing	increasing	steady	increasing	increasing	increasing	increasing	
	n_e	steady	increasing	increasing	increasing	steady	increasing	increasing	increasing	increasing	
	T_e	steady	inc/steady	decreasing	steady	steady	inc/steady	decreasing	steady	steady	
	V_p	steady	increasing	increasing	inc/steady	steady	increasing	increasing	inc/steady	inc/steady	
	V_f	steady	increasing	increasing	increasing	decreasing	increasing	increasing	increasing	increasing	

Table 5.4: A summary of the general tendency of the plasma parameters in ICP, for both upper and lower probe locations. The results are shown for region 3 (during the pulse plateau between $t=-4.0 \mu s$ to $t=-1.0 \mu s$) and region 4 (coincides with the fall time of the pulse between $t=-1.0 \mu s$ to $t=-0.0 \mu s$).

		Region 3					Region 4				
	in time	increasing z_p	increasing P_{Ar}	increasing P_{RF}	time	increasing z_p	increasing P_{Ar}	increasing P_{RF}			
-1 kV	n_i	small dip	increasing	increasing	increasing	steady	increasing	increasing	increasing		
	n_e	steady	increasing	increasing	increasing	steady	increasing	increasing	increasing		
	T_e	steady	inc/steady	decreasing	steady	steady	inc/steady	decreasing	steady		
	V_p	steady	increasing	increasing	decreasing	steady	increasing	decreasing	decreasing		
	V_f	steady	increasing	increasing	increasing	steady	increasing	increasing	increasing		
-4 kV	n_i	dip	increasing	increasing	increasing	increasing	increasing	increasing	increasing		
	n_e	steady	increasing	increasing	increasing	steady	increasing	increasing	increasing		
	T_e	steady	inc/steady	decreasing	decreasing	steady	inc/steady	decreasing	decreasing		
	V_p	dip	increasing	increasing	steady	increasing	increasing	increasing	steady		
	V_f	dip	increasing	increasing	increasing	increasing	increasing	increasing	increasing		

Table 5.5: A summary of the general tendency of the plasma parameters in ICP, for both upper and lower probe locations. The results are shown for region 5 (after the pulse ends at $t=0.0 \mu s$ to $t=20 \mu s$ when the current through the target becomes zero in the case of $V_{pulse}=-4 \text{ kV}$) and region 6 (after $t=-20.0 \mu s$ to the next pre-pulse at $t=4 \text{ ms}$).

		Region 5					Region 6					
	in time	increasing z_p	increasing P_{Ar}	increasing P_{RF}	time	increasing z_p	increasing P_{Ar}	increasing P_{RF}	time	increasing z_p	increasing P_{Ar}	increasing P_{RF}
-1 kV	n_i	increasing	increasing	increasing	steady	increasing	increasing	increasing	steady	increasing	increasing	increasing
	n_e	steady	increasing	increasing	steady	increasing	increasing	increasing	steady	increasing	increasing	increasing
	T_e	steady	increasing	decreasing	steady	increasing	decreasing	steady	steady	increasing	decreasing	steady
	V_p	steady	increasing	increasing	decreasing	steady	decreasing	decreasing	steady	increasing	increasing	decreasing
	V_f	first ppp	inc, stronger ppp	inc, stronger ppp	inc, weaker ppp	steady	inc, stronger ppp	inc, weaker ppp	steady	increasing	increasing	increasing
-4 kV	n_i	first ppp	inc, stronger ppp	inc, stronger ppp	inc, weaker ppp	inc, stronger ppp	inc, weaker ppp	inc, weaker ppp	steady	increasing	increasing	increasing
	n_e	dip, then steady	increasing	increasing	weaker dip	increasing	weaker dip	weaker dip	steady	increasing	increasing	increasing
	T_e	steady	increasing	decreasing	decreasing	decreasing	decreasing	decreasing	steady	increasing	decreasing	decreasing
	V_p	ppp	inc, stronger ppp	stronger ppp	weaker ppp	weaker ppp	stronger ppp	weaker ppp	steady	increasing	increasing	steady
	V_f	first ppp	stronger ppp	stronger ppp	weaker ppp	second ppp	stronger ppp	weaker ppp	second ppp	inc, same ppp	inc, same ppp	inc, same ppp

Figure 5.61 shows the general shape for the high voltage pulse and the current going through the stainless steel and silicon targets. The pulse starts at $t = -5 \mu\text{s}$, coincides with the start of region 2. The pulse highest value is reached at $t = -4 \mu\text{s}$, indicating the start of region 3. Region 4 starts after the pulse plateau, at $t = -1 \mu\text{s}$ when the pulse starts to fall to zero. At $t = 0.0 \mu\text{s}$ the pulse ends, starting region 5, when a negative current going through the targets is recorded by Rogowski coil. Region 5 ends at $t = 20 \mu\text{s}$ when both the current through the target and high voltage pulse are zero.

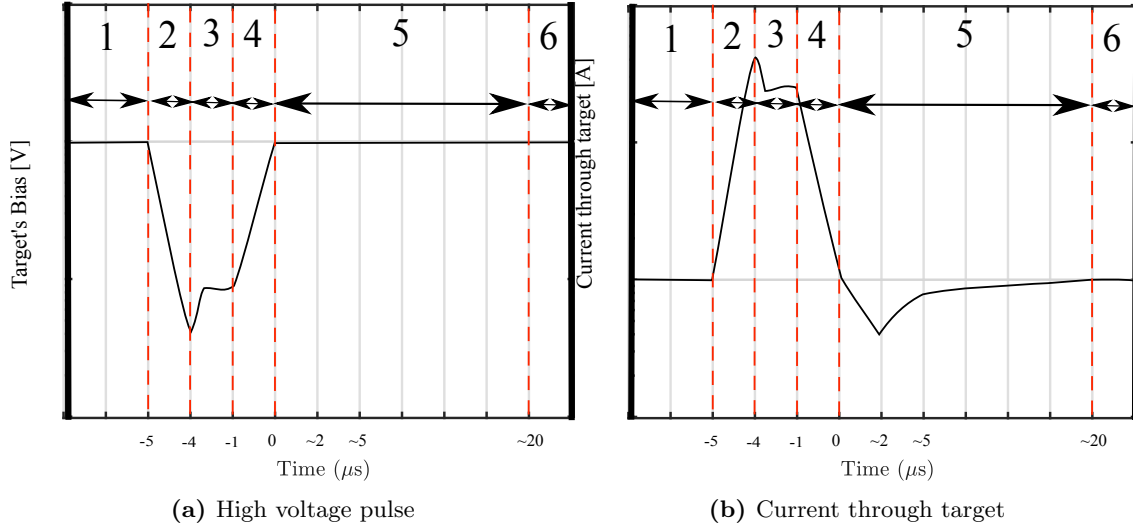


Figure 5.61: (a) A schematic of the high voltage pulse shape, applied to the stainless steel and silicon targets for the PII experiments. The duration for most of the experiments were $5 \mu\text{s}$. The height of the pulse plateau was -4 kV and -1 kV . (b) A schematic of the corresponding current as a function of time shape going through the target during a $5 \mu\text{s}$ pulse.

Figure 5.62 shows a visualisation of the general tendencies of bulk plasma parameters in time. The long range tendency is only shown for floating potential as the direct measurements of floating potential show a second PPP in the long range, while the other plasma parameters stay the same within their error boundaries.

- **Region 1:** Before the pulse starts, the plasma parameters are relatively steady. The electron temperature and floating potential values are higher than the measurements done in steady state. This indicates that the plasma did not have the time to recover to the steady state yet.
- **Region 2:** In the rise time of the pulse, The floating potential is decreasing following the rise of the negative high voltage bias. The floating potential decrease in probe's location is an instant result of changing the plasma boundary conditions. Plasma potential shows only a minimal change, stays at the pre-pulse value within the error boundary. The ion density, is starting to decrease, as the negative pulse attracts ions, forcing the ions in the bulk to rearrange. Electron density and temperature experience a fluctuation toward the higher values in probe's location, indicating a presence of fast electrons in the bulk region coinciding with the start of the negative pulse.

- **Region 3:** During the pulse, the ion density drops to a considerably low value. During the plateau of high voltage negative bias, the ions in the plasma are attracted to the target, leaving the local plasma around the probe with less ions. During the pulse, floating potential experiences a dip. This dip is almost constant for different RF-powers and different argon gas pressures. However the dip value is dependent on the pulse. The longer duration pulse has a longer duration dip, and the higher pulse has a higher dip value. As the floating potential value at each time is dependent on the boundary conditions of the plasma, this dip is a capacitive effect of the high voltage pulse applied to the target. After the high peak value of the pulse is reached, the plasma potential also experiences a dip, with a delay compared to the floating potential. The plasma potential shows some fluctuations during the pulse within the dip limits. Remembering that $V_p - V_f \propto T_e$, the electron temperature as well shows fluctuations in this region, leaning toward slightly higher values than the pre-pulse temperature. Looking at the density of electrons, their density as well shows a fluctuation toward a slightly higher value during the high voltage pulse. The -1 kV pulse do not show any change in the electron temperature and the electron density during the pulse. In addition to this, silicon target seems to show slightly more expanded boundaries of fluctuations for both electron temperature and densities, as well as plasma potential. This phenomena can be explained only by the fast secondary electrons released into the plasma from the target upon ion penetrations through the target.
- **Region 4:** During the fall of the pulse, both the floating potential, the plasma potential and the ion density rise to their pre-pulse values. Electron temperature and density values still have some fluctuations to a slightly higher values, indicating that the fast secondary electrons are still emitting from the target.
- **Region 5:** After the pulse, the floating and plasma potentials are experiencing an intense post-pulse-peak (PPP) at about $t = 2 \mu s$ with a relaxation time in order of $\sim 10 \mu s$. This PPP coincides with the highest value of negative current going through the targets after each pulse. The high voltage, builds a matrix sheath with a thickness of ~ 3 cm around the pulsed target. After the pulse, the highly mobile electrons from plasma bulk are rearranging to fill-in the depleted high voltage sheath, leading to the electron density drop between $t = 0.0 \mu s$ to $t \approx 5 \mu s$ after the pulse ends. The highest drop in electron density occurs at $t \approx 2 \mu s$, around the time of the highest negative electron current through the target. Though there are considerably less number of electrons in the local plasma close to the probe's tip at this time, the RF-source delivers roughly the same constant power to the plasma bulk, leading to heating of the remaining electrons. These hot electrons, ionise the neutral gas in the bulk. The electrons born from this ionisation bring the electron density to the pre-pulse value quickly. The ions however, are a lot less mobile, thus showing a higher density until the relaxation to the pre-pulse value at the end of this time region.
- **Region 6:** After the electron current through the target damps to zero, the floating potential gets

closer to the pre-pulse value after the first PPP. However, the floating potential experiences its second PPP between 0.1 to 1 ms after the end of the pulse. This peak is about 1 V in value but has a long lasting effect until the next pulse especially in lower power plasmas. The other parameters of the plasma has been acquired between $t=-320 \mu s$ and $t= 320 \mu s$. None of the other plasma parameters show a change in the acquired boundary within their error boundaries.

These experimental results are contradictory to the assumptions made by Lieberman's model, discussed in chapter 2. Lieberman's model assumes plasma as a stationary reservoir of ions and neglects plasma density and electron temperature evolution during PII, leading to discrepancies shown between simulation and measurements for fluence prediction in section 5.6. The simulations carried out was using the steady state plasma values obtained by Langmuir method. Throughout the chapter it was shown that plasma does not recover to the steady state values until the next pulse, the steady state assumption is not valid.

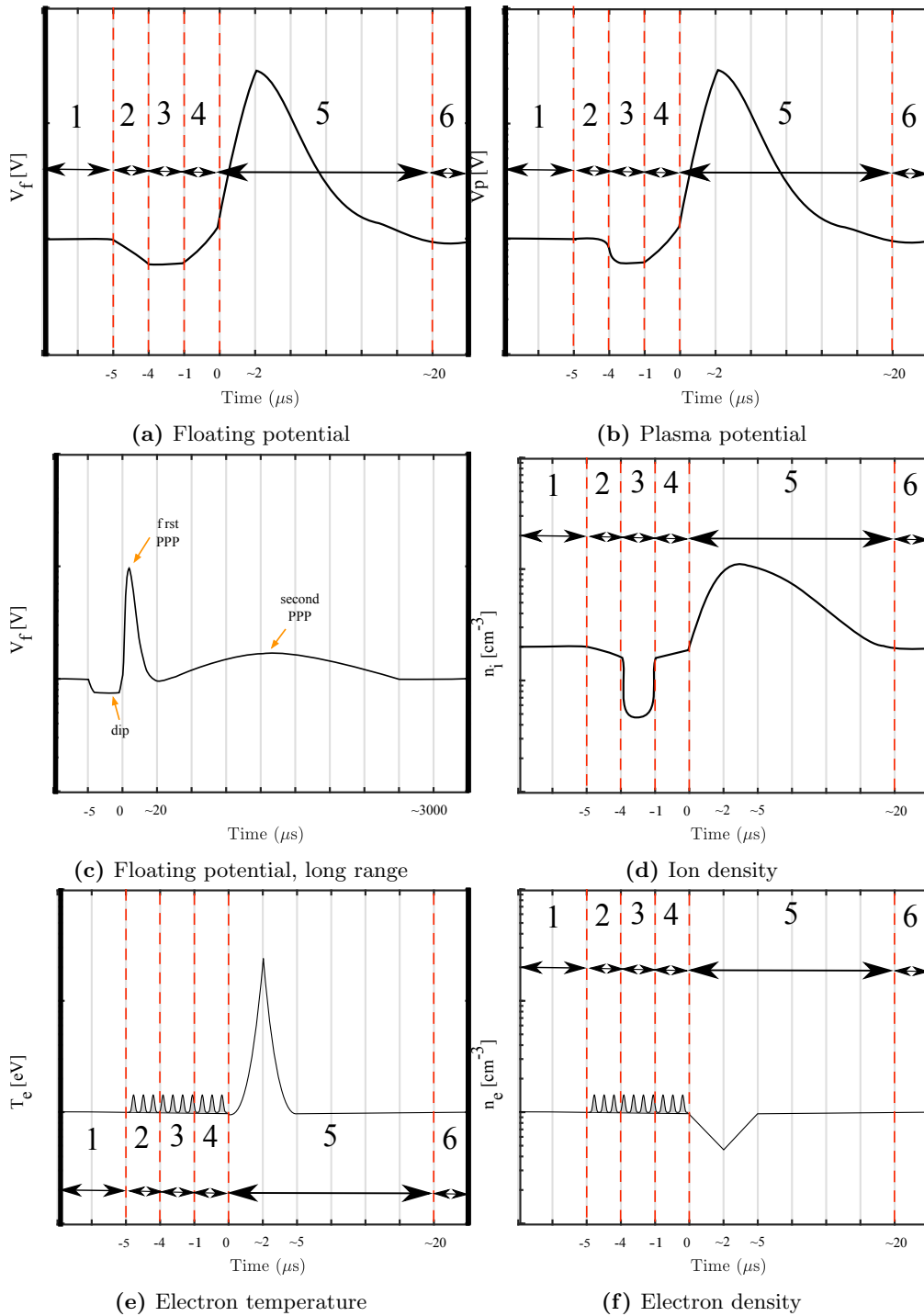


Figure 5.62: Schematics of the general tendency of plasma parameters in the bulk plasma during a high voltage pulse in PII processing in different regions. The schematics are the visualisation of the tendencies of the plasma parameters from tables 5.3, 5.4 and 5.5. A cartoon of the corresponding applied pulse and the current through the targets are presented in figure 5.61a. (a) Floating potential tendency in a short range. (b) Plasma potential tendency in a short range. Plasma potential is flat in region 6. (c) Floating potential tendency in a long range; showing the second post-pulse-peak in floating potential happening in region 6. (d) Tendency of ion density through time. (e) Tendency of electron temperature in time; the small fluctuations shown during the pulse indicate a slightly higher electron temperature. (f) Tendency of electron density in time; the small fluctuations are shown throughout the pulse, indicating a slightly higher electron density during the pulse.

6 CONCLUSION

The core of this project focuses on developing a method for prediction of ion implantation dose in processing plasmas. The vital variable is fluence, i.e. ion implantation dose, which is currently predicted by Lieberman model during high-voltage plasma ion implantation (PII). Having a better, more accurate model to get the fluence, is necessary for improving the implantation procedure.

In Lieberman's Sheath model, sheath current is given by Child law, as the implantation occurs when Child-Langmuir sheath is established during the negative high voltage bias. The important assumptions of the model for solving the Child law's differential equation analytically are, quasi-static ion motion and sheath position, collisionless ion flow, inertialess electrons and infinite ion reservoir.

Inductively coupled plasma (ICP) chambers are used widely for means of plasma ion implantation. One of the ICP chambers in University of Saskatchewan, ICP-600, is provided with a radio-frequency antenna to provide the power to heat the electrons and therefore ionise the gas. A substrate is pulsed with a negative high voltage to implant ions on the substrate. The apparatus is discussed in detail in chapter 3.

Langmuir probes are widely used diagnostic devices for plasma characterisation. As the plasma potential for radio frequency plasmas are oscillating, RF-compensated Langmuir probes are used to acquire accurate characteristics in RF discharges. In order to check the validity of Lieberman's assumptions in our plasma processing setup, I designed a set of experiments to measure the evolution of plasma parameters, namely electron temperature and electron and ion densities, in the bulk of argon plasma during PII.

Lieberman's model uses the steady state values of the plasma parameters. Therefore, having a spatially resolved measurements of the plasma in different discharge conditions provide a basis for the existing model. Additionally, acquisition of steady state measurements provide a steady basis to measure the effect of the pulsed target on the generated plasma in a variety of discharge conditions, i.e. different working RF-power and gas pressure values.

The important control parameters to tune the fluence through the target in each pulse, beside the RF-power and gas pressure, are the pulse magnitude, its duration and the substrate material. In this project, after acquiring a proper steady state characterisation of the plasma, a set of time resolved measurements with pulsed semiconductor, i.e. silicon, and conductor, i.e. stainless steel, were acquired. The direct measurement of the floating potential in the same steady state conditions gives a reference to acquire a dependable current-voltage characteristic of plasma during PII in the next step. By acquiring the floating potential during the pulse, one can know the boundaries of the probe bias sweeps for each given plasma condition, in order to gain a full current-voltage characteristic curve without leaving out plasma voltage. Having acquired

a steady state characteristic of plasma and the floating potential measurement during PII, the current-voltage characterisation in the four extreme discharge conditions, namely highest and lowest RF-powers and gas pressures in two different distances from the pulsed target was performed. The affect of changing the magnitude of the pulse on two materials were also studied in six time regions during each pulse cycle:

- **Region 1:** Right before the pulse starts, the measured plasma parameters, i.e. plasma density, electron temperature and plasma and floating potentials stay steady. Increasing RF-power, leads to increases in plasma density, floating and plasma potentials. However, electron temperature stays the same within the error limits. Increasing Argon gas pressure, results in the rise of plasma density, floating and plasma potentials. However, electron temperature decreases. Moving away from the target toward the RF source results in the rise of all measured plasma parameters. The floating potential increases slightly by increasing the pulse magnitude, while the other measurements stay roughly the same within their error limits.
- **Region 2:** During rise time of the pulse, the floating potential is decreasing. The ion density as well starts to decrease, while electron temperature, plasma potential and electron density show a slight fluctuation toward the higher values in comparison to their pre-pulse values. The effects of increasing RF-power and argon gas pressure, as well as moving away from the target, are the same as the pre-pulse region. Higher pulse magnitude results in higher deviation of the measured parameters from their pre-pulse values.
- **Region 3:** During the high voltage plateau, the floating potential experiences a dip. The ion density as well drops by orders of magnitude, while electron temperature, plasma potential and electron density continue to show a slight fluctuation toward the higher values in comparison to their pre-pulse values. The effects of increasing RF-power and argon gas pressure, as well as moving away from the target, are the same as the pre-pulse region. Higher pulse magnitude results in higher deviation of the measured parameters from their pre-pulse values.
- **Region 4:** During the fall of the voltage pulse, the floating potential and the ion density increase to their pre-pulse values, while electron temperature, plasma potential and electron density continue to show small fluctuations toward the higher values in comparison to their pre-pulse values. The effects of increasing RF-power and argon gas pressure, as well as moving away from the target, are the same as the pre-pulse region. Higher pulse magnitude results in higher deviation of the measured parameters from their pre-pulse values.
- **Region 5:** When the pulse has ended and the Rogowski coil measures a negative current after the pulse, the floating and plasma potentials as well as the electron temperature are experiencing an intense post-pulse-peak (PPP) at about $t = 2 \mu s$ with a relaxation time in order of $\sim 10 \mu s$. This PPP coincides with the highest value of negative current going through the targets after each pulse. At the same time,

the electron density experiences an intense dip which goes back to the pre-pulse value between $t=0$ and $t=5\ \mu\text{s}$ after the end of the pulse. Ion density on the other hand, experiences a peak at about $5\ \mu\text{s}$ after the pulse ends which relaxes back to the pre-pulse value in about $20\ \mu\text{s}$, almost with the end of this region. Increasing argon gas pressure amplifies the deviations from the pre-pulse values for electron temperature, ion and electron density and plasma and floating potentials, while increasing RF-power decreases the deviations from the pre-pulse values. Higher pulse magnitude results in higher deviation of the measured parameters from their pre-pulse values.

- **Region 6:** After the negative current has been damped, the floating potential gets closer to the pre-pulse value after the first PPP. However, the floating potential experiences its second PPP between 0.1 to 1 milliseconds after the end of the pulse. This peak is about 1 V in value but has a long lasting effect until the next pulse especially in lower power plasmas. None of the other plasma parameters show a change in the acquired boundary within their error boundaries.

Finally, using the plasma parameters measured in steady state for different discharge conditions, I carried out Lieberman's sheath simulation using Marcel Risch's p2i code [16] for six discharge conditions, each with two pulse magnitudes, in order to compare the obtained experimental data with Lieberman's sheath simulation results. Comparing the simulation results of the current through the target with the experimental measurements shows that during the pulse, p2i code predicts a higher overshoot at first for most discharge conditions. Additionally, p2i fails to simulate the plateau magnitude of the pulse correctly, leading to prediction of a less value for the current in the plateau. The discrepancies between the experimental data and the simulation are caused by Lieberman's model assumptions for plasma as a stationary reservoir of ions and neglecting plasma density and electron temperature evolution during PII, leading to the overall lower fluence prediction for PII in all plasma discharge conditions.

6.1 Future Work

6.1.1 Experimental Frontier

Characterisation of the steady state plasma can be done with different feed gasses. This will give a better idea of the dependency of the ion densities in different regions of plasma on the ion mass, as well as the effect of the molecular gasses in PII. Study of several gasses during PII can be beneficial in testing the idea of secondary electron emission further as well; due to breaking of molecular gasses into their atoms upon implantation on the substrate. This gives a better idea on the discrepancies between the experimental data and the modellings.

If one is interested in the radial profile of electron density in plasma, a more comprehensive radial measurement with more spacial resolution and coverage can be done. Using a better, less bulky probe design for future measurements, while maintaining the chokes close to the probe tip, would be ideal. The probe's

size plays a role in accuracy of the measurements as a more bulky probe leads to further measurement perturbation of the plasma [25].

The sheath region measurements are an important addition to the presented measurements. High voltage sheath evolution is the most important factor in plasma ion implantation processes and having a comprehensive spacial measurement of the voltage evolution in sheath, especially along the axis of the plate target will help to develop a better, more accurate model of the sheath evolution. This has been done previously by Bradley et al. [45] and can be expanded further in future for different substrates and gasses. Emissive Langmuir probes can be used to study the plasma potential variation in sheath accurately [47].

The plasma enhancement time constant after the pulse can be investigated for different gasses for further investigation of the mechanism responsible for the plasma enhancement during PII. An interesting measurement can be done by changing the pulser's repetition frequency rate. Currently the pulser is hard wired with 250 Hz frequency rate. One can measure the same plasma with same conditions in different pulse repetition frequency values to see the full recovery of plasma to its steady state. Afterwards, the comparison of results from PII with a very low repetition frequency to the models can confirm if the discrepancies are caused by the high voltage pulse perturbing plasma medium, and plasma not being able to recover from it.

RF-compensated Langmuir probe measurements can be complimented by other different methods such as Optical Emission Spectroscopy (OES). Langmuir probe measurements are convenient and practical, however immersing the measurement device into the plasma perturbs the medium. Laser Inductive Fluorescence (LIF) and spectroscopy measurements of the plasma are desirable as the perturbation is minimal. LIF measurements can be carried out in order to give an accurate idea of the local species in plasma regions.

6.1.2 Modelling

Carrying out an accurate simulation of plasma during PII, with taking into account plasma density enhancement due to secondary electron emission is desirable. The transition in sheath structure near the planar emissive surface is studied quite intensively since original work of Hobbs and Wesson in 1967 [48, 49, 50, 51], in which they included electron emission in Child-Langmuir sheath, and showed that when γ_{SE} approaches 1, a potential well forms in the sheath. For cases which γ_{SE} surpasses unity, they predicted that the well shouldn't allow more emission, because the sheath potential is negatively saturated. On the other hand another more recent study by M.D. Campanell [52] predicted a positive "inverse sheath" potential possibility near a surface with $\gamma_{SE} > 1$ [9].

Campanell's work has been done for simulating sheath close to a floating wall. Their model can be modified and used for plasma ion implantation process. In the modified 1D-1V model for PII, one of the floating walls is replaced with an emissive pulsed wall with the desired duration and voltage bias. Starting with a uniform Maxwellian plasma, the plasma then evolves based on the applied boundary conditions. These boundary conditions are included in the Boltzmann distribution equation which governs the evolution of the

electron and ion distribution [9]. One can define the distribution function for $j : e, i$ species as:

$$f_j(x, v_j) = n_0 \sqrt{\frac{m_j}{2\pi k_B T_j}} \exp\left(\frac{-m_j v_j^2}{2k_B T_j}\right), \quad (6.1)$$

to be used in Boltzmann's equation [9]:

$$\frac{\partial f_j}{\partial t} = -v_j \frac{\partial f_j}{\partial x} - \frac{q_j E}{m_j} \frac{\partial f_j}{\partial v_j} + S_{charge(j)} + S_{coll(j)}. \quad (6.2)$$

The code under development in Bradley-Couedel lab will simulate a sheath using a 1D-1V kinetic code following the recent work by Campanell et al. [9] The advancement of Boltzmann's relation 6.2 is carried out in 4 sub-steps: x advection, v_j advectons (governed by the calculated electric field). Advectons in space and velocity can be carried out with 4th order Runge-Kutta method. [9] During PII, one of the walls is at a given potential V_0 while the other wall is grounded (both walls governed by Dirichlet boundary conditions) [9]. Additionally, an external source, with a given power generates the energy for plasma to remain ionised. Plasma pressure as well is the other external parameter determined by the user.

A realistic Charge eXchange (CX) operator can be used which removes fast ions from f_i at each x and replaces them with an equal number of cold ions, in order to satisfy the cold ion condition in ICP plasma [9]. The collision frequency should be proportional to velocity, such that the mean free path is independent of velocity. The mean free path of ions should be set to a large enough value for plasma to be considered as collision-less [9].

In the paper by Campanell et al. [9], electrons in the plasma are assumed to undergo BGK (Bhatnagar-Gross-Krook) thermalisation collisions [53] that leads the electron velocity distribution function at each x towards a 4 eV Maxwellian distribution. See reference [54] for a discussion on the reliability of using BGK model in weakly ionised plasmas. Source term for electrons need to be modified strongly in comparison to Campanell's work in order to get self-consistent source terms for $n_{e,i}$ and T_e with given external conditions.

REFERENCES

- [1] Michael A Lieberman and Alan J Lichtenberg. *Principles of plasma discharges and materials processing*. John Wiley & Sons, 2005.
- [2] Paul K Chu. Recent applications of plasma-based ion implantation and deposition to microelectronic, nano-structured, and biomedical materials. *Surface and Coatings Technology*, 204(18-19):2853–2863, 2010.
- [3] Shu Qin, Michael P Bradley, Peter L Kellerman, and Kouros Saadatmand. Measurements of secondary electron emission and plasma density enhancement for plasma exposed surfaces using an optically isolated faraday cup. *Review of scientific instruments*, 73(3):1153–1156, 2002.
- [4] Michael A Lieberman. Model of plasma immersion ion implantation. *Journal of Applied Physics*, 66(7):2926–2929, 1989.
- [5] Isaac D Sudit and R Claude Woods. A study of the accuracy of various langmuir probe theories. *Journal of applied physics*, 76(8):4488–4498, 1994.
- [6] Gilbert A Emmert and Michael Arthur Henry. Numerical simulation of plasma sheath expansion, with applications to plasma-source ion implantation. *Journal of applied physics*, 71(1):113–117, 1992.
- [7] Boris Briehl and Herbert M Urbassek. Simulation of sheath and presheath dynamics in piii. *Surface and Coatings Technology*, 156(1-3):131–135, 2002.
- [8] William En and Nathan W Cheung. Analytical modeling of plasma immersion ion implantation target current using the spice circuit simulator. *Journal of Vacuum Science & Technology B: Microelectronics and Nanometer Structures Processing, Measurement, and Phenomena*, 12(2):833–837, 1994.
- [9] Michael D Campanell and MV Umansky. Are two plasma equilibrium states possible when the emission coefficient exceeds unity? *Physics of Plasmas*, 24(5):057101, 2017.
- [10] Shu Qin, Chung Chan, and Zhijiang Jin. Plasma immersion ion implantation model including multiple charge state. *Journal of applied physics*, 79(7):3432–3437, 1996.
- [11] James F Ziegler, Matthias D Ziegler, and Jochen P Biersack. Srim—the stopping and range of ions in matter (2010). *Nuclear Instruments and Methods in Physics Research Section B: Beam Interactions with Materials and Atoms*, 268(11-12):1818–1823, 2010.
- [12] Francis F Chen. *Introduction to plasma physics and controlled fusion*, volume 1. Springer, 1984.
- [13] June Young Kim, Hyo-Chang Lee, Dong-Hwan Kim, Yu-Sin Kim, Young-Cheol Kim, and Chin-Wook Chung. Investigation of the boltzmann relation in plasmas with non-maxwellian electron distribution. *Physics of Plasmas*, 21(2):023511, 2014.
- [14] Hyo-Chang Lee. Review of inductively coupled plasmas: Nano-applications and bistable hysteresis physics. *Applied Physics Reviews*, 5(1):011108, 2018.
- [15] RN Franklin. Where is the sheath edge? *Journal of Physics D: Applied Physics*, 37(9):1342, 2004.
- [16] Marcel Risch. *The promise of nitrogen plasma implanted gallium arsenide for band gap engineering*. PhD thesis, University of Saskatchewan, 2008.

- [17] Casper JT Steenkamp. *High power solid state modulator for plasma ion implementation*. PhD thesis, University of Saskatchewan, 2006.
- [18] Harold M Mott-Smith and Irving Langmuir. The theory of collectors in gaseous discharges. *Physical review*, 28(4):727, 1926.
- [19] Francis F Chen and Jane P Chang. *Lecture notes on principles of plasma processing*. Springer Science & Business Media, 2012.
- [20] VA Godyak, RB Piejak, and BM Alexandrovich. Probe diagnostics of non-maxwellian plasmas. *Journal of applied physics*, 73(8):3657–3663, 1993.
- [21] VA Godyak and VI Demidov. Probe measurements of electron-energy distributions in plasmas: what can we measure and how can we achieve reliable results? *Journal of Physics D: Applied Physics*, 44(23):233001, 2011.
- [22] Yakov N Sukhanov, Alexey P Ershov, Konstantin V Rudenko, and Alexander A Orlikovsky. Comparative study of inductively coupled and microwave bf3 plasmas for microelectronic technology applications. In *Micro-and Nanoelectronics 2003*, volume 5401, pages 55–63. International Society for Optics and Photonics, 2004.
- [23] Hong Li. *Measurements of electron energy distribution function and neutral gas temperature in an inductively coupled plasma*. PhD thesis, University of Saskatchewan, 2006.
- [24] Harmeet Singh and David B Graves. Measurements of the electron energy distribution function in molecular gases in an inductively coupled plasma. *Journal of Applied Physics*, 87(9):4098–4106, 2000.
- [25] VA Godyak, RB Piejak, and BM Alexandrovich. Electron energy distribution function measurements and plasma parameters in inductively coupled argon plasma. *Plasma Sources Science and Technology*, 11(4):525, 2002.
- [26] Francis F Chen. Langmuir probe diagnostics. In *IEEE-ICOPS Meeting, Jeju, Korea*, volume 2, 2003.
- [27] O Auciello and DL Flamm. *Plasma Diagnostics, Plasma-materials Interactions, vol. 1*. Academic Press, Boston,[Mass.], 1989.
- [28] MJ Druyvesteyn and Fi M Penning. The mechanism of electrical discharges in gases of low pressure. *Reviews of Modern Physics*, 12(2):87, 1940.
- [29] Kazunori Takahashi. *Pulsed Electrostatic Langmuir Probe Technique for Electron Energy Distribution Function Measurement in Radio-Frequency-Driven Plasmas*. Technical report, Australian National University, 2007.
- [30] Anthony Dyson, Paul Bryant, and John E Allen. Multiple harmonic compensation of langmuir probes in rf discharges. *Measurement Science and Technology*, 11(5):554, 2000.
- [31] JE Allen. Probe theory-the orbital motion approach. *Physica Scripta*, 45(5):497, 1992.
- [32] JE Allen, RLF Boyd, and P Reynolds. The collection of positive ions by a probe immersed in a plasma. *Proceedings of the Physical Society. Section B*, 70(3):297, 1957.
- [33] Francis F Chen. Numerical computations for ion probe characteristics in a collisionless plasma. *Journal of Nuclear Energy. Part C, Plasma Physics, Accelerators, Thermonuclear Research*, 7(1):47, 1965.
- [34] Ira B Bernstein and Irving N Rabinowitz. Theory of electrostatic probes in a low-density plasma. *The Physics of Fluids*, 2(2):112–121, 1959.
- [35] James G Laframboise. *Theory of spherical and cylindrical Langmuir probes in a collisionless, Maxwellian plasma at rest*. Technical report, University of Toronto, 1966.

- [36] Zoltan Sternovsky, Scott Robertson, and Martin Lampe. Ion collection by cylindrical probes in weakly collisional plasmas: theory and experiment. *Journal of applied physics*, 94(3):1374–1381, 2003.
- [37] Z Sternovsky, S Robertson, and M Lampe. The contribution of charge exchange ions to cylindrical langmuir probe current. *Physics of Plasmas*, 10(1):300–309, 2003.
- [38] BL Caughlin and MW Blades. Spatial profiles of electron density in the inductively coupled plasma. *Spectrochimica Acta Part B: Atomic Spectroscopy*, 40(7):987–993, 1985.
- [39] Javad Mostaghimi, Pierre Proulx, and Maher I Boulos. A two-temperature model of the inductively coupled rf plasma. *Journal of applied physics*, 61(5):1753–1760, 1987.
- [40] EAD Carbone, S Hübner, JM Palomares, and JJAM Van der Mullen. The radial contraction of argon microwave plasmas studied by thomson scattering. *Journal of Physics D: Applied Physics*, 45(34):345203, 2012.
- [41] G Shafir, D Zolotukhin, V Godyak, A Shlapakovski, Shmuel Gleizer, Ya Slutsker, Ronny Gad, Vladimir Bernshtam, Yu Ralchenko, and Ya E Krasik. Characterization of inductively coupled plasma generated by a quadruple antenna. *Plasma Sources Science and Technology*, 26(2):025005, 2017.
- [42] Rickey Faehl, Barbara De Volder, and Blake Wood. Application of particle-in-cell simulation to plasma source ion implantation. *Journal of Vacuum Science & Technology B: Microelectronics and Nanometer Structures Processing, Measurement, and Phenomena*, 12(2):884–888, 1994.
- [43] Michael Paulus, Linda Stals, U Rüde, and Bernd Rauschenbach. Two-dimensional simulation of plasma-based ion implantation. *Journal of Applied Physics*, 85(2):761–766, 1999.
- [44] Dixon Tat-Kun Kwok, Paul K Chu, Blake P Wood, and Chung Chan. Particle-in-cell and monte carlo simulation of the hydrogen plasma immersion ion implantation process. *Journal of applied physics*, 86(4):1817–1821, 1999.
- [45] Michael P Bradley and Casper JT Steenkamp. Time-resolved ion and electron current measurements in pulsed plasma sheaths. *IEEE transactions on plasma science*, 34(4):1156–1159, 2006.
- [46] Chris Waters. Current transformers provide accurate isolated measurements. *Power conversion & intelligent motion*, 12(12), 1986.
- [47] JP Sheehan, Yevgeny Raitses, and Noah Hershkowitz. Accurately determining the plasma potential using emissive probes. In *The 33rd International Electric Propulsion Conference, Washington, DC*, 2013.
- [48] GD Hobbs and JA Wesson. Heat flow through a langmuir sheath in the presence of electron emission. *Plasma Physics*, 9(1):85, 1967.
- [49] JP Sheehan, N Hershkowitz, ID Kaganovich, He Wang, Y Raitses, EV Barnat, BR Weatherford, and D Sydorenko. Kinetic theory of plasma sheaths surrounding electron-emitting surfaces. *Physical review letters*, 111(7):075002, 2013.
- [50] JP Sheehan, ID Kaganovich, He Wang, D Sydorenko, Y Raitses, and N Hershkowitz. Effects of emitted electron temperature on the plasma sheath. *Physics of Plasmas*, 21(6):063502, 2014.
- [51] JP Sheehan, Yevgeny Raitses, Noah Hershkowitz, Igor Kaganovich, and Nathaniel J Fisch. A comparison of emissive probe techniques for electric potential measurements in a complex plasma. *Physics of Plasmas*, 18(7):073501, 2011.
- [52] MD Campanell. Negative plasma potential relative to electron-emitting surfaces. *Physical Review E*, 88(3):033103, 2013.
- [53] Prabhu Lal Bhatnagar, Eugene P Gross, and Max Krook. A model for collision processes in gases. i. small amplitude processes in charged and neutral one-component systems. *Physical review*, 94(3):511, 1954.

- [54] D Else, R Kompaneets, and SV Vladimirov. On the reliability of the bhatnagar–gross–krook collision model in weakly ionized plasmas. *Physics of plasmas*, 16(6):062106, 2009.
- [55] N St J Braithwaite, NMP Benjamin, and JE Allen. An electrostatic probe technique for rf plasma. *Journal of Physics E: Scientific Instruments*, 20(8):1046, 1987.
- [56] PA Chatterton, JA Rees, WL Wu, and K Al-Assadi. A self-compensating langmuir probe for use in rf (13.56 mhz) plasma systems. *Vacuum*, 42(7):489–493, 1991.

APPENDIX A

RF-COMPENSATED PROBE: POTENTIAL MEASUREMENTS

A.1 Steady State Argon Plasma Potential

The difference between plasma potential and floating potential is given by the following formula [18]:

$$\Phi_p - \Phi_f = \frac{k_B T_e}{2e} \ln \frac{2M_i}{\pi m_e} \quad (\text{A.1})$$

Note that the knowledge of both electron temperature and ion mass M_i , already provides this information, however because of the possibility of other ion species being present (Ar^{2+} , O^+ , etc) independently measuring the difference ($\Phi_p - \Phi_f$) provides a useful check on the electron temperature results obtained in argon plasma steady state presented in chapter 5. The results for plasma potential and floating potentials are presented in this appendix.

A.1.1 Plasma Potential at Constant Pressure

In this subsection I present measurements of the steady state plasma and floating potentials in the RF-ICP system at two different locations on the axis of the cylindrical chamber, and vertically separated by distance of 13.0 cm. Plasma and floating potentials were made at a number of values of RF-power, ranging from a low of $P_{RF} = 80$ W to a high of $P_{RF} = 300$ W. Measurements were done at three different pressures of Argon, namely 1.5 mTorr, 10 mTorr and 25 mTorr. The following is a study of plasma and floating potential changes by changing RF-power in two constant pressures, namely 1.5mTorr and 25 mTorr.

Probe at Upper Location

Figure A.1 shows plasma and floating potentials in the higher of the two probe location (21.7cm above the stainless steel target plate). Figure A.1a shows results for 1.5 mTorr argon plasma pressure, and A.1b shows results for 25 mTorr gas pressure.

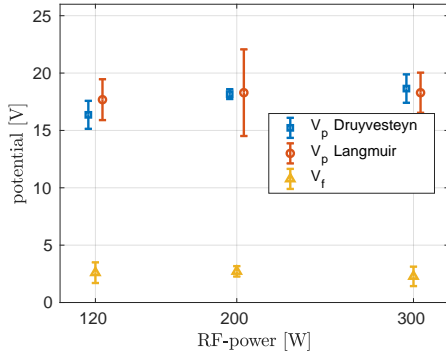
Looking at difference of plasma and floating potentials, in $P_{Ar} = 1.5$ mTorr, the results from Druyvesteyn analysis show a raise in of plasma potential while floating potential stays the same within their corresponding error bars, however the acquainted uncertainties in both floating and plasma potentials are in the range that the difference between plasma and floating potential, thus electron temperature, can be assumed to be unaffected by the power increase. The Langmuir analysis also suggest that RF-power does not affect this difference. The Druyvesteyn result for $P_{Ar} = 1.5$ mTorr and $P_{RF} = 300$ W shows a decrease of plasma potential in comparison to lower RF-power values in same pressure. Checking this result with figure 5.3b, the electron temperature result from Druyvesteyn analysis also shows a decrease in this power, but the corresponding error in finding the second derivative peak value is in the range that the electron temperature can be assumed to be almost constant, within error bars.

Figure A.2 shows the calculated electron temperature using equation A.1 from the difference of plasma and floating potentials in the higher of the two probe location (21.7cm above the stainless steel target plate). Figure A.1a shows results for 1.5 mTorr argon plasma pressure, and A.1b shows results for 25 mTorr gas pressure.

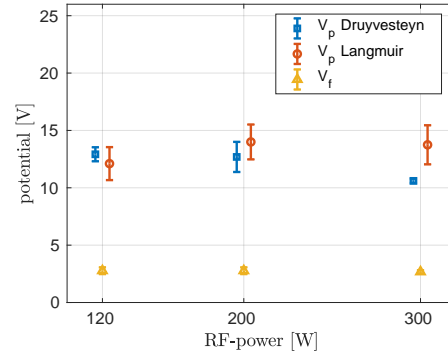
The electron temperature result shown in figure 5.3 from chapter 5 suggest that the electron temperature is not very sensitive to RF-power change within error limit. This is also the case here for the difference of plasma and floating potentials.

Probe at Lower Location

The following graphs show plasma and floating potentials in the lower of the two probe location (8.7 cm above the stainless steel target plate). Figure A.4a shows results for 1.5 mTorr Argon plasma, and A.4b shows results for 25 mTorr Argon gas pressure.

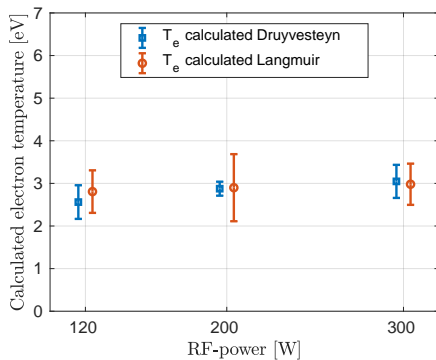


(a) $P_{Ar} = 1.5$ mTorr

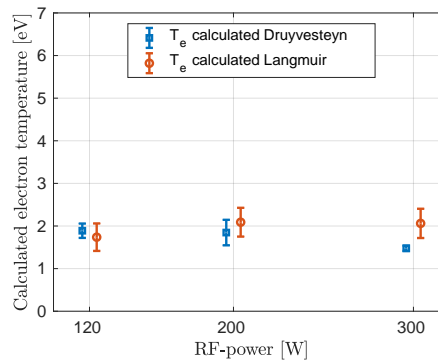


(b) $P_{Ar} = 25$ mTorr

Figure A.1: Steady state Ar plasma and floating potentials as a function of RF-power at two argon plasma pressures, on an axis location 21.7 cm above stainless steel target. Note that two different analysis methods (Druyvesteyn and Langmuir) were used to analyse each Langmuir probe curve as described in chapter 4.



(a) $P_{Ar} = 1.5$ mTorr



(b) $P_{Ar} = 25$ mTorr

Figure A.2: Steady state Ar electron temperature calculated directly from the difference of potentials using equation A.1, as a function of RF-power at two argon plasma pressures, on an axis location 21.7 cm above stainless steel target. Note that two different analysis methods (Druyvesteyn and Langmuir) were used to analyse each Langmuir probe curve as described in chapter 4. Compare these figures to T_e measurements from the analysis, figure 5.3.

Both Langmuir and Druyvesteyn analysis show almost no change in the difference of plasma and floating potentials, i.e. electron temperature, while Druyvesteyn results for 1.5 mTorr argon pressure shows increase from $P_{RF}=80$ W to $P_{RF}=200$ W. however one can see a decrease in this range from the Druyvesteyn analysis for $P_{Ar}=25$ mTorr. Comparing the lower with the upper probe location measurements, results show a decrease in plasma potential while floating potential is raising. One can conclude from the decrease of the plasma potential and floating potential difference, electron temperature at a given P_{RF} and P_{Ar} decreases with moving away from RF source on the chamber's axis.

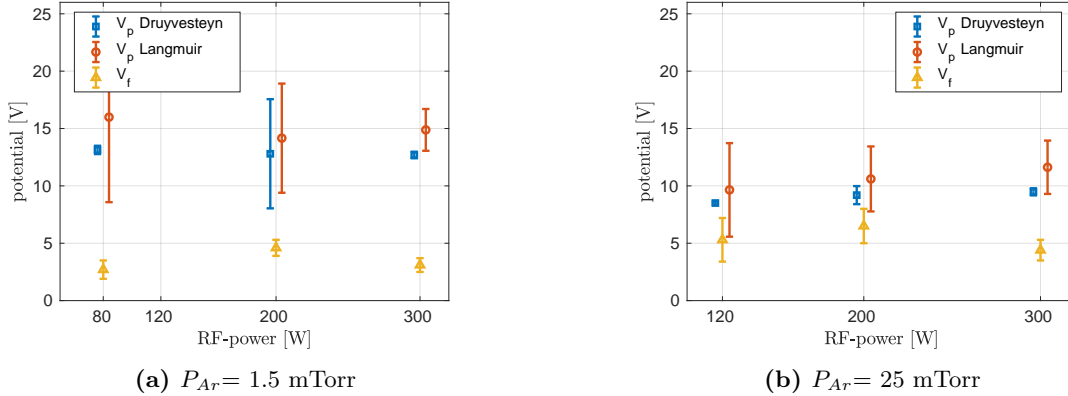


Figure A.3: Steady state Ar plasma and floating potentials as a function of RF-power at two argon plasma pressures, on an axis location 8.7 cm above stainless steel target. Note that four different analysis methods (Druyvesteyn and Langmuir) were used to analyse each Langmuir probe curve as described in chapter 4.

Figure A.4 shows the calculated electron temperature using equation A.1 from the difference of plasma and floating potentials in the higher of the two probe location (21.7cm above the stainless steel target plate). Figure A.4a shows results for 1.5 mTorr argon plasma pressure, and A.4b shows results for 25 mTorr gas pressure.

The electron temperature result shown in figure 5.4 from chapter 5 suggest that the electron temperature is not very sensitive to RF-power change within error limit. This is also the case here for the difference of plasma and floating potentials.

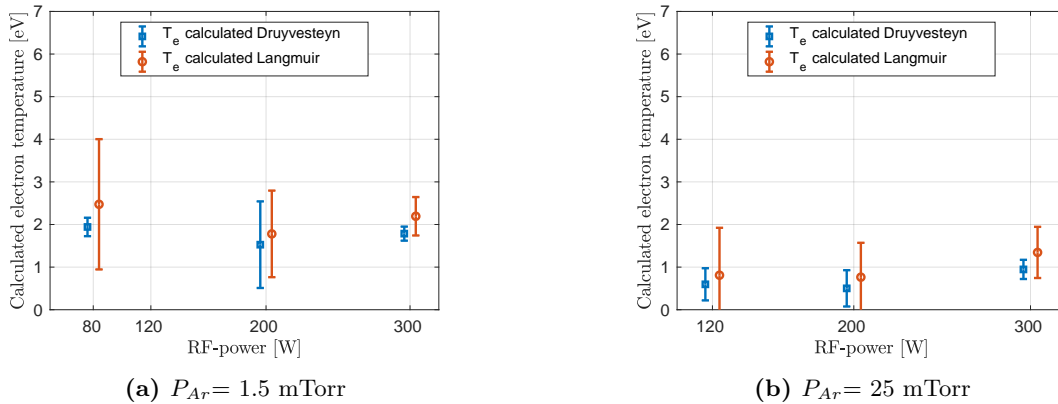


Figure A.4: Steady state Ar electron temperature calculated directly from the difference of potentials using equation A.1, as a function of RF-power at two argon plasma pressures, on an axis location 8.7 cm above stainless steel target. Note that four different analysis methods (Druyvesteyn and Langmuir) were used to analyse each Langmuir probe curve as described in chapter 4. Compare these figures to T_e measurements from the analysis, figure 5.4.

A.1.2 Plasma Potential at Constant RF-Power

In this subsection I present measurements of the steady state plasma density in the RF-ICP system at two different locations on the axis of the cylindrical chamber, and vertically separated by distance of 13.0 cm. Plasma density measurements presented here, were made at two different values of RF-power, $P_{RF} = 120$ W and $P_{RF} = 300$ W. Measurements were done at three different pressures of Argon, namely 1.5 mTorr, 10 mTorr and 25 mTorr. The evolution of electron temperature T_e as a function of pressure at constant P_{RF} is studied here.

Probe at Upper Location

Figure A.5 shows plasma and floating potentials in the higher of the two probe location (21.7 cm above the stainless steel target plate). Figure A.5a shows results for 200 W RF-power, and A.5b shows results for 300 W RF-power.

Both plots show a general increase of floating potential with increasing pressure and report a lower plasma potential while the pressure is increasing. These result in lower difference between the potentials, thus one can expect lower electron temperature by increasing gas pressure. These results confirm the graphs obtained for the electron temperature obtained in chapter 5.

Figure A.6 demonstrates the calculated electron temperature using equation A.1 from the difference of plasma and floating potentials in the higher of the two probe location (21.7cm above the stainless steel target plate). Figure A.6a shows results for $P_{RF} = 200$ W RF-power, and A.6b shows results for $P_{RF} = 300$ W RF-power.

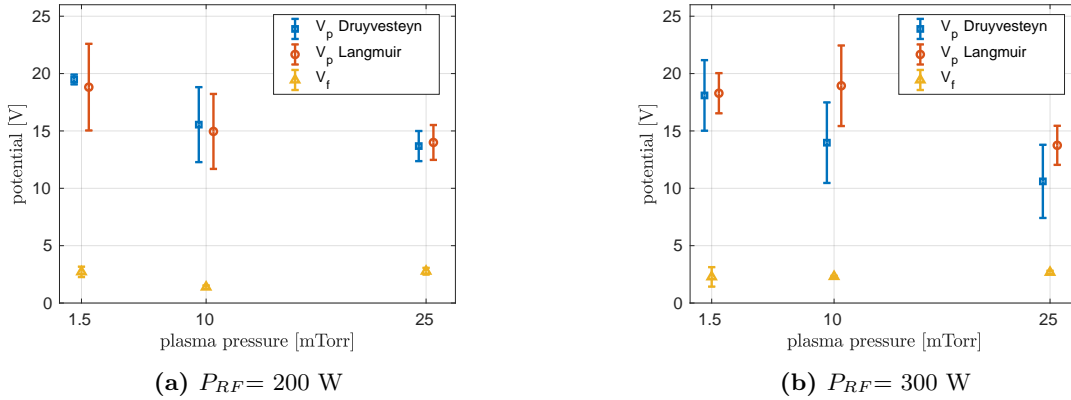


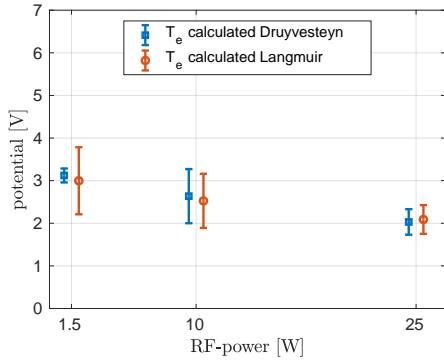
Figure A.5: Steady state Ar plasma and floating potentials as a function of argon plasma pressure at two RF-powers, on an axis location 21.7 cm above stainless steel target. Note that two different analysis methods (Druyvesteyn and Langmuir) were used to analyse each Langmuir probe curve as described in chapter 4.

Probe at Lower Location

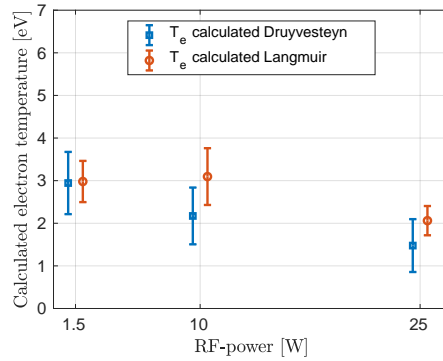
The following figures show plasma and floating potentials in the lower of the two probe locations (8.7 cm above the stainless steel target plate). Figure A.7a shows results for 200 W RF-power, and A.7b shows results for 300 W RF-power.

Both plots show a general increase of floating potential with increasing pressure and report a lower plasma potential while the pressure is increasing. These result in lower difference between the potentials, thus one can expect lower electron temperature by increasing gas pressure. These results confirm the graphs obtained for the electron temperature obtained in chapter 5 which report decrease in electron temperature with raising plasma pressure.

Figure A.8 demonstrates the calculated electron temperature using equation A.1 from the difference of plasma and floating potentials in the higher of the two probe location (21.7cm above the stainless steel target

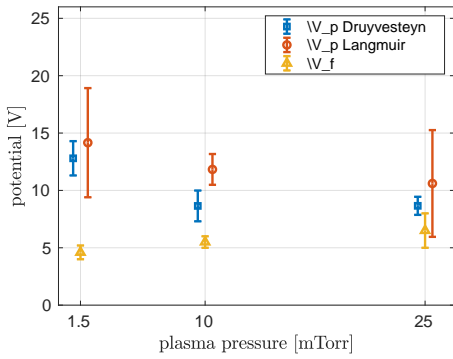


(a) $P_{RF} = 200$ W

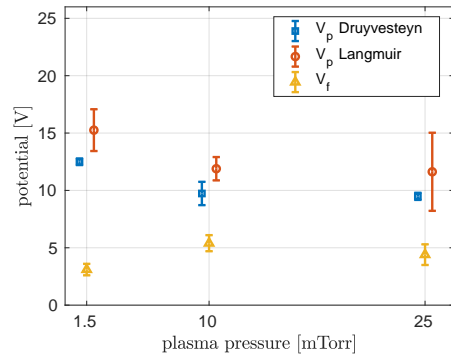


(b) $P_{RF} = 300$ W

Figure A.6: Steady state Ar plasma and floating potentials as a function of argon plasma pressure at two RF-powers, on an axis location 21.7 cm above stainless steel target. Note that two different analysis methods (Druyvesteyn and Langmuir) were used to analyse each Langmuir probe curve as described in chapter 4. Compare these figures to T_e measurements from the analysis, figure 5.7.



(a) $P_{RF} = 200$ W



(b) $P_{RF} = 300$ W

Figure A.7: Steady state Ar electron temperature calculated directly from the difference of potentials using equation A.1, as a function of argon plasma pressure at two RF-powers, on an axis location 8.7 cm above stainless steel target. Note that two different analysis methods (Druyvesteyn and Langmuir) were used to analyse each Langmuir probe curve as described in chapter 4.

plate). Figure A.8a shows results for $P_{RF} = 200$ W RF-power, and A.8b shows results for $P_{RF} = 300$ W RF-power.

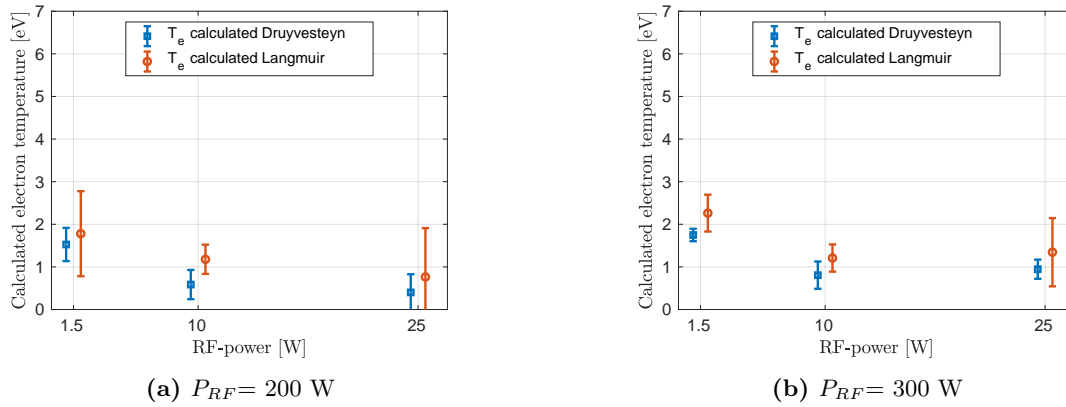


Figure A.8: Steady state Ar electron temperature calculated directly from the difference of potentials using equation A.1, as a function of argon plasma pressure at two RF-powers, on an axis location 8.7 cm above stainless steel target. Note that two different analysis methods (Druyvesteyn and Langmuir) were used to analyse each Langmuir probe curve as described in chapter 4. Compare these figures to T_e measurements from the analysis, figure 5.8.

APPENDIX B

UNCOMPENSATED LANGMUIR PROBE'S MEASUREMENTS

B.0.1 Plasma Density

Plasma density measured by an uncompensated probe, if same theories are applied in the analysis, should be as same as an RF-compensated probe measurement. Figure B.1 shows steady state argon plasma density measurements as a function of RF-power in constant pressure and as a function of Argon gas pressure in constant RF-power. Results are close to figure B.2a and B.2b obtained by the RF-compensated probe.

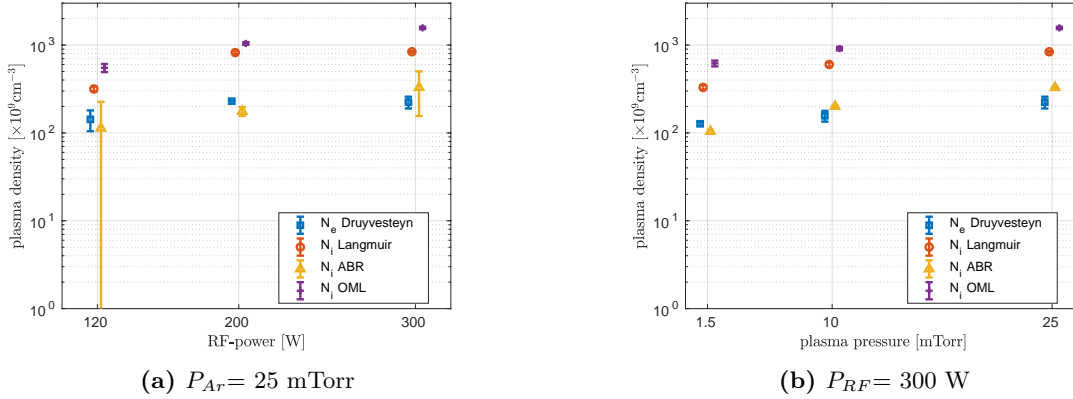


Figure B.1: Steady state Ar plasma density as a function of RF-power in constant pressure and as a function of Argon gas pressure in constant RF-power, on an axis location 21.7 cm above stainless steel target acquired by uncompensated Langmuir probe. Note that four different analysis methods (Druyvesteyn, Langmuir, ABR, and OML) were used to analyse each Langmuir probe curve as described in chapter 4.

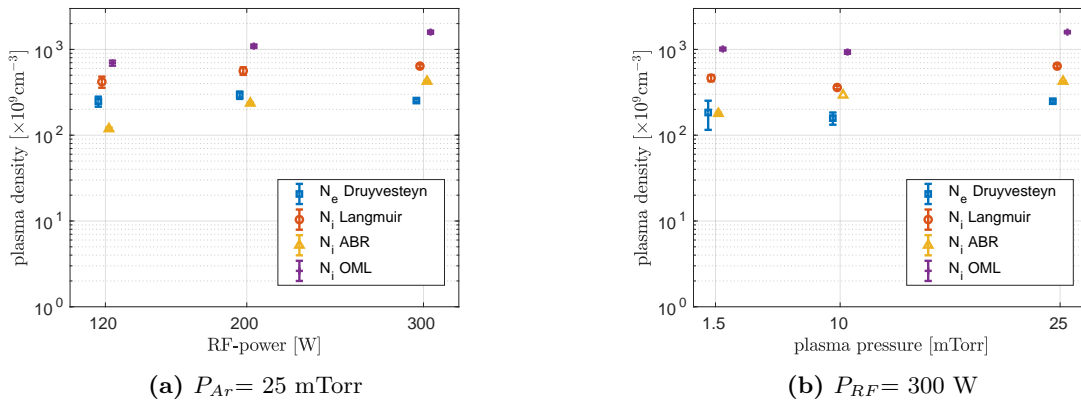


Figure B.2: Steady state Ar plasma density as a function of RF-power in constant pressure and as a function of Argon gas pressure in constant RF-power, on an axis location 21.7 cm above stainless steel target acquired by RF-compensated probe. Note that four different analysis methods (Druyvesteyn, Langmuir, ABR, and OML) were used to analyse each Langmuir probe curve as described in chapter 4.

B.1 Overestimation of Electron Temperature by Uncompensated Probe

As described in the beginning of chapter 5, the difference between plasma potential and floating potential after the analysis of a Langmuir probe's current-voltage characteristic curve, would easily give us the electron temperature of the plasma. An Uncompensated Langmuir probe in an RF-driven plasma would give an overestimation of electron temperature, as the plasma potential, Φ_p is fluctuating with RF-signal from the source antenna and its harmonics while Φ_f is determined with the probe's DC bias and is steady [19]. As the result of this, a wider than "true" Langmuir probe I-V characteristic curve is acquired.

Acquiring an I-V curve in 100 ms, the effect of getting a wider curve, thus acquiring higher than RF-compensated measured electron temperature is minimal, but nonetheless can be measured. The results are shown in the following subsections.

B.1.1 Plasma and floating Potentials

The following figure (figure B.3) is the plasma and floating potentials acquired by an "uncompensated" Langmuir probe immersed in the steady state argon plasma in upper probe location. Figure B.4 shows the same plasma results acquired by the RF-compensated Langmuir probe, presented here for ease of comparison.

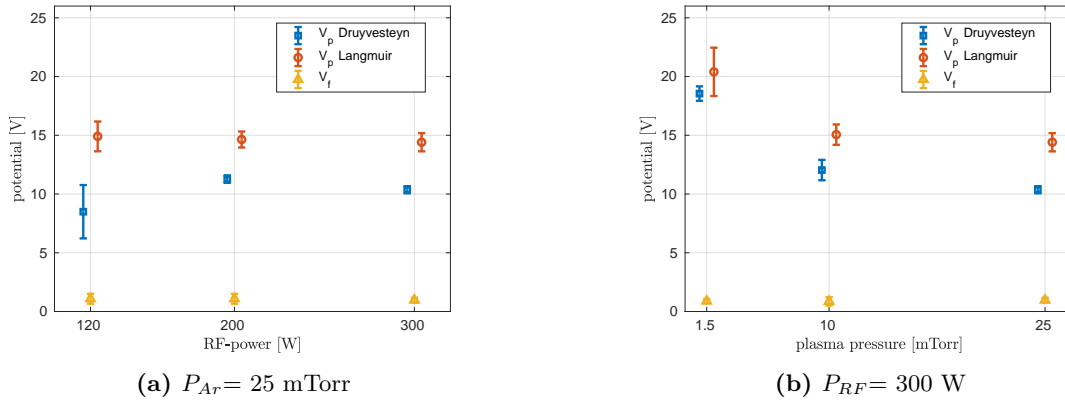


Figure B.3: Steady state Ar plasma density as a function of RF-power in constant pressure and as a function of Argon gas pressure in constant RF-power, on an axis location 21.7 cm above stainless steel target obtained by uncompensated Langmuir probe. Note that four different analysis methods (Druyvesteyn, Langmuir, ABR, and OML) were used to analyse each Langmuir probe curve as described in chapter 4.

B.1.2 Electron Temperature

Electron temperature measured by an uncompensated probe, if same theories are applied in the analysis, shows a higher value compared with RF-compensated probe measurement. Figure B.5 shows steady state argon plasma electron temperature measurements as a function of RF-power in constant pressure and as a function of Argon gas pressure in constant RF-power. Compare figure B.5 to figures B.7a and B.7b obtained by the RF-compensated probe, in order to see the slight overestimation of electron temperature measured by uncompensated Langmuir probe.

Additionally, Figure B.6 shows steady state argon plasma electron temperature calculated using equation A.1 from the uncompensated probe's potential measurements, both as a function of RF-power in constant pressure and as a function of Argon gas pressure in constant RF-power.

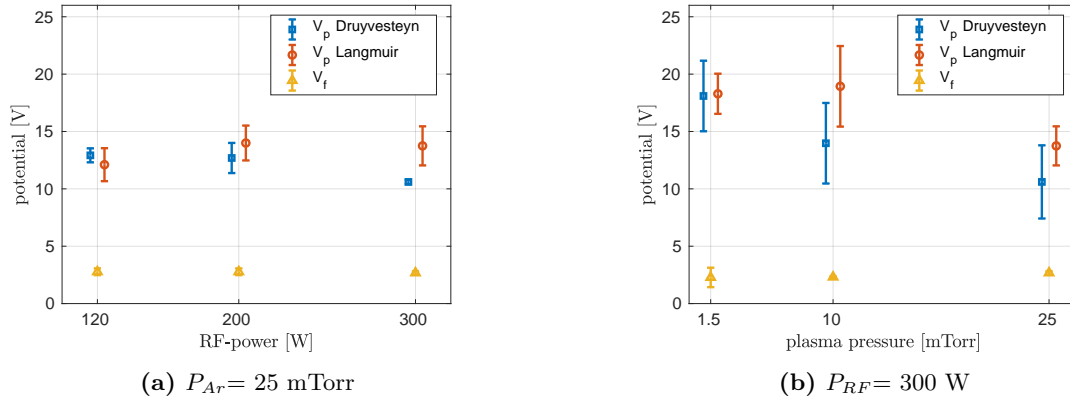


Figure B.4: Steady state Ar plasma density as a function of RF-power in constant pressure and as a function of Argon gas pressure in constant RF-power, on an axis location 21.7 cm above stainless steel target, obtained by RF-compensated Langmuir probe. Note that four different analysis methods (Druyvesteyn, Langmuir, ABR, and OML) were used to analyse each Langmuir probe curve as described in chapter 4.

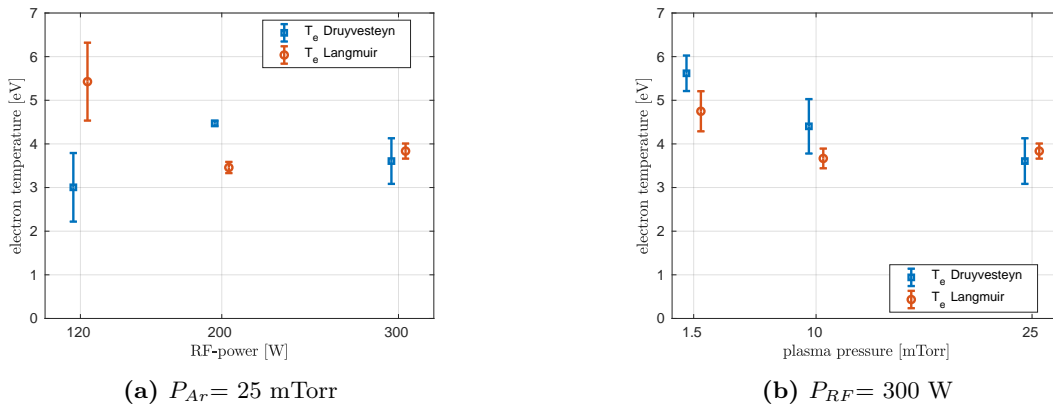
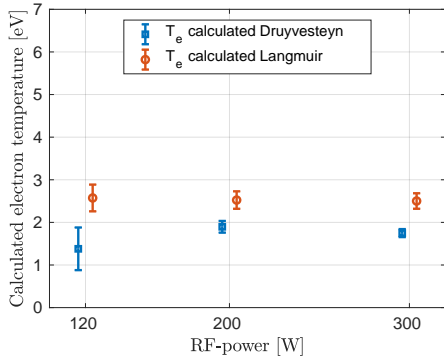
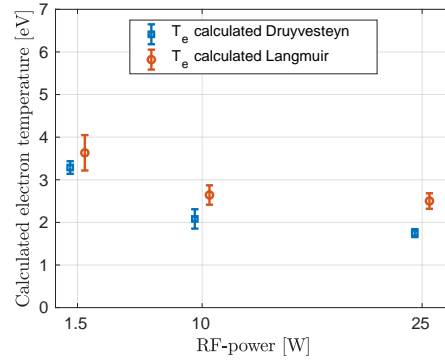


Figure B.5: Steady state Ar electron temperature as a function of RF-power in constant pressure and as a function of Argon gas pressure in constant RF-power, on an axis location 21.7 cm above stainless steel target, acquired by uncompensated Langmuir probe. Note that two different analysis methods (Druyvesteyn and Langmuir) were used to analyse each Langmuir probe curve as described in chapter 4. Compare with values acquired by RF-compensated Langmuir probe, presented in figures B.7a and B.7b.

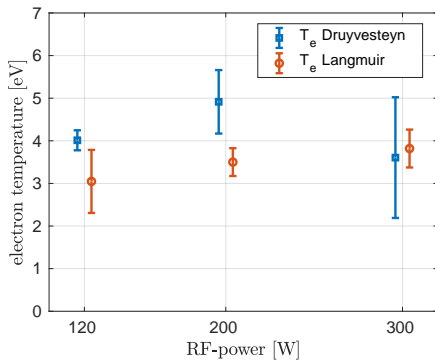


(a) $P_{Ar} = 25$ mTorr

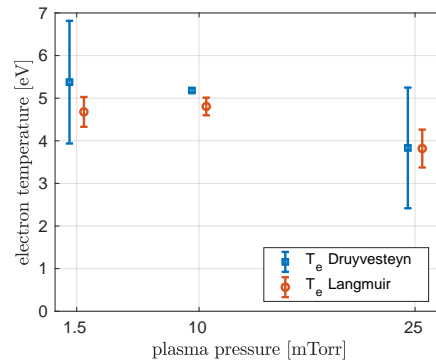


(b) $P_{RF} = 300$ W

Figure B.6: Steady state Ar electron temperature calculated directly from the difference of potentials using equation A.1, as a function of RF-power in constant pressure and as a function of Argon gas pressure in constant RF-power, on an axis location 21.7 cm above stainless steel target. Note that two different analysis methods (Druyvesteyn and Langmuir) were used to analyse each Langmuir probe curve as described in chapter 4. Compare with values acquired by RF-compensated Langmuir probe, presented in figures A.4b and A.8b.



(a) $P_{Ar} = 25$ mTorr



(b) $P_{RF} = 300$ W

Figure B.7: Steady state Ar electron temperature as a function of RF-power in constant pressure and as a function of Argon gas pressure in constant RF-power, on an axis location 21.7 cm above stainless steel target acquired by RF-compensated Langmuir probe. Note that two different analysis methods (Druyvesteyn and Langmuir) were used to analyse each Langmuir probe curve as described in chapter 4. Compare with figure B.5, to see the overestimation of uncompensated probe comparing to the "correct" electron temperature values, measured by RF-compensated Langmuir probe.

APPENDIX C

RF-COMPENSATED LANGMUIR PROBE MECHANICAL DESIGN

In this appendix, the design and the building process of the RF-compensated probe are presented. The designs presented in figure C.1 show the preliminary design of the probe done in SolidWorks. At first, the RF-compensated Langmuir probe was built without a reference electrode to pick up the plasma voltage oscillations. The series of the chokes in the circuitry inside the probe filter out the unwanted RF-oscillations, acquired by the probe; however, it is desirable to use the Langmuir probe in an electrostatic regime [19].

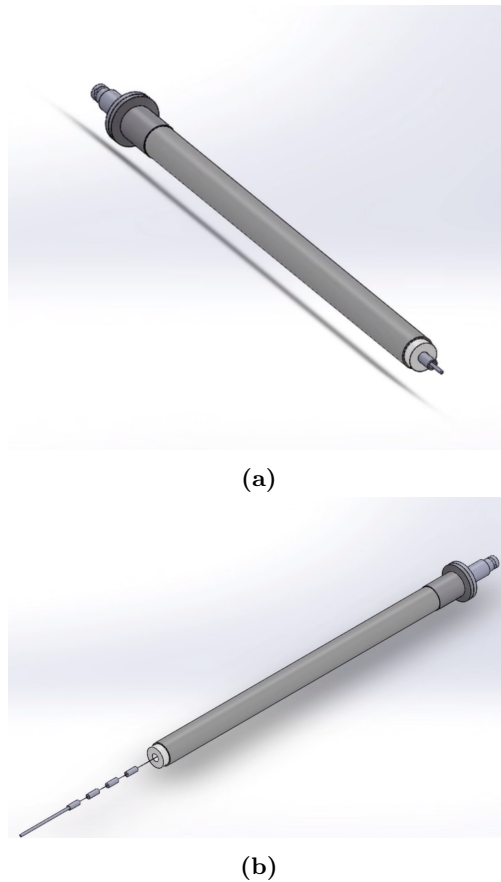


Figure C.1: The design for RF-compensated Langmuir probe without the reference electrode. The thin tungsten tip to be connected to the copper wire sticking out of the torr-sealed ceramic. The chokes should be as close as possible to the probe's tip, which is delivered in this design.

Several groups have reported the comparison of uncompensated, RF-compensated without electrode, and RF-compensated with electrode designs of Langmuir probes [55][56][?]. Their results show that while the RF-compensated probe's electron temperature measurements are not as accurate as RF-compensated with reference electrode, it still reports a less overestimation of the T_e . Figure C.2 shows the Langmuir probe made without the reference electrode.



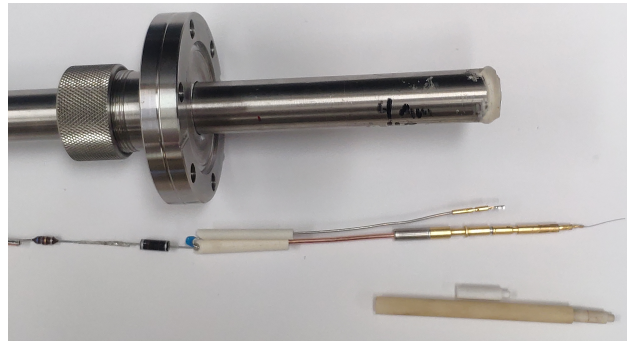
(a) Mechanical components, before assembly



(b) After assembly

Figure C.2: The RF-compensated probe's body made without the reference electrode. before and after the assembly.

Knowing that the reference electrode will improve the accuracy of the results, RF-compensated probe has been rebuilt with new chokes and a reference electrode. Figure C.3 shows the Langmuir probe made with the reference electrode, used in the current project.



(a) RF-compensated Langmuir probe's components



(b) The final assembly of RF-compensated Langmuir probe

Figure C.3: RF-compensated Langmuir probe with electrode. (a) A 18 nF capacitor was used between the reference electrode and a series of 13.56 MHz and 27.12 MHz self-resonant chokes. (b) P1 is the tungsten probe tip (5.0 mm length, 1.0 mm diameter) and P2 is a copper ring ($A_2 = 30\pi \text{ mm}^2$) acting as the reference electrode.